Multimodal image registration for the characterization of the hypertrophic cardiomyopathy and the cardiac asynchronism

Julian Andrés Betancur Acevedo

To cite this version:

Julian Andrés Betancur Acevedo. Multimodal image registration for the characterization of the hypertrophic cardiomyopathy and the cardiac asynchronism. Signal and Image processing. Université de Rennes, 2014. English. NNT : 2014REN1S089 . tel-01127642

HAL Id: tel-01127642
https://theses.hal.science/tel-01127642v1

Submitted on 7 Mar 2015

ANNÉE 2014

THÈSE / UNIVERSITÉ DE RENNES 1
sous le sceau de l'Université Européenne de Bretagne

pour le grade de
DOCTEUR DE L'UNIVERSITÉ DE RENNES 1

Mention : Traitement du Signal et Télécommunications
École doctorale Matisse

présentée par

Julian Andrés BETANCUR ACEVEDO

Préparée à l'unité de recherche LTSI-INSERM, U1099
Laboratoire Traitement du Signal et de l'Image
UFR ISTIC: Informatique et Électronique

Intégration d'images multimodales pour la caractérisation de cardiomyopathies hypertrophiques et d'asynchronismes cardiaques

Thèse à soutenir à Rennes
le 27 mai 2014
devant le jury composé de :

Jacques FELBLINGER
PU-PH, CHU Hôpitaux de Nancy-Brabois / *Rapporteur*
Denis FRIBOULET
PU, Creatis, Lyon / *Président, Rapporteur*
Alain LALANDE
MCU HDR, Le2I, Université de Bourgogne / *Examinateur*
Alfredo HERNÁNDEZ
DR INSERM, Université de Rennes 1 / *Examinateur*
Erwan DONAL
PU-PH, Université de Rennes 1, CHU de Rennes / *Invité*
Mireille GARREAU
PU, Université de Rennes 1 / *Directrice de thèse*
Antoine SIMON
MCU, Université de Rennes 1 / *Co-directeur de thèse*

À ma femme Zulma,
ma fille Helena,
et mes parents Jairo et Amanda.
Merci d'être toujours là pour moi.

To my wife Zulma,
my daughter Helena,
and my parents Jairo and Amanda.
Thanks for always being there for me.

Remerciements

Je tiens à remercier Monsieur L. SENHADJI, Professeur des universités à l'Université de Rennes 1 et Directeur du Laboratoire Traitement du Signal et de l'Image (LTSI-INSERM U1099), de m'avoir accueilli dans son laboratoire. Je tiens également à remercier Monsieur P. HAIGRON, Professeur des universités à l'Université de Rennes 1, et Monsieur R. DE CREVOISIER, Professeur des universités au Centre Eugène Marquis de Rennes, responsables de l'équipe IMPACT, de m'avoir accueilli dans leur équipe.

Je tiens à exprimer ma profonde reconnaissance et mes sincères remerciements à ma Directrice de Thèse, Madame M. GARREAU, Professeur des universités à l'Université de Rennes 1, et à mon co-directeur de thèse, Monsieur A. SIMON, Maître de conférences à l'Université de Rennes 1, pour le soutien scientifique et moral qu'ils ont su m'accorder tout au long de ce travail et pour les nombreuses aides qu'ils ont apportées dans la rédaction de ce manuscrit. Je tiens aussi à remercier Monsieur A. HERNANDEZ, Directeur de recherche de l'INSERM au LTSI-INSERM U1099, pour son soutien scientifique et moral et pour ses conseils avisés qui ont contribué au bon déroulement de ce travail. J'espère que les liens professionnnels et amicaux tissés entre nous quatre au cours de ces années ne cesseront de se renforcer.

J'exprime ma gratitude à Monsieur D. FRIBOULET, Professeur 61ème section CNU à CREATIS-INSA Lyon, pour l'honneur qu'il m'a témoigné en acceptant de présider mon jury. J'adresse mes sincères remerciements à lui et à Monsieur J. FELBLINGER, Professeur des universités à l'Université de Lorraine, pour avoir accepté d'être les rapporteurs de ma thèse. Je tiens à les remercier pour le temps et le dévouement qu'ils ont su consacrer à la rédaction du rapport et, plus particulièrement, pour les remarques et conseils qu'ils ont su me donner.

Je remercie Monsieur A. LALANDE, Maître de conférences à l'Université de Bourgogne, et Monsieur E. Donal, Professeur au CHU-Pontchaillou de Rennes, qui ont bien voulu participer à mon jury.

J'ai eu la chance de compter avec la collaboration d'un expert cardiologue, non seulement pour ses qualités scientifiques et médicales, mais aussi pour ses qualités humaines. Je remercie donc très chaleureusement Monsieur F. SCHNELL, Médecin du sport et cardiologue au CHU-Pontchaillou de Rennes. Ces années ont mis en relief le caractère amical et fructueux de notre collaboration.

Je remercie Monsieur O. ACOSTA, Maître de conférences à l'Université de Rennes 1, pour son soutien, ses remarques scientifiques et ses bons conseils.

Je remercie également tous ceux qui ont pu m'aider sur les plans scientifique, technique et humain.

Je pense à mes collègues et ex-collègues du laboratoire F. TAVARD, M. CASTRO, G. DREAN, A. OUKILI, J-D. OSPINA, X. NAVARRO, D. OJEDA, M. ALTUVE, S. WONG, F. MINA, G. CAZOULAT, J-J. MANTILLA, A. BRAVO, E. HALBERT, R. GUTIERREZ, R. RIOS, A. BEHAGHEL et S. BRUGE pour leur aide, soutien scientifique et technique, bonne humeur et amabilité. Je pense aussi à Mesdames P. BERNABE, M. DIOP et S. CHARPENTIER, qui ont su m'aider dans les différentes gestions administratives et ont fait preuve d'une grande gentillesse et sympathie.

Je remercie vivement ma famille pour son soutien inconditionnel. J'ai une pensée spéciale pour ma femme Zulma et ma fille Helena qui me comblent de bonheur. Aussi, j'ai eu la chance de compter sur les conseils avisés de Zulma. Ses remarques pertinentes m'ont été d'une aide précieuse pout mener à bien ce travail de recherche.

Ces travaux de Doctorat ont été réalisés à partir de données patients acquises par le LTSI-INSERM U1099 en collaboration avec le CHU-Pontchaillou de Rennes dans le cadre du projet IMOP ANR-CITH N° 04 187-188-189-190 et du projet européen euHeart FP7/2008-2012, N° 224495.

Résumé en français

Les pathologies cardiovasculaires restent la cause de mortalité la plus importante à travers le monde. Selon l'Organisation Mondiale de la Santé (WHO, 2011), le nombre de décès par maladies cardio-vasculaires s'élèvait à plus de dix-sept millions en 2008 et des prévisions l'estiment à plus de vingt-trois millions pour 2030. Parmi les maladies cardiovasculaires, la cardiomyopathie hypertrophique (CMH) est une pathologie cardiovasculaire génétique courante, avec une prévalence de l'hypertrophie du ventricule gauche de l'ordre de 0.2 % sur la population générale (MARON, 2004) (GERSH et al., 2011). D'un point de vue physiologique, les modifications tissulaires de la CMH se caractérisent non seulement par un épaississement du myocarde mais aussi par une désorganisation architecturale du myocarde er par la présence de fibrose. L'HCM est une maladie de pronostic très variable : certains patients décèderont de mort subite (MARON, 2010), d'autres développeront une fibrillation atriale (OLIVOTTO et al., 2001) avec embolies artérielles (HARRIS et al., 2006), d'autres souffriront d'insuffisance cardiaque avec, dans la plupart des cas, une fraction d'éjection ventriculaire gauche préservée, et certains resteront asymptomatiques. Le diagnostic précoce de l'HCM représente donc un grand enjeu médical et la caractérisation précise de cette pathologie par l'imagerie fait l'objet de nombreux travaux de recherche.

L'insuffisance cardiaque (IC) est une autre pathologie cardiovasculaire qui concerne 2 % à 3 % de la population dans les pays développés, atteignant plus de 20 % sur la population âgée (>70 ans). L'IC est définie comme une anomalie de la fonction cardiaque conduisant à l'incapacité du cœur à assurer un débit sanguin nécessaire au bon fonctionnement des organes et tissus du corps. Le diagnostic d'une IC est conduit à partir de l'enregistrement de différentes données relevant du signal et de l'image, dont l'échographie cardiaque (échocardiographie) qui représente un examen clinique de référence. Au sein de la population présentant une insuffisance cardiaque, on estime que 30 % à 40 % des patients souffrent d'un défaut de synchronisation ou asynchronisme cardiaque qui peut être de différentes natures : asynchronisme auriculo-ventriculaire, interventriculaire ou intra-ventriculaire. Les traitements peuvent en premier lieu concerner des mesures prises sur les habitudes de vie ou des prises médicamenteuses. Pour les patients non récepteurs au traitement pharmaceutique, une intervention est réalisée, correspondant à l'implantation d'un stimulateur cardiaque. La thérapie de resynchronisation cardiaque

(CRT) a été validée en tant qu'intervention efficace pour traiter des patients en insuffisance cardiaque. Elle est appliquée lorsque l'IC est chronique et que certains indicateurs sont vérifiés (fraction d'éjection inférieure à 35 %, durée de l'onde QRS supérieure à 120 ms, patient de classe NYHA III). Cette thérapie consiste en la pose d'un stimulateur cardiaque multisites relié à une pile. Plusieurs schémas d'implantation existent, parmi lesquels la stimulation bi-ventriculaire développée au CHU de Rennes. Les thérapies de resynchronisation cardiaque améliorent les conditions de vie des patients traités, ainsi que le taux de mortalité à court et à plus long terme dans 70 % des cas. Cependant environ 30 % des patients traités ne répondent pas positivement au traitement. Les différentes voies permettant d'envisager une optimisation de la procédure et une augmentation du nombre de répondeurs sont : (i) une meilleure sélection des patients ; (ii) une aide à la réalisation du geste par un choix optimal des sites de stimulation (en particulier le site de stimulation ventriculaire gauche) et par une meilleure caractérisation du réseau coronaire veineux ; (iii) un réglage optimal des paramètres du stimulateur notamment des délais d'activation auriculoventriculaire et inter-ventriculaires.

Nous proposons dans ce travail la fusion de données multimodales avec pour objectif d'améliorer la caractérisation et la prise en charge des maladies cardiovasculaires dans le contexte de la cardiomyopathie hypertrophique (HCM) d'une part, de l'asynchronisme chez les patients souffrant d'insuffisance cardiaque (IC) d'autre part.

Concernant l'HCM, une meilleure caractérisation est recherchée par la fusion d'images acquises en imagerie par résonance magnétique cardiaque (IRMC) et d'échocardiographies (US). L'analyse menée vise en particulier à évaluer l'apport de l'échocardiographie de speckle tracking (STE) pour une caractérisation précoce de l'HCM, l'échographie étant une modalité non invasive et de pratique courante. L'enjeu est ici d'étudier la corrélation entre modification tissulaire (ou présence de fibrose) détectée sur des séquences IRM de rehaussement tardif (LGE-MRI) et modification des paramètres mécaniques de déformation myocardique mesurés en échocardiographie de strain, ce qui conforterait la suspicion de fibrose en cas de strain diminué et mesuré précocement en échographie.

Concernant l'asynchronisme, la fusion d'images cardiaques a pour but d'optimiser la réalisation de la thérapie par resynchronisation cardiaque à travers une meilleure caractérisation des sites potentiels de stimulation. Cette caractérisation est recherchée au moyen de l'intégration et de la fusion de différentes sources d'informations complémentaires issues de modalités d'observation signal et/ou image, portant à la fois sur l'anatomie (imagerie scanner (CT) et IRM), la fonction mécanique (échocardiographie) et l'activité électrique du cœur (cartographies électro-anatomiques), et pouvant être enregistrées à différents stades de la prise en charge du patient, en situations pré-, per- et post-interventionnelles. Il s'agit donc de développer des méthodes d'intégration et de fusion de données permettant d'améliorer la caractérisation du cœur avec notamment la description du couplage électromécanique associé localement à la structure anatomique et tissulaire du myocarde. L'enjeu est de permettre une meilleure caractérisation des sites de stimulation du ventricule gauche dans le but d'extraire de nouveaux marqueurs de la non-réponse à la CRT.

Ces travaux se sont déroulés dans le cadre de deux projets de recherche portant sur la thérapie de resynchronisation cardiaque : (i) le projet IMOP (utilité de l'Imagerie Médicale dans l'Optimisation de la Pose de prothèses cardiaques implantables) financé par le Ministère de la recherche (2005-2008) mené au Laboratoire Traitement du Signal et de l'Image (LTSI) et mis en place en coopération avec le Centre d'Investigation Clinique Innovation Technologique (CIC-IT) du centre de cardiologie du CHU de Pontchaillou à Rennes ; (ii) le projet européen euHeart, coordonné par la société Philips (Aix, Allemagne) et rassemblant dix-sept partenaires (industriels, académiques et cliniques) dont le LTSI - INSERM en coopération avec le Département de Cardiologie et Maladies Vasculaires du CHU de Pontchaillou.

Les modalités d'imagerie considérées dans ce travail sont les suivantes : (i) l'IRM cardiaque, avec notamment les acquisitions ciné-IRM, qui fournissent une description anatomique dynamique du cœur, et les acquisitions de rehaussement tardif (LGE-MRI), permettant d'évaluer la présence de fibrose ; (ii) l'échographie et notamment l'échographie de speckle tracking, permettant l'analyse des déformations de la paroi ; (iii) l'imagerie scanner (CT) fournissant une description, éventuellement dynamique, précise de la paroi et des veines coronaires ; (iv) les cartographies électro-anatomiques qui, dans le contexte de l'asynchronisme, permettent d'acquérir l'activité électrique locale du cœur. Le recalage de ces images et la fusion des descripteurs qu'elles fournissent posent de nombreuses difficultés méthodologiques liées à l'hétérogénéité des données, que ce soit en termes de résolutions spatiales et temporelles, de nature de l'information présentée, d'éventuels artefacts d'acquisitions, etc.

Ainsi, des méthodes ont été tout d'abord proposées pour corriger les artefacts de mouvement fréquemment présents dans les images IRM et recaler les acquisitions cine-MRI avec les acquisitions LGE-MRI. La correction des artefacts de mouvement repose sur un recalage géométrique entre les coupes composant différentes vues (petit-axe, 4-cavités et 2-cavités) suivant des métriques estimées sur les profils d'intersection entre coupes. Différentes métriques ont été évaluées avec un protocole permettant de quantifier la performance de métriques de recalage (Skerl et al., 2006). Ainsi, la métrique reposant sur la différence entre images structurelles (obtenues par calcul d'entropies) est apparue comme étant la plus appropriée pour un recalage entre vues de type LGE-MRI. Pour le recalage inter-séquence entre les acquisitions cine-MRI et LGE-MRI, la métrique reposant sur l'information mutuelle normalisée a obtenu les meilleurs résultats. Enfin, la correction de mouvement de séquences cine-MRI a été évaluée visuellement par un expert, montrant de bons résultats, si ne c'est dans la région de l'apex, région plus difficile à imager correctement en IRM.

Ensuite, ce travail a porté sur le recalage entre images cine-MRI et images scanner (CT) pour lequel, à notre connaissance, aucune méthode n'a été proposée dans la littérature.

Une méthode de recalage spatio-temporel exploitant l'information dynamique à la fois du cine-MRI et du CT a été développée. Elle repose tout d'abord sur une méthode de Déformation Temporelle Dynamique Adaptative (Adaptive Dynamic Time Warping, ADTW) appliquée aux courbes de corrélation croisée normalisée extraites du CT et du cine-MRI. Cette méthode permet de compenser les non-linéarités des modifications de la dynamique cardiaque liées à des fréquences cardiaques différentes. Ensuite, un recalage multi-image, c'est-à-dire considérant l'ensemble des images composant les séquences dynamiques, est appliqué. Cette méthode a été évaluée en trois étapes : (i) évaluation de l'alignement temporel, montrant la supériorité de l'approche ADTW ; (ii) sélection de la métrique de recalage la plus adaptée, grâce au protocole de (SKERL et al., 2006), montrant que l'information mutuelle normalisée est la métrique la plus efficace ; (iii) évaluation du résultat du recalage sur données réelles suivant une erreur de mise en correspondance de points anatomiques, montrant que l'utilisation de l'ensemble des images des séquences améliore les résultats.

Une méthode pour le recalage d'images d'échographie par speckle tracking (STE) et d'images de cine-IRM a aussi été proposée. Cette méthode, reposant sur des travaux préalables du LTSI (TAVARD et al., 2014), utilise une métrique spatio-temporelle estimée par l'application de l'ADTW aux descripteurs de Fourier décrivant les contours dynamiques issus des deux images. Les positions de toutes les vues échographiques (2-, 3- et 4-cavités) sont optimisées conjointement. Les résultats ont été évalués, tout d'abord en évaluant l'alignement temporel et en sélectionnant le nombre optimal de descripteurs de Fourier, en évaluant ensuite la convergence de la métrique et enfin par une évaluation visuelle des résultats du recalage. Ainsi, l'alignement de 87.5 % des segments myocardiques a été validé, tous les autres segments étant localisés dans la région apicale. L'ensemble de ces méthodes de recalage multimodal a permis une description intégrée multi-physique du ventricule gauche de façon à améliorer la caractérisation de la cardiomyopathie hypertrophique et de l'asynchronisme cardiaque.

Dans l'étude sur la cardiomyopathie hypertrophique, les données IRM et US de 30 patients ont été étudiées. Pour chaque patient, le recalage entre cine-MRI et LGE-MRI a en premier lieu permis à la fois de corriger les artefacts de mouvements du cine-MRI et d'y intégrer l'information liée à la présence de fibrose. Ensuite, les contours issus du STE ont été recalés sur le cine-IRM. Ainsi, l'image échographique et l'image LGE-MRI étaient alignées spatialement. Une évaluation visuelle par un expert a montré que 306 segments sur 336 étaient bien alignés. La fusion des courbes de strain extraites des images échographiques et des images LGE a alors permis d'étudier la relation entre strain et fibrose et d'analyser si des descripteurs issus du strain peuvent être des indicateurs sur la présence de fibrose. Une méthode de classification de type C-moyenne floue (KACHENOURA et al., 2008) nous a permis de quantifier l'étendue de la fibrose et de montrer que le pourcentage de fibrose sur l'ensemble du myocarde est corrélé au strain global.

De façon à évaluer si les paramètres régionaux de strain sont liés à la présence de fibrose, une analyse locale a été menée, montrant que les valeurs du pic de strain et de l'instant de ce pic sont significativement différentes en fonction de la présence de fibrose ($p<1e-5$). Cependant, les valeurs de ces indicateurs, pour des régions avec et sans fibrose, peuvent se superposer, ce qui peut s'expliquer par la présence dans la base de patients considérés sains, mais avec fibrose diffuse, cette fibrose n'étant pas visualisable par la modalité LGE-MRI. Ces travaux ont montré que la présence de fibrose est donc un des facteurs modifiant les courbes de strain dans la population de patients CMH. Ainsi, si une échographie d'un patient CMH montre un strain dégradé, la présence de fibrose peut être fortement suspectée et une acquisition IRM prescrite pour confirmer cette hypothèse. Considérant que l'échographie est beaucoup plus répandue et moins onéreuse que l'IRM, la prise en compte de cette information dans l'élaboration du protocole clinique pourrait être avantageuse.

Dans l'étude sur l'asynchronisme cardiaque, l'objectif était de fournir une description améliorée du ventricule gauche de façon, dans un contexte de CRT, à aider à la sélection des sites d'implantation. Les méthodes de recalage proposées ont permis de recaler les données EAM, CT, IRM et STE de façon à établir une description incluant des informations anatomiques, électriques, mécaniques et tissulaires. Quatre étapes de recalage étaient donc nécessaires, en considérant l'image scanner comme étant la référence : LGE- et cine-MRI ; cine-MRI et CT ; STE et CT ; EAM et CT. Les méthodes proposées ont permis d'effectuer les trois premiers recalages, le recalage de l'EAM étant réalisé manuellement. Ce processus repose donc sur un volume de données très important, acquis parfois de manière invasive (EAM), ce qui n'est possible que dans le contexte d'étude cliniques, comme euHeart, incluant un nombre limité de patients. De façon à démontrer la faisabilité de l'approche, deux patients de l'étude euHeart ont été sélectionnés, notamment de par la cohérence des données acquises et en sélectionnant un patient répondeur et un patient non-répondeur. Grâce aux images recalées, la caractérisation de l'asynchronisme a été réalisée, dans un espace unique, avec les délais locaux d'activation électrique (grâce à l'EAM), les pics de strain et les délais mécaniques (grâce au STE) et les délais électro-mécaniques locaux (suivant la fusion entre STE et EAM). Si la caractérisation tissulaire est aussi possible grâce aux recalages entre cine-MRI et LGE et entre cine-MRI et CT, elle n'a pas été appliquée ici, les patients de la base de données n'ayant pas montré de fibrose.

Ce processus de recalage et de fusion a donc permis d'analyser le couplage électro-mécanique global, c'est-à-dire en considérant comme référence électrique l'ECG et donc sans considérer les délais électriques inter-segments. Cette analyse des données STE a aussi permis d'analyser l'efficacité de la contraction, c'est-à-dire si le pic de strain se produit avant la fermeture de la valve aortique. Ainsi, pour un des patients considérés, le stimulateur ne permet pas d'améliorer l'efficacité de contraction des segments, contrairement au deuxième patient analysé. Les délais électromécaniques locaux permettent quant à eux de caractériser localement le couplage électromécanique, c'est-à-dire la capacité du tissu cardiaque à répondre mécaniquement à son activation électrique. Ainsi, pour le premier patient étudié non-répondeur, leurs valeurs étaient très hétérogènes en rythme sinusal (sans la stimulation), notamment sur la paroi latérale où la sonde de stimulation a été positionnée. Une hypothèse sur la relation entre délais électromécaniques locaux et réponse à la stimulation est que, pour une bonne réponse à la stimulation, les segments stimulés doivent présenter des délais faibles et homogènes (Tavard et al., 2014). Cette hypothèse a été par ailleurs vérifiée sur le deuxième patient traité et répondeur. Ainsi, l'analyse de ces deux patients considérés est en adéquation avec cette hypothèse, même si sa validation nécessite l'étude sur un plus grand nombre de patients.

Les perspectives de ce travail incluent différents aspects. D'un point de vue méthodologique, la correction des artefacts de mouvement en IRM et le recalage interséquence pourraient être améliorés en ajoutant à la métrique des informations liées à la continuité spatiale du ventricule, de façon à ne plus considérer uniquement les profils d'intersection mais l'ensemble de la continuité qui doit être observée dans le volume 3D corrigé. Le recalage entre US et IRM ou CT pourrait potentiellement être amélioré en combinant la métrique basée contour à une métrique basée intensité. Enfin, même si des contraintes ont été ajoutées au processus d'ADTW, il peut résulter en des synchronisations temporelles non physiologiquement réalistes. L'ajout de nouvelles contraintes, liées par exemple à un modèle simple mais réaliste des variations des ECG, pourrait être investigué.

Les différentes évaluations des méthodes de recalage ont été menées sur données réelles. L'évaluation sur données simulées, grâce à des simulateurs d'images de différentes modalités, permettrait d'apporter des résultats complémentaires. Les deux études cliniques doivent aussi être complétées par la considération de plus de patients, en particulier pour l'étude sur la CRT. De même, en CRT, il serait pertinent d'étudier les données de patients présentant de la fibrose ou nécrose. Par ailleurs, de nouvelles modalités doivent être considérées. Ainsi, l'échographie tridimensionnelle permettra de fournir une description complète du ventricule gauche et facilitera probablement le recalage. Cependant, sa résolution temporelle plus faible devra être considérée attentivement pour le calcul des délais électromécaniques. Pour l'étude CMH, l'utilisation d'autres séquences IRM devra être investiguée. Ainsi, les séquences MOLI, permettant une visualisation de la fibrose diffuse, de même que des acquisitions de séquences à l'effort permettraient de préciser notre étude. Pour l'étude sur l'asynchronisme, remplacer les acquisitions EAM, qui sont très invasives, par des acquisitions de surface permettrait une avancée très significative dans l'utilisation clinique de ces approches. Enfin, la visualisation des descripteurs obtenus en salle d'implantation devra être menée, grâce par exemple au recalage entre angiographies per-opératoires et scanner pré-opératoire, de façon à réaliser une nouvelle avancée vers la thérapie de resynchronisation cardiaque guidée par l'image.

Références

Gersh, B. J., Maron, B. J., Bonow, R. O., Dearani, J. A., Fifer, M. A., Link, M. S., Naidu, S. S., Nishimura, R. A., Ommen, S. R., Rakowski, H., Seidman, C. E., Towbin, J. A., Udelson, J. E. et Yancy, C. W. (2011). « 2011 ACCF/AHA Guideline for the Diagnosis and Treatment of Hypertrophic Cardiomyopathy A Report of the American College of Cardiology Foundation/American Heart Association Task Force on Practice Guidelines ». en. In : *Circulation* 124.24, e783–e831.

Harris, K. M., Spirito, P., Maron, M. S., Zenovich, A. G., Formisano, F., Lesser, J. R., Mackey-Bojack, S., Manning, W. J., Udelson, J. E. et Maron, B. J. (2006). « Prevalence, Clinical Profile, and Significance of Left Ventricular Remodeling in the End-Stage Phase of Hypertrophic Cardiomyopathy ». en. In : *Circulation* 114.3, p. 216–225.

Kachenoura, N., Redheuil, A., Herment, A., Mousseaux, E. et Frouin, F. (2008). « Robust assessment of the transmural extent of myocardial infarction in late gadolinium-enhanced MRI studies using appropriate angular and circumferential subdivision of the myocardium ». eng. In : *European radiology* 18.10, p. 2140–2147.

Maron, B. J. (2004). « Hypertrophic cardiomyopathy: an important global disease ». In : *The American Journal of Medicine* 116.1, p. 63–65.

Maron, B. J. (2010). « Contemporary Insights and Strategies for Risk Stratification and Prevention of Sudden Death in Hypertrophic Cardiomyopathy ». en. In : *Circulation* 121.3, p. 445–456.

McMurray, J. J., Adamopoulos, S., Anker, S. D., Auricchio, A., Böhm, M., Dickstein, K., Falk, V., Filippatos, G., Fonseca, C., Gomez-Sanchez, M. A. et al. (2012). « ESC Guidelines for the diagnosis and treatment of acute and chronic heart failure 2012 The Task Force for the Diagnosis and Treatment of Acute and Chronic Heart Failure 2012 of the European Society of Cardiology. Developed in collaboration with the Heart Failure Association (HFA) of the ESC ». In : *European heart journal* 33.14, p. 1787–1847.

Nekolla, S. G., Rischpler, C. et Marinelli, M. (2013). « Image Fusion and Coregistration: State of the (He)art ». en. In : *From Basic Cardiac Imaging to Image Fusion.* Sous la dir. de P. Marzullo et G. Mariani. Springer Milan, p. 115–123.

Olivotto, I., Cecchi, F., Casey, S. A., Dolara, A., Traverse, J. H. et Maron, B. J. (2001). « Impact of Atrial Fibrillation on the Clinical Course of Hypertrophic Cardiomyopathy ». en. In : *Circulation* 104.21, p. 2517–2524.

Skerl, D., Likar, B. et Pernus, F. (2006). « A protocol for evaluation of similarity measures for rigid registration ». In : *IEEE Transactions on Medical Imaging* 25.6, p. 779–791.

Tavard, F., Simon, A., Leclercq, C., Donal, E., Hernández, A. et Garreau, M. (2014). « Multimodal Registration and Data Fusion for Cardiac Resynchronization

Therapy Optimization ». In : *IEEE Transactions on Medical Imaging* 33.6, p. 1363–1372.

WHO (2011). *Global status report on noncommunicable disaeses 2010.* report. Geneva : World Health Organization.

Contents

Introduction

In the world, more people die annually from diseases of the cardiovascular system (CVD) than from any other cause: 17.3 million people died from CVDs in 2008, representing 30% of all global deaths that year, according to the World Health Organization (WHO, 2011), and it is estimated that 23 million deaths will occur in 2030. Among CVDs, hypertrophic cardiomyopathy (HCM) is a common genetic cardiovascular disease with epidemiological studies from several parts of the world reporting a similar prevalence of left ventricular hypertrophy of about 0.2% in the general population (MARON, 2004) (GERSH et al., 2011). From a physiophatological point of view, tissue modifications in HCM are characterized not only by a thickening of the myocardium but also by an architectural disorganization of the myocardium and by fibrosis. HCM is a disease with an extremely variable prognosis. Some patients will die from sudden death (MARON, 2010), others will develop atrial fibrillation (OLIVOTTO et al., 2001) with accidents due to arterial embolism (HARRIS et al., 2006), others will suffer from heart failure in most cases with a preserved left ventricular ejection fraction, and some will be life-long asymptomatic.

Another CVD with high incidence is heart failure (HF). It concerns 2% to 3% of the population in developed countries, increasing to more than 20% in seniors ($>$ 70 years). Heart failure can be defined as an abnormality of cardiac structure or function leading to failure of the heart to deliver oxygen at a rate commensurate with the requirements of the metabolizing tissues (MCMURRAY et al., 2012). It is estimated that 30% to 40% of the HF population suffer from a synchronization defect or cardiac asynchronism. This asynchronism can be of different nature: atrioventricular, interventricular or intraventricular. HF can also lead to a geometrical, structural and architectural modification of the left ventricular myocardium, called cardiac remodeling. In fact, this remodeling can be the cause of the asynchronism.

Some HF patients with cardiac asynchronism will undergo Cardiac Resynchronization Therapy (CRT) in order to resynchronize the heart pumping action. The subpopulation undergoing CRT corresponds to patients with chronic HF not responding to pharmacological treatment, low left ventricular ejection fraction (LVEF) and long QRS complex. However, 30% of CRT patients do not respond to the therapy.

We propose in this work to *fuse multisensor cardiac data* in order to get insights about the diseased heart in the context of hypertrophic cardiomyopathy (HCM) and cardiac asynchronism. The fusion of cardiac images from CRT subjects (cardiac asynchronism) is part of a more ambitious goal: the optimization of CRT.

For hypertrophic cardiomyopathy, we aim at improving its characterization by the fusion of cardiac magnetic resonance imaging (MRI) and echocardiography (US) images of the heart. This analysis enables to get insights about the role of speckle tracking echocardiography (STE) analysis in HCM characterization at early stages, mainly concerning the detection of fibrosis. In this context, the challenge is to correlate the information about myocardial structure assessed with the late gadolinium-enhanced sequence of the cardiac MRI acquisition (LGE-MRI), with strain curves from STE, to define the significance of STE strain as surrogate of myocardial fibrosis.

Despite many efforts, the causes of CRT nonresponse remain unclear. In this context, image fusion arises as an important methodological tool enabling to study complementary information such as the electro-mechanical coupling and myocardial structure associated to a detailed anatomy of the heart including the coronary venous tree. The challenge in cardiac asynchronism characterization for CRT optimization is to locate and characterize the best sites of LV stimulation and to compute and analyze new potential markers of CRT nonresponse.

Multisensor datasets to be fused in *HCM and cardiac asynchronism characterization* describe cardiac morphology and function (mechanical and electrical). This information is acquired using the following modalities: multislice X-ray computed tomography (CT), cardiac magnetic resonance (MRI) including cine and LGE sequences, echocardiography (US) and electro-anatomical mappings of the left ventricular inner chamber (EAM). These datasets are, in most circumstances, not in the same spatial and temporal coordinate system due, for instance, to sequential acquisition, patient motion, or a different state of respiration or heart contraction (Nekolla et al., 2013). In fact, each modality has its own particularities regarding image resolution, dimension (2D, 3D) and representation (volumetric, surface, multiplanar, planar). Then, *multimodal image registration* is mandatory in order to describe the -complementary- information they contain in a common spatio-temporal coordinate system. The latter is the main methodological goal of this work.

The methods proposed in this work to register the multimodal datasets used in the characterization of HCM and cardiac asynchronism rely in two main processes: temporal registration and spatial registration. The temporal dimension of dynamic images are warped with an adaptive dynamic time warping (ADTW) method. This method handles the nonlinear temporal relationship between dynamic acquisitions caused by the underlying nonlinear change in cardiac dynamics between different acquisitions. Concerning the spatial registration, iconic methods were developed to correct for slice misalignments in cine image sequences (mainly in HCM database), to register cine-MRI and LGE-MRI, and to register cine-MRI with dynamic CT. On the other hand, the contour-based method proposed by (Tavard et al., 2014) were enhanced to integrate multiview STE acquisitions.

This document has three main parts. The first part, called *imaging the diseased heart*, is divided into two chapters: firstly, the description of the clinical context, the addressed issues in HCM characterization and cardiac asynchronism characterization for CRT optimization, as well as the description of the image modalities to be processed (Chapter 1); secondly, the formalization of both, the fusion and the multisensor image registration frameworks, followed by a state of the art in cardiac image registration (Chapter 2). The second part, called *the registered multisensed left ventricle* is divided into two chapters: the formalization of the multisensor image registration methods proposed here (Chapter 3) and their evaluation (Chapter 4). Finally, the third part, called *insights from the registered left ventricle* is dedicated to the application of the proposed methods to the characterization of hypertrophic cardiomyopathy (Chapter 5) and to the characterization of cardiac asynchronism for cardiac resynchronization therapy optimization (Chapter 6). This document ends with the conclusions and perspectives as well as the list of associated publications.

References

Gersh, B. J., Maron, B. J., Bonow, R. O., Dearani, J. A., Fifer, M. A., Link, M. S., Naidu, S. S., Nishimura, R. A., Ommen, S. R., Rakowski, H., Seidman, C. E., Towbin, J. A., Udelson, J. E., and Yancy, C. W. (2011). “2011 ACCF/AHA Guideline for the Diagnosis and Treatment of Hypertrophic Cardiomyopathy A Report of the American College of Cardiology Foundation/American Heart Association Task Force on Practice Guidelines”. en. In: *Circulation* 124.24, e783–e831.

Harris, K. M., Spirito, P., Maron, M. S., Zenovich, A. G., Formisano, F., Lesser, J. R., Mackey-Bojack, S., Manning, W. J., Udelson, J. E., and Maron, B. J. (2006). “Prevalence, Clinical Profile, and Significance of Left Ventricular Remodeling in the End-Stage Phase of Hypertrophic Cardiomyopathy”. en. In: *Circulation* 114.3, pp. 216–225.

Kachenoura, N., Redheuil, A., Herment, A., Mousseaux, E., and Frouin, F. (2008). “Robust assessment of the transmural extent of myocardial infarction in late gadolinium-enhanced MRI studies using appropriate angular and circumferential subdivision of the myocardium”. eng. In: *European radiology* 18.10, pp. 2140–2147.

Maron, B. J. (2004). “Hypertrophic cardiomyopathy: an important global disease”. In: *The American Journal of Medicine* 116.1, pp. 63–65.

Maron, B. J. (2010). “Contemporary Insights and Strategies for Risk Stratification and Prevention of Sudden Death in Hypertrophic Cardiomyopathy”. en. In: *Circulation* 121.3, pp. 445–456.

McMURRAY, J. J., ADAMOPOULOS, S., ANKER, S. D., AURICCHIO, A., BÖHM, M., DICKSTEIN, K., FALK, V., FILIPPATOS, G., FONSECA, C., GOMEZ-SANCHEZ, M. A., et al. (2012). “ESC Guidelines for the diagnosis and treatment of acute and chronic heart failure 2012 The Task Force for the Diagnosis and Treatment of Acute and Chronic Heart Failure 2012 of the European Society of Cardiology. Developed in collaboration with the Heart Failure Association (HFA) of the ESC”. In: *European heart journal* 33.14, pp. 1787–1847.

NEKOLLA, S. G., RISCHPLER, C., and MARINELLI, M. (2013). “Image Fusion and Coregistration: State of the (He)art”. en. In: *From Basic Cardiac Imaging to Image Fusion*. Ed. by P. MARZULLO and G. MARIANI. Springer Milan, pp. 115–123.

OLIVOTTO, I., CECCHI, F., CASEY, S. A., DOLARA, A., TRAVERSE, J. H., and MARON, B. J. (2001). “Impact of Atrial Fibrillation on the Clinical Course of Hypertrophic Cardiomyopathy”. en. In: *Circulation* 104.21, pp. 2517–2524.

SKERL, D., LIKAR, B., and PERNUS, F. (2006). “A protocol for evaluation of similarity measures for rigid registration”. In: *IEEE Transactions on Medical Imaging* 25.6, pp. 779–791.

TAVARD, F., SIMON, A., LECLERCQ, C., DONAL, E., HERNÁNDEZ, A., and GARREAU, M. (2014). “Multimodal Registration and Data Fusion for Cardiac Resynchronization Therapy Optimization”. In: *IEEE Transactions on Medical Imaging* 33.6, pp. 1363–1372.

WHO (2011). *Global status report on noncommunicable disaeses 2010*. report. Geneva: World Health Organization.

CHAPTER 1

Clinical context

The heart is a complex *multiphysics* organ involving and coupling different physical phenomena which can be -indirectly- captured using multisensor cardiac imaging. In this work, we propose to *register* multisensor cardiac images and to *associate* and to *fuse* morphological and functional information in order to get insights about the deceased heart in the context of hypertrophic cardiomyopathy (HCM) and cardiac asynchronism.

This chapter aims at providing the clinical context of this work. It is divided into three main parts. The first part describes cardiac anatomy, electrical and mechanical functions. The second part states the addressed issues: HCM characterization and cardiac asynchronism characterization for cardiac resynchronization therapy (CRT) optimization. The third part introduces the imaging modalities used to acquire multiphysics cardiac information: echocardiography (US), computed tomography (CT), cardiac magnetic resonance imaging (MRI) and electroanatomical mapping (EAM). This chapter finishes with a conclusion and a list of clinical and methodological challenges.

1.1 At the heart of the cardiovascular system

The *cardiovascular system* is made up of the heart and the vascular system (cf. Figure 1.1(left)). The human heart pumps four to five liters of blood that circulates around the body through the blood vessels (arteries, veins, arterioles, venules, capillaries), in a closed-loop circuit: the *circulatory system.* This system is divided into the systemic circulation (irrigating tissues, organs, etc.) and the pulmonary circulation (supplying de-oxygenated blood to lungs where it reoxygenates).

1.1.1 Anatomy of the human heart

The *heart* is located into the thoracic cavity in a zone called mediastinum, between the lungs and the diaphragm. An average adult human heart weights between 300 g

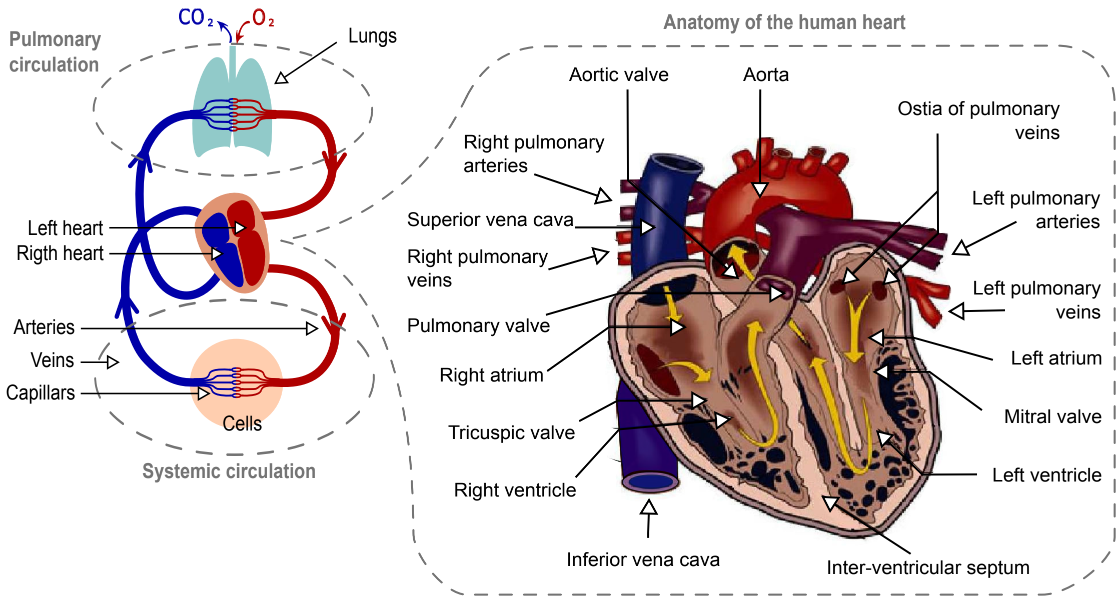

Figure 1.1: At the heart of the cardiovascular system: (left) blood circulation in human body and, (right) anatomy of the human heart. Modified from (SIMON, 2005).

and 350 g. The heart is a hollow organ with four chambers separated by valves and surrounded by muscles which squeeze and relax to pump the blood around the body (cf. Figure 1.1(right)). The four chambers are: the right atrium (RA), the right ventricle (RV), the left atrium (LA) and the left ventricle (LV). Although a single organ, the heart functions as two separate pumps: the *right heart* (RA and RV) and the *left heart* (LA and LV). Two septal walls separate the left and right sides: the inter-atrial septum, dividing RA and LA, and the inter-ventricular septum separating the two ventricles.

Cardiac hypertrophy and cardiac asynchronism concern the whole heart with effects on the entire body; however, the challenges addressed in this work concern the left ventricle (cf. 1.2.1.2, 1.2.2.4).

1.1.1.1 Ventricles

RV and LV are bounded by a thick muscle called *myocardium* (10 mm for a healthy LV), an interventricular septum, two atrioventricular valves (mitral and tricuspid valves, respectively), and two semilunar valves (pulmonary and aortic valves, respectively, cf. Figure 1.2a). RV and LV pump the blood into pulmonary and systemic circulations through the pulmonary artery and the aorta, respectively. Their contraction is longer and stronger than in atria in a healthy heart.

LV geometry can be approximated with a truncated ellipsoid with the base plane intersecting the mitral and aortic valves (cf. Figure 1.3). The vertex of this ellipsoid will correspond to the *apex*. The axis perpendicular to the base and containing the apex is called *long axis*. In cardiac imaging, planar images lying in planes parallel to this axis are

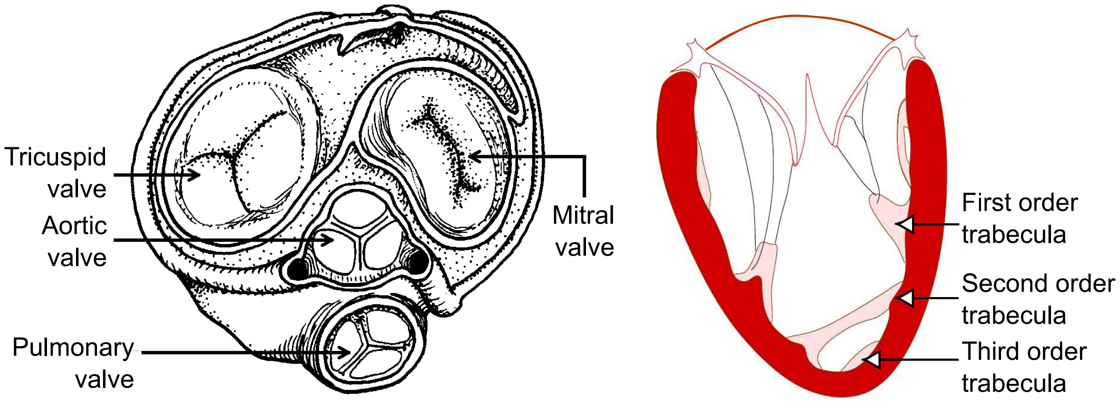

(a) Cardiac valves (from BIODIDAC, Ottawa University) (b) Trabeculæ carneæ (Simon, 2005)

Figure 1.2: Valves of the human heart and left ventricular trabeculæ carneæ. (a) Illustration of AV-valves (mitral, tricuspid) and sigmoid valves (aortic, pulmonary). (b) Illustration of the three types of trabeculæ carneæ in the left ventricle.

called *long-axis-view (LAX)* images and those perpendicular to the long axis are called *short-axis-view (SAX)* images. For instance, these reference planes are used in cardiac MRI routine to acquire multiplanar images of the heart (cf. 1.3.4.1).

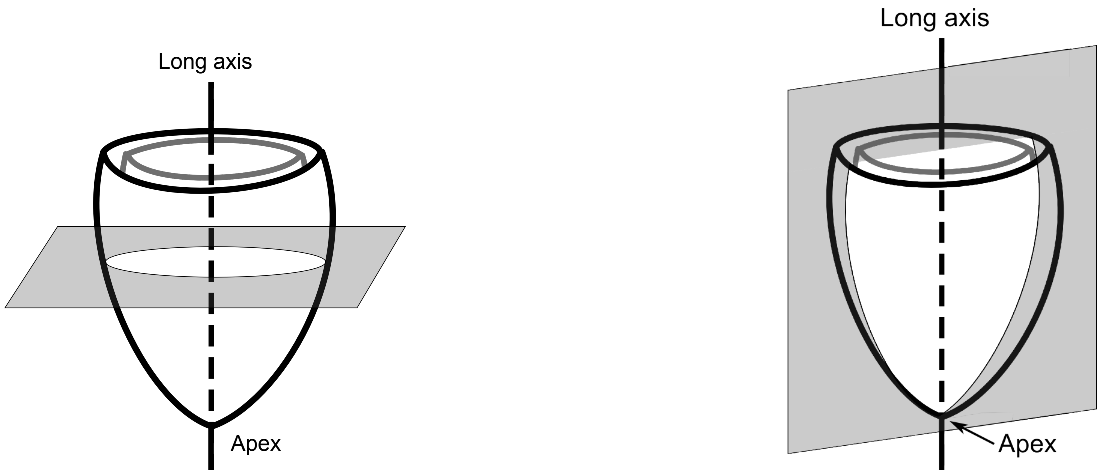

(a) Short-axis plane (b) Long-axis plane

Figure 1.3: Left ventricular long axis, apex and illustration of the long-axis and short-axis planes.

In reality, LV's inner wall is very irregular and made up of many meaty ridges or *trabeculæ carneæ*. They are of three types: first order (papillary muscles), second order and third order trabeculae (cf. Figure 1.2b). *Papillary muscles* are cone shaped with the base joined to the ventricular wall and the apex to *chordæ tendineæ*. The latter are in turn attached to the atrioventricular valves (AV-valves) which prevents the valves to open during ventricular systole.

1.1.1.2 Coronary blood vessels network

The coronary circulation supplies blood to the cardiac muscle. It is made up of two extensive networks of coronary blood vessels (cf. Figure 1.4): the network of coronary arteries and the network of coronary veins. The anatomy of the latter is important during CRT device implantation because an excitation lead is positioned in a coronary vein to pace the left ventricle (cf. 1.2.2.3). The main vessels of the *network of coronary veins* are: the great cardiac vein, the middle cardiac vein, the small cardiac vein, the antero-lateral vein and the posterior vein. These veins join together into a large vessel called *coronary sinus* that delivers de-oxygenated blood to the right atrium.

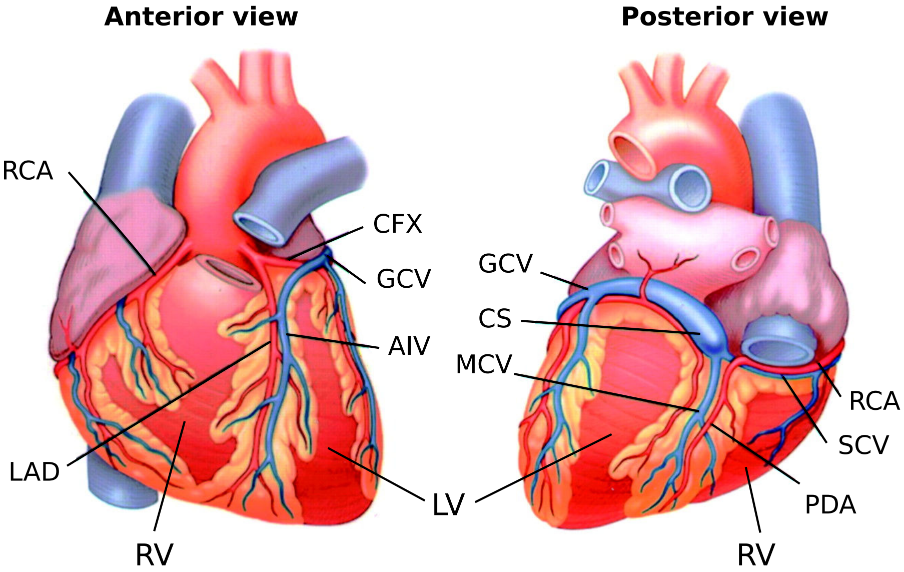

Figure 1.4: Anterior and posterior views of epicardial coronary circulation. ACRONYMS – AIV: anterior interventricular vein, CFX: circumflex coronary artery, CS: coronary sinus, GCV: great cardiac vein, LAD: left anterior descending coronary artery, LV: left ventricle, MCV: middle coronary vein, RCA: right coronary artery, RV: right ventricle, SCV: small coronary vein. From (OESTERLE et al., 2001).

1.1.1.3 Cardiac muscle

The cardiac muscle can be divided into three layers: the *endocardium* (a thin membrane that lines the inner chambers of the heart), the *myocardium* (a thick layer of muscular cells), and the pericardium (also subdivided into different layers).

The myocardium is made up of *cardiomyocytes* (cells) that arrange into fibers. Cardiomyocytes are unique in the human body due to their characteristics. They are contractile yet cannot remain in contraction, independent and good conductors (i.e. cell excitation is transmitted to neighbors). Cardiomyocytes are irrigated by coronary arteries and excited by the autonomic nervous system. *Myocardial fibers* are arranged into spiral and circular bundles (cf. Figure 1.5). Fiber disposition locally determines the favored direction to transmit cells excitation to neighbors.

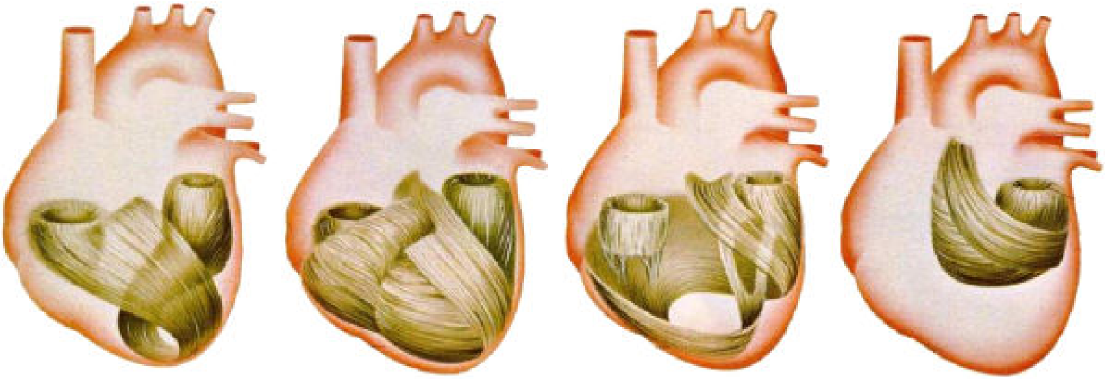

Figure 1.5: Distribution of cardiac muscular fibers. From (Malmivuo et al., 1995).

The pumping action of the heart is achieved by the contraction and relaxation of the cardiac muscle. This action is triggered by electrical signals propagating throughout the muscle. Thus, the electrical and mechanical function of the heart are coupled. Here, we describe each phenomenon individually (cf. 1.1.2, 1.1.3) in order to provide straightforward connection with the information that each cardiac imaging technique provides in the context of this work (cf 1.3).

1.1.2 Electrical function

A cardiomyocyte exhibits an electric potential difference (*voltage*, about -90 mV at rest) between intra and extra cellular media caused by different concentrations of sodium ions (Na^+), potassium ions (K^+), calcium ions (Ca^{2+}) and chloride ions (Cl^-). The contraction of a cardiomyocyte is the result of ionic exchanges at microscopic level between intra and extra cellular media. These exchanges modify the voltage between intra and extra cellular media of the cell. The resulting *cardiac action potential*, i.e. the evolution of this voltage over time, has four phases (cf. Figure 1.6):

Rapid depolarization. An electrical excitation of the cell above a given activation threshold causes a rapid inversion of its polarization or *depolarization*.

Beginning of repolarization. Characterized by a fast and acute return to equilibrium.

Plateau. The repolarization slows down into a "plateau" phase where the voltage does not change significantly.

Rapid repolarization. Fast decrease of cardiomyocyte's voltage until equilibrium is reached.

Cardiac muscle depolarization is triggered by the *sinus node* or *Keith-Flack node* (cf. Figure 1.7). This node plays the role of a natural pacemaker triggering the cardiac rhythm, called *sinus rhythm*. The sinus node is located on the RA wall, near the entrance of the superior vena cava.

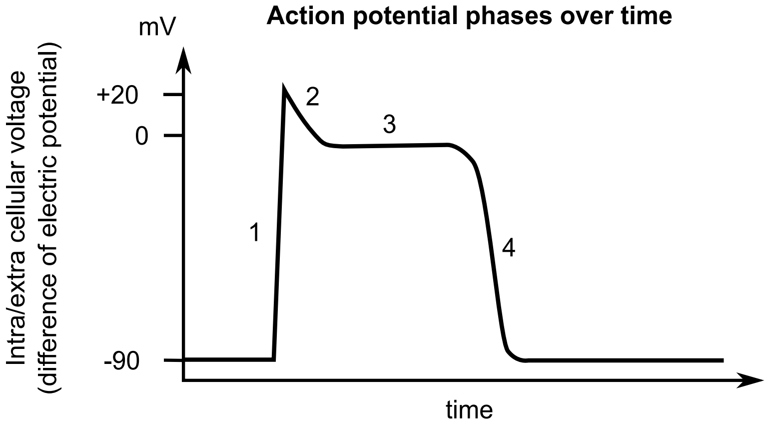

Figure 1.6: Action potential phases for a cardiomyocyte over time: 1. rapid depolarization, 2. beginning of repolarization (fast and acute), 3. plateau (slow repolarization), 4. rapid repolarization (return to voltage at rest).

The action potential induced at the sinus node propagates towards atria (left and right) causing atria contraction (cf. Figure 1.7). This depolarization front conveys at the *atrioventricular node* (AV-node) or *node Aschoff-Tawara.* The AV-node is located in RA near to the coronary sinus. It behaves as a filter blocking the propagation of very fast atrial depolarizations towards ventricles (e.g. during atria fibrillation). The AV-node marks the beginning of the *bundle of His.* This bundle continues towards the interventricular septum where it divides into two branches. Different ramifications of these branches continue to right and left ventricles. The separation between atria and ventricles (i.e. the *mitral and tricuspid annuli*), is made up of connective tissue which is an electrical isolator. Therefore, the bundle of His is the only pathway the depolarization front has to provoke ventricular contraction.

A depolarization is followed by a *repolarization*[1]. During repolarization cardiomyocytes relax, first at atria (during ventricle's depolarization), and then at ventricles. Although the depolarization, and so the contraction of the heart, is spontaneous, the sinus rhythm is influenced by other external elements such as effort or fear.

The local electrical activity of the cardiac muscle can be acquired with an electroanatomical mapping (cf. 1.3.2). The *electrocardiogram (ECG)* depicts the global electrical activity of the heart. The ECG can be decomposed into (cf. Figure 1.7 bottom-left): the *P-wave* representing atria depolarization (contraction), the *QRS-complex* corresponding to ventricular depolarization (contraction), and the *T-wave* corresponding to ventricular repolarization (relaxation). Atria repolarization is masked by the QRS-complex.

---

[1] Repolarization means, in this context, returning to equilibrium, i.e. returning to cardiomyocyte's voltage at rest.

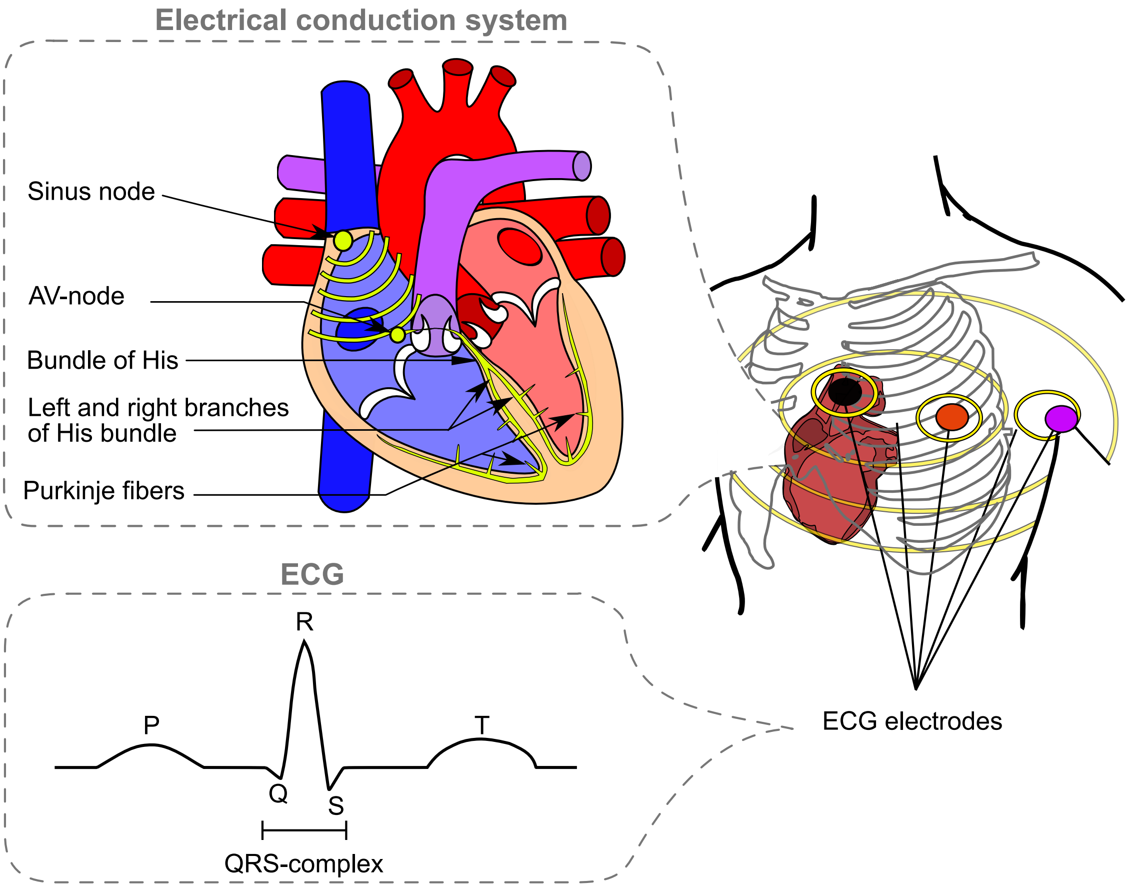

Figure 1.7: Electrical function of the heart. (Top-left) Electrical conduction system: impulses originating at sinus node travels to atria and then convey at the AV-node to then propagate towards the right and left ventricles through the bundle of His, its left and right branches, and Purkinje fibers. (Bottom-left) Schematic representation of an electrocardiogram (ECG) for a healthy heart in sinus rhythm. The ECG depicts the global electrical function of the heart. Modified from (Simon, 2005).

1.1.3 Mechanical function

The heart accomplishes its pumping role by circulating oxygenated blood arriving from lungs to the rest of the body. This is repeated cyclically with each period corresponding to a *heartbeat* or *cardiac cycle*. This cycle has four phases (cf. Figure 1.8):

Ventricular filling. In this phase, blood will flow from atria towards ventricles, first rapidly, and then slowly when the ventricular pressure approaches the atrial pressure.

Isovolumetric contraction. This phase starts when ventricular pressure increases and exceeds atrial pressure, causing AV-valves to close. During this phase, the ventricular pressure continues to increase while the ventricular volume remains unchanged.

Isotonic contraction (ejection phase). When ventricular pressure exceeds arterial pressure the sigmoid valves will open and the blood will be ejected outside the heart. As blood quits ventricles, the ventricular pressure decreases causing sigmoid valves to close when it is lower than the arterial pressure.

Isovolumetric relaxation. In this short phase, ventricular pressure decreases until it is inferior to atrial pressure causing AV-valves to open. This allows blood to flow from atria into ventricles and the cardiac cycle starts again.

The Contraction and ejection phases made the *ventricular systole* while the relaxation and filling phases made the *ventricular diastole*. In a healthy heart, both ventricles contract simultaneously.

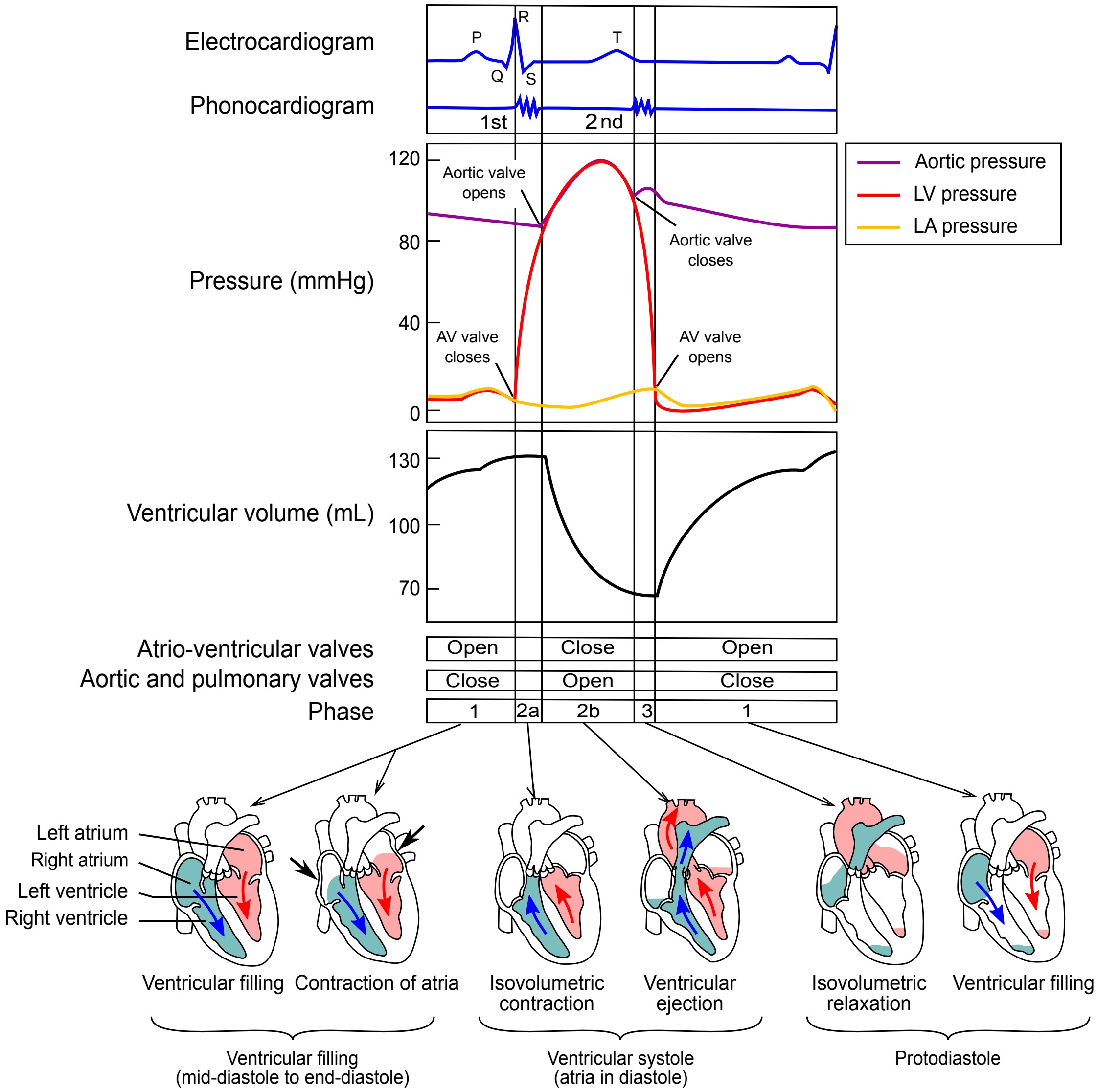

Figure 1.8: Cardiac cycle: (top) diagram depicting cardiac signals (ECG, pressures, volumes) and cardiac events occurring in the heart also called Wiggers diagram, (bottom) illustration of blood circulation in heart cavities at each phase. From (Marieb, 2005).

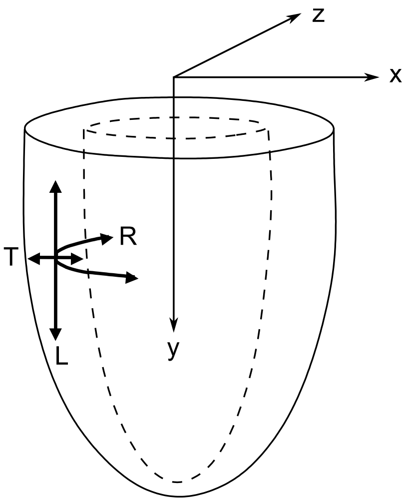

Figure 1.9: Components of the left ventricular wall motion. T: axis of the transversal (radial) motion, L: axis of the longitudinal motion, R: axis of the circumferential motion. From (Støylen, 2001).

LV local wall motion is routinely described using three components measured in a LV anatomical referential (cf. Figure 1.9). They are (Blessberger et al., 2010):

Longitudinal contractile motion. Motion in the direction of the LV long axis. LV base descends towards the apex during systole with the apex also moving in the same direction (Simonson et al., 1989) (Young et al., 1994).

Radial contractile motion. Myocardial fibers shortening towards the LV long axis and perpendicular to the epicardium. Radial strain represents myocardial thickening and thinning. It is relatively homogeneous around the ventricle with amplitudes between 4 and 8 mm (Young et al., 1994).

Circumferential motion. Circular motion tangent to the LV wall, around the LV long axis. It is perpendicular to both, radial and long axes. Observed from the apex, a normal circumferential motion during systole corresponds to a clockwise rotation at the base and an even greater counter-clockwise rotation at apex (Maier et al., 1992; Nagel et al., 2000; Young et al., 1994). The difference from apex to base is the LV twist. These make LV to squeeze (torsion).

LV wall motion is essentially *nonrigid* being non homogeneous around the ventricle. Nevertheless, a *rigid* component must be added (translation and rotation). The rigid component is caused by breathing and often distorts breath-hold image acquisitions (McLeish et al., 2002) (cf. 1.3.4.1).

1.2 Addressed cardiac issues: Hypertrophic cardiomyopathy and cardiac asynchronism

By 2010, the diseases of the cardiovascular system or *cardiovascular diseases (CVDs)* caused 223 deaths per 100 thousand individuals in France (about 27% of total deceases) [2], being the first cause of decease in the country for women and the second for men. CVDs mortality in the world is very similar: more people die annually from CVDs than from any other cause. According to the World Health Organization, 17.3 million people died from CVDs in 2008 representing 30% of all global deaths that year (WHO, 2011). CVDs affects the heart, blood vessels or both. Angina (chest pain), aneurysm, endocarditis, epicarditis, cardiomyopathy and heart failure are just some examples. In this work, we focus on (i) *cardiomyopathies*, in particular the *hypertrophic cardiomyopathy (HCM)* which is the abnormal thickening of left ventricular myocardium and, (ii) *cardiac asynchronism* in *heart failure (HF)* patients that occurs when both, the pumping action of the heart is not synchronized (asynchronism) and the heart is unable to provide sufficient pump action to maintain the blood flow needed to meet the metabolic and functional requirements of the body (HF). These clinical motivations are detailed in the following subsections.

1.2.1 Hypertrophic cardiomyopathy

Hypertrophic Cardiomyopathy (HCM) belong to the broad class of *cardiomyopathies (CM)*, meaning literally the diseases of cardiac muscle. They are an heterogeneous group of myocardial diseases. The classification proposed by a working group of the European Society of Cardiology (Elliott et al., 2008) defined CM as “a myocardial disorder in which the heart muscle is structurally and functionally abnormal, in the absence of coronary artery disease, hypertension, valvular disease and congenital heart disease sufficient to cause the observed myocardial abnormality”. They often evolve progressively and are related with a weakness in cardiac function. In fact, CMs represent an important cause of morbidity and mortality. There are four major types of CMs (cf. Figure 1.10) (Locca et al., 2009)(Elliott et al., 2008):

Hypertrophic cardiomyopathy (HCM). Right and/or left ventricular hypertrophy with altered diastolic and systolic function, often asymmetric, often involving the interventricular septum but sometimes with preserved left ventricular ejection fraction (LVEF).

Dilated cardiomyopathy (DCM). The heart cavity is enlarged and stretched (cardiac dilation), resulting in weak and slow pumping of blood that, in turn, can result in the formation of blood clots.

Arrhythmogenic right ventricular dysplasia (ARVD). Progressive replacement of heart muscle cells which become disorganized and damaged and are replaced by

---

[2] Source INSEE, sheet “Causes de décès 2010”.

fibrous-fatty tissues. ARVD involves primarily the right ventricle; however, the left ventricle can be affected in 15% of the cases.

Restrictive cardiomyopathy (RCM). Ventricular filling restriction related to a decrease in diastolic function of one or both ventricles with a normal or almost normal systolic function. Since the heart cannot relax adequately between contractions, it is harder for the ventricles to fill with blood between heartbeats. RCM is classified as non-obliterative (myocardial infiltration by an abnormal substance), or obliterative (fibrosis of the endocardium and subendocardium). Either type may be diffuse or nondiffuse (when the disorder affects only one ventricle or part of one ventricle unevenly).

A fifth type can be included: the **non-classified cardiomyopathies**, i.e. none of the cardiomyopathies listed above including the non-compaction CMs and Tako-Tsubo CMs.

This work aims at characterizing the hypertrophic cardiomyopathy. HCM is a common genetic cardiovascular disease, mostly sarcomeric (i.e. caused by sarcomere protein mutation) and autosomal dominant (i.e. an individual only need to get the abnormal gene from one parent in order to inherit the disease). Epidemiological studies from several parts of the world report a similar prevalence of left ventricular hypertrophy of about 0.2% (i.e., 1:500) in the general population (B. J. MARON, 2004) (GERSH et al., 2011).

HCM is a disease with an extremely variable prognosis. Some patients will die from sudden death (B. J. MARON, 2010), some will develop atrial fibrillation (OLIVOTTO et al., 2001) with accidents due to arterial embolism (HARRIS et al., 2006), some will suffer from heart failure in most cases with a preserved left ventricular ejection fraction, and some will be life-long asymptomatic.

The recommendations from ACC/AHA (American Heart Association) of 2011 (GERSH et al., 2011) elucidated the difficulties of dealing with this affection and indicated the modalities for diagnosis, follow-up and treatment. These recommendations are based on expert consensus and, whenever possible, on evidence. From a therapeutic point of view, β-blocker drugs and the development of implantable cardioverter-defibrillators (ICD) have enabled to prevent serious ventricular rhythm disorders in HCM patients (GERSH et al., 2011). However, the selection of the patients that will benefit from these therapies is still challenging. In the case of embolic accidents, their prevention is mainly supported on the prescription of oral anticoagulants (GERSH et al., 2011). The manifestations of HF with preserved ejection fraction remain difficult to handle. In this case, the treatment is relatively limited focusing in relieving the symptoms. Thus, it is important to enhance HCM understanding in order to improve patient detection and treatment at early stages.

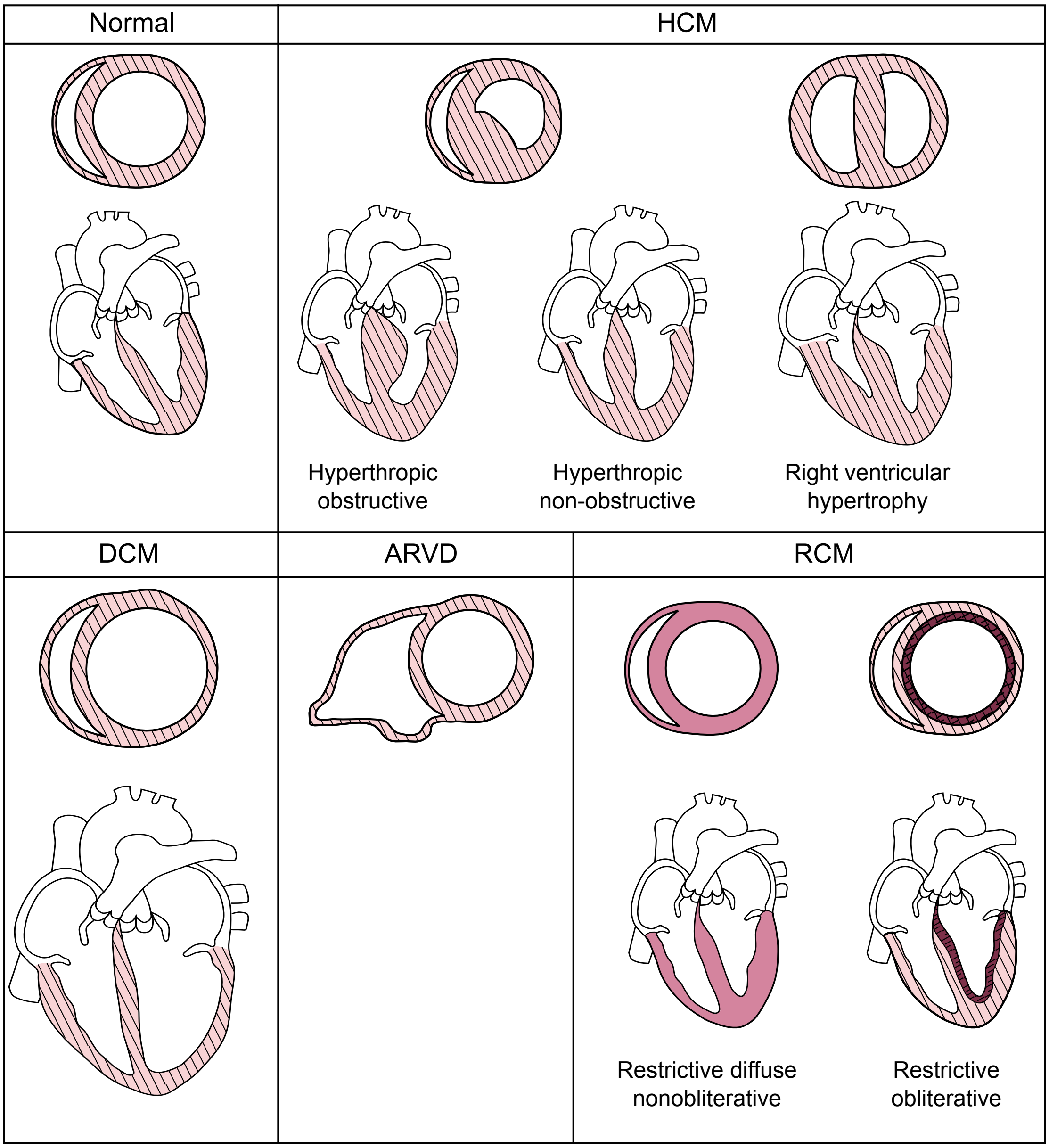

Figure 1.10: Illustration of the four major types of cardiomyopathies: hypertrophic cardiomyopathy (HCM), dilated cardiomyopathy (DCM), arrhythmogenic right ventricular dysplasia (ARVD) and restrictive cardiomyopathy (RCM). Includes images from (Schwitter et al., 2008)

1.2.1.1 Hypertrophic cardiomyopathy and fibrosis

From a physiophatological point of view, tissue modifications in HCM are characterized not only by myocardial thickening but also by an architectural disorganization of the myocardium and by fibrosis (Ohsato et al., 1992). Cardiac fibrosis commonly refers to the proliferation of fibroblasts (cell of connective tissue that synthesizes the extracellular matrix and collagen) in the cardiac muscle. The pathophysiological mechanisms that lead to this fibrosis are varied, some being acute as myocardial infarction and others being progressive and potentially reversible (Mewton et al., 2011). Myocardial fibrosis in animals and patient studies has been associated with ventricular systolic function worsening, abnormal cardiac remodeling and increased ventricular stiffness.

Different types of myocardial fibrosis have been reported (cf. Figure 1.11). They are classified according to the cardiomyopathic process. They were defined in (Mewton et al., 2011) as follows:

Reactive interstitial fibrosis. This type of fibrosis has a diffuse distribution within the interstitium (i.e. the space between cells in a tissue), but can be more specifically perivascular (i.e. located near or around a vessel). This type of fibrosis has a progressive onset and follows the increase in collagen synthesis by myofibroblasts[3] under the influence of different stimuli. It is a marker of disease severity and precedes irreversible replacement fibrosis. It is reversible under specific therapy.

Infiltrative interstitial fibrosis. This subtype of fibrosis is induced by the progressive deposit of insoluble proteins (amyloidosis) or glycosphingolipids (Anderson Fabry's disease) in the cardiac interstitium.

Replacement fibrosis. The replacement or scarring fibrosis corresponds to the replacement of myocytes after cell damage or necrosis by plexiform fibrosis (i.e. fibrosis resembling a plexus or network), mainly type I collagen. Replacement fibrosis appears as soon as myocyte integrity is affected. It can have localized distribution (ischemic cardiomyopathy, myocarditis, hypertrophic cardiomyopathy, sarcoidosis), or a diffuse distribution (chronic renal insufficiency, miscellaneous infammatory disease), according to the underlying etiology. Interstitial fibrosis and infiltrative fibrosis ultimately lead to replacement fibrosis in the later stages of disease.

Reactive interstitial or replacement myocardial fibrosis are common features of a broad variety of cardiomyopathies, including hypertrophic cardiomyopathy (HCM). Myocardial fibrosis leads to both *systolic and diastolic dysfunction*. On the one hand, fibrotic segments will deform less than normal ones (Bijnens et al., 2009) (systolic). On the other hand, fibrosis will lead to a decrease in compliance[4] thus to difficulties to fill the left cardiac chambers (diastolic). Other studies proved that the extent of LGE was also correlated with adverse cardiac events such as sudden cardiac death, fatal arrhythmia or worsening heart failure in patients with HCM (Bruder et al., 2010).

---

[3] A *myofibroblast* is a fibroblast (i.e. a cell in connective tissue that synthesizes collagen), having some of the characteristics of smooth muscle cells such as contractile properties.

[4] The term compliance is used to describe how easily a chamber of the heart or the lumen of a blood vessel expands when it is filled with a volume of blood.

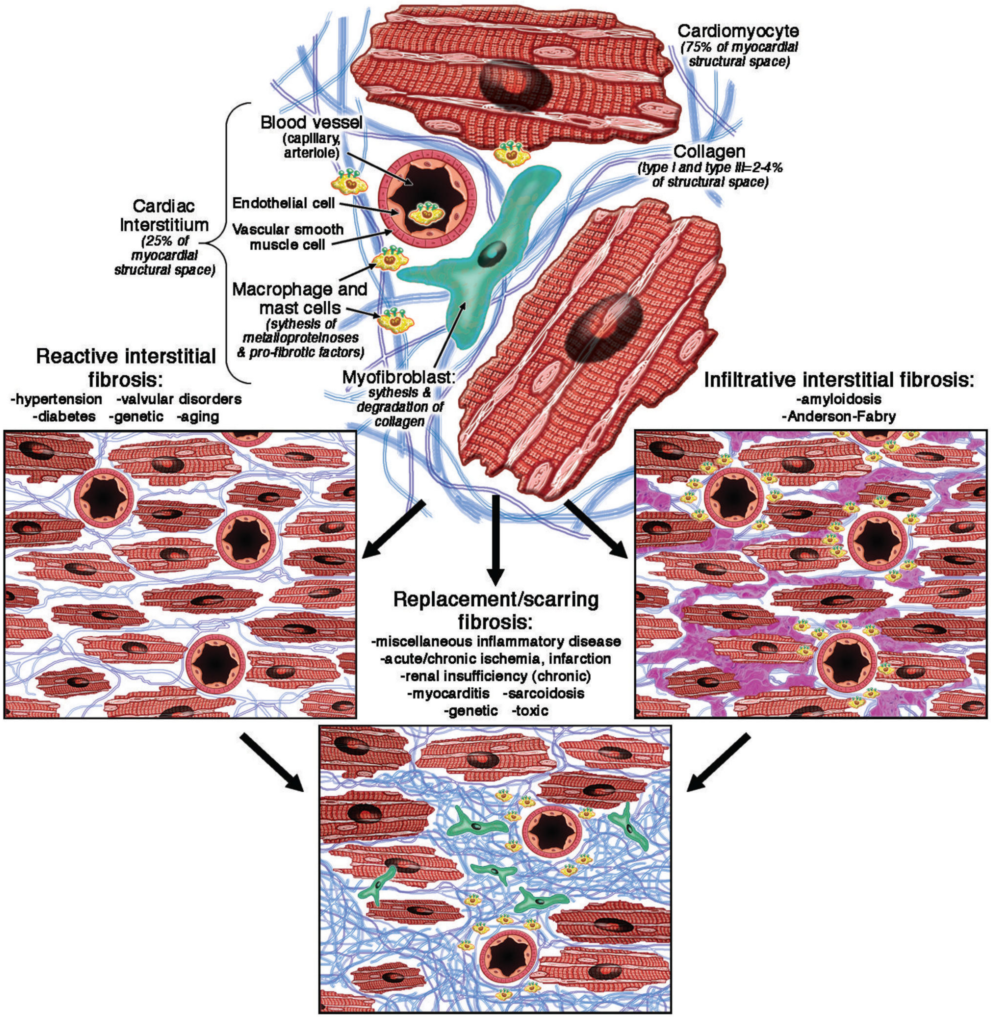

Figure 1.11: Etiophysiopathology of myocardial fibrosis. Myocardial fibrosis is a complex process that involves each cellular component of the myocardial tissue. The myocardial fibroblast has a central position in this process by increasing the production of collagen and other extracelular matrix components under the influence of different factors. From (MEWTON et al., 2011).

1.2.1.2 Problem statement: HCM characterization

HCM, being a very heterogeneous disease with variable outcome, needs a better characterization, particularly with regards to the potential presence of fibrosis. In this context, cardiac imaging can provide significant information enabling to elucidate those factors explaining HCM evolution.

HCM characterization and cardiac imaging. Cardiac magnetic resonance is the new gold standard to measure myocardial wall thickness and to diagnose HCM (Gersh et al., 2011). It is also used to characterize myocardial tissue state. In particular, it enables to quantify the fibrosis/scar extension (Moon et al., 2004). It is now documented that approximately half of patients with HCM have late gadolinium enhancement (LGE) suggestive of areas of fibrosis (M. S. Maron et al., 2008) (cf. 1.3.4.1).

Trans-thoracic echocardiography (TTE) is an examination of first intention in HCM diagnosis and patient's follow-up (Gersh et al., 2011). It enables not only to quantify the degree of hypertrophy but also the systolic and diastolic function of the left ventricle. Myocardial strain is a sensitive parameter of ventricular systolic function (N. L. Greenberg et al., 2002). In this context, 2D speckle tracking echocardiography (STE) provides an angle-independent, rapid and accurate method for strain measurement (Leitman et al., 2004). In addition, previous studies have described an alteration in left ventricular strain in HCM patients even with normal ejection fraction (Serri et al., 2006).

Some studies reported that regional myocardial strain and wall thickening are affected by regional myocardial fibrosis in patients with HCM (Popović et al., 2008)(Saito et al., 2012). Thus, the description of the relationship between myocardial strain and fibrosis may lead to a better understanding and interpretation of the strain curve. It would also enable a low cost and early characterization of myocardial tissue and an improvement in diagnostic.

In this context, multisensor image fusion provides a valuable tool to improve HCM understanding. For this purpose, we propose in this work to study the relationship between the local strain and the presence of fibrosis in HCM patients. We will consider regional strain curves from STE and myocardial fibrosis from the late gadolinium-enhanced (LGE) sequence of the cardiac magnetic resonance imaging (MRI). Then, we seek to evaluate the statistical significance of the change of strain indicators with regards to the presence or not of myocardial fibrosis as well as their strength to predict the presence of fibrosis. This study is presented in Chapter 5.

1.2.2 Heart failure and asynchronous contraction

According to the European Society of Cardiology, HF can be defined as an abnormality of cardiac structure or function leading to failure of the heart to deliver oxygen at a rate commensurate with the requirements of the metabolizing tissues, despite normal filling pressures (or only at the expense of increased filling pressures) (McMurray et al., 2012). In some cases, the heart cannot fill with enough blood. In other cases, the heart cannot pump blood to the rest of the body with enough force. Some patients have both problems.

HF prevalence is estimated between 1% and 2% of the adult population in developed countries (McMurray et al., 2012), with the prevalence rising to 10% or more among persons 70 years of age or older. From HF population, it is estimated that between 30% and 40% suffer from a synchronization defect or *cardiac asynchronism*. In fact, HF can be caused by cardiac asynchronism. Below we present different mechanisms that are triggered when HF appears, the relationship between HF and cardiac asynchronism, the Cardiac Resynchronization Therapy (CRT) and the optimization of CRT.

1.2.2.1 Mechanisms of the uncompensated heart failure

Several natural compensatory mechanisms are called into action in HF patients in order to buffer the fall in cardiac output; however, their benefits are of short term. These mechanisms have a neuro-hormonal origin. Two main compensatory mechanisms are involved: increasing the cardiac rate (tachycardia) and augmenting the volume of the myocardium (dilated cardiomyopathy). In the latter, the heart is dilated and cardiomyocytes stretch. This increases under certain limit the contractility of cardiomyocytes (Artigou et al., 2007).

Symptomatic mechanisms appear once HF cannot be compensated. They cause pre-charge and post-charge to increase (i.e. ventricular end-diastolic pressure and arterial pressure, respectively). HF mechanisms lead to different physiological changes either if HF is mainly originated at right ventricle or at left ventricle.

Left-sided heart failure. The left side of the heart must work harder than normal to pump the same amount of blood. Blood can be hardly evacuated from LV for multiple reasons (hypertension, coronary insufficiency, mitral insufficiency, myocardiopathy, etc.), and accumulates in RV. Depending of HF severity, this may result in shortness of breath and pulmonary edema.

Right-sided heart failure. In right-sided heart failure the right ventricle loses its pumping function, and blood may back up into other areas of the body, producing congestion.

Congestive heart failure. Sometimes the terms congestive HF and HF are used interchangeably. This type of HF requires timely medical care. As blood flow out of the heart slows down, blood returning to the heart through the veins backs up, causing congestion in the body's tissues.

The functional classification of the New York Heart Association (NYHA) (New York Heart Association, 1964) provides a simple way to classify HF extent based on the severity of dyspnea (shortness of breath), into four classes:

NYHA class I. Cardiac disease but no symptoms and no limitation in ordinary physical activity, e.g. shortness of breath when walking, climbing stairs, etc.

NYHA class II. Mild symptoms (mild shortness of breath and/or angina) and slight limitation during ordinary activity. The patient does not have symptoms at rest but normal effort produce fatigue, palpitations or dyspnea.

NYHA class III. Marked limitation in activity due to symptoms, even during less-than-ordinary activity, e.g. walking short distances (20-100 m). Comfortable only at rest.

NYHA class IV. Severe limitations. Experiences symptoms even at rest. Mostly bedbound patients.

1.2.2.2 Asynchronous contraction

HF can lead to an asynchronous contraction of the heart. The causes of such an asynchronism can be electrical (cardiac conduction disorder), mechanical (muscular disorder) or electromechanical. This is reflected in the ECG by an abnormally wide QRS complex (QRS greater than 120 ms) (McMurray et al., 2012). Cardiac asynchronism can be atrioventricular, interventricular or intraventricular (Gabriel, 2006):

Asynchronous atrioventricular contraction. It can be caused by a conduction disorder at sinus node (SA block) and/or at AV-node (AV block), both resulting in an abnormal delay of electrical conduction between atria and ventricles. This asynchronism causes mitral insufficiency at atrial end-systole and reduces the time of atria filling, thus decreasing the volume of ejected blood.

Asynchronous interventricular contraction. A given delay between RV and LV contractions delays blood ejection from one ventricle related to the other and often results in a decrease of cardiac function. This asynchronism is most commonly caused by a blocked bundle branch (a disorder of His bundle branches). There are two types of bundle branch block:

Right bundle branch block (RBBB). During RBBB the RV is not directly excited. However, LV is normally activated by the left bundle branch and transmits electrical impulses to RV through the myocardium.

Left bundle branch block (LBBB). During LBBB the LV is not directly excited and, reciprocally to RBBB, LV activation is delayed. RV contraction can provoke the septum to move towards LV before it contracts. This phenomenon is called *septal flash* and can be observed during an echocardiography (cf. 1.3.5).

Asynchronous intraventricular contraction. It is characterized either by an early or a late contraction of ventricular regions. When LV is affected, an early contraction increases ventricular pressure and slows mitral valve opening which alters ventricular

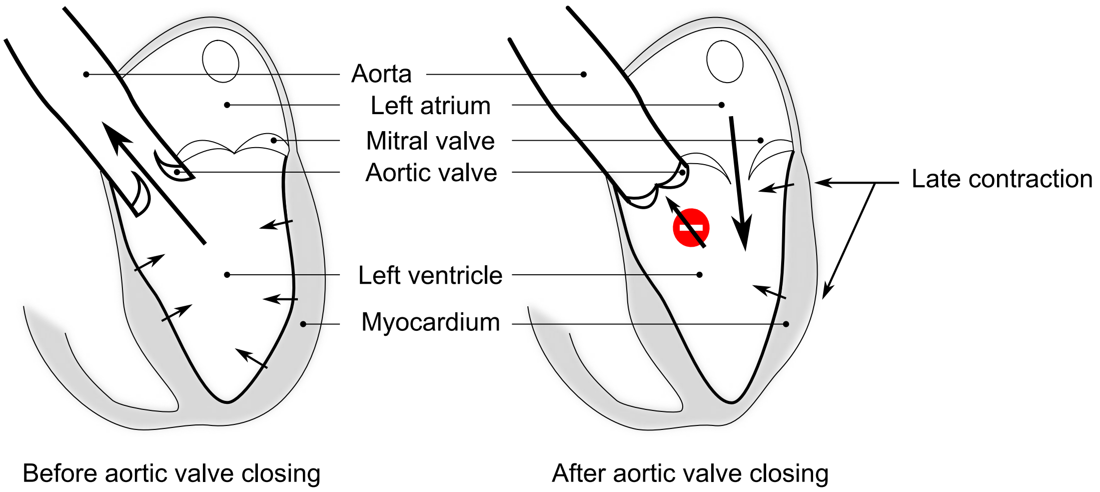

Figure 1.12: Contraction inefficiency after aortic valve closing: ventricular contraction after aortic valve closing is worthless because it does not increase cardiac function given that blood cannot flow into aorta. Modified from (TAVARD, 2012).

filling. On the other hand, a late contraction increases mitral insufficiency and decreases blood output volume, particularly when LV contraction starts after aortic valve closing and ventricular filling phase is already started (cf. Figure 1.12) .

1.2.2.3 Cardiac resynchronization therapy (CRT)

CRT consists in the implantation of a CRT-device (an electronic device with multiple stimulation leads) to correct cardiac asynchronism. This device triggers and controls myocardial contraction in order to reestablish inter- and intra-ventricular synchronism. The implantation procedure lasts about one hour and the patient needs one day of hospitalization.

Patient selection guidelines. CRT patient selection guidelines include:

- Chronic HF with systolic LV dysfunction, a left ventricular ejection fraction (LVEF) below or equal to 35% and a LV diameter at end-diastole greater than 27 mm/m^2,
- NYHA class III or class IV despite optimal medical treatment,
- Patient at sinus rhythm,
- QRS duration greater or equal than 120 ms.

CRT-device implantation. A *bi-ventricular pacemaker (BIV pacemaker)* is the most used CRT-device. This is a battery-powered electronic device with three stimulation leads (cf. figure 1.13). BIV pacemaker implantation is subcutaneous, generally below the clavicle. During CRT, the three stimulation leads must be correctly positioned: one in the right atrium (at atrium's summit), one in the right ventricle (at the apex) and the last in the left ventricle (CAZEAU et al., 2001; CLELAND et al., 2005).

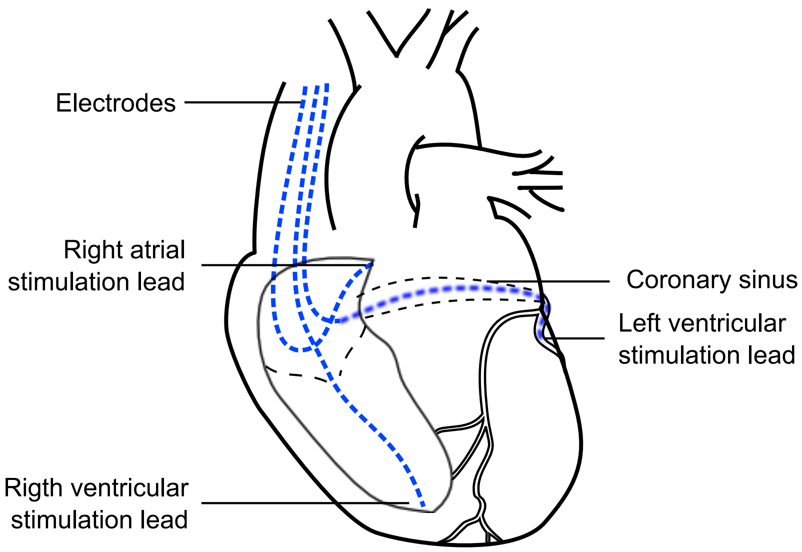

Figure 1.13: Implantation of the BIV pacemaker stimulation leads during cardiac resynchronization therapy. Three leads are implanted in order to stimulate the right atrium, right ventricle and left ventricle. Modified from (Tavard, 2012).

Different CRT stimulation approaches of the left ventricle are currently in study. The most used in clinical routine has been proposed by the Department of Cardiology and Vascular Diseases (DCMV) of CHU in Rennes as earlier as 1998 (Daubert et al., 1998; Leclercq et al., 2000). In this approach, the left ventricle is stimulated in only one site that is reached inserting the stimulation lead into one of the left coronary veins that join at the coronary sinus. This type of epicardial stimulation of the left ventricle is the one considered in this work.

BIV pacemaker configuration. Recent cardiac stimulators allow to adjust the atrioventricular delay (AV-delay) and the interventricular delay (VV-delay). AV-delay and VV-delay are adapted using echocardiography to obtain the best ventricular filling profile preserving an optimal left ventricular depolarization. A study on 43 patients obtained an average optimal AV-delay of 148 mm (Purnode et al., 2004).

Benefits from CRT. CRT main benefits are:

- After CRT-device implantation the LVEF increases, cardiac rhythm diminishes and the heart remodels. In fact, LV can loss 20 to 50 mL of its volume after six months compared to pre-implantation volume.
- At extra-cardiac level, CRT improves HF symptoms in about 50% of patients who have been treated maximally with medications but still have severe or moderately severe HF symptoms. CRT improves survival, quality of life, heart function, the ability to exercise and helps to decrease hospitalizations in these patients (Moss et al., 2009) (McAlister et al., 2007).

1.2.2.4 Problem statement: CRT optimization

CRT is a recognized treatment widely validated on chronic HF patients. Randomized studies suggest that cardiac resynchronization is effective on 70% of CRT-patients fulfilling the current selection guidelines (cf. 1.2.2.3) (Bax et al., 2005) (Mehra et al., 2004). Then, the percentage of patients non responding to CRT is still high: about 30% (Pavlopoulos et al., 2010) (Khan et al., 2009). *Non-responders* patients do not attain symptomatic benefits due to inappropriate selection for CRT, presence of myocardial scar, suboptimal LV lead position and/or inadequate post-implant device programming (Khan et al., 2009). The factors to consider in CRT optimization can be grouped into three main aspects:

1. **Improvement of patient selection guidelines.** The following aspects undermine the chances for CRT response: patients not fulfilling the selection criteria, absence of ventricular asynchronism, cardiomyopathy at a terminal stage (no possible remodeling), or additional contraindications originated in previous cardiac surgery.
2. **Optimization of device implantation.** Most of reported works focus on the optimization of the site for LV stimulation. Then, a better identification of potential stimulation sites (in particular, LV stimulation site), or a better characterization of the coronary venous network in order to get an optimal approach to the best stimulation site (in the case of an epicardial stimulation of LV), are of interest.
3. **Optimization of the stimulation.** Either using new stimulation approaches or optimizing the parameters of the BIV pacemaker, including AV-delay and VV-delay.

Image guided CRT optimization. Cardiac imaging plays a central role in CRT optimization. In this context, most of published works focus on the two first aspects of CRT optimization. Concerning the improvement of patient selection guidelines, (Chung et al., 2008) presented one of the first studies assessing the predictive strength of different indicators of CRT response. Different tissue Doppler imaging (TDI, cf. 1.3.5.2) and non-TDI echocardiographic indicators were evaluated in a multicenter-based study. They concluded that none of the studied indicators had statistical relevance as indicator of CRT responsiveness. (Pavlopoulos et al., 2010) presented a comprehensive perspective from the point of view of echocardiographic modalities, their advantages and limitations. They analyzed 18 indicators that could be measured from echo images and that had been proposed to predict CRT response. Their analysis listed the echo modality, cut-off value and response criterion. They also analyzed the selection of patients to CRT from the point of view of their clinical state. The general conclusion is that a comprehensive approach to CRT, accounting not only for electrical or mechanical dyssynchrony but also for several other covariates, is needed.

Concerning the optimization of CRT device implantation, it is commonly described in literature that the optimal site for LV stimulation is the one with the latest electromechanical activation (normally defined as the delay between the QRS and the peak-strain, as measured in echocardiography) (Morgan et al., 2009) (Khan et al., 2009). Also, an overall conclusion is that both, posterio-lateral (transmural) scar and dyssynchrony markers (Jansen et al., 2008), are important. This leads to a two folded optimization of LV tip location: (i) to locate the site of latest (electromechanical) activation and (ii) to characterize the scar burden at this location (Morgan et al., 2009) (Khan et al., 2009). In this context, studies assessing tissue state from cardiac magnetic resonance imaging have shown its relationship with the response to CRT (Leyva et al., 2011) (L. Chan et al., 2011) (Marsan et al., 2009) (Bilchick et al., 2008) (Jansen et al., 2008) (Chalil et al., 2007) (Valle et al., 2007) (Ypenburg et al., 2007) (J. A. White et al., 2006) (Bleeker et al., 2006). Besides, Computed tomography (CT) also plays an important role because it enables to obtain anatomical information (cavities and, mainly, the coronary tree) with high spatial resolution (M. Garcia et al., 2010) (Garreau, M. .-.-P. Garcia, et al., 2010) (Garreau, Simon, et al., 2006)(Simon et al., 2005) (Veire et al., 2008).

1.3 Multisensor cardiac imaging

This work focuses on multisensor fusion of electroanatomical mapping (EAM), computed tomography (CT), cardiovascular magnetic resonance imaging (MRI) and echocardiography (US, ultrasound) images that are used to characterize target HCM and cardiac asynchronism. On the one hand, they provide complementary information about cardiac anatomy, myocardial structure, electrical function and mechanical function. On the other hand, the fusion of these heterogeneous multisensor acquisitions enables an unified description of cardiac multiphysics phenomena of interest for a given patient. This may enable to detect the underlying sources and mechanism explaining the function of the diseased heart which, in long term, will allow to improve the understanding of the diseases, to improve their diagnosis and to optimize/predict the outcome of their treatment.

Despite this section focuses on cardiac imaging modalities of interest, it begins with a brief introduction of electrocardiography. This is because the ECG is commonly used to acquire EAM, MRI, CT and US images.

1.3.1 Electrocardiography

Electrocardiography (*ECG*) is a non-invasive examination of cardiac function that records the electrical activity of the heart during a period of time. In fact, ECG initial denotes both the examination and the signal recorded (i.e. the *electrocardiogram*).

1.3.1.1 Principle

ECG depicts the propagation wavefront of myocardial depolarization as seen on the chest (cf. Figure 1.7). ECG is acquired using electrodes placed on the skin of the patient's chest often using a sampling frequency of 15 kHz.

A first reading of the ECG reflects the regularity of cardiac frequency. ECG examination also enables to assess the size and position of the cardiac cavity, to detect an abnormality in cardiac rhythm, to verify the efficiency of a treatment or to adapt it (e.g. during pacemaker fine-tunning). In fact, ECG analysis is the most efficient way for abnormal cardiac rhythm measurement and diagnosis, in particular when it has electrical origins (electrical conduction defect).

The classical ECG acquisition, called *12-lead ECG*, requires the placement of ten electrodes (cf. Figure 1.14). The 12-lead ECG was standardized after an international convention (BARNES et al., 1938). In this context, *lead* means one ECG trace (i.e. a plot of voltage over time). There are six frontal leads and six precordial leads. Frontal leads are computed from three electrodes placed in the right arm, the left arm and the left leg, respectively. Precordial leads are computed from six electrodes positioned on the chest.

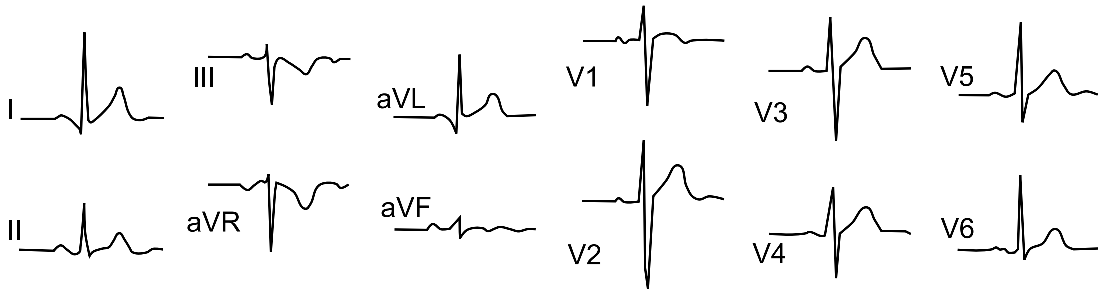

Figure 1.14: A 12-lead ECG for a healthy subject. From a trace using MèdiStory http://www.prokov.com.

ECG leads are commonly filtered to avoid artifacts: frequencies lower than 0.5-1.0 Hz and superior to 40 Hz, are rejected. The 40Hz cutoff frequency eliminates the interference of the power supply frequency of electrical appliances.

The ECG signal depicts the global electrical activity of the heart. It is divided into the P-wave, the QRS-complex and the T-wave (cf. Figure 1.7(bottom-left)). ECG analysis enables to detect arrhythmias, dyssynchrony and other electrical disorders. Electrical asynchronism diagnosis can also be done with ECG analysis.

1.3.1.2 Role of ECG in CRT

ECG is an important acquisition for CRT because QRS length is measured from patient's ECG. In fact, QRS-width has been used as an indicator of CRT response. ECG is acquired in pre-, per- and post-operative stages. Post-operative acquisitions allow to

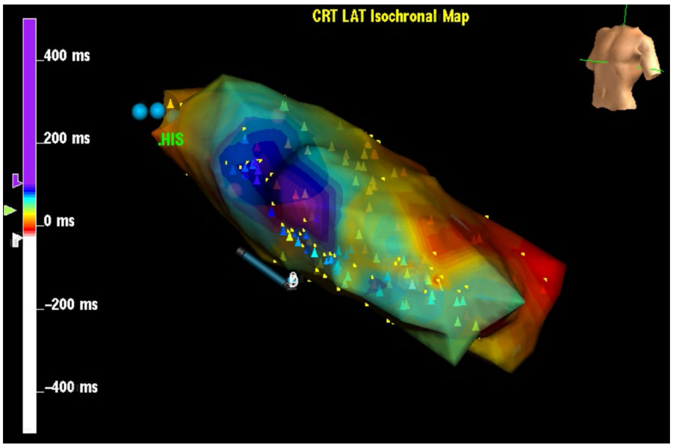

Figure 1.15: Instance of an electroanatomical mapping depicting the local activation time mapping of the inner LV and annotated anatomical landmarks (HIS). From (Tavard, 2012)

follow-up the improvement of cardiac function. Moreover, the ECG signal is commonly used as a global electrical reference to derive delay measurements, such as the global electromechanical delays measured in echocardiography.

1.3.2 Electroanatomical mapping (EAM)

An electrical conduction disorder can be assessed from ECG. However, very different electrical activation schemes can result in the same ECG signal. The knowledge and description of these activation schemes may provide more insights about the mechanisms leading to CRT response. EAM systems offer precise local electrical recordings. In contrast to ECGi [5] systems that estimate local electrical information from measurements in patient's surface (thorax), EAM systems records the local electrical activity or *electrograms* (*EGMs*) from the inner cavities of the heart (atrium, ventricles) along with the geometry of the cavity. The information derived from these recordings are mapped to the geometry resulting in an electroanatomical map (cf. Figure 1.15). These maps describe the local electrical function of heart's inner cavities. Below we present a description of the main EAM systems currently available (Schmitt et al., 2006).

1.3.2.1 Acquisition principle

The systems of endocavitary electrical mapping are made up of:

— Two leads that are mounted on catheters inserted into the femoral artery and advanced up the aorta to approach the left ventricle. They are used to acquire electrophysiological potentials:

---

5. *Electrocardiographic imaging.* This is a noninvasive mapping technique providing electrical information on the epicardial, and recently, the endocardial surface of the heart. These information is reconstructed from multiple electrical recordings on the chest, also called Body Surface Potential Mapping (BSPM).

∗ one reference electrode (fixed), placed into a cavity (right atrium or ventricle in the case of an acquisition in the left ventricle),

∗ one electrode or a constellation of electrodes measuring electrophysiological potentials of the endocardial surface.

- A spatial positioning system made up of three magnetic field sources of low intensity placed in the examination table. The magnetic field is captured by one sensor located on the tip of the acquisition lead. Then, the position of this lead is estimated by triangulation.
- A visualization console enabling to survey the progression of the acquisition (lead displacement, measurement, points acquired, signals).

A global view of an EAM acquisition is presented in Figure 1.16.

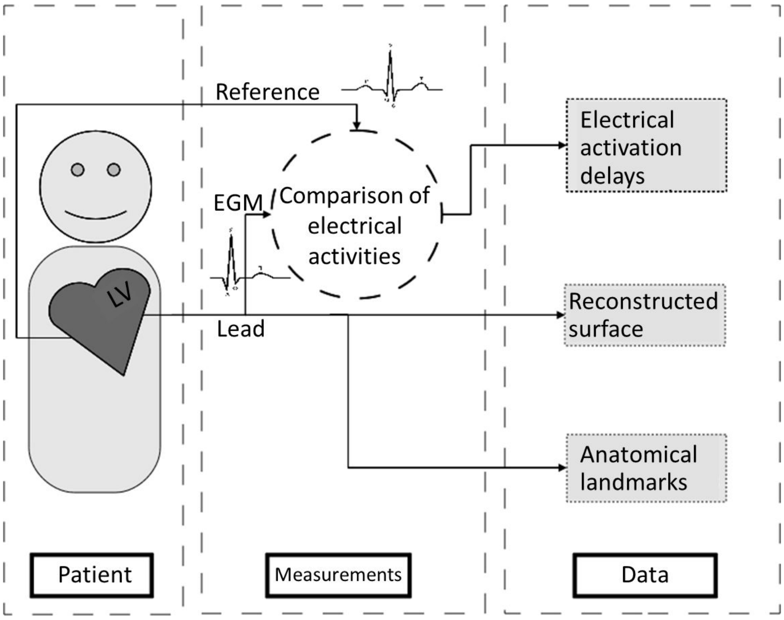

Figure 1.16: Schematic description of EAM acquisition. In this case the acquired information are the local electrical activation delays also known as *local activation time* (*LAT*). From (TAVARD, 2012).

The data acquired with EAM systems contains both, anatomical and electrical information. In a first stage, the endocardial surface is estimated from a point cloud lying into the cavity. Roughly speaking, this surface corresponds to the boundaries of this cloud. The reconstruction of LV endocardial surface is difficult because of LV trabeculae. LV apical and septal zones as well as the region close to the mitral valve are of difficult access and could not be contoured adequately.

EAM surface can be enhanced with anatomical landmarks marked by the physician during the acquisition. The annotated fiducials make easier to orientate the surface during posterior visualization. These fiducials are annotated by positioning the lead in the anatomical region of interest. The aorta (or the aortic chamber), the apex, one wall (e.g. the septal wall) and the mitral region are often annotated during LV mapping. However, these landmarks indicate an anatomical region rather than a precise point on the surface.

The electrical maps of the endocardial surface are acquired in a second stage. Local intra-cavity EGMs are acquired by a mobile electrode. Another EGM is recorded in parallel and used as a reference signal. This reference can be either the ECG or, more often, the EGM recorded by an electrode placed into another cavity (often the RV).

Two types of information are routinely extracted from recorded EGMs: *electrical delays* and *electrical magnitude*. Electrical delays are computed from a reference time stamp marked in the reference signal. In such a way, a mapping of the *local activation time* (*LAT*) can be computed (cf. Figure 1.15). Each LAT is the delay between the reference time stamp and the instant of the peak of a cavity EGM. The selection of the reference lead determines the electrical mapping quality. In fact, a low signal to noise ratio (i.e. the ratio between the power of the signal c.ontaining the information and the power of noise/parasite signal), will affect the positioning of the time reference. Thus, a lead near to the coronary sinus is often preferred because EGM amplitude at this localization, near to AV-node, is equivalent or even stronger than an EGM at atria (Bhakta et al., 2008).

There are two types of electrodes used to record EGMs:

Contact system (sequential acquisition). One electrode mounted in a catheter is moved until it touches the endocardium. In such a system, EGMs are acquired *sequentially*, i.e. EGMs are acquired point by point around the endocardial surface. The CARTO® mapping system uses this approach. The acquisition of each EGM takes about one second. The number of points with associated EGMs will define the duration of the electrical acquisition (around 20 min without considering the time needed to acquire LV geometry). This time will extend to some hours if different mappings are acquired (e.g. mappings for different types of excitation of the BIV pacemaker).

Non-contact system (simultaneous acquisition). In this case, the catheter used for EGM acquisition contains a *multi-electrode array* (*MEA*) that is a constellation of electrodes arranged in a known distribution (Ensite, Endocardial Solutions Inc., St. Paul, MN, USA, Figure 1.17). Normally, these electrodes are not in contact with the endocardial surface. The MEA catheter (e.g. a balloon catheter) allow to acquire the entire electrical activity of the cavity in a unique heartbeat which is clearly an advantage, e.g. when non sustained arrhythmias need to be mapped. To obtain endocardial EGMs, the *inverse problem* needs to be solved (Khoury et al., 1995). EAM acquisition with MEA catheters needs less time than using contact catheters; however, the patient can be discomforted with the balloon catheter placed into the heart. In addition, EGM precision is lower than using contact catheters.

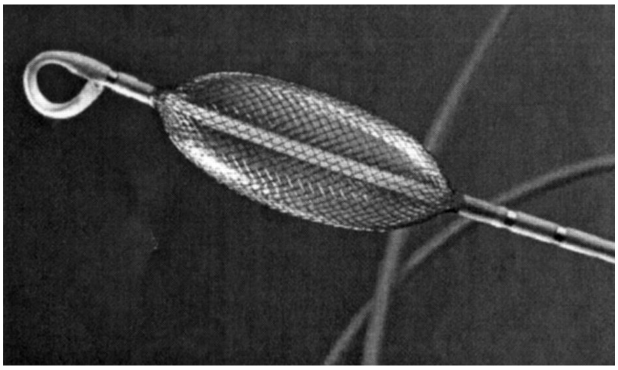

Figure 1.17: A balloon catheter used in a non-contact EAM system. The catheter is an array of 64 electrodes distributed on an ellipsoidal surface.

1.3.2.2 Role of EAM in CRT optimization

EAM acquisitions are of great interest to plan CRT and to study CRT effects on cardiac electrical propagation (TAVARD et al., 2014). These acquisitions are rare in clinical routine; however, the data they provide is very rich in information. EAM acquisitions were included in IMOP (feasibility study) and euHeart protocols (cf. 6.2.1). They were acquired after BIV pacemaker implantation. The acquisition was performed under different modes of stimulation (no stimulation or sinus rhythm, RV stimulation, LV stimulation and BIV stimulation), in order to analyze and derive new criteria that could be used to optimize CRT gesture and patient selection.

1.3.3 Cardiac computed tomography (CT)

X-ray computed tomography is a technology that uses computer-processed X-rays to produce *tomographic images* of specific areas of the scanned object. Digital geometry processing is used to generate a three-dimensional image of the inside of an object from a large series of two-dimensional radiographic images captured around a single axis of rotation (HERMAN, 2009). Because X-ray computed tomography is the most common form of computed tomography in medicine and various other contexts, the term *computed tomography* alone (or *CT*) is often used to refer to X-ray CT, although other types exist (such as *positron emission tomography* (*PET*) and *single-photon emission computed tomography* (*SPECT*)). In this work, we use the term CT to refer to *cardiac X-ray computed tomography.*

CT reconstruction uses multiple X-ray projections meaning that the intensity of each reconstructed voxel is related with the radiological density of the tissue it belongs, i.e. the measurement of its X-ray absorption properties. The first commercial CT was invented by Sir Godfrey Hounsfield who gave his name to the unit of absorption coefficients or a *Hounsfield* (*H*). For instance, X-ray absorption coefficients for air, water (similar to blood) and bones are -1000 H, 0 H and 1000 H, respectively. Thus, the differences of X-ray

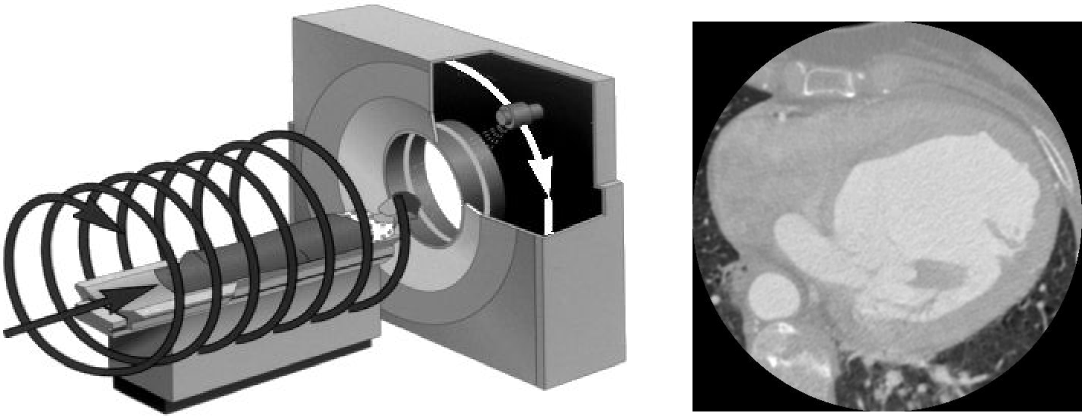

(a) Spiral computed tomography system (b) Slice from a cardiac CT

Figure 1.18: Computed tomography. (a) Spiral computed tomography system: table moves during acquisition while the pair emitter-detector rotates around it. From (Germain, 2005). (b) Slice from a cardiac computed tomography image (axial view).

absorption coefficient between tissues enable to distinguish different organs into the body (cf. Figure 1.18). *Spiral CT* is the dominant type of CT scanner technology. In this type of machines, the patient is placed on a table and moved during CT acquisition while the pair X-ray emitter-detector rotates around it. The number of X-ray projections (angular resolution) and the size of the field of view (spatial extent of the object to be imaged), are important parameters defining CT image resolution. In cardiac CT, it is common to obtain sub-millimeter spatial resolutions. A typical resolution is $0.3 \times 0.3 \times 0.6$ mm^3 for an extent of $512 \times 512 \times 193$ voxels and a cylindrical field of view covering all heart chambers (cf. Figure 1.18b).

1.3.3.1 Temporal synchronization

Cardiac CT image reconstruction needs to "freeze" the moving heart to avoid reconstruction artifacts due to cardiac motion. Most CT systems need more than one heartbeat to reconstruct a 3D image of the heart. Therefore, data acquired at different heartbeats need to be synchronized in order to obtain a meaningful image. Such synchronization is performed using ECG that triggers CT acquisition. There are two types of *ECG-triggering* (J. K. Lee, 2006):

Prospective ECG-triggering (or post-synchronization). The heart is scanned in *sequential* (step-and-shoot) mode at a determined delay after the onset of the R-wave. This delay can be either relative (e.g. a percentage of the time interval between the onset of two continuous R-waves, called *RR-interval*) or absolute (in milliseconds), and either forward (i.e. triggered from new R-waves) or reverse (i.e. based on a series of preceding R-waves). This technique regains new interest today because the radiation dose is lower than in retrospective ECG; however, it is not possible to reconstruct dynamic volumes over the cardiac cycle.

Retrospective ECG-triggering. The heart is scanned *continuously* by a spiral scan while the ECG is recorded simultaneously. A CT image volume is reconstructed from acquired data at an ECG cardiac phase selected *retrospectively.* As a result, the radiation dose in a retrospective ECG-triggering study is higher than in a prospective ECG-triggering study. This technique enables the acquisition of dynamic images of the heart. A typical temporal resolution of 5% of a heartbeat, resulting in 20 image volumes evenly distributed over the cardiac cycle, is obtained.

1.3.3.2 Role of cardiac CT in CRT optimization

CT imaging continues to be used in clinical routine even if it uses X-ray ionizing radiation. Although cardiac MRI is an alternative to CT because it does not expose the patient to ionizing radiation, it cannot replace CT in all applications. In the context of CRT, CT imaging may be preferred to acquire and visualize the coronary tree (arteries and veins) before BIV pacemaker implantation (TAVARD et al., 2014). It also provides an anatomical description of the heart with higher spatial resolution than MRI.

1.3.4 Magnetic resonance imaging (MRI)

MRI systems exploit the *nuclear magnetic resonance* of hydrogen nuclei to build an image of biological tissues that can furnish information about morphology and function of the human organism. The water and fat in human tissues are the primary origin of the MR signal used to generate images because they contain high quantities of hydrogen nuclei.

MRI systems apply a strong magnetic field B_0 (measured in *Tesla* units or T) to align the magnetic momentum of hydrogen nuclei (cf. Figure 1.19b). The attained *moment equilibrium* is then perturbed with a radio-frequency field (*RF-field*) at a particular frequency: the *Larmor frequency.* This RF-field is generated by RF-coils (cf. Figure 1.19a) and is normally applied as a short pulse (*RF-pulse*). RF-pulse causes the net magnetisation (macroscopic magnetization) to move away from its alignment with B_0 and to rotate around it at a frequency equals to the Larmor frequency, also called *frequency of precession.* Immediately after the application of the RF-pulse, the system starts to return back to equilibrium. This process is known as *relaxation.*

There are two distinct relaxation processes that can be detected by MRI systems: the longitudinal relaxation (along the axis of B_0 i.e the z axis) called *T1-relaxation*, and the transverse relaxation (along x and y axes). T1-relaxation is an exponential process with a time constant T1. Transverse relaxation is made up of *T2-relaxation* and *T2*-relaxation* with time constants T2 and T2*, respectively. T2*-relaxation results from the combined effect of T2-relaxation and the effect of magnetic field non-uniformities (RIDGWAY, 2010). In the case of T2-relaxation, the signal that the receiver coil detects

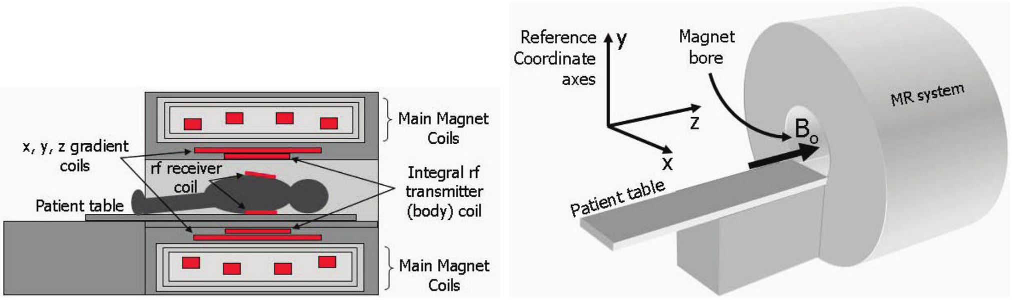

(a) Relative location of MR coils (b) Cylindrical bore MR system

Figure 1.19: MRI system components. (a) Relative location of the main magnet coils, x,y and z gradient coils, integral RF transmitter body coil and RF receiver coils. (b) Typical arrangement for a cylindrical bore MRI system showing the magnet bore and the reference coordinate axes with the static B_0 field direction along the horizontal z axis. From (Ridgway, 2010).

(if no further RF-pulses or magnetic field gradients are applied), is seen as an oscillating magnetic field that gradually decays, known as a *free induction decay (FID)*. While the FID can be detected as a MR signal, for MRI it is more common to generate and to measure the MR signal in the form of an *echo*. The two most common types of used echo are *gradient echoes* and *spin echoes*. In general, the amplitude of the spin echo signal is greater than the gradient echo signal. Imaging based on spin echo is also less affected by the presence of field inhomogeneities caused by metallic artifacts.

1.3.4.1 Cardiovascular magnetic resonance imaging (cardiac MRI)

Cardiovascular magnetic resonance imaging (cardiac MRI) is the current gold standard modality for non-invasive evaluation of cardiac function. It is also used to evaluate cardiac morphology and myocardial substrate. High-quality imaging can be achieved in most patients in all orientations, all chambers and wall segments including those of the right ventricle. The analysis of regional and global myocardial function can also be performed using cardiac MRI. Moreover, dobutamine stress cardiac MRI offers ischemia evaluation, with the same examination protocol known from stress echocardiography. Finally, myocardial substrate can be assessed with contrast enhanced sequences.

Capturing an image of the heart that is unaffected by motion requires the image to be acquired in just a few tens of milliseconds. However, to achieve acceptable image quality, the image acquisition time becomes too long to “freeze” heart motion. Therefore, MRI signals are acquired over multiple heartbeats, synchronizing the signal acquisition to a particular time point in the cardiac cycle using the ECG, as for CT (cf. 1.3.3.1) (cf. Figure 1.20).

Spin echo sequences acquire a static anatomic image with black blood, providing information about heart morphology (cardiac cavities and vessels appear black contrasting

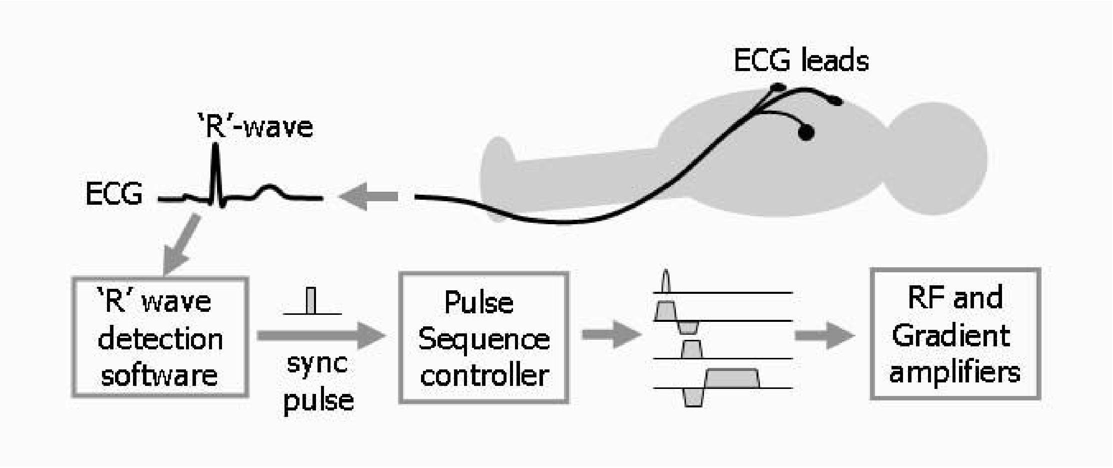

Figure 1.20: ECG synchronization of imaging pulse sequences. From (RIDGWAY, 2010).

with myocardial and vessel walls in gray). On the other hand, gradient echo sequences enable to acquire dynamic images (called cine) with white blood and gray myocardium, allowing to assess heart dynamics.

Dealing with respiratory motion. Conventional spin echo and gradient echo imaging techniques are degraded by respiratory motion. Image degradation caused by respiratory motion can be reduced either with respiratory compensation methods, cardiac synchronized fast imaging techniques combined with patient breath-holding (used in clinical routine), or ultra-fast (single-shot) imaging techniques. Magnetic resonance images processed in this work were acquired under the breath-hold approach with the Philips T1-weighted Turbo Field Echo (T1-TFE) and Balanced Turbo Field Echo (BTFE) sequences; however, they were not exempt of slice misalignment due to respiratory motion (cf. 4.3.3).

There is a rich diversity of sequences describing anatomical and functional information of the heart. We present below those related with the work presented here and, especially, the *late gadolinium-enhanced cardiac MRI* which enables the assessment of myocardial fibrosis.

Cine imaging. *Cine-MRI* is acquired using fast gradient echo imaging. This type of acquisitions is particularly appropriate to study global and regional ventricular function (GAROT, 2005). Retrospective ECG synchronization can be used successfully when imaging patients with small beat-to-beat variation (RIDGWAY, 2010). The images for all cardiac phases can be then acquired and viewed as a movie sequence or *cine*. A typical cardiac cine-MRI will have a temporal resolution of 30 ms for 20 to 60 cardiac phases imaged, a spatial resolution of 1.5 mm (in-plane) and a slice thickness of 8 to 10 mm (cf. Figure 1.21).

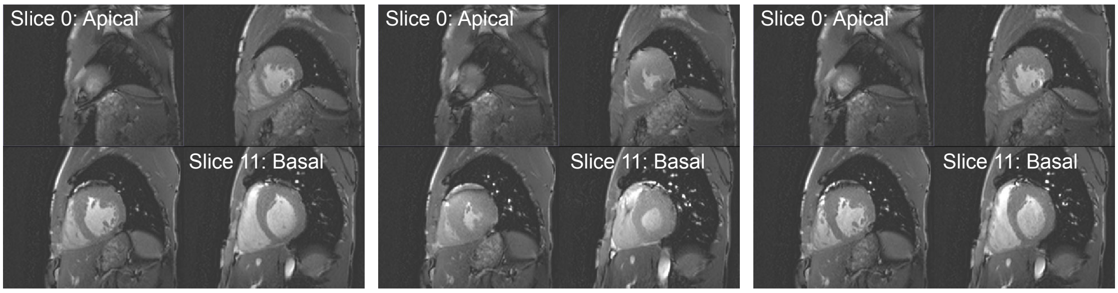

0 ms 310 ms 659 ms

Figure 1.21: Cardiac cine-MRI SAX of a HCM patient with average heart rate of 52 bpm.

Delayed enhanced MRI (DE-MRI). Cardiac DE-MRI is used to assess *myocardial viability* (i.e. the retained capacity to recover contractile function following revascularization), and has been extensively validated, both in animal models and in clinical studies (Choi et al., 2001) (Kim, Wu, et al., 2000) (Kim, Fieno, et al., 1999). The identification of *scarred* myocardial tissue in patients with acute or chronic myocardial infarction is one of the most important clinical applications of DE-MRI. It is also used to assess macroscopic fibrosis in the myocardium. Cardiac DE-MRI involves intravenous administration of *gadolinium-based contrast agent* followed by the acquisition of T1 weighted images of the myocardium using an *inversion recovery (IR)* technique. IR technique is commonly employed to suppress the signal from *viable* myocardium by modifying the contrast of the acquired image between viable and nonviable myocardium. Typically, IR uses inversion pulses followed by a prescribed delay to allow recovery of the prepared magnetization before a spin echo or gradient echo pulse sequence used to “read out” the magnetic resonance signal. The associated delay is known as *time after inversion (TI)* (Jacquier et al., 2010).

There are two types of cardiac DE-MRI: *early gadolinium-enhanced* (*EGE*) and *late gadolinium-enhanced* (*LGE*). EGE- and LGE-MRI are essentially the same, but the timing of the acquisition following intravenous administration of the contrast agent is a distinguishing factor, being greater than 10 min for LGE-MRI. In a typical LGE exam, 10 to 12 breath hold slices are acquired in short axis orientation, followed by long axis and 4-chamber views when clinically indicated.

Late gadolinium enhancement: physiopathology. Gadolinium is an extracellular contrast agent; thus, it distributes from the vascular sector to the interstitial sector and never enters the cellular sector. In myocardium, the vascular sector represents 5%, the interstitial sector 15% and the cellular sector 80% (Jacquier et al., 2010). Therefore, the intensity of the gadolinium enhancement depends upon (i) tissue perfusion and (ii) the volume in which the gadolinium is distributed. Then, whatever the underlying pathology, late gadolinium enhancement is always related to an increasing in the volume of gadolinium distribution and to a slowing down in the wash-out (Kazmierczak, 2011):

gadolinium contrast agents are not markers for myocardial fibrosis but for the interstitial space as well as wash-in and out kinetics of the contrast agent into this interstitial space (Mewton et al., 2011). However, as mentioned previously (cf. 1.2.1.1), the presence of fibrosis increase the proportion of interstitial space: it has been shown that those zones with late gadolinium enhancement correspond to zones with fibrosis in autopsy (Roberts et al., 1987). (Moon et al., 2004) described the histological basis of late gadolinium enhancement in hypertrophic cardiomyopathy, finding LGE zones representing regions with increased collagen but not disarray (cf. Figure 1.22).

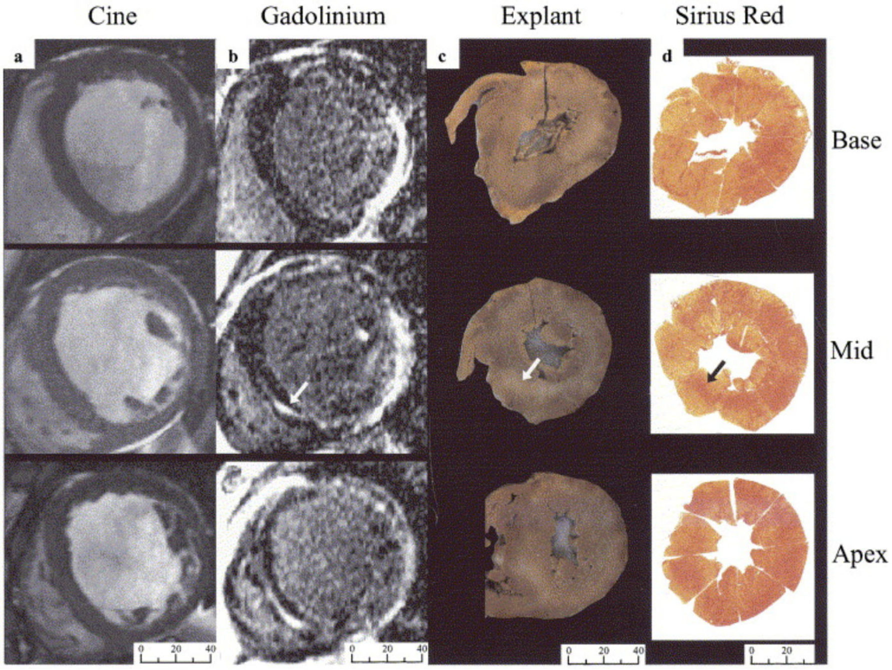

Figure 1.22: Comparison of (a) in vivo diastolic cine image (cf. 1.3.4.1), (b) in vivo gadolinium-enhanced cardiovascular magnetic resonance (cf. 1.3.4.1), (c) gross specimen of sections from explanted heart, and (d) histologic sections stained with sirius red (used for collagen determination). All images are the same scale. After fixation, considerable contraction has occurred. Regions of gadolinium enhancement correlate with regions of macroscopic unstained pale myocardium and regions of red-stained collagen. A representative mesocardial region, which is well defined, is marked by an arrow. From (Moon et al., 2004).

Sequences of LGE acquisition. In LGE imaging, the optimal TI is obtained from a previous step called *TI scout* (cf. Figure 1.23a). In such a way, non-viable tissue (scarred or with macroscopic fibrosis) will appear as bright regions into the myocardium. There are two types of LGE sequences: *inversion recovery MRI* (*IR-MRI*) and *phase sensitive inversion recovery MRI* (*PSIR-MRI*). IR sequences acquire the magnitude of the magnetization at the time of inversion. This time must be carefully selected to null viable myocardium; this increases the range of gray levels between viable and non-viable tissue. In contrast, PSIR sequences are less sensitive to the selection of TI because they take account of the sign of the magnetization at the time of data acquisition; therefore, the dynamic range of IR signal intensities (SI levels) increases (compare Figures 1.23a and 1.23c). Instances of IR and PSIR images revealing myocardial fibrosis in one HCM patient are showed in Figure 1.23b and Figure 1.23d, respectively.

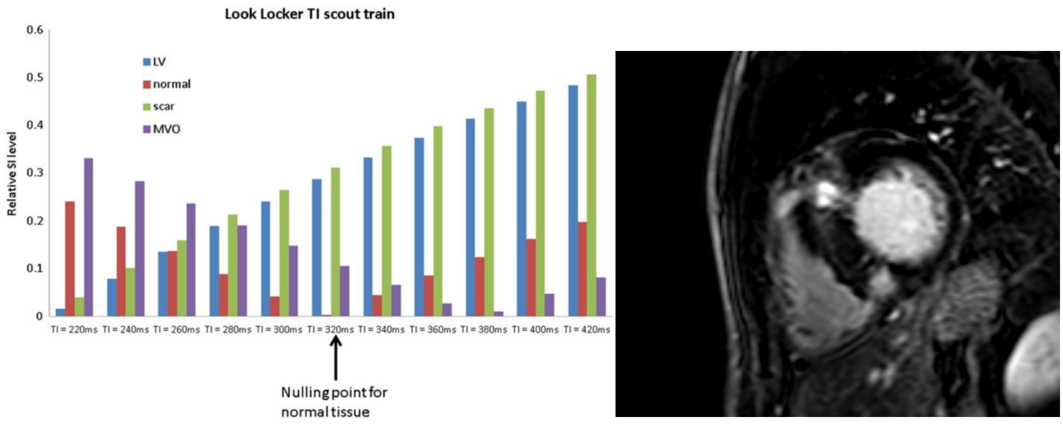

(a) TI scout (Look-Locker technique) for IR-MRI (b) LGE-MRI SAX, IR sequence

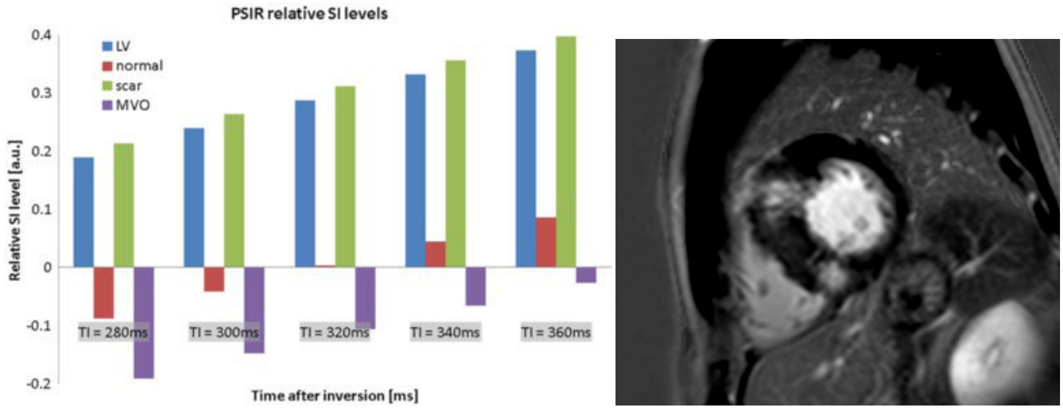

(c) Relative SI levels in PSIR-MRI (d) LGE-MRI SAX, PSIR sequence

Figure 1.23: Late gadolinium-enhanced MRI. (a) Relative signal intensities (SI) for LV blood pool, normal myocardium, scar tissue and MVO for images acquired at different TI values using a TI scout (Look-Locker technique). The image where the normal myocardium appears darkest is identified as the optimal TI time (about 320 ms in this case). From (Ridgway, 2010). (b) IR image for a patient with HCM diagnosis and late gadolinium enhancement indicating myocardial fibrosis. (c) Relative SI levels in PSIR sequence. From (Ridgway, 2010). (d) PSIR image for the same patient in (b). Acronyms – IR: inversion recovery, MVO: microvascular obstruction, PSIR: phase sensitive IR, SI: signal intensity, TI: time after inversion.

T1-mapping with Modified Look-Locker Inversion Recovery (MOLLI). Despite being very sensitive to small areas of regional fibrosis, where regional collagen deposits appear in areas of myocyte injury (well defined areas), LGE has a limited sensitivity for interstitial diffuse fibrosis (Fernandes et al., 2014). Moreover, the ability of cardiac LGE-MRI to image diffused fibrosis is limited because this type of fibrosis appears distributed into the myocardium; hence, no region will contain healthy tissue to null. Recent works suggest that *T1-mapping* sequence can overcome this problem (Lima, 2013) (Puntmann et al., 2013). The most widely used T1-mapping sequence is based on the Modified Look-Locker Inversion-recovery (MOLLI) technique. This is a technique merging image sets from multiple Look-Locker sequences with varying inversion times into one data set (Messroghli, Radjenovic, et al., 2004). In such a way, a curve depicting the increasing read intensity for different TI enables to get the T1 value of each voxel in the merged image. There are different variations of the original MOLLI technique proposed by (Messroghli, Radjenovic, et al., 2004): the optimized MOLLI sequence (Messroghli, Greiser, et al., 2007) and the shortened MOLLI sequence (Piechnik et al., 2010). However, more evidence is needed in order to be used in clinical routine.

1.3.4.2 Role of cardiac MRI in HCM characterization

The assessment of myocardial fibrosis plays an important role in the comprehension of HCM. As described in 1.2.1.2, fibrosis from LGE-MRI and regional myocardial strain assessed in patient with HCM diagnosis seem to be related. Thus, it is pertinent to acquire MRI sequences allowing to assess myocardial fibrosis in HCM patients with the perspective of correlating it with the information from other imaging techniques. The latter would improve patient detection and treatment at early stages as well as the knowledge of the information that other imaging techniques contain.

1.3.4.3 Role of cardiac MR in CRT optimization

In the context of CRT optimization, cardiac MRI is of interest to study myocardial scar/fibrosis and mechanical function. For CRT, it also allows to extract anatomical and functional information of the heart and to study the quality of the parietal wall and the coronary tree (using contrast enhanced magnetic resonance angiography). However, the quality of extracted coronary veins from MRI is lower than from CT.

1.3.5 Echocardiography (US)

Echocardiography is the acquisition of an *ultrasound image* of the heart (cf. Figure 1.24). It is a routine examination for diagnosis and follow-up of patients with suspected or known heart diseases. Echocardiographic systems are ubiquitous, present in almost every cardiac service around the world because they are non-invasive, cheap, painless and offer different information about heart anatomy and function. Below, we introduce the principle of echography and the main acquisition modes, before describing Speckle Tracking Echography which is extensively used in this work to assess cardiac mechanics.

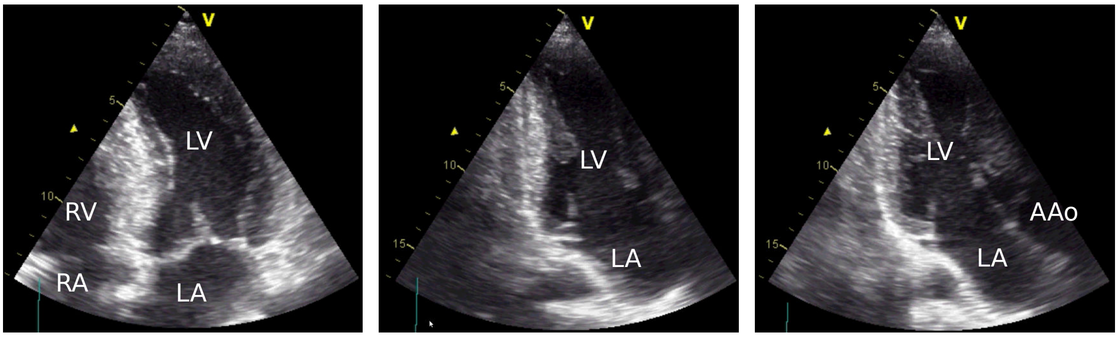

Figure 1.24: Transthoracic echocardiographic (TTE-US) images at end-diastole. From left to right: apical four-chamber view (4CH), apical two-chamber view (2CH), and apical three-chamber view (3CH). Acronyms – AAo: ascending aorta, LA: left atrium, LV: left ventricle, RA: right atrium, RV: right ventricle.

1.3.5.1 Principle

Cardiac ultrasound is an imaging technique detecting the frontiers between tissues having different *acoustic impedances*. This technique use a beam of ultrasounds to acquire an image of the heart. The image is formed from *echo signals* depending of the interaction of ultrasounds with the matter they propagate through. There exists different propagation phenomena affecting these echoes: absorption, reflexion, refraction and diffusion.

An echocardiographic system includes an echo probe with an ultrasound emitter/receptor couple. There exist different types of echocardiographic examinations according to where this probe is located. The two most common are *transthoracic echocardiography (TTE)* and *transesophageal echocardiography (TEE)*. The probe is located on the chest during TTE while it is located on a catheter positioned in the esophagus during TEE.

Echocardiographic examination often includes a *Doppler acquisition*. The *Doppler effect* is observed when an incident wave with frequency f_i and propagation vector $\vec{u_i}$ is reflected by a moving wall with velocity $\vec{v}$ in a medium with wave velocity c. The frequency of the reflected wave (f_r) with direction $\vec{u_r} = -\vec{u_i}$ is given by:

$$f_r = (1 - \frac{\vec{v}.\vec{u_i}}{c}) \times f_i \tag{1.1}$$

Doppler effect enables to determine the speed and direction of blood flow and the motion of cardiac muscle (*tissue Doppler imaging, TDI*) and, in such a way, to analyze cardiac function (Bank et al., 2006; Yu, Sanderson, et al., 2007).

1.3.5.2 Echocardiographic modes

There are different echocardiographic modes (i.e. how US echoes are represented) used to image the heart. Some of them are:

Motion mode (M-mode). This represents the motion of structures over time. Initially a 2D image is acquired and a single scan line is placed along the area of interest. M-mode will then show how the structures intersecting that line move towards or away from the probe over time;

Dynamic 2D. This is a 2D cross sectional dynamic view of underlying structures made up of numerous B-mode (brightness mode) scan lines. The *field of view (FOV)* is the portion of the organs or tissues that intersects the scanning planes, being a cone in the case of echocardiography;

Continuous Wave Doppler (CWD). A part of the transducer is transmitting continuously and a part of the transducer is receiving continuously the Doppler signal along a single line that is placed on the 2D image. Thus, there is no spatial resolution;

Pulse wave Doppler (PWD). A pulse means that the transducer transmits the ultrasound and receives it after a preset delay. This enables to localize precisely the site of origin of a velocity signal. A key disadvantage with PWD is the inability to measure high velocities accurately. In fact, high velocities result in a undesirable phenomenon called *aliasing*; however, it can be attenuated;

Color flow Doppler imaging (CFI). It has the same principle as PWD but the flow are encoded by colors according to the underlying velocity and direction (warm color: flow towards the probe, cold: away);

Tissue Doppler imaging (TDI). This mode is similar to the PWD except that it is used to measure velocities of tissue motion that are much lower than blood velocities;

3D echography. Real-time 3D echocardiography using an array of US sensors to image the heart.

Speckle tracking echocardiography (STE). STE is usually considered as an echocardiographic mode yet being a US image processing instead. Echoes are locally modified by an interference pattern and natural acoustic reflections called as a whole *speckle noise*. This speckle is particular for a given portion of a tissue being a sort of *local acoustic signature* of a particular subregion. A technique called *speckle tracking* analysis tracks this speckle frame to frame and resolves it ultimately into an angle-independent two-dimensional and three-dimensional strain-based sequences (cf. figure 1.25).

STE analysis provides both quantitative and qualitative information about tissue deformation and motion (Blessberger et al., 2010). Displacement, velocity, deformation (*strain*), tissue kinetics (*tissue velocity imaging* or *tissue synchronization imaging*) are examples of what can be analyzed with STE. Moreover, today it is possible to have their extension to 3D echocardiography (e.g. to compute surface strain) (Maffessanti et al., 2009).

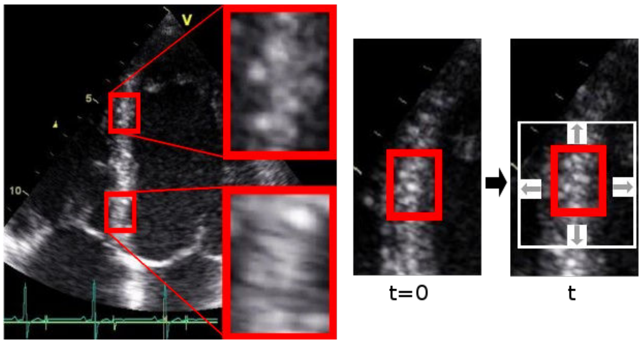

Figure 1.25: Speckle tracking principle: speckle noise pattern (left) are tracked from one image at phase 0 (t=0) to the next at phase 1 (time t). From (Støylen, 2001).

The assessment of 2D strains by STE is a semiautomatic method that requires the cardiologist to define few points along the endocardial border. Furthermore, the sampling *region of interest* (*ROI*), that is automatically defined by the echo system from the endocardial delineation, needs to be adjusted to ensure that most of the wall thickness is incorporated in the analysis and to avoid the pericardium (cf. Figure 1.26). Then, strains are computed by tracking the local speckle for defined regions. Regional strain is defined as the fractional or percentage change in a myocardial region (e.g. basal-lateral, cf. Figure 1.26) in comparison to its original dimension, along a direction (e.g. LV long axis). From this, it can be obtained both a 2D mapping of the region's deformation during a heartbeat and local *strain curves* (2D plot of myocardial deformation over time), as depicted in Figure 1.27

1.3.5.3 Role of US in HCM characterization

STE plays a potential central role in HCM characterization. Strain curves are of interest because they describe the mechanical behavior of myocardial tissue that can be correlated with fibrosis. Potentially, STE may provide the information to detect the myocardial regions affected by fibrosis.

1.3.5.4 Role of US in CRT optimization

Echocardiography is commonly used to measure mechanical delays, cardiac function and, therefore, to diagnose cardiac asynchronism (Donal et al., 2011). It is acquired before and right after BIV pacemaker implantation which enables to improve BIV pacemaker parametrization. Also, it is used in patient's follow-up (at three and six months after implantation).

STE is of particular interest for CRT optimization. Potentially, it provides the information pertinent either to derive new markers of cardiac function from displacement, velocity or strain curves (Delgado et al., 2008; Yu, Zhang, et al., 2006), or to compute the level of asynchronism (Tournoux et al., 2010), that would improve CRT outcome

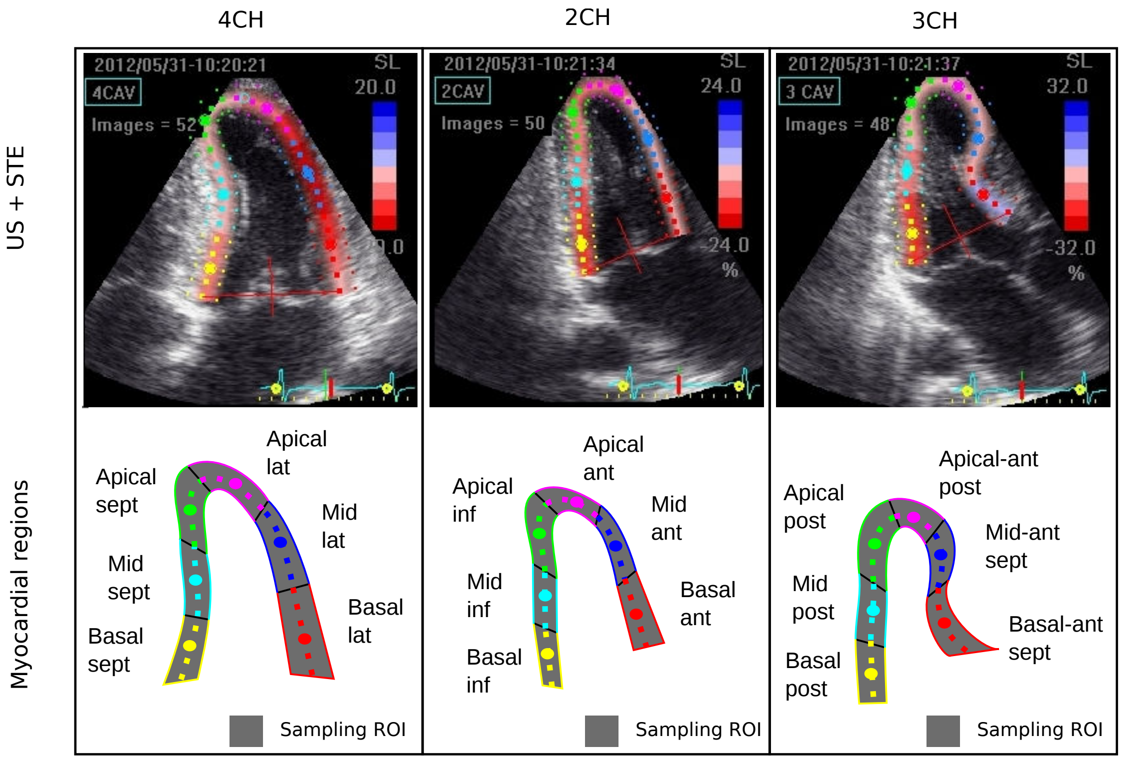

Figure 1.26: STE from apical TTE-LAX with corresponding LV segmentation used for regional longitudinal strain quantification for a HCM patient: (left) 4CH, (center) 2CH and (right) 3CH. ACRONYMS – lat: lateral, post: posterior, ROI: region of interest, sept: septal.

(TAVARD et al., 2014). Moreover, the fusion of STE with other image modalities such as CT or cardiac MRI (anatomy), EAM (electrical function) and cardiac LGE-MRI (myocardial structure) enables to analyze STE indicators with complementary information issued from these modalities in order to characterize, for instance, the regional electromechanical coupling along with the regional myocardial structure.

1.4 Conclusion

This chapter described the clinical context and addressed issues of this work. The main components of the heart were described, highlighting its multiphysics nature, coupling the anatomical, the substrate (myocardial tissue), the electrical and the mechanical components.

The two addressed clinical issues were then described. First, in the context of hypertrophic cardiomyopathy, it is needed to improve the characterization of the pathology and, especially, the relationship between the mechanical function (e.g. strain from speckle tracking echocardiography analysis), and the state of myocardial tissue (e.g. fibrosis from late gadolinium-enhanced MRI). This may lead to a better understanding and interpretation of US, especially speckle tracking echocardiography, enhancing the role of

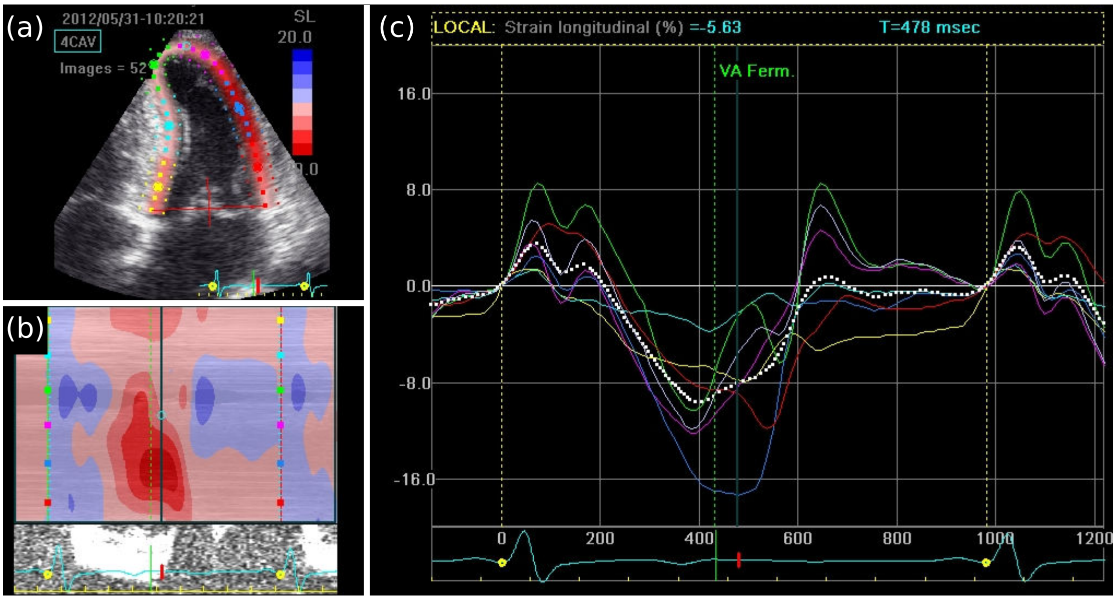

Figure 1.27: Speckle tracking echocardiography from a TTE apical-4CH US image of the heart of a HCM patient. Myocardial wall is delimited and then its regional longitudinal strains (in %) are measured by STE analysis for six regions. (a) LV contour corresponding to the centerline of the myocardium, and sampling region of interest as defined by the cardiologist. (b) Bidimensional map of the myocardial deformation over a cardiac cycle. In abscissa: time in ms; in ordinate: longitudinal strain along the trace (STE contour) from basal-lateral (bottom) to basal-septal (top) regions. (c) Longitudinal strain curves over time for each region. Acronyms – VA Ferm.: aortic valve closure, SL: longitudinal strain.

US in HCM diagnosis.

Second, in the context of cardiac asynchronism, Cardiac Resynchronization Therapy is recognized as a reference treatment. However, there is still a need to optimize the different steps of the treatment in order to overcome the high rate of implanted patients who do not respond to the therapy. A multiphysics description of the heart, combining the electrical and the mechanical information, but also the state of myocardial tissue, would enable to improve both, the selection of the implantation site and the planning of the intervention.

To achieve these goals, means of observation are required. However, given the heterogeneity and complexity of cardiac multiphysics phenomena, there is not a unique modality enabling to characterize the heart. For this reason, the last section of this chapter focused on the description of image acquisition modalities, highlighting their complementarity. For HCM characterization, echocardiography enables to evaluate the cardiac regional function but the presence of fibrosis is assessed from LGE-MRI in clinical routine. For cardiac asynchronism characterization, CT images are used to describe the anatomy, echocardiography is used to assess the mechanical function, electroanatomical mappings (EAM) are used to acquire the local electrical activity and MRI is used to evaluate myocardial tissue state.

Thus, in order to address these two clinical challenges, we propose to use multisensor image fusion. This approach presents the following challenges:

Multiphysics. Data acquired from the heart represent an indirect measurement of the phenomena of interest and carry a mixture of activities from different, intertwined processes and regulatory mechanisms. These justifies the acquisition of heterogeneous multisensor images but, at the same time, harden their fusion;

Multimodality. We need to fuse an heterogeneous set of cardiac image acquisitions. The multisensor nature of input images harden their integration (registration);

Multiresolution. The precision of acquired images differs between modalities and, yet all modalities share information regarding LV anatomy, the necessary precision of few millimeters is not always available, for instance, due to sequential acquisition, patient motion, or simply a different state of respiration or contraction. Besides, it is needed to synchronize static and dynamic acquisitions, having in common that their acquisition is synchronized to the ECG signal (ECG gating), but with different temporal resolutions (e.g. 1 phase for LGE-MRI and 30 to 60 phases for cine-MRI). Moreover, acquisition ECGs are not available for all acquisitions and differ between them;

Multidimensionality. The heterogeneity of the dimension of input images (3D, 2D, 3D+t, 2D+t) harden their fusion. This difference in spatial and/or temporal dimension leads to consider the implementation of dynamic approaches both to register input images and to fuse the information they contain;

The approaches developed to fuse multisensor cardiac images to face these methodological challenges are presented in chapter 3. The next chapter presents a brief theoretical context of multisensor image registration and fusion followed by a state of the art in multisensor cardiac image registration.

References

Artigou, J. and Monsuez, J. (2007). *Cardiologie et maladies vasculaires.* Ed. by Masson. Elsevier, p. 1639.

Bank, A. and Kelly, A. (2006). "Tissue Doppler imaging and left ventricular dyssynchrony in heart failure". In: *Journal of cardiac failure* 12.2, pp. 154–162.

Barnes, A., Pardee, H., White, P., Wilson, F., Wolferth, C., et al. (1938). "Standardization of precordial leads: Supplementary report". In: *American Heart Journal* 15.2, pp. 235–239.

Bax, J., Abraham, T., Barold, S., Breithardt, O., Fung, J., Garrigue, S., Gorcsan III, J., Hayes, D., Kass, D., Knuuti, J., et al. (2005). “Cardiac Resynchronization Therapy:: Part 1–Issues Before Device Implantation”. In: *Journal of the American College of Cardiology* 46.12, pp. 2153–2167.

Bhakta, D. and Miller, J. M. (2008). “Principles of Electroanatomic Mapping”. In: *Indian Pacing and Electrophysiology Journal* 8.1, pp. 32–50.

Bijnens, B. H., Cikes, M., Claus, P., and Sutherland, G. R. (2009). “Velocity and deformation imaging for the assessment of myocardial dysfunction”. In: *European Journal of Echocardiography* 10.2, pp. 216–226.

Bilchick, K. C., Dimaano, V., Wu, K. C., Helm, R. H., Weiss, R. G., Lima, J. A., Berger, R. D., Tomaselli, G. F., Bluemke, D. A., Halperin, H. R., Abraham, T., Kass, D. A., and Lardo, A. C. (2008). “Cardiac Magnetic Resonance Assessment of Dyssynchrony and Myocardial Scar Predicts Function Class Improvement Following Cardiac Resynchronization Therapy”. In: *J Am Coll Cardiol Img* 1.5, pp. 561–568.

Bleeker, G. B., Kaandorp, T. A., Lamb, H. J., Boersma, E., Steendijk, P., Roos, A. de, Wall, E. E. van der, Schalij, M. J., and Bax, J. J. (2006). “Effect of Posterolateral Scar Tissue on Clinical and Echocardiographic Improvement After Cardiac Resynchronization Therapy”. In: *Circulation* 113.7, pp. 969–976.

Blessberger, H. and Binder, T. (2010). “Two dimensional speckle tracking echocardiography: basic principles”. In: *Heart* 96.9, pp. 716–722.

Bruder, O., Wagner, A., Jensen, C. J., Schneider, S., Ong, P., Kispert, E.-M., Nassenstein, K., Schlosser, T., Sabin, G. V., Sechtem, U., and Mahrholdt, H. (2010). “Myocardial Scar Visualized by Cardiovascular Magnetic Resonance Imaging Predicts Major Adverse Events in Patients With Hypertrophic Cardiomyopathy”. In: *Journal of the American College of Cardiology* 56.11, pp. 875–887.

Cazeau, S., Leclerc, C., and Lavergne, T. (2001). “Effects of multisite biventricular pacing in patients with heart failure and intraventricular conduction delay”. In: *N Engl J Med* 344, pp. 802–873.

Chalil, S., Foley, P. W., Muyhaldeen, S. A., Patel, K. C., Yousef, Z. R., Smith, R. E., Frenneaux, M. P., and Leyva, F. (2007). “Late gadolinium enhancement-cardiovascular magnetic resonance as a predictor of response to cardiac resynchronization therapy in patients with ischaemic cardiomyopathy”. In: *Europace* 9.11, pp. 1031–1037.

Chan, L., Suever, J., Fornwalt, B., Clement-Guinaudeau, S., D’Andrea, A., Del Viscovo, L., Prinzen, F., Bracke, F., Leon, A., Delurgio, D., Lloyd, M., and Oshinski, J. (2011). “Presence of transmural posterolateral scar by LGE MRI is associated with non-response to CRT”. In: *Journal of Cardiovascular Magnetic Resonance* 13.Suppl 1, P256–P256.

Choi, K. M., Kim, R. J., Gubernikoff, G., Vargas, J. D., Parker, M., and Judd, R. M. (2001). “Transmural Extent of Acute Myocardial Infarction Predicts Long-Term Improvement in Contractile Function”. en. In: *Circulation* 104.10, pp. 1101–1107.

Chung, E. S., Leon, A. R., Tavazzi, L., Sun, J., Nihoyannopoulos, P., Merlino, J., Abraham, W. T., Ghio, S., Leclercq, C., Bax, J. J., Yu, C., Gorcsan, J., Sutton, M. S. J., Sutter, J. D., and Murillo, J. (2008). “Results of the Predictors of Response to CRT (PROSPECT) Trial”. In: *Circulation* 117.20, pp. 2608–2616.

Cleland, J., Daubert, J., Erdmann, E., Freemantle, N., Gras, D., Kappenberger, L., and Tavazzi, L. (2005). “The effect of cardiac resynchronization on morbidity and mortality in heart failure”. In: *N Engl J Med* 352.15, pp. 1539–49.

Daubert, J., Ritter, P., BRETON, H., Gras, D., LeClercq, C., Lazarus, A., Mugica, J., Mabo, P., and Cazeau, S. (1998). “Permanent left ventricular pacing with transvenous leads inserted into the coronary veins”. In: *Pacing and clinical electrophysiology* 21.1, pp. 239–245.

Delgado, V., Ypenburg, C., Bommel, R. van, Tops, L., Mollema, S., Marsan, N., Bleeker, G., Schalij, M., and Bax, J. (2008). “Assessment of Left Ventricular Dyssynchrony by Speckle Tracking Strain Imaging:: Comparison Between Longitudinal, Circumferential, and Radial Strain in Cardiac Resynchronization Therapy”. In: *Journal of the American College of Cardiology* 51.20, pp. 1944–1952.

Donal, E., Leclercq, C., and Daubert, J. (2011). “Prediction of the Response to Cardiac Resynchronization Therapy: Is it Worthwhile Doing an Echocardiography and Looking for Mechanical Dyssynchrony?” In: *Journal of cardiac failure* 17.5, p. 403.

Elliott, P., Andersson, B., Arbustini, E., Bilinska, Z., Cecchi, F., Charron, P., Dubourg, O., Kühl, U., Maisch, B., McKenna, W. J., et al. (2008). “Classification of the cardiomyopathies: a position statement from the European Society Of Cardiology Working Group on Myocardial and Pericardial Diseases”. In: *European heart journal* 29.2, pp. 270–276.

Fernandes, J. L., Strecker, R., Greiser, A., and Kalaf, J. M. (2014). “Myocardial T1-Mapping: Techniques and Clinical Applications”. In: *MAGNETOM Flash* 49.1.

Gabriel, L. (2006). “De la notion d’asynchronisme ventriculaire au traitement de l’insuffisance cardiaque”. In: *LOUVAIN MEDICAL* 125.9, p. 344.

Garcia, M., Toumoulin, C., Haigron, P., Velut, J., Garreau, M., and Boulmier, D. (2010). “Coronary vein tracking from MSCT using a minimum cost path approach”. In: *2010 IEEE International Symposium on Biomedical Imaging: From Nano to Macro.* Rotterdam, Netherlands, pp. 17–20.

Garot, J. (2005). “Apport de l’IRM à l’évaluation des cardiopathies ischémiques”. In: *MT Cardio.* 1, pp. 148–157.

Garreau, M., Garcia, M. .-.-P., Tavard, F., Simon, A., Fleureau, J., Velut, J., Boulmier, D., Haigron, P., Toumoulin, C., and Leclercq, C. (2010). “Abilities of cardiac MSCT imaging to provide useful anatomical and functional information for Cardiac Resynchronization Therapy optimization". In: *Computing in Cardiology, 2010*, pp. 237–240.

Garreau, M., Simon, A., Boulmier, D., Coatrieux, J. L., and Breton, H. (2006). "Assessment of left ventricular function in cardiac MSCT imaging by a 4D hierarchical surface-volume matching process". In: *International Journal of Biomedical Imaging* 2006, pp. 1–10.

Germain, F. (2005). "L'utilisation de marges personnalisées dans le traitement du cancer du poumon en radiothérapie. Analyse des mouvements physiologiques et des impacts dosimétriques". PhD thesis. Université de Laval - Faculté de Médecine.

Gersh, B. J., Maron, B. J., Bonow, R. O., Dearani, J. A., Fifer, M. A., Link, M. S., Naidu, S. S., Nishimura, R. A., Ommen, S. R., Rakowski, H., Seidman, C. E., Towbin, J. A., Udelson, J. E., and Yancy, C. W. (2011). "2011 ACCF/AHA Guideline for the Diagnosis and Treatment of Hypertrophic Cardiomyopathy A Report of the American College of Cardiology Foundation/American Heart Association Task Force on Practice Guidelines". en. In: *Circulation* 124.24, e783–e831.

Greenberg, N. L., Firstenberg, M. S., Castro, P. L., Main, M., Travaglini, A., Odabashian, J. A., Drinko, J. K., Rodriguez, L. L., Thomas, J. D., and Garcia, M. J. (2002). "Doppler-Derived Myocardial Systolic Strain Rate Is a Strong Index of Left Ventricular Contractility". In: *Circulation* 105.1, pp. 99–105.

Harris, K. M., Spirito, P., Maron, M. S., Zenovich, A. G., Formisano, F., Lesser, J. R., Mackey-Bojack, S., Manning, W. J., Udelson, J. E., and Maron, B. J. (2006). "Prevalence, Clinical Profile, and Significance of Left Ventricular Remodeling in the End-Stage Phase of Hypertrophic Cardiomyopathy". en. In: *Circulation* 114.3, pp. 216–225.

Herman, G. T. (2009). *Fundamentals of computerized tomography: image reconstruction from projections*. Springer.

Jacquier, A., Bartoli, B., Flavian, A., Varoquaux, A., Gaubert, J., Cohen, F., Vidal, V., Bartoli, J., and Moulin, G. (2010). "Delayed myocardial enhancement: Optimizing the MR imaging protocol". In: *Journal de radiologie* 91.5 Pt 2, pp. 598–601.

Jansen, A. H., Bracke, F., Dantzig, J. m. van, Peels, K. H., Post, J. C., Bosch, H. C. van den, Gelder, B. van, Meijer, A., Korsten, H. H., Vries, J. de, and Hemel, N. M. van (2008). "The influence of myocardial scar and dyssynchrony on reverse remodeling in cardiac resynchronization therapy". In: *European Journal of Echocardiography* 9.4, pp. 483–488.

Kazmierczak, C. (2011). "IRM et Cardiopathie Dilatée: Relation avec les troubles du rythme ventriculaire." PhD thesis. Université Henri Poincaré (Nancy 1) - Faculté de Médecine.

Khan, F. Z., Virdee, M. S., Fynn, S. P., and Dutka, D. P. (2009). “Left ventricular lead placement in cardiac resynchronization therapy: where and how?” In: *Europace* 11.5, pp. 554–561.

Khoury, D. S., Taccardi, B., Lux, R. L., Ershler, P. R., and Rudy, Y. (1995). “Reconstruction of Endocardial Potentials and Activation Sequences From Intracavitary Probe Measurements: Localization of Pacing Sites and Effects of Myocardial Structure”. In: *Circulation* 91.3, pp. 845–863.

Kim, R. J., Fieno, D. S., Parrish, T. B., Harris, K., Chen, E.-L., Simonetti, O., Bundy, J., Finn, J. P., Klocke, F. J., and Judd, R. M. (1999). “Relationship of MRI Delayed Contrast Enhancement to Irreversible Injury, Infarct Age, and Contractile Function”. en. In: *Circulation* 100.19, pp. 1992–2002.

Kim, R. J., Wu, E., Rafael, A., Chen, E.-L., Parker, M. A., Simonetti, O., Klocke, F. J., Bonow, R. O., and Judd, R. M. (2000). “The Use of Contrast-Enhanced Magnetic Resonance Imaging to Identify Reversible Myocardial Dysfunction”. In: *New England Journal of Medicine* 343.20, pp. 1445–1453.

Leclercq, C., Cazeau, S., Ritter, P., Alonso, C., Gras, D., Mabo, P., Lazarus, A., Daubert, J., et al. (2000). “A pilot experience with permanent biventricular pacing to treat advanced heart failure”. In: *American heart journal* 140.6, pp. 862–870.

Lee, J. K. (2006). *Computed body tomography with MRI correlation.* Vol. 1. Lippincott Williams & Wilkins.

Leitman, M., Lysyansky, P., Sidenko, S., Shir, V., Peleg, E., Binenbaum, M., Kaluski, E., Krakover, R., and Vered, Z. (2004). “Two-dimensional strain–a novel software for real-time quantitative echocardiographic assessment of myocardial function”. In: *Journal of the American Society of Echocardiography* 17.10, pp. 1021–1029.

Leyva, F., Foley, P. W., Chalil, S., Ratib, K., Smith, R. E., Prinzen, F., and Auricchio, A. (2011). “Cardiac resynchronization therapy guided by late gadolinium-enhancement cardiovascular magnetic resonance”. In: *Journal of Cardiovascular Magnetic Resonance* 13.1, pp. 29–29.

Lima, J. A. (2013). “The Promise of Myocardial Fibrosis Assessment by T1 Mapping∗∗”. In: *JACC: Cardiovascular Imaging* 6.4, pp. 485–487.

Locca, D., Jeanrenaud, X., Schwitter, J., Girod, G., Monney, P., De Palma, R., Rizzo, E., Prasad, S. K., and Vogt, P. (2009). “Rôle de l’IRM cardiaque dans le dépistage des cardiomyopathies de l’adulte”. fre. In: *Revue médicale suisse* 5.221, pp. 2051–2057.

Maffessanti, F., Nesser, H., Weinert, L., Steringer-Mascherbauer, R., Niel, J., Gorissen, W., Sugeng, L., Lang, R., and Mor-Avi, V. (2009). “Quantitative evaluation of regional left ventricular function using three-dimensional speckle tracking echocardiography in patients with and without heart disease”. In: *The American journal of cardiology* 104.12, pp. 1755–1762.

Maier, S., Fischer, S., McKinnon, G., Hess, O., Krayenbuehl, H., and Boesiger, P. (1992). “Evaluation of left ventricular segmental wall motion in hypertrophic cardiomyopathy with myocardial tagging”. In: *Circulation* 86.6, pp. 1919–1928.

Malmivuo, J. and Plonsey, R. (1995). *Bioelectromagnetism: principles and applications of bioelectric and biomagnetic fields.* Oxford University Press, USA.

Marieb, E. (2005). *Anatomie et physiologie humaines: adaptation de la 6ème édition américaine.* Ed. by E. P. education. 7. Lavoisier, pp. 1011–10115.

Maron, B. J. (2004). “Hypertrophic cardiomyopathy: an important global disease”. In: *The American Journal of Medicine* 116.1, pp. 63–65.

Maron, B. J. (2010). “Contemporary Insights and Strategies for Risk Stratification and Prevention of Sudden Death in Hypertrophic Cardiomyopathy”. en. In: *Circulation* 121.3, pp. 445–456.

Maron, M. S., Appelbaum, E., Harrigan, C. J., Buros, J., Gibson, C. M., Hanna, C., Lesser, J. R., Udelson, J. E., Manning, W. J., and Maron, B. J. (2008). “Clinical Profile and Significance of Delayed Enhancement in Hypertrophic Cardiomyopathy”. In: *Circulation: Heart Failure* 1.3, pp. 184–191.

Marsan, N. A., Westenberg, J. J., Ypenburg, C., Bommel, R. J. van, Roes, S., Delgado, V., Tops, L. F., Geest, R. J. van der, Boersma, E., Roos, A. de, Schalij, M. J., and Bax, J. J. (2009). “Magnetic resonance imaging and response to cardiac resynchronization therapy: relative merits of left ventricular dyssynchrony and scar tissue”. In: *European Heart Journal* 30.19, pp. 2360–2367.

McAlister, F., Ezekowitz, J., Hooton, N., Vandermeer, B., Spooner, C., Dryden, D., Page, R., Hlatky, M., and Rowe, B. (2007). “Cardiac resynchronization therapy for patients with left ventricular systolic dysfunction”. In: *JAMA: the journal of the American Medical Association* 297.22, p. 2502.

McLeish, K., Hill, D. L. G., Atkinson, D., Blackall, J., and Razavi, R. (2002). “A study of the motion and deformation of the heart due to respiration”. In: *IEEE Transactions on Medical Imaging* 21.9, pp. 1142–1150.

McMurray, J. J., Adamopoulos, S., Anker, S. D., Auricchio, A., Böhm, M., Dickstein, K., Falk, V., Filippatos, G., Fonseca, C., Gomez-Sanchez, M. A., et al. (2012). “ESC Guidelines for the diagnosis and treatment of acute and chronic heart failure 2012 The Task Force for the Diagnosis and Treatment of Acute and Chronic Heart Failure 2012 of the European Society of Cardiology. Developed in collaboration with the Heart Failure Association (HFA) of the ESC”. In: *European heart journal* 33.14, pp. 1787–1847.

Mehra, M. and Greenberg, B. (2004). “Cardiac resynchronization therapy: caveat medicus!” In: *Journal of the American College of Cardiology* 43.7, p. 1145.

Messroghli, D. R., Greiser, A., Fröhlich, M., Dietz, R., and Schulz-Menger, J. (2007). “Optimization and validation of a fully-integrated pulse sequence for modified look-locker inversion-recovery (MOLLI) T1 mapping of the heart". In: *Journal of Magnetic Resonance Imaging* 26.4, pp. 1081–1086.

MESSROGHLI, D. R., RADJENOVIC, A., KOZERKE, S., HIGGINS, D. M., SIVANANTHAN, M. U., and RIDGWAY, J. P. (2004). "Modified Look-Locker inversion recovery (MOLLI) for high-resolution T1 mapping of the heart". In: *Magnetic Resonance in Medicine* 52.1, pp. 141–146.

MEWTON, N., LIU CHIA, Y., CROISILLE, P., DAVID, B., and JOÃO, L. (2011). "Assessment of Myocardial Fibrosis with Cardiac Magnetic Resonance". In: *J. Am. Coll. Cardiol.* 57.8, pp. 891–903.

MOON, J. C., REED, E., SHEPPARD, M. N., ELKINGTON, A. G., HO, S., BURKE, M., PETROU, M., and PENNELL, D. J. (2004). "The histologic basis of late gadolinium enhancement cardiovascular magnetic resonance in hypertrophic cardiomyopathy". In: *Journal of the American College of Cardiology* 43.12, pp. 2260–2264.

MORGAN, J. M. and DELGADO, V. (2009). "Lead positioning for cardiac resynchronization therapy: techniques and priorities". In: *Europace* 11.Supplement 5, pp. v22–v28.

MOSS, A., HALL, W., CANNOM, D., KLEIN, H., BROWN, M., DAUBERT, J., ESTES III, N., FOSTER, E., GREENBERG, H., HIGGINS, S., et al. (2009). "Cardiac-resynchronization therapy for the prevention of heart-failure events". In: *New England Journal of Medicine* 361.14, pp. 1329–1338.

NAGEL, E., STUBER, M., BURKHARD, B., FISCHER, S., SCHEIDEGGER, M., BOESIGER, P., and HESS, O. (2000). "Cardiac rotation and relaxation in patients with aortic valve stenosis". In: *European heart journal* 21.7, p. 582.

NEW YORK HEART ASSOCIATION (1964). *Diseases of the heart and blood vessels: nomenclature and criteria for diagnosis.* Ed. by BOSTON. Vol. 224. Little, Brown & Company, p. 114.

OESTERLE, S. N., REIFART, N., HAUPTMANN, E., HAYASE, M., and YEUNG, A. C. (2001). "Percutaneous In Situ Coronary Venous Arterialization: Report of the First Human Catheter-Based Coronary Artery Bypass". In: *Circulation* 103.21, pp. 2539–2543.

OHSATO, K., SHIMIZU, M., SUGIHARA, N., KONISHI, K., and TAKEDA, R. (1992). "Histopathological factors related to diastolic function in myocardial hypertrophy". eng. In: *Japanese circulation journal* 56.4, pp. 325–333.

OLIVOTTO, I., CECCHI, F., CASEY, S. A., DOLARA, A., TRAVERSE, J. H., and MARON, B. J. (2001). "Impact of Atrial Fibrillation on the Clinical Course of Hypertrophic Cardiomyopathy". en. In: *Circulation* 104.21, pp. 2517–2524.

PAVLOPOULOS, H. and NIHOYANNOPOULOS, P. (2010). "Recent advances in cardiac resynchronization therapy: echocardiographic modalities, patient selection, optimization, non-responders – all you need to know for more efficient CRT". In: *The International Journal of Cardiovascular Imaging (formerly Cardiac Imaging)* 26.2, pp. 177–191.

Piechnik, S. K., Ferreira, V. M., Dall'Armellina, E., Cochlin, L. E., Greiser, A., Neubauer, S., and Robson, M. D. (2010). "Shortened Modified Look-Locker Inversion recovery (ShMOLLI) for clinical myocardial T1-mapping at 1.5 and 3 T within a 9 heartbeat breathhold". In: *Journal of Cardiovascular Magnetic Resonance* 12.1, p. 69.

Popović, Z., Kwon, D., Mishra, M., Buakhamsri, A., Greenberg, N., Thamilarasan, M., Flamm, S., Thomas, J., Lever, H., and Desai, M. (2008). "Association Between Regional Ventricular Function and Myocardial Fibrosis in Hypertrophic Cardiomyopathy Assessed by Speckle Tracking Echocardiography and Delayed Hyperenhancement Magnetic Resonance Imaging". In: *Journal of the American Society of Echocardiography* 21.12, pp. 1299–1305.

Puntmann, V. O., Voigt, T., Chen, Z., Mayr, M., Karim, R., Rhode, K., Pastor, A., Carr-White, G., Razavi, R., Schaeffter, T., and Nagel, E. (2013). "Native T1 mapping in differentiation of normal myocardium from diffuse disease in hypertrophic and dilated cardiomyopathy". eng. In: *JACC. Cardiovascular imaging* 6.4, pp. 475–484.

Purnode, P., Blommaert, D., Eucher, P., Scavee, C., Collet, B., Gonta, A., Mancini, I., Gabriel, L., Marchandise, B., and De Roy, L. (2004). "Stimulation biventriculaire et insuffisance cardiaque". In: *Louvain médical* 123.1, pp. 18–27.

Ridgway, J. P. (2010). "Cardiovascular magnetic resonance physics for clinicians: part I". en. In: *Journal of Cardiovascular Magnetic Resonance* 12.1, p. 71.

Roberts, W. C., Siegel, R. J., and McManus, B. M. (1987). "Idiopathic dilated Cardiomyopathy: Analysis of 152 necropsy patients". In: *The American Journal of Cardiology* 60.16, pp. 1340–1355.

Saito, M., Okayama, H., Yoshii, T., Higashi, H., Morioka, H., Hiasa, G., Sumimoto, T., Inaba, S., Nishimura, K., Inoue, K., Ogimoto, A., Shigematsu, Y., Hamada, M., and Higaki, J. (2012). "Clinical significance of global two-dimensional strain as a surrogate parameter of myocardial fibrosis and cardiac events in patients with hypertrophic cardiomyopathy". en. In: *European Heart Journal – Cardiovascular Imaging*, jer318.

Schmitt, C., Deisenhofer, I., and Zrenner, B., eds. (2006). *Catheter Ablation of Cardiac Arrhythmias*. Darmstadt: Steinkopff-Verlag.

Schwitter, J. and Abdel-Aty, H. (2008). *CMR Update*. J. Schwitter.

Serri, K., Reant, P., Lafitte, M., Berhouet, M., Bouffos, V. L., Roudaut, R., and Lafitte, S. (2006). "Global and Regional Myocardial Function Quantification by Two-Dimensional Strain: Application in Hypertrophic Cardiomyopathy". In: *Journal of the American College of Cardiology* 47.6, pp. 1175–1181.

Simon, A. (2005). "Extraction et caractérisation du mouvement cardiaque en imagerie scanner multibarrette". PhD thesis. LTSI, INSERM U642, Université de Rennes 1.

SIMON, A., GARREAU, M., BOULMIER, D., COATRIEUX, J.-L., and BRETON, H. L. (2005). “A Surface-Volume Matching Process Using a Markov Random Field Model for Cardiac Motion Extraction in MSCT Imaging”. In: *FIMH*. Ed. by A. F. FRANGI, P. RADEVA, A. SANTOS, and M. HERNANDEZ. Vol. 3504. Lecture Notes in Computer Science. Springer, pp. 457–466.

SIMONSON, J., SCHILLER, N., et al. (1989). “Descent of the base of the left ventricle: an echocardiographic index of left ventricular function.” In: *Journal of the American Society of Echocardiography: official publication of the American Society of Echocardiography* 2.1, p. 25.

STØYLEN, A. (2001). “Strain rate imaging of the left ventricle by ultrasound”. PhD thesis. Norwegian University of Science and Technology. Faculty of Medicine.

TAVARD, F., SIMON, A., LECLERCQ, C., DONAL, E., HERNÁNDEZ, A., and GARREAU, M. (2014). “Multimodal Registration and Data Fusion for Cardiac Resynchronization Therapy Optimization”. In: *IEEE Transactions on Medical Imaging* 33.6, pp. 1363–1372.

TAVARD, F. (2012). “Recalage et fusion d’informations multimodales pour l’optimisation de la thérapie de resyncrhonisation cardiaque”. PhD thesis. Université de Rennes 1.

TOURNOUX, F., CHAN, R., MANZKE, R., HANSCHUMACHER, M., CHEN-TOURNOUX, A., GÉRARD, O., SOLIS-MARTIN, J., HEIST, E., ALLAIN, P., REDDY, V., et al. (2010). “Integrating functional and anatomical information to guide cardiac resynchronization therapy”. In: *European journal of heart failure* 12.1, p. 52.

VALLE, A., NADAL, M., ESTORNELL, J., JACAS, V., TRIGO, A., QUESADA, A., PAYA, R., and RIDOCCI, F. (2007). “578 Delayed enhancement magnetic resonance imaging utility to predict response to cardiac resynchronization therapy”. In: *European Journal of Heart Failure Supplements* 6.1, pp. 135–135.

VEIRE, N. R. V. DE, MARSAN, N. A., SCHUIJF, J. D., BLEEKER, G. B., WIJFFELS, M. C., ERVEN, L. VAN, HOLMAN, E. R., SUTTER, J. D., WALL, E. E. VAN DER, SCHALIJ, M. J., and BAX, J. J. (2008). “Noninvasive Imaging of Cardiac Venous Anatomy With 64-Slice Multi-Slice Computed Tomography and Noninvasive Assessment of Left Ventricular Dyssynchrony by 3-Dimensional Tissue Synchronization Imaging in Patients With Heart Failure Scheduled for Cardiac Resynchronization Therapy”. In: *The American Journal of Cardiology* 101.7, pp. 1023–1029.

WHITE, J. A., YEE, R., YUAN, X., KRAHN, A., SKANES, A., PARKER, M., KLEIN, G., and DRANGOVA, M. (2006). “Delayed Enhancement Magnetic Resonance Imaging Predicts Response to Cardiac Resynchronization Therapy in Patients With Intraventricular Dyssynchrony”. In: *Journal of the American College of Cardiology* 48.10, pp. 1953–1960.

WHO (2011). *Global status report on noncommunicable disaeses 2010.* report. Geneva: World Health Organization.

Young, A., Kramer, C., Ferrari, V., Axel, L., and Reichek, N. (1994). “Three-dimensional left ventricular deformation in hypertrophic cardiomyopathy”. In: *Circulation* 90.2, pp. 854–867.

Ypenburg, C., Roes, S. D., Bleeker, G. B., Kaandorp, T. A., Roos, A. de, Schalij, M. J., Wall, E. E. van der, and Bax, J. J. (2007). “Effect of Total Scar Burden on Contrast-Enhanced Magnetic Resonance Imaging on Response to Cardiac Resynchronization Therapy”. In: *The American Journal of Cardiology* 99.5, pp. 657–660.

Yu, C., Sanderson, J., Marwick, T., and Oh, J. (2007). “Tissue Doppler imaging: a new prognosticator for cardiovascular diseases”. In: *Journal of the American College of Cardiology* 49.19, pp. 1903–1914.

Yu, C., Zhang, Q., Chan, Y., Chan, C., Yip, G., Kum, L., Wu, E., Lee, P., Lam, Y., Chan, S., et al. (2006). “Tissue Doppler velocity is superior to displacement and strain mapping in predicting left ventricular reverse remodelling response after cardiac resynchronisation therapy”. In: *Heart* 92.10, pp. 1452–1456.

CHAPTER 2

State of the art

The description of heart's multiphysics phenomena of interest may be used to improve disease diagnosis and treatment, and to predict treatment outcome; however, it requires the fusion of heterogeneous multisensor acquisitions. In this context, cardiac image registration is the first challenge to address.

This chapter presents the considered multisensor fusion framework and a state of the art in cardiac image registration. First, multisensor image fusion is described and image registration is detailed. Then, cardiac image registration methods are briefly classified. A state of the art in cardiac image registration is presented afterwards. It focuses on reported approaches processing the acquisitions we are interested in this work: cardiac MRI, CT, echocardiography and EAM. This chapter ends with the conclusions.

2.1 Multisensor image fusion

Multisensor image fusion is the process of integrating multiple images and/or image-derived data and knowledge representing the same object (heart) into a consistent, accurate, enhanced and useful representation. This enables a combined analysis of input data. A high level functional view of the data fusion process is presented in Figure 2.1. This model is a modification made by (HERNANDEZ, 2000) of the Joint Director of Laboratories (JDL) model (ANTONY, 1995) (WHITE, 1991). Such a description of multisensor data fusion includes different levels of processing:

Level 1. This level aims at refining the object of interest using input multisensor images. It is associated with image registration, information association, object detection and object classification processes.

Level 2. This level is associated with the detection of the object state and defined as the estimation of the diagnosis. This level of fusion includes the analysis of the associated information at level 1 to derive new information (indicators), the

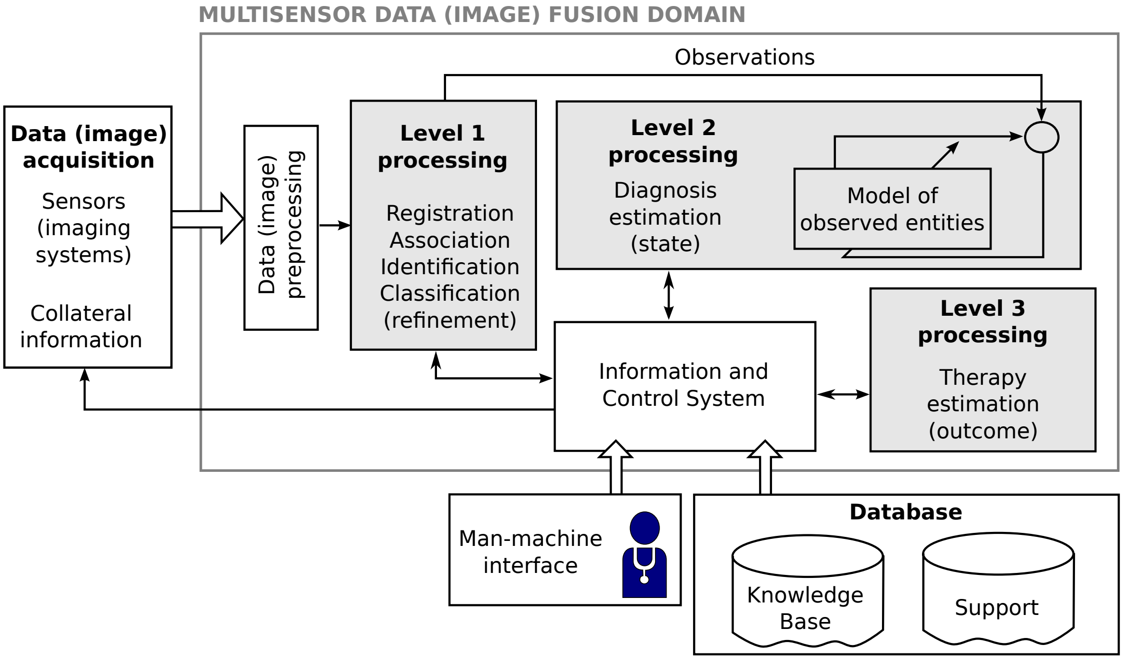

Figure 2.1: Adapted high level functional model of the multisensor data (image) fusion process. Modified from (HERNANDEZ, 2000).

modeling of observed entities, the detection of underlying sources and mechanism explaining the multiphysics phenomena needed to describe the function of the underlying organ (i.e. the heart).

Level 3. This level is defined as the estimation of the therapy i.e. the prediction of the future state from a given previous state. This definition can be related with the estimation of the therapy outcome, for instance, from personalized models of the heart as aimed by the euHeart project (WEESE et al., 2013).

A degree of data fusion is obtained at each level, being the output of level 1 decisive for next levels. Our work mainly concerns the *multisensor image registration* process which is a decisive task to do in level 1. Image registration methods exploit the common information in input images, mainly the anatomy, in order to register them such that complementary (multisensor) information are or can be associated and fused. Below we present a brief formalization of the image registration procedure.

2.2 Multisensor image registration: Background

Image registration is the problem of finding a transformation that allows to describe a pair of images using a common referential. This enables to *associate* their information. Let I_F and I_M be two images where subscripts F and M stand for fixed and moving, respectively. The coordinate system of I_F (fixed image) is the target referential to which I_M (moving image) will be moved to. Lets consider that I_F and I_M are static acquisitions

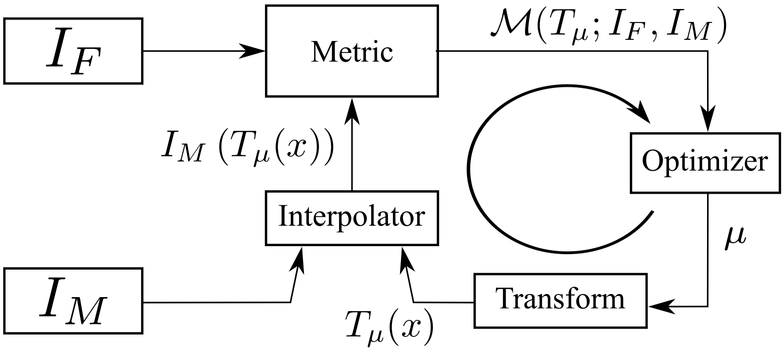

Figure 2.2: Registration of two images: searching the optimal transform parameters that allows to describe the moving image in the fixed image referential.

lying on their own spatial domain of dimension d (Klein et al., 2010): $\Omega_F \subset \mathbb{R}^d$ and $\Omega_M \subset \mathbb{R}^d$, respectively. Let $T_\mu(x)$ be a geometrical transform of pixel (voxel) $x \in \Omega_F$ with μ the transform parameters. T_μ maps the fixed image domain to the moving image domain, i.e. T_μ:$\Omega_F \subset \mathbb{R}^d \rightarrow \Omega_M \subset \mathbb{R}^d$. Registration is the problem of finding an optimal set of parameters μ' such that $T_{\mu'}(x)$ aligns $I_M\ (T_{\mu'}(x))$ to $I_F(x)$:

$$\mu' = \arg\max_{\mu} \mathcal{M}(T_\mu; I_F, I_M), \tag{2.1}$$

where $\mathcal{M}(T_\mu; I_F, I_M)$ is a similarity measure.

Figure 2.2 shows the general components of a classical registration procedure (Ibanez et al., 2005). Four main components are included: the transform, the interpolator, the metric and the optimizer.

2.2.1 Geometrical transform

During the registration procedure, the *transform* component T represents the spatial mapping of points in the fixed image space to points in the moving image space. The problematic and the images to be registered (organ, intra/inter patient registration, dimensions, etc.) define the degrees of freedom of the transform to be used. This is an important aspect because it determines the speed, the type and the precision of the registration algorithm.

One way to classify spatial transforms is to consider if it is linear and non-linear. Linear transforms are defined by a transformation matrix, often defined using homogeneous coordinates, and that is applied to the global image. Non-linear transforms are local transforms and correspond to elastic transforms for which a regularization process is considered (e.g. using splines for the free-form deformation method or smoothing for the Demon's algorithm).

In this work we use linear spatial transforms. For these transforms, we have a vector μ containing the parameters defining a given transformation. Figure 2.3 presents a

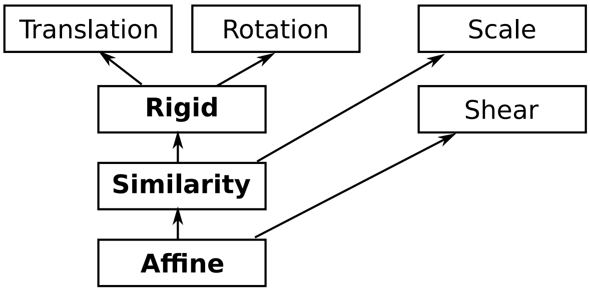

Figure 2.3: Taxonomy of parametric spatial transforms. Each transform has an arrow pointing to the transforms it can represent as a particular case. From (YOO, 2004).

taxonomy of the classical linear transforms. Below we present the description of those in bold type:

Rigid. A rigid transformation of a point x in a 3D space ($x \in \mathbb{R}^3$), denoted as $T_{\mu^R}(x) = R \cdot x + t$, is defined by six parameters (i.e. it has six degrees of freedom): three parameters defining the translation $t \in \mathbb{R}^3$ and three parameters for the angles of rotation ($\theta \in \mathbb{R}^3$) around the axis of the coordinate system. These angles define the rotation matrix R. Thus $\mu^R = (t, \theta)$, with $\mu^R \in \mathbb{R}^6$. Rigid transforms are also called isometric transforms because they preserve distances, angles and orientation.

Similarity. A similarity transform includes translation, rotation and scaling s which increases the number of parameters to seven when using isotropic scaling (i.e. the same scaling factor for all dimensions). It is noted as $T_{\mu^S}(x) = s \cdot R \cdot x + t$, with $\mu^S = (\mu^R, s)$. Similarity transforms preserve shapes, angles between any two lines and the proportions of distances.

Affine. An affine transform is defined by adding to the rigid transform anisotropic scaling (i.e. a scaling factor for each dimension) and shear along the three axes which leads to 12 parameters. It is noted as $T_{\mu^A}(x) = A \cdot x + t$ with $A \in \mathbb{R}^{3,3}$ a 3×3 matrix. Thus $\mu^A = (a_{00}, \ldots, a_{22}, t)$, with a_{ij} the entry (i, j) of matrix A. Affine transforms preserve lines, parallel lines, and ratios of distances between points lying on a straight line.

2.2.2 Interpolator

During the registration process, a metric typically compares the intensity values in the fixed image with the corresponding values in the transformed moving image. When a point is mapped from one image space to another, it will generally be mapped to a non-grid point. Thus, an interpolation is needed to obtain an intensity value for the mapped point using the information from the neighboring grid positions (YOO, 2004).

There is a trade off between the number of image values needed to interpolate a given point and the computation efficiency. The classical interpolation methods are:

Nearest-neighbor. This interpolator outputs the intensity of the nearest grid position. This interpolation scheme is quick and does not require floating point calculations. It is useful for the interpolation of labeled images.

Linear. The returned value is a weighted average of the surrounding voxels, with the distance to each voxel taken as weight.

N-th order or B-spline. The underlying image is represented using B-spline basis functions. The intensity of a non-grid position can then be computed by multiplying the B-spline coefficients with the shifted B-spline kernels within the support region of the requested position (Yoo, 2004).

2.2.3 Metric

The *metric* component is perhaps the most critical. This component quantitatively measures the similarity between the transformed moving image and the fixed images. This similarity indicates how well these images match. The metric is used by the optimizer to evaluate the quantitative criterion at different positions of the transform parameter search space (Yoo, 2004). Several choices for the similarity measure can be found in the literature. Some common choices are described below.

2.2.3.1 Mean squares

When images to be registered come from the same imaging modality, the image intensity at corresponding positions between two images should be similar. One of the simplest measures of similarity is the mean squared difference over all pixels, defined as:

$$\mathcal{MS}(T_\mu; I_F, I_M) = \frac{1}{N}\sum_i^N \left(I_F(x_i) - \psi\left(I_M(T_\mu(x_i))\right)\right)^2 \tag{2.2}$$

where x_i is a voxel in I_F, N is the number of voxels and $\psi(\cdot)$ is an interpolator. The mean square metric has an ideal value of zero, i.e. two images are perfectly matched for the transformation that makes $\mathcal{MS}$ as close as possible to zero.

2.2.3.2 Normalized correlation

This metric computes the pixel-wise cross-correlation between the intensity of the images to be registered, normalized by the square root of the autocorrelation of each image. When two images are identical the measure equals one. It is defined as:

$$\mathcal{NC}(T_\mu; I_F, I_M) = \frac{\sum_i^N I_F(x_i) \cdot \psi\left(I_M(T_\mu(x_i))\right)}{\sqrt{\sum_i^N I_F^2(x_i) \cdot \sum_i^N \psi^2\left(I_M(T_\mu(x_i))\right)}} \tag{2.3}$$

2.2.3.3 Mutual information

Mutual information (MI) is an information theoretic entity that qualitatively measures how much information about one random variable can be obtained from the information of another random variable (Yoo, 2004). The use of mutual information for multimodal registration was independently introduced by two different groups (Viola et al., 1997) (Collignon et al., 1995). It considers the intensity of input images as the random variable. The advantage of mutual information is that complex mappings between the two images can be modeled, making it well-suited for multimodal registration. MI is defined as:

$$\mathcal{MI}(T_\mu; I_F, I_M) = H(I_F) + H\left(T_\mu(I_M)\right) - H\left(I_F, T_\mu(I_M)\right) \tag{2.4}$$

where $H(\cdot)$ and $H(\cdot,\cdot)$ denote the entropy and joint entropy, respectively. They are defined as:

$$H(A) = -\int p_A(a) \cdot log\left(p_A(a)\right) \cdot da \tag{2.5}$$

$$H(A,B) = -\int p_{AB}(a,b) \cdot log\left(p_{AB}(a,b)\right) \cdot da \cdot db \tag{2.6}$$

where p_A is the probability density of the intensities in image A and p_{AB} is the joint probability density of images A and B.

2.2.3.4 Normalized mutual information

Traditional MI is not invariant to changes in the overlapping region through the course of registration (Cahill, 2010). The normalization of MI aims at overcoming this drawback. There are different approaches to normalize the mutual information measure. One of them is given by:

$$\mathcal{NMI}(T_\mu; I_F, I_M) = \frac{H(I_F) + H\left(T_\mu(I_M)\right)}{H\left(I_F, T_\mu(I_M)\right)} \tag{2.7}$$

Mutual information has been extensively used in the context of multimodal registration, with different variations available such as the *Mattes mutual information* (MMI) which use Parzen histogram estimates to compute the probability density distribution (Mattes, D. Haynor, et al., 2003) (Mattes, D. R. Haynor, et al., 2001). An implementation using the Edgeworth-based third order expansion of MI was proposed in the LTSI (Rubeaux et al., 2010). It allows to improve the variability of the metric; moreover, its computational burden is lower compared to classical implementations.

2.2.3.5 Optimizer

The role of the *optimizer* component is to optimize the measurements of similarity, provided by the metric component, with regards to the *parameters of the transform* component. Starting from an initial set of parameters, the optimization procedure iteratively searches for the optimal solution by evaluating the similarity at different positions of the parameter search space (Yoo, 2004). Optimization algorithms can be broadly divided into two main classes: deterministic methods and stochastic methods.

Starting from an initial value, deterministic methods use simple rules, generally based on the study of the local shape of the function to be optimized, to iteratively refine the solution. The local study enables to determine a searching direction and a step is selected to update the solution. These methods can be classified according to the derivative order they use to study the function to be optimized: (i) no derivative (e.g. downhill-simplex method or Amoeba); (ii) first-derivative (e.g. gradient descent, regular step gradient descent, conjugate gradient); (iii) second-order derivative (e.g. Broyden-Fletcher-Goldfarb-Shanno method). The use of higher order derivatives generally improves the searching direction; however, their computational cost has to be carefully considered. The strength of deterministic optimization methods is that, if the initialization is quite close to the optimum, they quickly converge to a highly close estimation of the optimum. The weakness is that they converge to a local optimum if the initialization is far from the optimum.

Stochastic optimization methods rely on randomness and re-trials to better sample the parameter space in searching for an optimum solution. The three most commonly used stochastic methods are Monte Carlo, simulated annealing, and genetic algorithm. For instance, at each iteration of the simulated annealing method, a random value is generated in order to accept or reject the new guess, even if this solution is degraded compared to the previous one. Thus, these methods have the potential to not being trapped in local optima but; however, their computational cost is generally higher than using deterministic methods.

In an image registration procedure the range of the transform parameters can have big differences; hence, a particular attention should be paid to scaling input parameters during optimization. For instance, a unit change in rotation (expressed in radians) has a much greater impact on an image than a unit change in translation (expressed in millimeters). A common implementation of rescaling is to multiply the metric gradient by weights chosen to balance the range of the transform parameters.

The heart is a dynamic organ; thus, the registration framework described above should account for the temporal dimension. In this context, either μ are the parameters of a spatio-temporal transform (e.g. T_μ is a 4D transform) or the temporal registration is detached of the spatial registration, leading to a different transformation (such in this work, see DTW in 3.2.1.2). For the latter, the temporal registration can be performed in combination (simultaneous) or before spatial registration (sequential). Below we analyze state-of-the-art methods to elucidate how to register multisensor cardiac images of interest for this work, both in time and in space.

2.3 Cardiac image registration: A state of the art

Considerable efforts have been dedicated to cardiac image registration in intra- and inter-patient contexts. Mixed nonrigid motions of heart and thorax structures [1], dynamic nature, multimodality and differences in spatio-temporal resolutions harden this registration. A state of the art is presented aiming at highlighting approaches to overcome these challenges. This section, without being an exhaustive survey of all published techniques, aims at situating key methods in the context of this work.

2.3.1 Classification of medical image registration methods

Different classifications of image registration methods have been reported in literature. (PLUIM et al., 2003) classified mutual-information-based procedures according to *methodological aspects* (preprocessing, similarity measure, transformation and implementation) or *application aspects* (image dimensionality, number of images, image modality, subject of registration and object of registration). (MAKELA et al., 2002) classified cardiac image registration methods in two categories: *geometric image features based* (point-based, edge- and surface-based) and *voxel similarity based* (based on moments and principal axes, intensity difference and correlation methods, mutual information). (RUECKERT et al., 2010) classified nonrigid registration [2] procedures in two categories: *intra-subject* and *inter-subject*.

The registration of images acquired with the same sensor type is called *monomodality registration* whereas the registration of images acquired with different sensor types is called *multimodality registration*. Two other categories can be added: *intra-sequence* and *inter-sequence registration* defined as the registration of images from the same or different sequences issued with a common acquisition system (thus, the same sensor type), respectively. For instance, inter-sequence registration is the case of the registration of cine-MRI and LGE-MRI which are two sequences acquired in the same MRI machine. Inter-sequence image registration is commonly considered as a multimodal registration in literature.

Image modalities limit the choice of the registration components while clinical applications define the modalities involved. In this work, state-of-the-art registration methods were classified according to the modalities involved: cardiac MRI (cf. 2.3.2), CT (cf. 2.3.3), US (cf. 2.3.4) and EAM (cf. 2.3.5). Each section presents two aspects of the registration process: (i) temporal alignment and (ii) spatial alignment. The description of the spatial alignment mainly focuses on the similarity measure used.

---

[1] Nonrigid motion because heart and thorax structures deform.

[2] In opposition to rigid registration which aims to find an optimal transform whose parameters μ' (eq. 2.1) are a translation and a rotation.

2.3.2 Cardiac MRI registration

Cardiac magnetic resonance images are multiplanar i.e. MRI systems stack different 2D (+t) slices resulting in a 3D (+t) image volume (cf. Figure 2.4a). Moreover, a given cardiac phase is imaged throughout multiple heartbeats during a short acquisition window and then combined under the assumption that cardiac motion is the same between heartbeats (Prieto, 2013). Although many efforts to improve cardiac MRI acquisition, physiological motion remains a major problem (cf. Figure 2.4b). Apnea is demanded in clinical routine to reduce breathing induced motion. However, the problem of misalignment between slices occurs because many patients are unable to hold their breath for prolonged periods or because the quality of the breath-hold (McLeish et al., 2002).

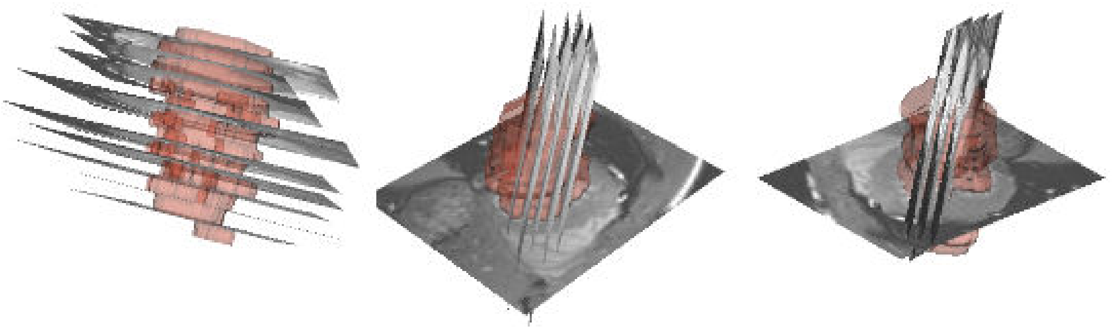

(a) From left to right: cine-SAX, cine-4CH and cine-2CH multiplanar cardiac MRI and left ventricular endocardial surface from cine-SAX.

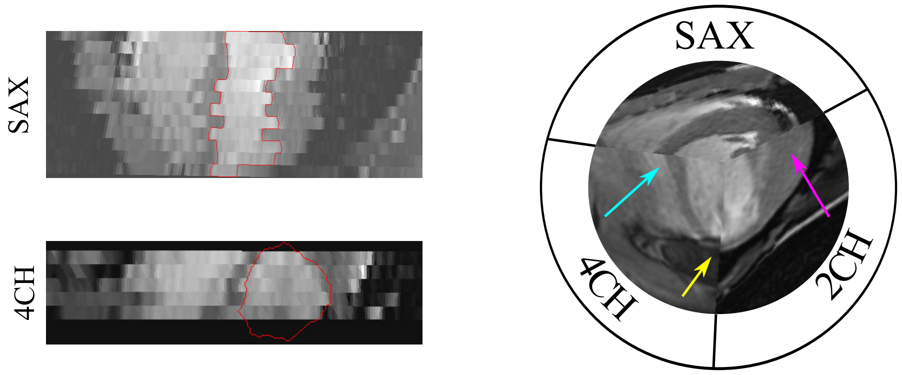

(b) Slice misalignment in cine-SAX and cine-4CH (left), and between multiview cine-MRI (right).

Figure 2.4: Slice misalignment in multiview cine-MRI of the left ventricle.

Magnetic resonance systems enable to acquire different types of sequences (cf. 1.3.4.1). The state of the art in cardiac MRI registration discussed here concerns cine and late gadolinium-enhanced (LGE) sequences. The temporal alignment is first discussed.

2.3.2.1 Temporal alignment

Linear matching is usually considered to align dynamic multiview images over time in intra-sequence or inter-sequence registration approaches. Multiview intra-sequence acquisitions often have the same temporal resolution (i.e. the number of imaged cardiac phases) and the temporal alignment between views is performed with an identity transformation (CARMINATI et al., 2012) (ELEN et al., 2010) (SLOMKA et al., 2007) (LÖTJÖNEN et al., 2005) (LÖTJÖNEN et al., 2004). When a static acquisition (e.g. LGE-MRI) needs to be aligned over time with a dynamic one (e.g. cine-MRI), the acquisition time after the peak-R and the cardiac rate are used. This information is extracted from DICOM tags of corresponding acquisitions (trigger time (0018,1060), average heart rate (0018,1088)). (HENNEMUTH et al., 2008) used this method to align LGE-MRI with dynamic constrast enhanced MRI (DCE-MRI).

2.3.2.2 Spatial alignment

State-of-the-art methods for the spatial registration of cardiac MRI exploit the image information contained in the intersection between image slices from multiview volumetric acquisitions of the same patient. In this approach, output images will be both, (i) registered and (ii) corrected for slice misalignment. We classified these methods in intra-sequence or inter-sequence approaches.

Multiview intra-sequence cardiac MRI registration. Slice misalignment in cine-MRI volumes due to physiological motion lead to a bias in the measurement of cardiac function (CARMINATI et al., 2012). It has been reported that respiratory motion of the heart leads to a 3D rotation and translation of the acquisition plane (MCLEISH et al., 2002). The resulting slice misalignment can be avoided at image acquisition using acceleration methods; however, they suffer from signal-to-noise ratio loss. Recent approaches have been proposed to improve image quality enabling to perform cardiac MRI acquisition in free-breathing (MENINI et al., 2014) (FILIPOVIC et al., 2011) (ODILLE et al., 2008). Other approaches rely on the registration of different views of the heart (SAX, LAX) to correct for slice misalignment in/between them (CARMINATI et al., 2012) (ELEN et al., 2010) (LÖTJÖNEN et al., 2005) (LÖTJÖNEN et al., 2004).

Reported registration-based procedures for cine-MRI dealt with in-plane slice misalignment (CARMINATI et al., 2012) (LÖTJÖNEN et al., 2005) (LÖTJÖNEN et al., 2006) and with a combination of in-plane and out-of-plane slice misalignment (ELEN et al., 2010) (SLOMKA et al., 2007). The reported approaches have used an iconic registration approach, i.e. they exploit the information about the intensity voxel value to measure the similarity between views. Different similarity measures have been used as the correlation coefficient (CC) (CARMINATI et al., 2012) (ELEN et al., 2010), the normalized mutual information (NMI) (ELEN et al., 2010) (LÖTJÖNEN et al., 2005) (LÖTJÖNEN et al., 2006), the sum of absolute voxels differences (ADD) (Elen et al., 2010) (Slomka et al., 2007) and the Slomka metric (Sk) (Slomka et al., 2007). (Elen et al., 2010) reported a comprehensive study of the abilities of these measures to correct for slice misalignment in cine-MRI. They proved that ADD and NMI obtain the best performance.

Concerning the registration of multiview LGE-MRI, few works has been reported in literature. We cite the one of (Wei et al., 2013) who corrected for misalignment artifacts using a novel measure that considers both, the similarity between image slices and the continuity of the heart throughout SAX stack. The slices in LGE-MRI were corrected for in-plane artifacts only.

Inter-sequence LGE-MRI registration: Integrating myocardial viability. (Hennemuth et al., 2008) presented a workflow of image processing for the analysis of intra-patient contrast enhanced sequences. This workflow integrates LGE-MRI and DCE-MRI to a static anatomical reference extracted from whole heart cardiac MRI coronary angiography, using an interactive region growing method (coronary tree from MRI angiography) and a semi-interactive Live-Wire algorithm (myocardium from LGE-MRI) (Boskamp et al., 2004) (Schenk et al., 2000). The correction of slice misalignment from DCE- and LGE-MRI was performed by registering them to the whole heart image after temporal alignment. The accuracy of the slice misalignment correction was visually evaluated by two experts for NMI and normalized cross-correlation measures. NMI performed the best for the registration of LGE-MRI and no difference was obtained between them for DCE-MRI. This approach allowed both, to remove slice misalignments and to register multisequence images.

Local intensity differences in myocardial tissue, caused by the accumulation of contrast agent in non-viable tissues, makes LGE-MRI registration difficult. For instance, the myocardium appears as an homogeneous tissue in cine-MRI while it can present bright regions in LGE-MRI indicating non-viable tissue (cf. Figure 1.21 and Figure 1.23b, respectively). (Cordero-Grande et al., 2012) proposed a fusion scheme of LGE-MRI and cine-MRI including image interpolation and slice misalignment removal. Their approach enhanced the workflow of (Hennemuth et al., 2008). The interpolation step aimed to obtain a nearly isotropic 3D reconstruction of input images. The slice misalignment step was first performed on the cine-SAX image at peak-R using corresponding cine-LAX images. Then, corrected cine-SAX was used to register LGE-SAX, using their *local entropy images* representation (Wachinger et al., 2012), and a mean-squares similarity measure. However, the convenience of using this representation was not evaluated, only corrected in-plane misalignments and supposed that LGE-MRI was acquired at end-diastole while it is routinely acquired at mid-diastole (cf. 1.3.4.1).

State-of-the-art methods cited above prove that an intra-patient multiview cardiac MRI registration approach enables to correct slice misalignment. The temporal alignment has been performed by linear matching of the cardiac phases acquired during intra-patient MRI. Concerning the spatial registration, a spatial transformation is computed for each slice in cardiac MRI such that a measure of similarity between imaged slices is optimized. Image profiles resulting from plane intersections are used to compute this similarity. In the registration of inter-sequence MRI, such an approach allows to associate complementary information (e.g. myocardial viability from LGE-MRI). Key aspects such as the best similarity measure and the most appropriated framework to use need to be studied in depth.

2.3.3 Registration of cardiac CT and MRI

The registration of cardiac CT and MRI aims at associating high density CT images (i.e. images with high spatial resolution) with MRI acquisitions. This registration permits to fuse morphological information from CT that have high spatial resolution with functional and myocardial tissue information from MRI. To our knowledge, the registration of intra-patient cine-MRI and cardiac CT has not been reported. Thus, in this section we discuss state-of-the-art approaches for monomodal registration of dynamic LV anatomy from CT or cine-MRI acquisitions either in an inter-patient or an intra-patient context.

2.3.3.1 Temporal alignment

Cardiac CT and MRI are not acquired simultaneously. This harden their temporal registration. Indeed, cardiac frequency can change significantly between acquisitions. ECGs used to gate cardiac CT and MRI acquisitions can be used to align them over time (Huang, Moore, et al., 2009). However, they are not always available. In this work, available CT and MRI acquisitions lack of ECG; thus, we focus on how temporal alignment has been performed in the absence of ECG recordings.

Temporal registration followed by spatial registration. The information issue from input dynamic images has been used in this approach to align the image sequences over time before their spatial registration. This allows to match corresponding cardiac phases. (Perperidis et al., 2005) used temporal landmarks of the left ventricle extracted from a cross-correlation curve (maximum contraction and end-relaxation phases). This curve was computed by stacking the normalized cross-correlation between the start-of-cardiac-cycle image and consecutive images over the RR-interval. It was proved (inter-subject registration, one reference subject and 14 moving subjects) that a temporal alignment using these extracted landmarks followed by a spatial alignment results in a negligible change (though lower) in performance indicators (overlap and surface distance calculated over all subjects and time frames), with a considerable lower computational cost when compared with a combined (spatio-temporal) approach.

Temporal alignment combined with spatial registration. In a simultaneous spatio-temporal registration approach, input image volumes are interpolated over time in order to be compared at the same instants. This temporal interpolation is challenging due to the complexity of cardiac motion. Hence, spatio-temporal registration approaches must compute nonrigid transformations consistent with the characteristics of the myocardial tissue (Mansi et al., 2011). All works listed below use nonrigid registration approaches.

(Ehrhardta et al., 2006) presented a study of temporal interpolation of cine-MRI using an optical flow algorithm. A calculated velocity field was used to obtain an interpolated image at a desired time. Although optical flow assumes intensity conservation in time variant regions, which is not the case for cine-MRI, a phantom study led to a good performance. (Schaerer et al., 2010) used a deformable elastic template to segment and track the motion of the myocardium in cine-MRI volume sequences (Rouchdy et al., 2007). A recent study of (McLeod, Seiler, Sermesant, et al., 2013) evaluated the accuracy of polyaffine[3] (McLeod, Seiler, Toussaint, et al., 2013) and iLogDemons ("demons" based approach[4]) (Mansi et al., 2011) methods in registering five *in-silico* cine-MRI volume sequences simulated with the method of (Prakosa et al., 2013). The polyaffine method obtained the best performance.

(Perperidis et al., 2005) divided the spatial and temporal inter-patient registration of cine-MRI into a global and local component. The global component corresponds to an affine transform while the local component is a free-form deformation (FFD) registration. (Lopez et al., 2008) presented an intra- and inter-subject registration with temporal association (3D registration using 4D information). Their method relied on a previous temporal alignment and incorporates the concept of "bridging points" which allowed to include image information from neighboring phases. This approach was enhanced in (Peyrat et al., 2010) where the intra-patient registration of CT images was divided into two steps: (i) 4D global temporal alignment mapping physiological states; (ii) 4D spatial registration mapping trajectories of physical points. The latter allowed to add "trajectory contraints" from motion tracking, i.e. to consistently map the same physical points over time in both sequences. The 4D spatial registration was formulated as a multichannel registration of 3D images at a reference time point and solved by Multichannel Diffeomorphic Demons (MDD). The evaluation of this approach used an electromechanically simulated cardiac CT sequence (in-silico phantom) as ground truth. This synthetic (in-silico) CT image has known deformation field to compare against after registration.

---

[3] In polyrigid and polyaffine registration, the transformation codes locally rigid or affine deformations: the image is divided into patches each transformed by a rigid or affine transform.

[4] Non-parametric nonrigid registration approach where each pixel has a displacement vector. In this approach, *demons* push according to local characteristics of the images in a similar way Maxwell did for solving Gibbs paradox. The forces are inspired from the optical flow equations (Vercauteren et al., 2009).

2.3.3.2 Spatial alignment

Mutual information (MI) metrics have been widely used to register CT and MRI (Rueckert et al., 2010) (Pluim et al., 2003) (Makela et al., 2002). However, different implementations of MI-based metrics [5] and other multimodal metrics proposed in literature harden the selection of the most appropriate (Rubeaux et al., 2010) (Mattes, D. Haynor, et al., 2003) (Viola et al., 1997) (Collignon et al., 1995).

No work registering cardiac CT and MRI acquisitions was found. In consequence, below we present some methods proposed for non-cardiac applications.

2.3.3.3 Registration of dynamic-CT and MRI in non-cardiac applications

Some intra-patient methods to register CT and MRI have been proposed in the context of radiotherapy. (Schreibmann et al., 2008) proposed a 4D registration procedure for image guided radiotherapy. One multimodal registration case was reported using a 3D gated-MRI (static) and a 4D-CT (dynamic) image from a neuroblastoma patient with metastatic liver foci. Spatial and temporal alignment resulted from the maximization of a mutual information metric using a translation and time shift transform. (Passera et al., 2008) used a free-form deformation method based on B-Splines to register DCE-MRI (gadolinium contrast agent) and DCE-CT (iodine contrast agent) images of bladder tumors. The alignment of time series generated from mean signals inside the CT and MRI tumor volume of interests (VOIs) was performed by analyzing the cross-correlation of the temporal gradient of mean signal intensities.

State-of-the-art registration methods cited above align input monomodal images over time either in combination with spatial alignment (spatio-temporal registration) or before spatial alignment. Temporal landmarks such as the end-diastolic phase or the minimum-volume phase can be computed from the intensity information in dynamic image volume sequences. Spatio-temporal registration approaches aimed at registering inter-patient cardiac images such that moving image volume sequences are interpolated to match the time instants of the fixed image volume sequence. Performing this interpolation remains a challenging open problem. In both approaches, the matching of corresponding cardiac phases in multimodal acquisitions needs to be evaluated. Given that the RR-interval can change between intra-patient acquisitions, this evaluation is important in the context of this work due to the nonlinear relationship between the ECG and the heart rate.

Concerning the measures of similarity used to register CT and MRI, mutual information metrics have been commonly used in non-cardiac intensity-based registration approaches; yet, this must be evaluated in depth for cardiac image registration.

---

[5] See (Pluim et al., 2003) for a description of some MI implementation considerations.

2.3.4 Registration of echocardiography

2D and 3D echocardiography (US) enable the assessment of cardiac function. It is an ubiquitous modality in current cardiology practice due to its size and portability, real time, low-cost, absence of radiation and easy of use in initial diagnosis as well as for follow-up studies (Chandra et al., 2010). However, image quality harden their processing and interpretation. Two main goals have motivated the integration of US and cardiac MRI/CT in literature:

1. The projection of pre-operative data in the operating room: high-resolution (CT/MRI) spatial information provides a valuable support during US-guided interventions (Housden et al., 2013) (Wein, Brunke, et al., 2008) (Zhang et al., 2006),
2. The combination of complementary descriptors. For instance, a disease can be detected and described using US, but also with CT and/or MRI which provide a complementary characterization of the anatomy, tissue and function.

Few multimodal registration methods involving echocardiography have been proposed. This is mainly due to the nature of US images which make challenging their registration (Makela et al., 2002). Besides, given the constraints of the field of view of US transducer, output geometries do not fit perfectly with those depicted in volumetric acquisitions. Even if 3D-US is emerging as an important tool for the measurement of cardiac function (Sugeng et al., 2010) (Maffessanti et al., 2009) (Otsuji et al., 2001), 2D-US remains more widespread in clinical routine. 2D-US systems acquire a reduced number of views by changing the position of the US transducer. In this context, dynamic registration of 2D-US and 3D-CT/MRI aims to obtain the pose of the US plane and to align the cardiac structures depicted in both acquisitions.

Dynamic 2D-US and 3D-CT/MRI registration is generally performed by first aligning input acquisitions over time and then in space.

2.3.4.1 Temporal alignment

Input images can be aligned over time using *only one instant* or *temporal interpolation*. If just one cardiac phase is used, then two images corresponding to the same instant are aligned. Usually, the peak-R phase is preferred because it is the phase used to synchronize cardiac CT/MRI acquisition (Ledesma-Carbayo et al., 2005).

In a dynamic approach, the entire image dynamics are aligned. ECGs recorded during acquisition (acquisition ECGs) have been used to register dynamic US images. Because cardiac CT/MRI has a lower temporal resolution than US, acquisition ECGs enable to locate an US instant t_{US} between two CT/MRI instants t_1 and t_2 such that $t_{US} \in [t_1, t_2]$. (Zhang et al., 2006) (Huang, N. A. Hill, Ren, Guiraudon, and Peters, 2007) exploited this in a temporal interpolation procedure to get a new volumetric image at t_{US}.

Sometimes *no temporal alignment* is performed (e.g. when the goal is to compare functional data). In this case, it is only needed to represent the information in a common spatial referential. This referential is given by a common division of input geometry into cardiac segments (bulleye). Therefore, integrated cardiac function can be analyzed by matching corresponding segments. However, if 2D-US is analyzed using this approach, such an integration is inaccurate because the real pose of the US-plane in the 3D volume is unknown.

2.3.4.2 Spatial alignment

The spatial registration of US images can be divided into *stereotactic*, *iconic*, *geometrical* and *simulation-based* approaches.

Stereotactic-based. This approach is used in surgical interventions (stereotactic surgery). The term stereotactic refers to the precise spatial positioning. Here, the pose (origin and orientation) of the US-probe is tracked in real time using magnetic fields or optical localizers and triangulation. It is then possible to place the US image into the CT/MRI space using this information (HUANG, MOORE, et al., 2009) (HUANG, N. A. HILL, REN, GUIRAUDON, and PETERS, 2007) (ZHANG et al., 2006) (HUANG, N. A. HILL, REN, GUIRAUDON, BOUGHNER, et al., 2005) (COMEAU et al., 2000) (PAGOULATOS et al., 1999) (TROBAUGH et al., 1994).

(HUANG, MOORE, et al., 2009) followed three steps to register dynamic intra-patient 2D-US with 3D-CT/MRI:

1. One CT/MRI and one US image are acquired pre-operatively. US-probe position is tracked during US acquisition. An alignment of these pre-operative images provides a first initialization.
2. The US-probe is also tracked during surgery.
3. The pre-operative alignment in 1. and the tracked US-probe position in step 2. are used together to perform the per-operative registration in real time.

This kind of procedures enable to improve the surgeon gesture by augmented reality, i.e. the enhancement of surgeon's perception by the visualization in real-time of US images superimposed to -dynamic- CT/MRI images during the intervention (WEIN, KHAMENE, et al., 2007).

If a non-stereotactic approach is selected then the usual procedure includes a manual alignment procedure followed by an iconic-based or a geometry-based registration.

Iconic-based. In this approach voxel intensities are used during registration. In this case, the selection of the most appropriate similarity measure to be optimized arises as the most difficult problem because of the huge heterogeneity of the considered images.

(Heldmann et al., 2009) presented the difficulties related with the differences in dimension between US slices and CT volumes mainly to select the similarity criteria, when dealing with liver images. In fact, they proved the inefficiency of the sum of squared differences.

(Huang, Moore, et al., 2009) (Huang, N. A. Hill, Ren, Guiraudon, and Peters, 2007) (Huang, N. A. Hill, Ren, Guiraudon, Boughner, et al., 2005) used the mutual information instead. Their procedure was first tested on 3D+t US with MRI registration (Zhang et al., 2006) (Huang, N. A. Hill, Ren, Guiraudon, Boughner, et al., 2005) and then extended to dynamic 2D-US with 3D-CT (Huang, N. A. Hill, Ren, Guiraudon, and Peters, 2007) and US endo-vascular with CT registration (Huang, Ren, et al., 2009). Input acquisitions are first manually aligned and a following stage improves this alignment by maximizing their mutual information.

Finally, the correlation ratio measured between US images and simulated US-images derived from CT acquisitions was used in (Wein, Khamene, et al., 2007) (Wein, Röper, et al., 2005).

Geometry-based. It is common to use manually placed landmarks to register US images. (Savi et al., 1995) used three anatomical landmarks (two in LV papillary muscles and one in the inferior junction of the right ventricle) to register positron emission tomography (PET) and US images of the heart. These points defined the US-plane in PET's coordinate system. (Tournoux et al., 2010) used five landmarks (one apical, four around the mitral annulus) to locate the US cardiac segments in a space referential from a LV geometry model. This model enabled the registration of 2D-US with the LV geometry extracted from CT images. An additional landmark (centerline of a coronary sinus tube) was used to register the coronary veins extracted from rotational X-Ray angiography.

Simulation-based registration. The idea behind this approach is to exploit the information from one modality to simulate the other and, in such a way, to perform a mono-modality registration. In the case of echocardiography, it is advantageous because the acoustic properties of heart's tissues and the foundations behind US image are well known. Besides, the implementation is mitigated because different tools are available such as Field II simulation program[6] (Jensen et al., 1992) (Glatard et al., 2013), or CREANUIS (Nonlinear Ultrasound Image Simulator)(Varray, Basset, et al., 2013) (Varray, Ramalli, et al., 2011). (Wein, Khamene, et al., 2007) (Wein, Röper, et al., 2005) simulated US images using the information of X-Ray attenuation from CT acquisitions (Schneider et al., 1996). The similarity between US images was measured using a statistical metric. (King et al., 2010) augmented a segmentation from MRI by adding a simulated echo using tissue acoustic properties in order to optimize a measure

---

[6] http://field-ii.dk

of consistency with real US. A similar approach has been used in the three modalities scheme proposed by (Housden et al., 2013) which is discussed in 2.3.6.

Recently, a tool for image simulation as been made available by CREATIS Lyon, the virtual image platform (VIP)[7] (Glatard et al., 2013). This platform shares medical image simulators (PET, CT, MRI and US). VIP platform includes the FIELD II ultrasound simulator.

State-of-the-art methods cited above exploit ECGs recorded during cardiac image acquisition to register US images over time. This cannot be used here to align cardiac CT and MRI with US because the ECG was not recorded during CT and MRI acquisitions. Then, image-derived information or additional information from US (e.g. LV traces from STE) must be exploited to register them over time. Concerning spatial registration, the stereotactic approach cannot be used here because we do not have an estimation of US-probe pose in CT, MRI nor EAM spaces.

2.3.5 Registration of cardiac EAM

In the context of this work, the goal of EAM registration is to describe the electrical information on a -dynamical- anatomical referential of high resolution (i.e. containing fine anatomical details). EAM systems project cardiac electrograms (EGMs) to a 3D surface to generate electrical activity maps (cf. 1.3.2). This surface corresponds to a rough estimation of the inner cavity's surface such as the LV endocardium. This geometry is computed from a point cloud describing the trajectory of a contact catheter. Some approaches had exploited this trajectory information to obtain rough estimations of endocardial wall motion (Camara et al., 2009) or deformation (Porras et al., 2011). Therefore, mechanical and electrical information can be obtained using mapping systems. However, the accuracy of non-electrical information is lower than using other modalities such as CT, MRI or US.

(Powell et al., 2009) (Bertaglia et al., 2009) highlighted the fact that more anatomic details may allow for increased accuracy in lesion application and, therefore, to improved procedure outcome in atrial fibrillation treatment. However, the same editorial stated that the minimum amount of imaging detail needed to achieve excellent outcome is still debated. Works like (Kettering et al., 2009) (Chillou et al., 2008) (Tops et al., 2005) discussed about this problem. Indeed, it has been proved that the geometrical model of the left atrium obtained with EAM commercial systems can be inaccurate. The analysis of available EAM acquisitions enables us to state that this is also the case for LV; however, any work describing the accuracy of EAM geometrical description of the inner LV geometry was found.

---

[7] http ://vip.creatis.insa-lyon.fr

We divided EAM registration methods into (i) registration of quasi-simultaneous acquisitions and (ii) point- and geometry-based registration.

Registration of quasi-simultaneous acquisitions. This category includes those methods aiming to integrate the acquisition of multiview X-Ray images (C-arm), MRI and EAM into the operating room. (RHODE and SERMESANT, 2011), (GAO et al., 2010), (RHODE, SERMESANT, et al., 2005) and (RHODE, D. L. G. HILL, et al., 2003) presented a system integrating X-ray and MRI guidance that is partially motivated to track the catheters involved in the treatment of atria ablation. In this system, the registration of EAM and CT/MRI is straightforward because they are acquired per-operatively and described a common referential. Two registration approaches were presented according to the type of mapping system used (with/without contact). In a non-contact approach, the constellation catheter was rigidly registered. When a contact catheter was used, the referential information was exploited to initialize an iterative closest point registration.

Point- and geometry-based registration. Static LV geometries do not contain enough information enabling to obtain an accurate registration. Among other reasons, this is because the left ventricle is almost symmetric to its great axis. Most of EAM registration methods typically match distinct landmarks or fiducial points marked during EAM examination with corresponding annotations in CT/MRI. Commercial systems as CartoMerge™and EnSite NavX have the capability to integrate 3D images with EAM using fiducial registration. These systems superimpose activation or voltage maps on CT/MRI heart chambers by catheter navigation within the CT/MRI models (SCHMITT et al., 2006). (CHILLOU et al., 2008) (FEUCHTNER et al., 2008) (KHAYKIN et al., 2008) (OKUMURA et al., 2008) (TOPS et al., 2005) aligned data imported to Carto™ system using proprietary software. Recently, (CARPEN et al., 2013) proved the feasibility to integrate 3D rotational angiography and EAMs to guide catheter ablation in atria fibrillation treatment. They used fiducial points at easily recognizable anatomical locations such as the antral and the carinal portion of the pulmonary veins and the left atrium appendage ridge. However, (POWELL et al., 2009) proved that individual points placed manually in inner atria can be inaccurate by more than 10–15 mm. Indeed, excessive catheter contact force applied during mapping may distort the map.

In (DONG et al., 2006), an initial matching based on three pairs of fiducial points was used to compute a rigid transformation between right atrium surfaces obtained from EAM and CT. This was followed by an iterative closest point (ICP) procedure incorporating new anatomical information. (WILSON et al., 2009) proposed an EAM system that used an initial fiducial registration to start an iterative procedure adding new points during the acquisition of EGMs until a satisfactory registration had been obtained. They applied ICP and multibin ICP (MICP, descibed in (WILSON et al., 2006)) to register dynamic heart models. This method was validated on phantom and porcine (*in-vivo*) hearts. This is a novel perspective to integrate dynamic surfaces directly with EGMs during EAM acquisition. (Chiang et al., 2012) aimed to improve surface geometry accounting for each acquired point into a progressive deformation of the surface in order to obtain a geometrical model adjusted to ventricle's physiology. Although this improved the spatial resolution it did not acquire surface dynamics.

Catheter trajectory can be exploited to register EAM surfaces. Catheters used in commercial mapping systems like Ensite NavX (St. Jude Medical, St. Paul, MN, USA) or Carto (BiosenseWebster, Haifa, Israel) approach LV chamber either by retrograde access via aortic valve or by transseptal access (Schmitt et al., 2006). Aortic access gives additional information that was used in (Reddy et al., 2004) (Malchano et al., 2006) in an initial registration stage.

(Soto-Iglesias et al., 2013) evaluated the integration of EAM surfaces using rigid fiducial-based registration, iterative closest point and nonrigid currents-based registration (Vaillant et al., 2005). They also tested two procedures to map electrical information to registered surfaces: closest point and surface-homeomorphism-based. Their results suggested that homeomorphic registration improves the overlap between left ventricular substrate from EAM and delayed-enhanced MRI.

State-of-the-art methods cited above used fiducial- and/or surface-based approaches to register EAM acquisitions. However, the low resolution and low precision of the anatomical geometry acquired during EAM acquisition harden this registration. Commercial systems compute a surface from points positioned by the contact catheter at the moment of maximal relaxation (cf. 1.3.2). Normally, this corresponds to the endocardium at the phase of maximum volume (end-diastole). However, this is not necessarily the case in diseased hearts. For instance, the time of maximal relaxation can differ between left ventricular regions due to ventricular dyssynchrony. Some works proved that wall motion and deformation can be computed from EAM point cloud acquisition (which is acquired to delineate the imaged inner chamber) (Camara et al., 2009). This information can be exploited in a dynamic registration approach to improve EAM integration yet no work using this approach has been reported.

2.3.6 Simultaneous registration of multiple acquisitions

Three or more multimodal images can be registered either pairwise (i.e. selecting a reference image to which the others will be registered) or using all images simultaneously. A mimic of the latter was proposed in (Housden et al., 2013) to align pre-procedure MRI/CT with intra-procedure X-ray and 3D trans-esophageal echo (TEE) images. MR/CT images offered the anatomical referential while X-Ray and tracked 3D-TEE provided live device visualization and live anatomical visualization, respectively. Basically, the method registers a simulated ultrasound from MRI/CT heart's structures to 3D-TEE. Then, this alignment is propagated to X-Ray by probe tracking. This enabled to integrate three image modalities; however, the information contained in the images was not exploited in a combined procedure but rather in a sequential one.

2.4 Conclusion

This chapter, without being an exhaustive survey, situates state-of-the-art methods on cardiac image registration in the context of this work: multisensor image fusion to characterize the diseased heart (HCM, HF). Their discussion followed the modalities involved in this work:

MRI. *Intra-* and *inter-sequence* cardiac MRI registration approaches were discussed. State-of-the-art methods register multiview cardiac MRI in order to *correct for slice misalignment*. The extrapolation of this approach to inter-sequence registration enables to integrate complementary information. In the integration of LGE-MRI, key aspects such as a reliable image interpolation, the best similarity measure and the most appropriated framework to use need to be studied in depth.

CT and MRI registration. No work dealing with the registration of intra-patient cardiac CT and MRI was found. In order to elucidate how to align dynamic images over time, state-of-the-art monomodal registration were studied. These methods used either *combined registration* or *temporal registration before spatial registration*. From combined approaches, it is clear that volume interpolation over time remains an open challenging issue; thus, the second approach arises as the most convenient here. On the other hand, some multimodal registration approaches in the context of radiotherapy proved that mutual information based metrics enable to register these acquisitions in space. This has to be evaluated for multisensor cardiac images.

US and 3D image registration. US registration remains a difficult task. Usually, a *spatial registration follows a first temporal alignment*. State-of-the-art methods exploit ECGs acquired during acquisition to align US images with 3D images over time. This approach cannot be used here because ECGs were not recorded during the acquisition of available CT, MRI and EAM (during inner chamber geometry acquisition). Regarding spatial alignment, four approaches had been used: stereotactic-, iconic-, geometry- and simulation-based. Their output is strongly dependent on preprocessing, landmark annotation and/or transform initialization. The last three approaches may potentially be used in this work.

EAM to 3D image registration. Reported methods registering EAM were categorized into registration of *quasi-simultaneous* acquisitions, *point-* and *geometry-based* registration. Two challenges arose: first, the registration of low-resolution EAM surfaces that are a rough depicting of the inner cavity at a given phase; second, the association of EGMs into a high-resolution anatomy obtained from CT/MRI. Some published works proved the lack of precision in EAM geometry acquisition that, with the low resolution of EAM geometry, harden its registration. Nevertheless, the point cloud acquisition used to estimate the inner chamber geometry may be exploited to improve EAM registration.

The approaches developed to register multisensor cardiac images of interest are presented in next chapter.

References

ANTONY, R. T. (1995). *Principles of data fusion automation.* Artech House, Inc.

BERTAGLIA, E., BELLA, P. D., TONDO, C., PROCLEMER, A., BOTTONI, N., PONTI, R. D., LANDOLINA, M., BONGIORNI, M. G., CORÒ, L., STABILE, G., RUSSO, A. D., VERLATO, R., MANTICA, M., and ZOPPO, F. (2009). "Image integration increases efficacy of paroxysmal atrial fibrillation catheter ablation: results from the CartoMerge™ Italian Registry". en. In: *Europace* 11.8, pp. 1004–1010.

BOSKAMP, T., RINCK, D., LINK, F., KÜMMERLEN, B., STAMM, G., and MILDENBERGER, P. (2004). "New Vessel Analysis Tool for Morphometric Quantification and Visualization of Vessels in CT and MR Imaging Data Sets". In: *RadioGraphics* 24.1, pp. 287–297.

CAHILL, N. (2010). "Normalized Measures of Mutual Information with General Definitions of Entropy for Multimodal Image Registration". English. In: *Biomedical Image Registration.* Ed. by B. FISCHER, B. DAWANT, and C. LORENZ. Vol. 6204. Lecture Notes in Computer Science. Springer Berlin Heidelberg, pp. 258–268.

CAMARA, O., OELTZE, S., DE CRAENE, M., SEBASTIAN, R., SILVA, E., TAMBORERO, D., MONT, L., SITGES, M., BIJNENS, B., and FRANGI, A. (2009). "Cardiac Motion Estimation from Intracardiac Electrical Mapping Data: Identifying a Septal Flash in Heart Failure". In: *Functional Imaging and Modeling of the Heart.* Ed. by N. AYACHE, H. DELINGETTE, and M. SERMESANT. Vol. 5528. Lecture Notes in Computer Science. 10.1007/978-3-642-01932-6_3. Springer Berlin / Heidelberg, pp. 21–29.

CARMINATI, M., MAFFESSANTI, F., and CAIANI, E. (2012). "Automated motion artifacts removal between cardiac long- and short-axis magnetic resonance images". In: *Computing in Cardiology (CinC), 2012*, pp. 689–692.

CARPEN, M., MATKINS, J., SYROS, G., GOREV, M. V., ALIKHANI, Z., WYLIE, J. V., NATAN, S. R., GRIBEN, A., HICKS, A., ARMSTRONG, J., and ORLOV, M. V. (2013). "First experience of 3D rotational angiography fusion with NavX electroanatomical mapping to guide catheter ablation of atrial fibrillation". In: *Heart Rhythm* 10.3, pp. 422–427.

CHANDRA, S., PATEL, A. R., and SUGENG, L. (2010). "Multimodality Imaging in Cardiovascular Medicine". en. In: ed. by C. M. KRAMER. Demos Medical Publishing. Chap. Multimodality imaging in Valvular Heart Disease.

Chiang, P., Zheng, J., Mak, K. H., Thalmann, N. M., and Cai, Y. (2012). “Progressive surface reconstruction for heart mapping procedure”. In: *Computer-Aided Design* 44.4, pp. 289–299.

Chillou, C. d., Andronache, M., Abdelaal, A., Ernst, Y., Magnin-Poull, I., Magdi, M., Zhang, N., Tissier, S., Mandry, D., Barbary, C., Régent, D., and Aliot, E. (2008). “Evaluation of 3D guided electroanatomic mapping for ablation of atrial fibrillation in reference to CT-Scan image integration”. en. In: *Journal of Interventional Cardiac Electrophysiology* 23.3, pp. 175–181.

Collignon, A., Maes, F., Delaere, D., Vandermeulen, D., Suetens, P., and Marchal, G. (1995). “Automated multi-modality image registration based on information theory”. In: *Information processing in medical imaging.* Vol. 3, pp. 263–274.

Comeau, R. M., Sadikot, A. F., Fenster, A., and Peters, T. M. (2000). “Intraoperative ultrasound for guidance and tissue shift correction in image-guided neurosurgery”. eng. In: *Medical physics* 27.4, pp. 787–800.

Cordero-Grande, L., Merino-Caviedes, S., Alba, X., Figueras i Ventura, R., Frangi, A. F., and Alberola-Lopez, C. (2012). “3D fusion of cine and late-enhanced cardiac magnetic resonance images”. In: *2012 9th IEEE International Symposium on Biomedical Imaging (ISBI)*, pp. 286–289.

Dong, J., Calkins, H., Solomon, S. B., Lai, S., Dalal, D., Lardo, A., Brem, E., Preiss, A., Berger, R. D., Halperin, H., and Dickfeld, T. (2006). “Integrated Electroanatomic Mapping With Three-Dimensional Computed Tomographic Images for Real-Time Guided Ablations”. en. In: *Circulation* 113.2, pp. 186–194.

Ehrhardta, J., Säringa, D., and Handelsa, H. (2006). “Optical flow based interpolation of temporal image sequences”. In: *Proc. of SPIE Vol.* Vol. 6144, 61442K–1.

Elen, A., Hermans, J., Ganame, J., Loeckx, D., Bogaert, J., Maes, F., and Suetens, P. (2010). “Automatic 3-D Breath-Hold Related Motion Correction of Dynamic Multislice MRI”. In: *IEEE Transactions on Medical Imaging* 29.3, pp. 868–878.

Feuchtner, G. M., Dichtl, W., DeFrance, T., Stühlinger, M., Klauser, A., Berger, T., Junker, D., Spuller, K., Pachinger, O., Nedden, D. z., and Hintringer, F. (2008). “Fusion of multislice computed tomography and electroanatomical mapping data for 3D navigation of left and right atrial catheter ablation”. In: *European Journal of Radiology* 68.3, pp. 456–464.

Filipovic, M., Vuissoz, P.-A., Codreanu, A., Claudon, M., and Felblinger, J. (2011). “Motion compensated generalized reconstruction for free-breathing dynamic contrast-enhanced MRI”. In: *Magnetic Resonance in Medicine* 65.3, pp. 812–822.

Gao, G., Chinchapatnam, P., Wright, M., Arujuna, A., Ginks, M., Rinaldi, A., and Rhode, K. (2010). “An MRI/CT-based cardiac electroanatomical mapping system with scattered data interpolation algorithm”. In: *2010 IEEE International*

Symposium on Biomedical Imaging: From Nano to Macro. Rotterdam, Netherlands, pp. 464–467.

GLATARD, T., LARTIZIEN, C., GIBAUD, B., FERREIRA DA SILVA, R., FORESTIER, G., CERVENANSKY, F., ALESSANDRINI, M., BENOIT-CATTIN, H., BERNARD, O., CAMARASU-POP, S., CEREZO, N., CLARYSSE, P., GAIGNARD, A., HUGONNARD, P., LIEBGOTT, H., MARACHE, S., MARION, A., MONTAGNAT, J., TABARY, J., and FRIBOULET, D. (2013). "A Virtual Imaging Platform for Multi-Modality Medical Image Simulation". In: *IEEE Transactions on Medical Imaging* 32.1, pp. 110–118.

HELDMANN, S. and PAPENBERG, N. (2009). "A Variational Approach for Volume-to-Slice Registration". In: *Scale Space and Variational Methods in Computer Vision*. Ed. by X.-C. TAI, K. MØRKEN, M. LYSAKER, and K.-A. LIE. Vol. 5567. Lecture Notes in Computer Science. 10.1007/978-3-642-02256-2_52. Springer Berlin / Heidelberg, pp. 624–635.

HENNEMUTH, A., SEEGER, A., FRIMAN, O., MILLER, S., KLUMPP, B., OELTZE, S., and PEITGEN, H.-O. (2008). "A Comprehensive Approach to the Analysis of Contrast Enhanced Cardiac MR Images". In: *IEEE Transactions on Medical Imaging* 27.11, pp. 1592–1610.

HERNANDEZ, A. (2000). "Fusion de signaux et de modèles pur la caractérisation d'arythmies cardiaques". PhD thesis. LTSI, Université de Rennes 1.

HOUSDEN, R. J., BASRA, M., MA, Y., KING, A. P., BULLENS, R., CHILD, N., GILL, J., RINALDI, C. A., PARISH, V., and RHODE, K. S. (2013). "Three-Modality Registration for Guidance of Minimally Invasive Cardiac Interventions". In: *Functional Imaging and Modeling of the Heart*. Ed. by S. OURSELIN, D. RUECKERT, and N. SMITH. Lecture Notes in Computer Science 7945. Springer Berlin Heidelberg, pp. 158–165.

HUANG, X., HILL, N. A., REN, J., GUIRAUDON, G., BOUGHNER, D., and PETERS, T. M. (2005). "Dynamic 3D Ultrasound and MR Image Registration of the Beating Heart". In: *Medical Image Computing and Computer-Assisted Intervention – MICCAI 2005*. Ed. by J. DUNCAN and G. GERIG. Vol. 3750. Lecture Notes in Computer Science. 10.1007/11566489_22. Springer Berlin / Heidelberg, pp. 171–178.

HUANG, X., HILL, N. A., REN, J., GUIRAUDON, G., and PETERS, T. M. (2007). "Intra-Cardiac 2D US to 3D CT Image Registration". In: *Proc. SPIE 6509, Medical Imaging 2007*. Vol. 6509, pages.

HUANG, X., MOORE, J., GUIRAUDON, G., JONES, D., BAINBRIDGE, D., REN, J., and PETERS, T. (2009). "Dynamic 2D Ultrasound and 3D CT Image Registration of the Beating Heart". In: *Medical Imaging, IEEE Transactions on* 28.8, pp. 1179–1189.

HUANG, X., REN, J., GUIRAUDON, G., BOUGHNER, D., and PETERS, T. (2009). "Rapid Dynamic Image Registration of the Beating Heart for Diagnosis and Surgical Navigation". In: *Medical Imaging, IEEE Transactions on* 28.11, pp. 1802–1814.

IBANEZ, L., SCHROEDER, W., NG, L., and CATES, J. (2005). *The ITK Software Guide*. Second. Kitware, Inc. ISBN 1-930934-15-7. http://www.itk.org/ItkSoftwareGuide.pdf.

Jensen, J. and Svendsen, N. (1992). "Calculation of pressure fields from arbitrarily shaped, apodized, and excited ultrasound transducers". In: *IEEE Transactions on Ultrasonics, Ferroelectrics and Frequency Control* 39.2, pp. 262–267.

Kettering, K., Greil, G. F., Fenchel, M., Kramer, U., Weig, H.-J., Busch, M., Miller, S., Sieverding, L., Laszlo, R., and Schreieck, J. (2009). "Catheter ablation of atrial fibrillation using the Navx-/Ensite-system and a CT-/MRI-guided approach". en. In: *Clinical Research in Cardiology* 98.5, pp. 285–296.

Khaykin, Y., Skanes, A., Whaley, B., Hill, C., Beardsall, M., Seabrook, C., Wulffhart, Z., Oosthuizen, R., Gula, L., and Verma, A. (2008). "Real-time integration of 2D intracardiac echocardiography and 3D electroanatomical mapping to guide ventricular tachycardia ablation". In: *Heart Rhythm* 5.10, pp. 1396–1402.

King, A. P., Rhode, K. S., Ma, Y., Yao, C., Jansen, C., Razavi, R., and Penney, G. P. (2010). "Registering preprocedure volumetric images with intraprocedure 3-D ultrasound using an ultrasound imaging model". eng. In: *IEEE transactions on medical imaging* 29.3, pp. 924–937.

Klein, S., Staring, M., Murphy, K., Viergever, M., and Pluim, J. (2010). "Elastix: a toolbox for intensity based medical image registration". In: *IEEE TMI* 29.1, pp. 196–205.

Ledesma-Carbayo, M., Kybic, J., Desco, M., Santos, A., Suhling, M., Hunziker, P., and Unser, M. (2005). "Spatio-temporal nonrigid registration for ultrasound cardiac motion estimation". In: *Medical Imaging, IEEE Transactions on* 24.9, pp. 1113–1126.

Lopez, A., Fritscher, K. D., Trieb, T., Schubert, R., and Mattes, J. (2008). "3D inter-subject cardiac registration using 4D information". In: *Proc. SPIE 6914, Medical Imaging 2008: Image Processing*, pp. 691413–691413.

Lötjönen, J., Pollari, M., Kivistö, S., and Lauerma, K. (2004). "Correction of Movement Artifacts from 4-D Cardiac Short- and Long-Axis MR Data". In: *Medical Image Computing and Computer-Assisted Intervention – MICCAI 2004*. Vol. 3217. Lecture Notes in Computer Science. Springer Berlin / Heidelberg, pp. 405–412.

Lötjönen, J., Pollari, M., Kivistö, S., and Lauerma, K. (2005). "Correction of motion artifacts from cardiac cine magnetic resonance images". eng. In: *Academic radiology* 12.10, pp. 1273–1284.

Lötjönen, J., Pollari, M., Kivistö, S., and Lauerma, K. (2006). "Correction of misalignment artifacts among 2-D cardiac MR images in 3-D space". In: *Proc. 1st Int. Workshop Comput. Vis. Intravascular Intracardiac Imag (MICCAI 2006)*. Vol. 1, pp. 114–121.

Maffessanti, F., Nesser, H.-J., Weinert, L., Steringer-Mascherbauer, R., Niel, J., Gorissen, W., Sugeng, L., Lang, R. M., and Mor-Avi, V. (2009). "Quantitative Evaluation of Regional Left Ventricular Function Using Three-Dimensional

Speckle Tracking Echocardiography in Patients With and Without Heart Disease". In: *The American Journal of Cardiology* 104.12, pp. 1755–1762.

Makela, T., Clarysse, P., Sipila, O., Pauna, N., Pham, Q. C., Katila, T., and Magnin, I. (2002). "A review of cardiac image registration methods". In: *Medical Imaging, IEEE Transactions on* 21.9, pp. 1011–1021.

Malchano, Z. J., Neuzil, P., Cury, R. C., Holmvang, G., Weichet, J., Schmidt, E. J., Ruskin, J. N., and Reddy, V. Y. (2006). "Integration of Cardiac CT/MR Imaging with Three-Dimensional Electroanatomical Mapping to Guide Catheter Manipulation in the Left Atrium: Implications for Catheter Ablation of Atrial Fibrillation". en. In: *Journal of Cardiovascular Electrophysiology* 17.11, pp. 1221–1229.

Mansi, T., Pennec, X., Sermesant, M., Delingette, H., and Ayache, N. (2011). "iLogDemons: A Demons-Based Registration Algorithm for Tracking Incompressible Elastic Biological Tissues". en. In: *International Journal of Computer Vision* 92.1, pp. 92–111.

Mattes, D., Haynor, D., Vesselle, H., Lewellen, T., and Eubank, W. (2003). "PET-CT image registration in the chest using free-form deformations". In: *Medical Imaging, IEEE Transactions on* 22.1, pp. 120–128.

Mattes, D., Haynor, D. R., Vesselle, H., Lewellyn, T. K., and Eubank, W. (2001). *Nonrigid multimodality image registration.*

McLeish, K., Hill, D. L. G., Atkinson, D., Blackall, J., and Razavi, R. (2002). "A study of the motion and deformation of the heart due to respiration". In: *IEEE Transactions on Medical Imaging* 21.9, pp. 1142–1150.

McLeod, K., Seiler, C., Sermesant, M., and Pennec, X. (2013). "Spatio-Temporal Dimension Reduction of Cardiac Motion for Group-Wise Analysis and Statistical Testing". In: *To appear in Medical Image Computing and Computer-Assisted Intervention – MICCAI 2013*. Lecture Notes in Computer Science.

McLeod, K., Seiler, C., Toussaint, N., Sermesant, M., and Pennec, X. (2013). "Regional Analysis of Left Ventricle Function Using a Cardiac-Specific Polyaffine Motion Model". In: *Functional Imaging and Modeling of the Heart*. Ed. by S. Ourselin, D. Rueckert, and N. Smith. Lecture Notes in Computer Science 7945. Springer Berlin Heidelberg, pp. 483–490.

Menini, A., Slavin, G., Stainsby, J., Ferry, P., Felblinger, J., and Odille, F. (2014). "Motion correction of multi-contrast images applied to T1 and T2 quantification in cardiac MRI". English. In: *Magnetic Resonance Materials in Physics, Biology and Medicine*, pp. 1–12.

Odille, F., Cîndea, N., Mandry, D., Pasquier, C., Vuissoz, P.-A., and Felblinger, J. (2008). "Generalized MRI reconstruction including elastic physiological motion and coil sensitivity encoding". In: *Magnetic Resonance in Medicine* 59.6, pp. 1401–1411.

Okumura, Y., Henz, B. D., Johnson, S. B., Bunch, T. J., O'Brien, C. J., Hodge, D. O., Altman, A., Govari, A., and Packer, D. L. (2008). "Three-Dimensional

Ultrasound for Image-Guided Mapping and Intervention Methods, Quantitative Validation, and Clinical Feasibility of a Novel Multimodality Image Mapping System". en. In: *Circulation: Arrhythmia and Electrophysiology* 1.2, pp. 110–119.

Otsuji, Y., Handschumacher, M. D., Liel-Cohen, N., Tanabe, H., Jiang, L., Schwammenthal, E., Guerrero, J., Nicholls, L. A., Vlahakes, G. J., and Levine, R. A. (2001). "Mechanism of ischemic mitral regurgitation with segmental left ventricular dysfunction: three-dimensional echocardiographic studies in models of acute and chronic progressive regurgitation". In: *Journal of the American College of Cardiology* 37.2, pp. 641–648.

Pagoulatos, N., Edwards, W., Haynor, D., and Kim, Y. (1999). "Interactive 3D registration of ultrasound and magnetic resonance images based on a magnetic position sensor". In: *IEEE Transactions on Information Technology in Biomedicine* 3.4, pp. 278–288.

Passera, K., Mainardi, L., McGrath, D., Naish, J., Buckley, D., Cheung, S., Watson, Y., Caunce, A., Buonaccorsi, G., Logue, J., et al. (2008). "A non-linear registration method for DCE-MRI and DCE-CT comparison in bladder tumors". In: *Biomedical Imaging: From Nano to Macro, 2008. ISBI 2008. 5th IEEE International Symposium on.* IEEE, pp. 1095–1098.

Perperidis, D., Mohiaddin, R., and Rueckert, D. (2005). "Spatio-temporal free-form registration of cardiac MR image sequences". In: *Medical Image Analysis* 9.5, pp. 441–456.

Peyrat, J.-M. and al., et (2010). "Registration of 4D Cardiac CT Sequences Under Trajectory Constraints With Multichannel Diffeomorphic Demons". In: *IEEE TMI* 29.7, pp. 1351–1368.

Pluim, J., Maintz, J., and Viergever, M. (2003). "Mutual-information-based registration of medical images: a survey". In: *Medical Imaging, IEEE Transactions on* 22.8, pp. 986–1004.

Porras, A. R., Piella, G., Cámara, O., Silva, E., Andreu, D., Berruezo, A., and Frangi, A. F. (2011). "Cardiac Deformation from Electro-Anatomical Mapping Data: Application to Scar Characterization". In: *Functional Imaging and Modeling of the Heart.* Ed. by D. N. Metaxas and L. Axel. Vol. 6666. Berlin, Heidelberg: Springer Berlin Heidelberg, pp. 47–54.

Powell, B. D. and Packer, D. L. (2009). "Does image integration improve atrial fibrillation ablation outcomes, or are other aspects of the ablation the key to success?" en. In: *Europace* 11.8, pp. 973–974.

Prakosa, A., Sermesant, M., Delingette, H., Marchesseau, S., Saloux, E., Allain, P., Villain, N., and Ayache, N. (2013). "Generation of synthetic but visually realistic time series of cardiac images combining a biophysical model and clinical images". eng. In: *IEEE transactions on medical imaging* 32.1, pp. 99–109.

Prieto, C. (2013). “The Problem of Motion in Cardiovascular MRI”. In: *Proc. Intl. Soc. Mag. Reson. Med. 21.*

Reddy, V. Y., Malchano, Z. J., Holmvang, G., Schmidt, E. J., d’Avila, A., Houghtaling, C., Chan, R. C., and Ruskin, J. N. (2004). “Integration of cardiac magnetic resonance imaging with three-dimensional electroanatomic mapping to guide left ventricular catheter manipulation: Feasibility in a porcine model of healed myocardial infarction”. In: *J Am Coll Cardiol* 44.11, pp. 2202–2213.

Rhode, K. and Sermesant, M. (2011). “Modeling and Registration for Electrophysiology Procedures Based on Three-Dimensional Imaging”. In: *Current Cardiovascular Imaging Reports* 4.2, pp. 116–126.

Rhode, K., Hill, D. L. G., Edwards, P., Hipwell, J., Rueckert, D., Sanchez-Ortiz, G., Hegde, S., Rahunathan, V., and Razavi, R. (2003). “Registration and tracking to integrate X-ray and MR images in an XMR Facility”. In: *IEEE Transactions on Medical Imaging* 22.11, pp. 1369–1378.

Rhode, K., Sermesant, M., Brogan, D., Hegde, S., Hipwell, J., Lambiase, P., Rosenthal, E., Bucknall, C., Qureshi, S., Gill, J., Razavi, R., and Hill, D. (2005). “A system for real-time XMR guided cardiovascular intervention”. In: *IEEE Transactions on Medical Imaging* 24.11, pp. 1428–1440.

Rouchdy, Y., Pousin, J., Schaerer, J., and Clarysse, P. (2007). “A nonlinear elastic deformable template for soft structure segmentation: application to the heart segmentation in MRI”. In: *Inverse Problems* 23.3, p. 1017.

Rubeaux, M., Nunes, J., Albera, L., and Garreau, M. (2010). “Edgeworth-based approximation of Mutual Information for medical image registration”. In: *2nd International Conference on Image Processing Theory Tools and Applications (IPTA).* Vol. 22. IEEE, pp. 195–200.

Rueckert, D. and Aljabar, P. (2010). “Nonrigid Registration of Medical Images: Theory, Methods, and Applications [Applications Corner]”. In: *Signal Processing Magazine, IEEE* 27.4, pp. 113–119.

Savi, A., Gilardi, M. C., Rizzo, G., Pepi, M., Landoni, C., Rossetti, C., Lucignani, G., Bartorelli, A., and Fazio, F. (1995). “Spatial registration of echocardiographic and positron emission tomographic heart studies”. eng. In: *European journal of nuclear medicine* 22.3, pp. 243–247.

Schaerer, J., Casta, C., Pousin, J., and Clarysse, P. (2010). “A dynamic elastic model for segmentation and tracking of the heart in MR image sequences”. In: *Medical Image Analysis* 14.6, pp. 738–749.

Schenk, A., Prause, G., and Peitgen, H.-o. (2000). “Efficient semiautomatic segmentation of 3d objects in medical images”. In: *In Proc. of Medical Image Computing and Computer-assisted Intervention (MICCAI.* Springer, pp. 186–195.

Schmitt, C., Deisenhofer, I., and Zrenner, B., eds. (2006). *Catheter Ablation of Cardiac Arrhythmias.* Darmstadt: Steinkopff-Verlag.

Schneider, U., Pedroni, E., and Lomax, A. (1996). “The calibration of CT Hounsfield units for radiotherapy treatment planning”. eng. In: *Physics in medicine and biology* 41.1, pp. 111–124.

Schreibmann, E., Thorndyke, B., Li, T., Wang, J., and Xing, L. (2008). “Four-dimensional image registration for image-guided radiotherapy”. In: *International Journal of Radiation Oncology* Biology* Physics* 71.2, pp. 578–586.

Slomka, P. J., Fieno, D., Ramesh, A., Goyal, V., Nishina, H., Thompson, L. E. J., Saouaf, R., Berman, D. S., and Germano, G. (2007). “Patient motion correction for multiplanar, multi-breath-hold cardiac cine MR imaging”. eng. In: *Journal of magnetic resonance imaging: JMRI* 25.5, pp. 965–973.

Soto-Iglesias, D., Butakoff, C., Andreu, D., Fernández-Armenta, J., Berruezo, A., and Camara, O. (2013). “Evaluation of Different Mapping Techniques for the Integration of Electro-Anatomical Voltage and Imaging Data of the Left Ventricle”. In: *Functional Imaging and Modeling of the Heart.* Ed. by S. Ourselin, D. Rueckert, and N. Smith. Vol. 7945. Lecture Notes in Computer Science. Heidelberg: Springer, pp. 391–399.

Sugeng, L., Mor-Avi, V., Weinert, L., Niel, J., Ebner, C., Steringer-Mascherbauer, R., Bartolles, R., Baumann, R., Schummers, G., Lang, R. M., and Nesser, H.-J. (2010). “Multimodality Comparison of Quantitative Volumetric Analysis of the Right Ventricle”. In: *JACC: Cardiovascular Imaging* 3.1, pp. 10–18.

Tops, L. F., Bax, J. J., Zeppenfeld, K., Jongbloed, M. R., Lamb, H. J., Wall, E. E. van der, and Schalij, M. J. (2005). “Fusion of multislice computed tomography imaging with three-dimensional electroanatomic mapping to guide radiofrequency catheter ablation procedures”. In: *Heart Rhythm* 2.10, pp. 1076–1081.

Tournoux, F., Chan, R. C., Manzke, R., Hanschumacher, M. D., Chen-Tournoux, A. A., Gérard, O., Solis-Martin, J., Heist, E. K., Allain, P., Reddy, V., Ruskin, J. N., Weyman, A. E., Picard, M. H., and Singh, J. P. (2010). “Integrating functional and anatomical information to guide cardiac resynchronization therapy”. eng. In: *European journal of heart failure* 12.1, pp. 52–57.

Trobaugh, J. W., Richard, W. D., Smith, K. R., and Bucholz, R. D. (1994). “Frameless stereotactic ultrasonography: Method and applications”. In: *Computerized Medical Imaging and Graphics* 18.4, pp. 235–246.

Vaillant, M. and Glaunès, J. (2005). “Surface Matching via Currents”. In: *Information Processing in Medical Imaging.* Ed. by G. E. Christensen and M. Sonka. Lecture Notes in Computer Science 3565. Springer Berlin Heidelberg, pp. 381–392.

Varray, F., Basset, O., Tortoli, P., and Cachard, C. (2013). “CREANUIS: A Non-linear Radiofrequency Ultrasound Image Simulator”. In: *Ultrasound in Medicine & Biology* 39.10, pp. 1915–1924.

Varray, F., Ramalli, A., Cachard, C., Tortoli, P., and Basset, O. (2011). “Fundamental and second-harmonic ultrasound field computation of inhomogeneous nonlinear medium with a generalized angular spectrum method". In: *Ultrasonics, Ferroelectrics and Frequency Control, IEEE Transactions on* 58.7, pp. 1366–1376.

VERCAUTEREN, T., PENNEC, X., PERCHANT, A., and AYACHE, N. (2009). "Diffeomorphic demons: Efficient non-parametric image registration". In: *NeuroImage* 45.1, Supplement 1. Mathematics in Brain Imaging, S61–S72.

VIOLA, P. and WELLS III, W. (1997). "Alignment by Maximization of Mutual Information". English. In: *International Journal of Computer Vision* 24.2, pp. 137–154.

WACHINGER, C. and NAVAB, N. (2012). "Entropy and Laplacian images: Structural representations for multi-modal registration". In: *Medical Image Analysis* 16.1, pp. 1–17.

WEESE, J., SMITH, N., RAZAVI, R., CHAPELLE D.AND DELINGETTE, H., FRANGI, A., HOSE, R., HUNTER, P., and SPAAN, J. (2013). *euHeart: Project Final Report.* project report. FP7-ICT-2007, IP Contract no: 224495.

WEI, D., SUN, Y., ONG, S.-H., CHAI, P., TEO, L., and LOW, A. (2013). "A Comprehensive 3-D Framework for Automatic Quantification of Late Gadolinium Enhanced Cardiac Magnetic Resonance Images". In: *Biomedical Engineering, IEEE Transactions on* 60.6, pp. 1499–1508.

WEIN, W., BRUNKE, S., KHAMENE, A., CALLSTROM, M. R., and NAVAB, N. (2008). "Automatic CT-ultrasound registration for diagnostic imaging and image-guided intervention". In: *Medical Image Analysis* 12.5, pp. 577–585.

WEIN, W., KHAMENE, A., CLEVERT, D.-A., KUTTER, O., and NAVAB, N. (2007). "Simulation and Fully Automatic Multimodal Registration of Medical Ultrasound". In: *Medical Image Computing and Computer-Assisted Intervention – MICCAI 2007*. Ed. by N. AYACHE, S. OURSELIN, and A. MAEDER. Lecture Notes in Computer Science 4791. Springer Berlin Heidelberg, pp. 136–143.

WEIN, W., RÖPER, B., and NAVAB, N. (2005). "Automatic registration and fusion of ultrasound with CT for radiotherapy". eng. In: *Medical image computing and computer-assisted intervention: MICCAI ... International Conference on Medical Image Computing and Computer-Assisted Intervention* 8.Pt 2, pp. 303–311.

WHITE, F. (1991). *Data Fusion Lexicon. Rapport 4202 NOSC.* Technical panel report. Data Fusion Subpanel of the Joint Directors of Laboratories.

WILSON, K., GUIRAUDON, G., JONES, D., and PETERS, T. (2009). "Mapping of Cardiac Electrophysiology Onto a Dynamic Patient-Specific Heart Model". In: *IEEE Transactions on Medical Imaging* 28.12, pp. 1870–1880.

WILSON, K., GUIRAUDON, G., JONES, D., and PETERS, T. (2006). "4D Shape Registration for Dynamic Electrophysiological Cardiac Mapping". In: *Medical Image Computing and Computer-Assisted Intervention – MICCAI 2006*. Vol. 4191. Lecture Notes in Computer Science. Springer Berlin / Heidelberg, pp. 520–527.

Yoo, T. S. (2004). *Insight Into Images: Principles and Practice for Segmentation, Registration, and Image Analysis*. Ak Peters Series. Taylor & Francis.

Zhang, Q., Eagleson, R., and Peters, T. (2006). “Real-time visualization of 4D cardiac MR images using graphics processing units”. In: *3rd IEEE International Symposium on Biomedical Imaging: Nano to Macro, 2006*, pp. 343–346.

CHAPTER 3

Registration of multisensor cardiac images

In this chapter, we address the registration of cardiac MRI, CT and US. The registration of these multisensor cardiac images is a challenging process. This process is mandatory because the considered data are not described in a common spatial and temporal coordinate system. This registration is required to fuse multisensor image information. The fusion of multisensor cardiac information enables to compute local/global markers of interest to characterize HCM and cardiac asynchronism. The registration methods proposed here exploit the common information (mainly the anatomy) that available acquisitions contain.

Multisensor images to be fused in this work correspond to acquisitions of a given HCM or CRT patient. Therefore, the registration process is *intra-patient*. In addition, there is no suspected cardiac remodeling between acquisitions except between those acquired before CRT and during CRT follow-up. In consequence, the anatomy imaged at a given cardiac phase (e.g. end-diastole) does not change; thus, the *spatial registration is mostly rigid*. Concerning the temporal alignment, the heart rate can change during a given image acquisition (e.g. during cardiac MRI) and also between acquisitions (e.g. between CT and US). Thus, the underlying alignment of corresponding cardiac phases is nonlinear: a *nonlinear temporal registration method* is required.

This chapter discusses the methods developed here in order to register available cardiac images. It is organized with regards to the modalities to be registered. First, methods for *intra-sequence and inter-sequence* cardiac MRI registration are presented (cf. 3.1). They aim at (i) eliminating the slice misalignment caused by patient respiration and (ii) registering LGE and cine sequences. Then, a *cine-MRI and CT registration* method is proposed (cf. 3.2). This method is followed by a *multiview 2D+t US registration approach* used to associate strain curves (mechanical function) resulting from speckle tracking echocardiography, with 3D images (CT or MRI) (cf. 3.3). The chapter ends with the conclusions.

3.1 Image registration of Cine- and LGE-MRI

The registration of cine and LGE images aims to fuse the data they contain. Despite the fact that these images are acquired during the same MRI examination, they are commonly misaligned due to patient and/or respiratory motion. We present in this section the methods aiming at (i) correcting for slice misalignment in cine- and LGE-MRI volumes and (ii) aligning them in time and space. On the one hand, slice misalignment correction is performed with a profile-based registration approach of multiview MRI images. On the other hand, LGE to cine spatial alignment is computed with an inter-sequence rigid registration approach. Finally, different approaches may be used to interconnect these two processes in a complete workflow.

Below we detail the profile-based registration, the inter-sequence rigid registration and we propose different strategies to combine them.

3.1.1 Slice misalignment correction using profile-based registration

Multiview cardiac MRI registration aims at correcting for slice misalignment MRI. Figure 3.1(left) shows multiview cine-MRI volumes at peak-R. Voxel intensities of image profiles resulting from the intersection of different MRI views (white lines in Figure 3.1), are commonly used to guide this correction.

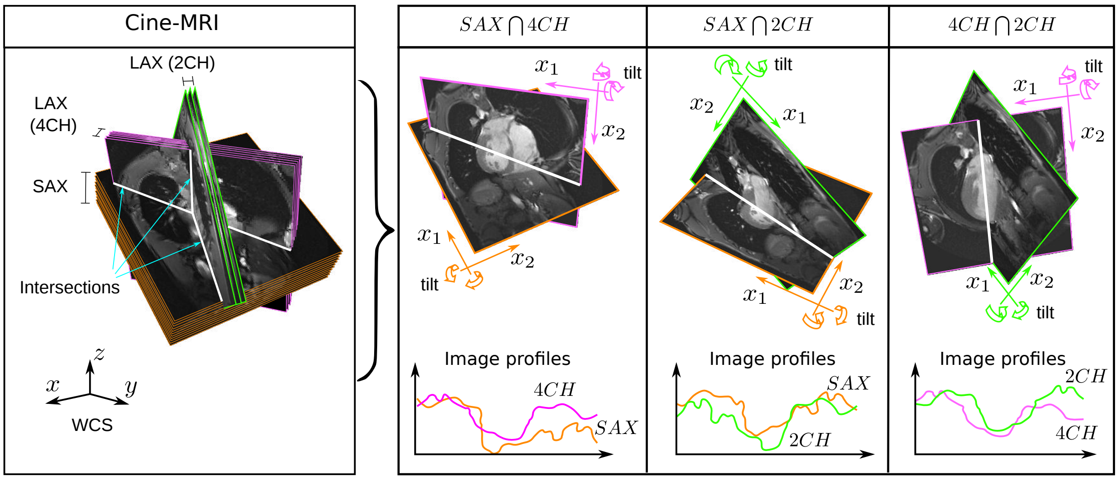

Figure 3.1: Multiview multiplanar cardiac MRI. (Left) Cine-MRI volumes at peak-R and visible intersections (white lines). (Right) Instances of the three possible plane intersections, their corresponding intersection domain (white line), obtained intersection profiles (color curves) and used transform (in-plane translation and tilt). Each plane has a unique set of transform parameters even if it intersects with different planes. ACRONYMS – WCS: world coordinate system.

Let I be a multiview cardiac MRI to be corrected made up of the union of the SAX, 4CH and 2CH acquisitions. Each view is a multiplanar image volume obtained by stacking multiple slices. A *slice* is an image containing a slab of anatomy effectively acquired, located at a given plane in 3D space. Figure 3.1(left) illustrates the slices of a multiview cine acquisition at peak-R. Let N be the number of slices in I (considering all the views). The intensity of the n-th slice of I at a voxel x and cardiac phase τ, is given by:

$$I^n(x,\tau) \mid n \in \{0,\ldots,N-1\}, \;\; x \in \Omega^n, \; \tau \in \{0,\ldots,\top-1\}, \tag{3.1}$$

where x is a voxel belonging to the voxel domain $\Omega^n \subset \mathbb{R}^3$ (the voxel domain of I^n corresponding to a plane in 3D space), and $\top$ is the number of imaged cardiac phases. Image registration has been used in state-of-the-art methods aiming to correct for slice misalignment in intra-sequence MRI (cf. 2.3.2.2). In this approach, a transformation T_{μ^n} is calculated for each slice I^n such that a similarity measure, computed from voxels intensities in the intersection domains, is optimized (μ^n is the vector of transform parameters). The transform parameters for the planes in I to be corrected are joined in a unique array. If all slices are corrected in a single procedure, this array is given by:

$$\boldsymbol{\mu} = \left(\mu^0,\ldots,\mu^n,\ldots,\mu^{N-1}\right), \tag{3.2}$$

$\boldsymbol{\mu}$ is included in an optimization procedure that minimizes a similarity measure between the slices in I; therefore, all planes are corrected in a single procedure. The profiles obtained from the intersection domains are used to compute the similarity measure.

As illustrated in Figure 3.1(right) two slices belonging to different views intersect in a common spatial domain. This domain corresponds to a line from which two profiles are obtained. These profiles contain the intensities of the two slices along their intersection line. The profile pairs resulting from the intersections between slices are joined together into a unique pair. The optimization of the metric between these joint profiles over $\boldsymbol{\mu}$ is what is called *profile-based registration.* This profile-based registration is illustrated in Figure 3.2. We detail below its components.

3.1.1.1 Transform

Recent methods have evaluated the use of 3D rigid transforms for each slice; however, their implementation need the use of spatial constraints (region of interest around the heart) and the incidence of the rotation component seems to be secondary (Elen et al., 2010). Then, a transformation consisting of an in-plane translation and tilt is used to correct each slice. An anisotropic in-plane scale transform was selected to mimic the tilt component (Slomka et al., 2007). Therefore, $\mu^n = (t,s)$ with $t = (x_1,x_2)$ an in-plane translation and $s = (s_0,s_1)$ an scaling along plane axes. In-plane translation and tilt transformations are illustrated in Figure 3.1 (right). The transformation vector

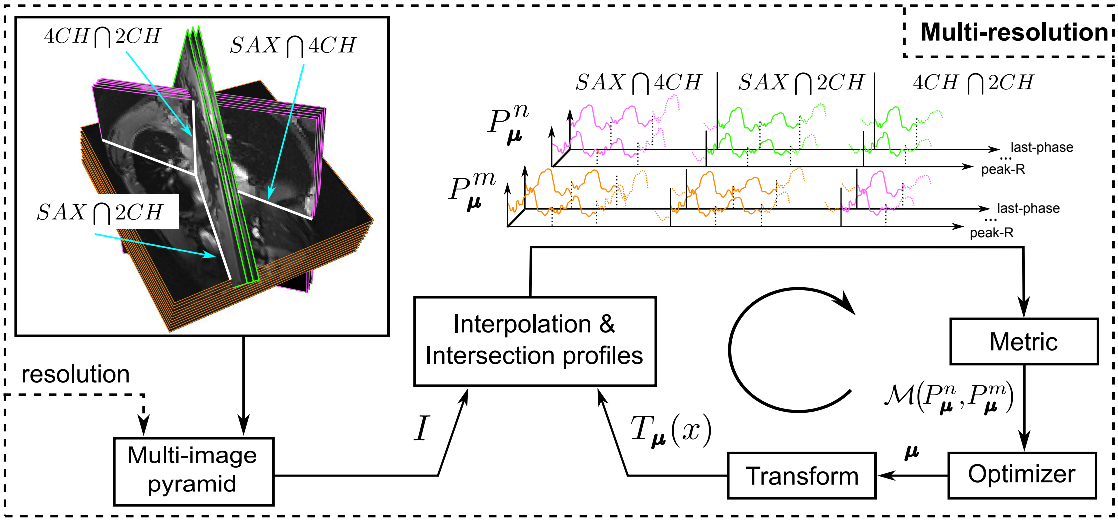

Figure 3.2: Multiresolution intra-sequence profile-based registration: MRI slices are transformed until the metric (similarity measure) between intersection profiles ($P^n_{\boldsymbol{\mu}}$, $P^m_{\boldsymbol{\mu}}$) is optimized. The use of multiple resolutions permits to avoid local optima.

containing the transform for all slices is:

$$T_{\boldsymbol{\mu}} = \left(T_{\mu^0}, \ldots, T_{\mu^n}, \ldots, T_{\mu^{N-1}}\right), \tag{3.3}$$

We note the transformation of I as $T_{\boldsymbol{\mu}}(I)$, such that the transformed n-th slice at phase τ is $T_{\mu^n}\left(I^n(x,\tau)\right)$.

3.1.1.2 Interpolation and intersection profiles

The profiles intensity between two slices belonging to two different views $I^n, I^m \in I \subset \mathbb{R}^3$, and at a cardiac phase τ, are defined as:

$$P^n_{n\cap m}(x,\tau;T_{\mu^n}) = I^n\left(T^{-1}_{\mu^n}(x), \tau\right) \mid x \in \Omega^{n\cap m}, \tag{3.4}$$

$$P^m_{n\cap m}(x,\tau;T_{\mu^m}) = I^m\left(T^{-1}_{\mu^m}(x), \tau\right) \mid x \in \Omega^{n\cap m}, \tag{3.5}$$

where x belongs to the intersection domain between slices n and m ($\Omega^{n\cap m}$). The mapping of a point in the intersection line to the slices intersecting at this line, using the slice transformations, is illustrated in Figure 3.3a: a point x in the intersection domain corresponds to two positions, one in the domain of I^n (using $T^{-1}_{\mu^n}$) and another in the domain of I^m (using $T^{-1}_{\mu^m}$). Note that, because a transform consisting of an in-plane translation and scaling is used for each slice, the intersection domain does not change. During the optimization procedure the value $I^n\left(T^{-1}_{\mu^n}(x), \tau\right)$ is evaluated at non-voxel positions, then, intensity interpolation is required. A linear interpolation is used: the returned value is a weighted average of the surrounding voxels with the distance to each voxel taken as weight.

The intersection domain can be obtained using the slice to world transformation contained into DICOM images[1] defining the pose of each slice in the *world coordinate system* (*WCS*). Voxel intensities in this domain are stacked following the intersection line to obtain the image profiles, as those in Figure 3.1 (right). Besides, given that the slice thickness of I^m is often greater than the in-plane resolution of I^n, the intersection domain is not a line but a belt when seen from I^n (Figure 3.3b). In this case, the intensity of $P^n_{n \cap m}$ in x corresponds to the average of voxels intensities in I^n along the perpendicular direction of the belt. This is illustrated in Figure 3.3b: the pixels in I^n intersecting with x (white solid rectangle) are averaged.

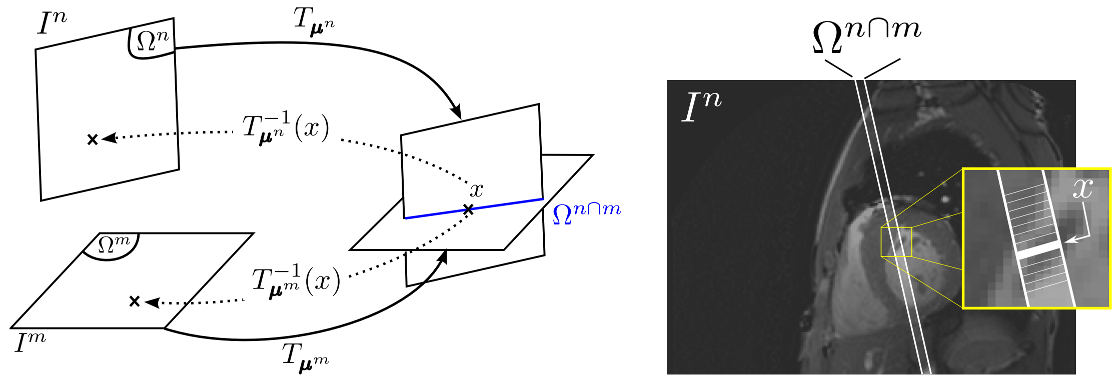

(a) Relationship between intersecting slices (I^n, I^m), intersection line (in blue) and slice transforms (T).

(b) Slice thickness leading to a intersection belt instead of a line.

Figure 3.3: Illustration of the intersection domain between two slices in cardiac MRI. (a) Relationship between a point x in the intersection domain $\Omega^{n \cap m}$ and the domain of intersecting slices: x corresponds to two positions in the spatial domain of input slices (Ω^n, Ω^m), given by the inverse of the slice transforms ($T^{-1}_{\mu^n}$, $T^{-1}_{\mu^m}$). (b) Effect of the slice thickness in the common spatial domain $\Omega^{n \cap m}$ as observed from I^n. Note that, because of the slice thickness, the shape of $x \in \Omega^{n \cap m}$ is a rectangle while a pixel in I^n is a square.

Finally, all dynamic profiles are stacked, first along $\Omega^{n \cap m}$ (space) and then along τ (time), into two unique profiles $P^n_{\boldsymbol{\mu}}$ and $P^m_{\boldsymbol{\mu}}$, as shown in Figure 3.2. To illustrate this stacking, lets consider one 2CH image and one 4CH image made up of 2 and 3 slices, respectively, both with a temporal resolution of three cardiac phases. Then, the number of intersection domains between all slices is six: each slice in 2CH will intersect with each slice in 4CH, resulting in six intersections. From each intersection, two dynamic profiles will be obtained. For instance, from the intersection of the first dynamic slice in 2CH and the first dynamic slice in 4CH, two dynamic profiles with three cardiac phases will result, one per view. If all intersections are considered, then 6 pairs of dynamic profiles, each with three phases, will result. Then, in order to compute the similarity between all intersecting slices, these six pairs of dynamic profiles are stacked into a unique dynamic pair.

---

[1] DICOM tags (0020,0032) and (0020,0037) corresponding to Image Position and Image Orientation, respectively

3.1.1.3 Similarity measures between image profiles

Three different similarity measures are used in order to correct slice misalignment in cardiac MRI using multiview registration (cf. 2.3.2.2):

Normalized correlation. Correlation metrics were used by (CARMINATI et al., 2012) (ELEN et al., 2010) (SLOMKA et al., 2007) to register multiview cine-MRI. The normalized correlation is defined as:

$$\mathcal{NC}(P^n_{\boldsymbol{\mu}}, P^m_{\boldsymbol{\mu}}) = -\frac{\sum\limits_{k=0}^{K-1} P^n_{\boldsymbol{\mu}}(k) \cdot P^m_{\boldsymbol{\mu}}(k)}{\sqrt{\sum\limits_{k=0}^{K-1} P^n_{\boldsymbol{\mu}}(k)^2 \cdot \sum\limits_{k=0}^{K-1} P^m_{\boldsymbol{\mu}}(k)^2}}, \tag{3.6}$$

where $P^n_{\boldsymbol{\mu}}(k)$ and $P^m_{\boldsymbol{\mu}}(k)$ are the k-th element of $P^n_{\boldsymbol{\mu}}$ and $P^n_{\boldsymbol{\mu}}$, respectively, and K is their number of elements.

Normalized mutual information. Mutual information metrics were used by (ELEN et al., 2010) (LÖTJÖNEN et al., 2005) (LÖTJÖNEN et al., 2004) to register multiview cine images. The normalized mutual information is given by:

$$\mathcal{NMI}(P^n_{\boldsymbol{\mu}}, P^m_{\boldsymbol{\mu}}) = -\frac{H\left(P^n_{\boldsymbol{\mu}}\right) + H\left(P^m_{\boldsymbol{\mu}}\right)}{H\left(P^n_{\boldsymbol{\mu}}, P^n_{\boldsymbol{\mu}}\right)}, \tag{3.7}$$

were $H(\cdot)$ and $H(\cdot, \cdot)$ denote the entropy and joint entropy, respectively (cf. Equations (2.5) and (2.6)).

Mean squares of structural images. Profile-based registration has been used to correct the slice misalignment of multiview cine-MRI volume sequences, but it can also be used to correct the slice misalignment in LGE images with regards to cine MRI images. However, cine and LGE images correspond to different MRI sequences and, therefore, image intensities varies for those tissues/organs represented in both acquisitions. Moreover, the alteration of myocardial tissue due to fibrosis/scar cannot be imaged with cine-MRI. An approach to handle this is to integrate similarity metrics that are robust to these variations, assuming a functional or statistical intensity relationship (WACHINGER et al., 2012). This is why correlation and mutual information metrics, as the ones described above, have been used. The registration of these images can be, however, affected by more substantial variations like the fact that gadolinium concentration changes between multiview LGE images, and because of field inhomogeneities during MRI acquisition. In this context, the so-called image *structural representation* introduced by (WACHINGER et al., 2012) seems to be advantageous. This representation, obtained by calculating a dense set of descriptors that capture the structural information of local patches in the image, depends only on the depicted structures and not on the intensities used to encode them.

In this work we evaluate the convenience of using the structural representation in MRI slice misalignment correction and in inter-sequence MRI registration (cf. 4.3) which has not been reported yet in literature. The structural representation have the potential of highlighting those structures best guiding the registration. They are also advantageous because (i) L1 and L2 metrics (e.g. mean squares) can be used to perform the optimization and (ii) metric properties such as capture range are improved. In consequence, we use the entropy-image representation and measure the mean squares between them. This approach was used previously by (Cordero-Grande et al., 2012) in the context of LGE-SAX to cine-SAX registration. The local entropy of an image I at voxel x is given by:

$$H(I(x)) = -\frac{1}{|\mathcal{N}|} \sum_{x^{\mathcal{N}} \in \mathcal{N}(x)} p(I(x^{\mathcal{N}}) \log \left(I(x^{\mathcal{N}}) \right) \cdot w(x^{\mathcal{N}}) \tag{3.8}$$

where $\mathcal{N}(x)$ is a neighborhood centered at pixel (voxel) x, $x^{\mathcal{N}}$ is a pixel in this neighborhood and $w(x^{\mathcal{N}})$ a weighting factor. Two image patches (i.e. a piece of I of the same size as $\mathcal{N}$) depicting different structures can lead to the same value of entropy because they can have the same intensity histogram. Thus, the contribution of each pixel in Equation (3.8) is weighted with an asymmetric Gaussian kernel. This kernel is an alteration of the Gaussian kernel such that a unique weight at each patch location is provided, forcing the kernel to be asymmetric. This asymmetric kernel will then avoid to have the same value of entropy from two patches describing different structures but with the same histogram, as illustrated in Figure 3.4. The entropy image representation of cine and LGE is then used to register them using the mean squares metric. The selection of this metric is justified because these two entropy representations can be considered as monomodal images. The mean squares metric is given by:

$$\mathcal{MS}(P^n_{\boldsymbol{\mu}}, P^m_{\boldsymbol{\mu}}) = \frac{1}{K} \sum_{k=0}^{K-1} \left(P^n_{\boldsymbol{\mu}}(k) - P^m_{\boldsymbol{\mu}}(k) \right)^2, \tag{3.9}$$

where $P^n_{\boldsymbol{\mu}}(k)$ and $P^m_{\boldsymbol{\mu}}(k)$ are computed from the structural representation of cine and LGE images, respectively.

The metrics defined above can be then included into the profile-based registration procedure in Figure 3.2.

3.1.1.4 Optimization of slice transform parameters

The optimal parameters of the slice transformations correcting for slice misalignment in I are computed as follows:

$$\tilde{\boldsymbol{\mu}} = \arg\min_{\boldsymbol{\mu}} \ \mathcal{M} \left(P^n_{\boldsymbol{\mu}}, P^m_{\boldsymbol{\mu}} \right), \tag{3.10}$$

where $\mathcal{M}$ is one of the similarity metrics defined in Equations (3.6), (3.7) and (3.9). The simplex downhill algorithm was selected to optimize Equation (3.10) (cf. 2.2.3.5) because

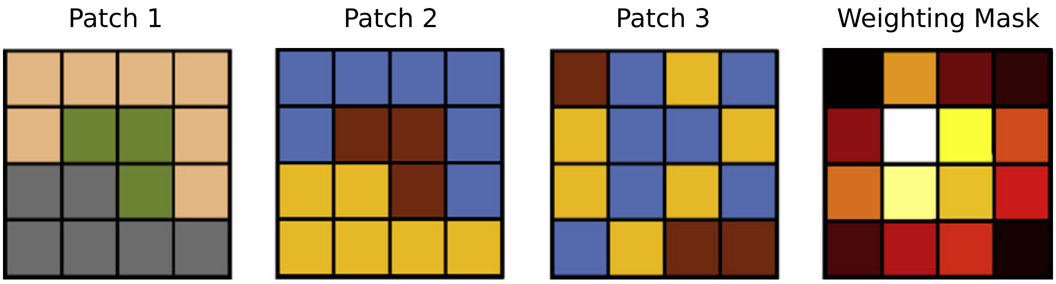

Figure 3.4: Use of a modified Gaussian kernel to discriminate between three image patches with equal histogram. Patches 1 and 2 show the same structure but encoded with different intensities. All three patches have the same entropy value if a symmetric weighting mask is used. Integrating the modified Gaussian mask shown at right enables to differentiate patch 3 from the others. From (WACHINGER et al., 2012).

it has been used in the literature for this purpose (SLOMKA et al., 2007) and does not require the computation of metric derivatives.

A sequential approach, initially proposed by (SLOMKA et al., 2007), was used in this work. This method considered that the 2CH and 4CH acquisitions have each one slice only. We generalize here this method in order to correct for multiview MRI images, each view containing multiple slices. Our generalization is made up of three steps, each step of this approach correcting for slice misalignment in a given view, as illustrated in Figure 3.5.

3.1.2 Inter-sequence rigid registration

Inter-sequence rigid registration aims at aligning the static LGE image with the closest phase of the cine-MRI. It follows the classic registration framework illustrated in Figure 2.2. Given $\mu^R = (t, \theta)$ the parameters of a 3D rigid transformation (cf. 2.2.1), the optimal parameters aligning the cine image (I^{cine}) and the LGE image (I^{LGE}), are given by:

$$\tilde{\mu}^R = \underset{\mu^R}{\arg\min} \sum_{\forall v} \mathcal{M}(T_{\mu^R}; I^{\text{cine},v}(\tau^{\text{LGE}}), I^{\text{LGE},v}) \tag{3.11}$$

with τ^{LGE} the cardiac phase aligning cine- and LGE sequences over time, $v \in \{\text{SAX, 4CH, 2CH}\}$ a given view and $\mathcal{M}$ either an information based similarity metric (Equations (2.4) to (2.7)), or the mean squares of the structural images between two image volumes (defined as in Equation (3.9) but using volumetric images instead of image profiles). The selection of the best metric is described in 4.3. To our knowledge, such evaluation as not been reported in literature. τ^{LGE} was computed using the TriggerTime (0018,1060) and average heart rate (0018,1088) DICOM tags extracted from both acquisitions, as follows:

$$\tau^{\text{LGE}} = \underset{\tau^{\text{cine}}}{\arg\min} \left| \text{TT}^{\text{cine}}(\tau^{\text{cine}}) - \text{TT}^{\text{LGE}} \cdot \frac{\text{HR}^{\text{cine}}}{\text{HR}^{\text{LGE}}} \right|, \tag{3.12}$$

with TT the trigger time and HR the heart rate.

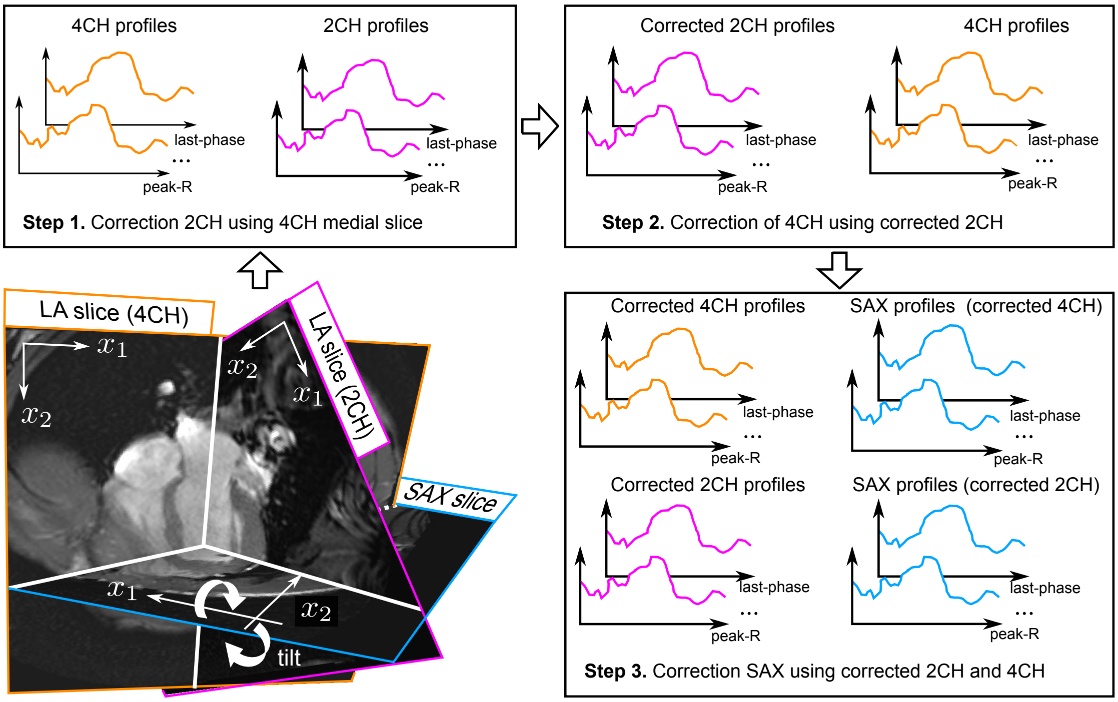

Figure 3.5: Sequential procedure for slice misalignment correction in multiview cardiac MRI (Slomka et al., 2007). (Bottom-left) Multiview slices from cine-MRI at peak-R (blue: SAX slice, magenta: one 2CH slice, orange: one 4CH slice). White solid lines correspond to the intersection between slices. (Top-left, right) Steps of the sequential procedure: step 1, correction of 2CH using the medial slice of 4CH as fixed image; step 2, correction of 4CH using the corrected 2CH as fixed image; step 3, correction of SAX using correct 2CH and 4CH as fixed images.

3.1.3 Registration of LGE- and cine-MRI images: Combining slice misalignment and rigid registration

Profile-based registration and rigid registration procedures described above are used together to register LGE- and cine-MRI.

Slice misalignment correction and rigid registration procedures were interconnected in three different ways (cf. Figure 3.6), leading to three LGE- to cine-MRI registration methods to be studied. They register multiplanar/multiview/multisequence cardiac MRI acquisitions. Let I^{cine} and I^{LGE} be the cine and LGE sequences of the MRI acquisition, respectively. We assume here that the temporal alignment between I^{cine} and I^{LGE} is known and that the registration is performed between the static LGE-MRI and the closest phase of the cine-MRI. Therefore, both images are made of up of static multiview (SAX, 2CH and 4CH) images. Besides, the rigid registration procedure sets the *cine image* as the *fixed image*:

— The simplest method, depicted in Figure 3.6a, corrects for slice misalignment in cine-MRI to then register LGE-MRI to the corrected cine-MRI using a rigid registration process. This approach can be used when no slice misalignment is

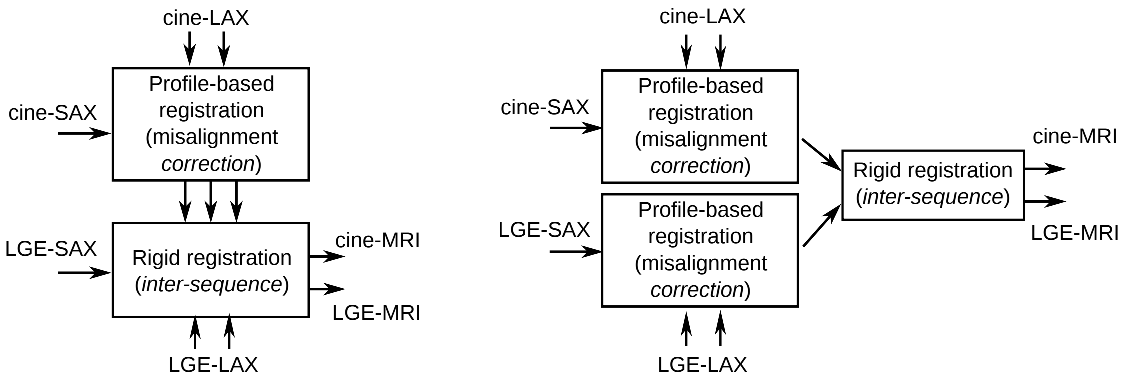

(a) Cine correction and LGE rigid registration.

(b) Cine and LGE correction, rigid registration.

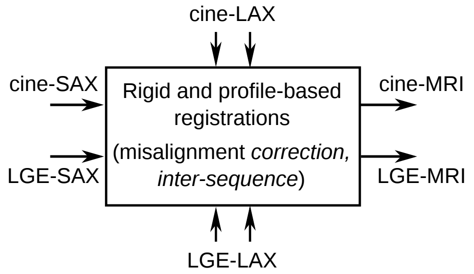

(c) Combined registration.

Figure 3.6: Registration-based methods correcting for slice misalignment and aligning multiview cine-MRI and multiview LGE-MRI. (a) Cine slice misalignment correction followed by a rigid registration with LGE-MRI. (b) Cine and LGE correction, rigid registration: slice misalignment are corrected for each sequence and then output images are registered. (c) Combined approach: both intra-sequence slice misalignment correction and inter-sequence registration are performed in a unique combined procedure. Acronyms – LAX: long axis view, SAX: short axis view.

present in LGE-MRI which is often the case. Indeed, LGE-MRI is a static image acquired at mid-diastole; thus, it is less prone to slice misalignment than cine-MRI.

— The second approach (cf. Figure 3.6b), corrects for slice misalignment in both, cine- and LGE-MRI, and then registers them. This approach enables to correct slice misalignment in the LGE acquisition.

— The third method aims at correcting for slice misalignment and registering cine- and LGE-MRI in a single process (cf. Figure 3.6c). However, this approach has shown to be much more computationally expensive. Thus, it has no more been used in the following of this work.

We presented above the procedures used to register cine- and LGE-MRI acquisitions of a given patient (intra-patient). These methods exploit the common information contained in the intersection of multiview MRI. The evaluation of these methods is presented in 4.3. The use of registered MRI in HCM and cardiac asynchronism characterization is presented in Chapters 5 and 6, respectively. We now present the proposed method developed to register dynamic CT and cine-MRI of the heart.

3.2 Spatio-temporal registration of dynamic CT and cine-MRI

Dynamic-CT and cine-MRI are dynamic acquisitions of the heart and, in our case, they focus on the LV. These modalities have to be registered in order to get a common LV referential. Cardiac MRI and CT acquisitions are triggered using the peak of R-wave (peak-R) detected in ECG. In the absence of cardiac remodeling, a rigid transformation enables to align these intra-patient acquisitions in space. Concerning the temporal registration, the cardiac frequency of the patient may change from one acquisition to the other. It is well known that there is a nonlinear relationship between the RR-interval and other ECG intervals (e.g. QT-interval) (HELDT et al., 2002) (BAZETT, 1920). In fact, if RR-intervals differ then the relationship between corresponding dynamics in ECGs is nonlinear. As a consequence, the intra-patient temporal alignment (i.e. the alignment of corresponding cardiac phases) should be performed nonlinearly.

A first challenge is therefore the nonlinear temporal alignment. Despite the fact that ECGs recorded during image acquisition could be exploited to match corresponding cardiac phases (HUANG et al., 2009), they are commonly not available. We propose to use correlation curves instead (PERPERIDIS et al., 2005). To our knowledge, the use of this curves in dynamic CT images has not been reported before. A novel adaptive dynamic time warping (ADTW) procedure is used to align dynamic CT and cine-MRI over time. The second challenge is the selection of an appropriate similarity measure between these multisensor images allowing to register them in space. We use a multi-image registration to exploit the information in these dynamic images, and a mutual-information-based metric.

The proposed ADTW-based method is illustrated in Figure 3.7. It has two main steps: (i) temporal alignment (ADTW) and (ii) multi-image spatial registration.

3.2.1 Temporal alignment: Adaptive Dynamic Time Warping of normalized cross-correlation curves

The DTW procedure measures the similarity between two sequences varying in time, and provides a nonlinear approach to align them over time (ITAKURA, 1975). ECG-gated acquisitions of dynamic CT and cine-MRI provides two sequences of image volumes evenly distributed along the RR-interval. This interval is routinely constrained into a confidence range during acquisition; however, it can differ between cine-MRI and CT. In

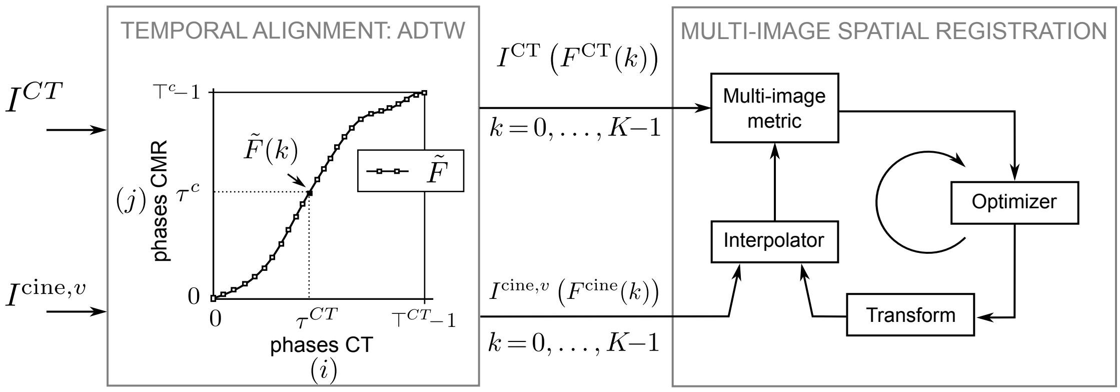

Figure 3.7: ADTW-based registration of dynamic CT (I^{CT}) and cine-MRI (I^{cine}).

this context, the DTW procedure enables both, to match corresponding cardiac phases and to deal with the underlying nonlinear relationship between cardiac dynamics. It is applied to normalized correlation curves computed from input images.

3.2.1.1 Normalized cross-correlation curves

Two normalized correlation curves (one per dynamic image) are computed. Let $I^{\text{SAX}}(\tau^{\text{SAX}})$ be the cine-SAX image at cardiac phase τ^{SAX} such that both, $\tau^{\text{SAX}} = 0$ and $\tau^{\text{SAX}} = \top^{\text{SAX}}$, correspond to the peak-R phase. $\top^{\text{SAX}}$ is the number of cardiac phases. Similarly, let $I^{\text{CT}}(\tau^{\text{CT}})$ be a dynamic CT image such that both, $\tau^{\text{CT}} = 0$ and $\tau^{\text{CT}} = \top^{\text{CT}}$, correspond to the peak-R as well. The normalized correlation curve of CT images depicts the variation in time of the normalized cross-correlation of I^{CT} and is given by:

$$NC^{\text{CT}} = \left(NC^{\text{CT}}(0), \ldots, NC^{\text{CT}}(\top^{\text{CT}} - 1), NC^{\text{CT}}(0)\right), \quad \text{with,} \tag{3.13}$$

$$NC^{\text{CT}}(i) = \mathcal{NC}\left(I^{\text{CT}}(0), I^{\text{CT}}(i)\right), \tag{3.14}$$

with $\mathcal{NC}$ the normalized cross-correlation between two image volumes. Note that the first and last elements of the curve are the equal to one. This reflects the fact that the cardiac cycle is periodic. Let $\hat{NC}^{\text{CT}}$ be the normalized NC^{CT} such that:

$$\hat{NC}(i) = \frac{NC(i) - \min(NC^{\text{CT}})}{\max(NC^{\text{CT}}) - \min(NC^{\text{CT}})}, \tag{3.15}$$

$\hat{NC}^{\text{SAX}}$ can be computed from Equations (3.13) to (3.15) using I^{SAX} and $\top^{\text{SAX}}$. These normalized correlation curves are then entered to the ADTW procedure.

3.2.1.2 Adaptive DTW of normalized correlation curves from dynamic CT and cine-SAX

The temporal alignment of $\hat{NC}^{\text{CT}}$ and $\hat{NC}^{\text{SAX}}$ using ADTW is illustrated in Figure 3.8. DTW computes the optimal time warping curve ($\tilde{F}$) of input sequences. This optimal curve warps the cardiac phases of CT and cine-SAX images such that an objective function

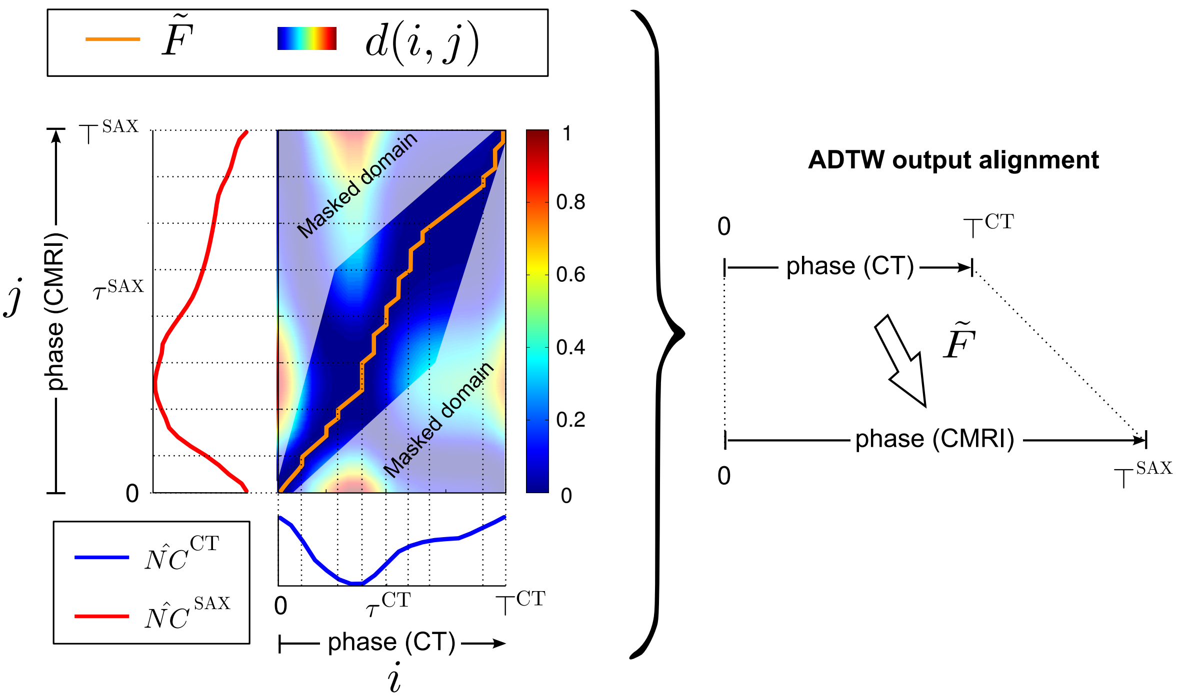

Figure 3.8: Adaptive dynamic time warping of CT $\widehat{NC}^{\mathrm{CT}}$ and $\widehat{NC}^{\mathrm{cine}}$ (masked domain appears shadowed). ADTW outputs the optimal time warping curve ($\tilde{F}$) between I^{CT} and I^{cine} (solid line in orange) aligning their cardiac phases (right).

is minimized. Let d be the so called *cross-distance* matrix between vectors $\widehat{NC}^{\mathrm{CT}}$ and $\widehat{NC}^{\mathrm{SAX}}$ (Giorgino, 2009). d is of size $\top^{\mathrm{CT}} \times \top^{\mathrm{SAX}}$ and provides the distance of matching a couple of time indexes:

$$d(i,j) = \left\| \widehat{NC}^{\mathrm{CT}}(i) - \widehat{NC}^{\mathrm{SAX}}(j) \right\| \tag{3.16}$$

d is the only input to the DTW algorithm. Note that it enables to enter the elements of $\widehat{NC}^{\mathrm{CT}}$ and $\widehat{NC}^{\mathrm{SAX}}$ into the DTW computation by using the time indexes i and j. At the core of the DTW technique lies the time warping curve F with its k-th entry given by:

$$F(k) = \left(F^{\mathrm{CT}}(k), F^{\mathrm{SAX}}(k)\right), \tag{3.17}$$

with $F^{\mathrm{CT}}(k) \in \{0,\ldots,i,\ldots,\top^{\mathrm{CT}}\}$ and $F^{\mathrm{SAX}}(k) \in \{0,\ldots,j,\ldots,\top^{\mathrm{SAX}}\}$. The following conditions must be satisfied by F:

Monotonic condition. Because the time warping curve aligns cardiac phases, they must be matched monotonically, i.e. the next cardiac phase to be matched must either be the present phase or one in the future. This is stated as follows: $F^{\mathrm{CT}}(k) \geq F^{\mathrm{CT}}(k-1)$ and $F^{\mathrm{SAX}}(k) \geq F^{\mathrm{SAX}}(k-1)$,

Continuity condition. This condition implies that arbitrary time compressions and expansions are allowed and that all phases must be matched (Giorgino, 2009). This is stated as: $|F^{\mathrm{CT}}(k) - F^{\mathrm{CT}}(k-1)| \leq 1$ and $|F^{\mathrm{SAX}}(k) - F^{\mathrm{SAX}}(k-1)| \leq 1$,

Boundary condition. This condition forces the first phases and last phases to match each other. In the case of normalized correlation curves, it implies to match the peak-R phases of input images. This is stated as: $F(0) = (0, 0)$ and $F(K-1) = (\top^{\mathrm{CT}}, \top^{\mathrm{SAX}})$

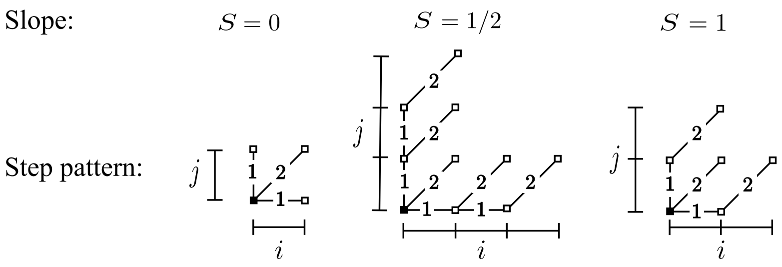

(a) Slope constraints and step patterns

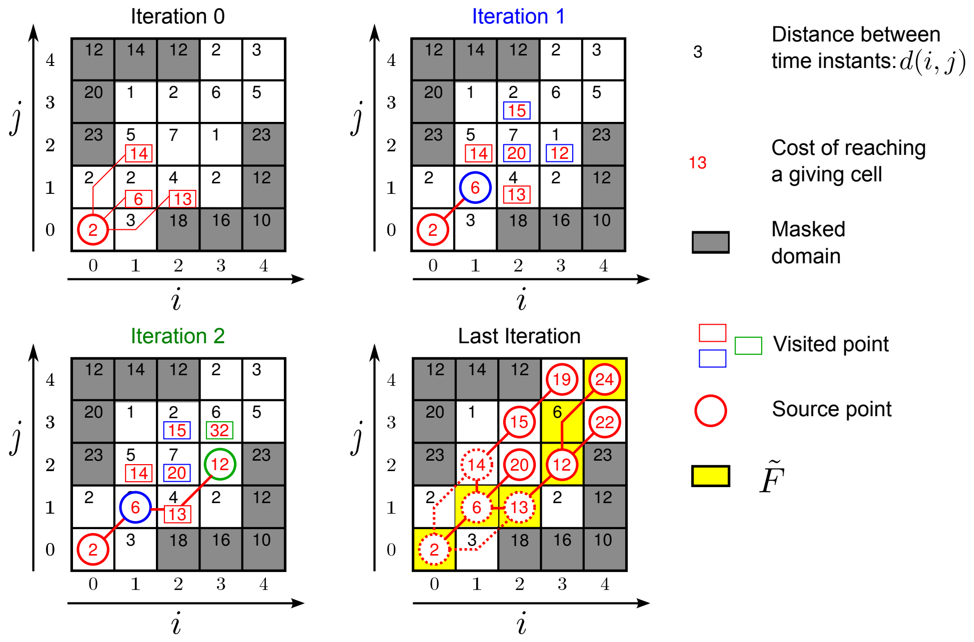

$\tilde{F} = \{(0,0)(1,1)(2,1)(3,2)(3,3)(4,4)\}$

(b) Iterations of the constrained dynamic programming using $S = 1$

Figure 3.9: Constrained dynamic programming used in the ADTW procedure to compute $\tilde{F}$. (a) Three instances of slope constraints (S) and corresponding step patterns. (b) Illustration of the dynamic programming algorithm for $S = 1$: at iteration 0, the point (0,0) is added to the list of source points (color circles), and its accumulated cost is calculated. Then, its neighbor points are added to the list of visited points (color rectangles). At iteration 1, the visited point with lowest cost is added as a source (blue circle). The procedure then iterates until the extrema points are linked.

The idea underlying ADTW is to find the optimal alignment $\tilde{F}$:

$$\tilde{F} = \arg\min_{F} \sum_{k=0}^{K-1} d\left(F^{\mathrm{CT}}(k), F^{\mathrm{SAX}}(k)\right) \cdot w(k), \tag{3.18}$$

where $w(k)$ is a nonnegative weight defined using an adaptive slope constraint (explained below, cf. Equation (3.19)). The equation (3.18) is solved using dynamic programming. This procedure starts from the point (0,0) and iteratively searches for potential time warping curves minimizing their dissimilarity until the shortest-curve linking the two extrema points is found. Two constraints are added to this algorithm: (i) the slope constraint S and (ii) the search domain constraint. The slope constraint is adapted according to the temporal resolution ratio of input images (r), leading to the used *Adaptive DTW (ADTW)*, as follows:

$$S = \begin{cases} 0, & \text{if } r = 1 \\ \frac{1}{2\cdot(r-1)} & \text{if } r > 1 \end{cases}, \quad \text{with} \quad r = \left\lceil \frac{\max(\top^{\mathrm{CT}}, \top^{\mathrm{SAX}})}{\min(\top^{\mathrm{CT}}, \top^{\mathrm{SAX}})} \right\rceil \tag{3.19}$$

Figure 3.9a illustrates three slope constraints using the symmetric form (SAKOE et al., 1978). The slope constraint provides the step pattern which, in turn, guides how new points are linking to F during the ADTW procedure. A *step pattern* is a graph defining the neighbors that can be reached from a given point (origin) and the cost of linking them. For instance, it can be observed in Figure 3.9a that S=1 provides a graph with 6 nodes linking its origin (black square) to three possible neighbors (squares at the end of the branches). The cost of linking horizontal/vertical neighbors is 1 and the cost of linking diagonal neighbors is 2 (these weights correspond to $w(k)$ in Equation 3.18).

The search domain constraint is illustrated as a gray region in Figure 3.9b. Points into this region are discarded from the computation of $\tilde{F}$. We restricted the search domain using a combination of Itakura's parallelogram (ITAKURA, 1975) and Sakoe's ribbon (SAKOE et al., 1978), as depicted in Figure 3.8.

Figure 3.9b illustrates the dynamic programming procedure for $S = 1$. At iteration 0, the procedure adds (0,0) to the list of *source points*[2] and searches for its neighbors that are, in turn, added to the list of *visited points*. The accumulated costs of reaching these neighbors are also stored. This accumulated cost is noted as $g(i, j)$. For instance, $g(1, 2) = 14$ results from the expression $g(0, 0)$ + [1 2]·$[d(0, 1)\ d(1, 2)]^T$ with $d(0, 1)$=2, $d(1, 2)$=5 and 1, 2 the weights for one vertical and one diagonal neighbor, respectively. At iteration 1, the point (1,1), corresponding to the visited point with lowest g, is added to the source points list and extracted from the visited points list. This procedure is iterated until the extrema point (4,4) is added to the source list (last iteration). The curve linking (0,0) with (4,4) corresponds to $\tilde{F}$.

The output of the ADTW algorithm is quite rich: first of all, the value D, which is the minimum global dissimilarity or "DTW distance" (i.e. the sum of cross-distances along $\tilde{F}$), can be assumed as the stretch-insensitive measure of the "inherent difference" between two given time series (GIORGINO, 2009). On the other hand, $\tilde{F}$ is the deformation of the time axes of $\hat{NC}^{\mathrm{CT}}$ and $\hat{NC}^{\mathrm{SAX}}$ which brings the two time series as close as possible to each other.

---

[2] A *source point* is a point for which the accumulated cost cannot be improved (decreased).

3.2.2 Spatial registration of dynamic CT and cine-MRI

After aligning input images over time using the ADTW procedure, they are registered in space. A multi-image rigid registration procedure is used in order to align I^{CT} and I^{cine} intra-patient images in space because there is no suspicion of cardiac remodeling between their acquisition. The procedure optimizes a multi-image metric that accounts for the dynamic information of input images. The multi-image metric is given by:

$$\mathcal{M}\left(T_{\mu^R}; I^{\mathrm{CT}}, I^{\mathrm{SAX}}\right) = \frac{1}{K}\sum_{k=0}^{K-1} \mathcal{M}\left(T_{\mu^R}\left(I^{\mathrm{CT}}\left(\tilde{F}^{\mathrm{CT}}(k)\right)\right), I^{\mathrm{SAX}}\left(\tilde{F}^{\mathrm{SAX}}(k)\right)\right), \quad (3.20)$$

where μ^R is the vector containing the parameters of a 3D rigid transform (translation, rotation). The optimal parameters are calculated using this metric in Equation (3.11).

The ADTW-based registration described above allows to register dynamic CT and cine-MRI acquisitions of the left ventricle. Such a registration permits to describe LV anatomy with the high spatial resolution from CT and the improved temporal resolution from MRI. Moreover, given that cine- and LGE-MRI are already registered, myocardial viability is also fused. The evaluation of this registration method is presented in 4.4 and its using in the context of cardiac asynchronism characterization is presented in Chapter 6.

We focus now in the registration of echocardiography aiming at associating the mechanical function of LV (regional strain curves) computed with speckle tracking echocardiography.

3.3 Dynamic registration of multiview US images

Below we improve the multiview spatio-temporal approach proposed by (Tavard et al., 2012). We aim at integrating strain curves computed from 2D+t US images with the anatomy from CT/MRI. We select a surface-based approach in order to exploit available STE-contours extracted from US-images. The goal of this approach is to find the US planes in the 3D reference system of CT/MRI. The parameters of the acquisition planes containing the different views of the US acquisition are iteratively optimized in a single procedure. Each plane cuts the segmented dynamic LV surface from CT/MRI to obtain a dynamic LV contour to compare with corresponding STE-contour. The segmentation of dynamic CT/MRI depends of the modality: cine-MRI, used in HCM characterization, is segmented with a contour based approach (Yushkevich et al., 2006) (cf. 5.3.2.2), while CT, used in the characterization of cardiac asynchronism, is segmented with a multi-agent approach (Fleureau et al., 2008) (cf. 6.3.1).

Different approaches can be used to describe and compare LV-contours (Trinh et al., 2011). During the optimization procedure, dynamic LV and dynamic STE contours are represented by their Fourier descriptors. This representation is selected because the comparison of LV geometries contoured from different modalities becomes straightforward. The comparison in the Fourier descriptors domain enables to compare the shape information at different levels of detail. It is advantageous because (i) the resolution of input contours differs and, (ii) LV-contours can be distorted (e.g. at apical region in apical-US and MRI SAX). Then, Fourier representation is used to compute the similarity between LV contours. The static registration of a LV-surface from CT/MRI with a LV-contours from STE is challenging because LV geometry is often smooth and symmetric with regards to its long axis. This is the reason why input dynamic geometries are aligned by optimizing the ADTW-based spatio-temporal similarity measure proposed by (TAVARD et al., 2012).

Dynamic multiview STE-contours (obtained from US images) are registered in a two-step procedure. First, acquisition planes of the US images are computed using a spatio-temporal approach. The planes parameters are optimized in a single procedure (combined approach). Output acquisition planes contain acquired 2D US images and locate them into the coordinate system of the anatomical reference (CT/MRI), both in space and time. The second step computes the apices and long axes of dynamic LV-contours from CT and STE to align them in space (the temporal alignment already provided by the first step).

3.3.1 US planes localization and temporal alignment

The method used to find the pose of multiview US-planes (moving) in the CT/cine-MRI coordinate system (fixed) is illustrated in Figure 3.10. The registration optimizes the ADTW-measure between the LV-contours from CT/MRI (extracted by slicing the CT/MRI segmentation with US planes) and the STE-contours, both encoded by their Fourier descriptors. On the one hand, ADTW allows both, to compute the similarity between dynamic LV-contours and to align them over time. On the other hand, Fourier descriptors enable to measure the similarity between a pair of LV-contours (one per modality) by comparing their shapes using the same level of details. In fact, it enables to weight the contribution of rough, medium or fine details. The output US-planes for apical long axis acquisition are illustrated in Figure 3.11b.

We describe below the blocks of the ADTW-based registration procedure in Figure 3.10a.

3.3.1.1 LV surface slicing

The LV-surface slicing is illustrated in Figure 3.11a where a contour is obtained by slicing the LV-geometry at the cardiac phase τ^A. Let $\mathscr{I}^{\mathrm{A}}$ be a dynamic LV-surface extracted from the dynamic anatomy in CT/MRI (the super index $\mathrm{A} \in \{\mathrm{CT}, \mathrm{MRI}\}$ stands for anatomy). Also, let $\mu^v = \{\vec{n}, o\}$ be the parameters defining a US-plane in a 3D space for the acquisition view $v \in \{2\mathrm{CH}, 3\mathrm{CH}, 4\mathrm{CH}\}$, namely, its normal vector

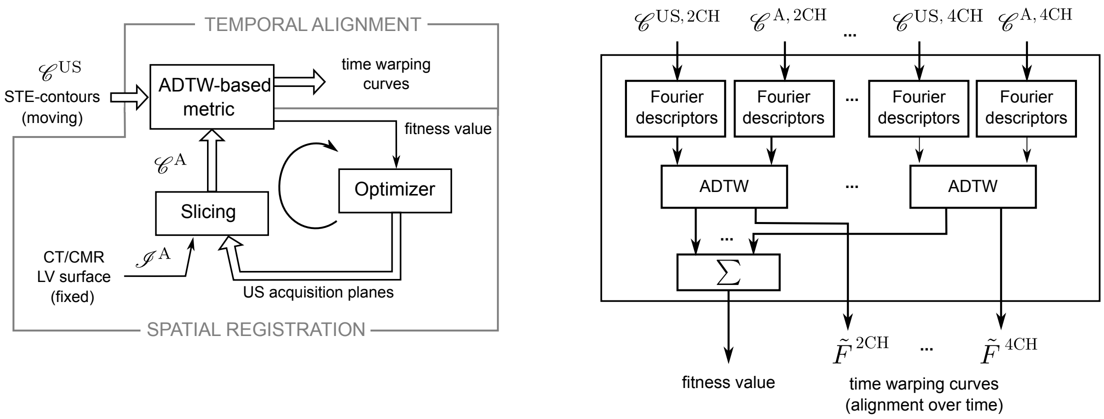

(a) Diagram of the US registration method.

(b) Diagram of the ADTW-based metric block

Figure 3.10: Combined multiview 2D+t US registration: (a) general scheme of the spatio-temporal registration (output are in bold type); (b) diagram depicting the computation of the ADTW-based metric optimized during the registration. Acronyms – ⇒: multiview signal (contours, time warping curves), $\tilde{F}$: optimal time warping curve after ADTW, M-v: multiview.

($\vec{n} \in \mathbb{R}^3$) and origin ($o \in \mathbb{R}^3$). The output contour after slicing the LV-surface at phase $\tau^{\mathrm{A}} \in \{0, \ldots, \mathrm{T}^{\mathrm{A}} - 1\}$ with a US plane with parameters μ^v, is:

$$\mathscr{C}^{\mathrm{A},v}(\tau^{\mathrm{A}}) = \left(x^0, \ldots, x^\ell, \ldots, x^{L-1}\right), \tag{3.21}$$

where $x_\ell \in \Omega^{\mathrm{A},v}$, $\Omega^{\mathrm{A},v} \subset \mathbb{R}^2$ is the spatial domain of $\mathscr{C}^{\mathrm{A},v}$, i.e. the domain defined by the US-plane with parameters μ^v. The points composing the contour $\mathscr{C}^{\mathrm{A},v}(\tau^{\mathrm{A}})$ are ordered e.g. clockwise. The similarity between dynamic STE-contours and LV-contours after LV-surface slicing is then computed using the ADTW.

3.3.1.2 ADTW-based similarity measure

The ADTW is used (i) to align them over time (to match corresponding cardiac phases) and, (ii) to compute the similarity between dynamic contours. This ADTW-based metric is computed in two steps: (i) encoding $\mathscr{C}^{\mathrm{A},v}$ and $\mathscr{C}^{\mathrm{US},v}$ using their Fourier descriptors and, (ii) performing the temporal alignment of these contours described in Fourier domain using the ADTW. This procedure provides a similarity measure that exploits the dynamic information they contain.

Fourier descriptors. Let $x_\ell \in \mathbb{R}^2$ be a point of the contour $\mathscr{C}(\tau)$. Let $z \in \mathbb{C}$ be the complex number whose real and imaginary parts are $x_\ell(0)$ and $x_\ell(1)$, respectively: $z_\ell = x_\ell(0) + \sqrt{-1} \cdot x_\ell(1)$. The encoding of $\mathscr{C}$ into its Fourier descriptors (FDs), denoted as $\hat{\mathscr{C}}$, is obtained as follows:

$$\hat{\mathscr{C}}(\tau) = (Z_0, \ldots, Z_\kappa, \ldots, Z_{L-1}), \quad \text{with} \quad Z_\kappa = \sum_{\kappa=0}^{L-1} z_\ell \cdot \exp\left(-\frac{2\pi\sqrt{-1}}{J}\kappa \cdot j\right), \tag{3.22}$$

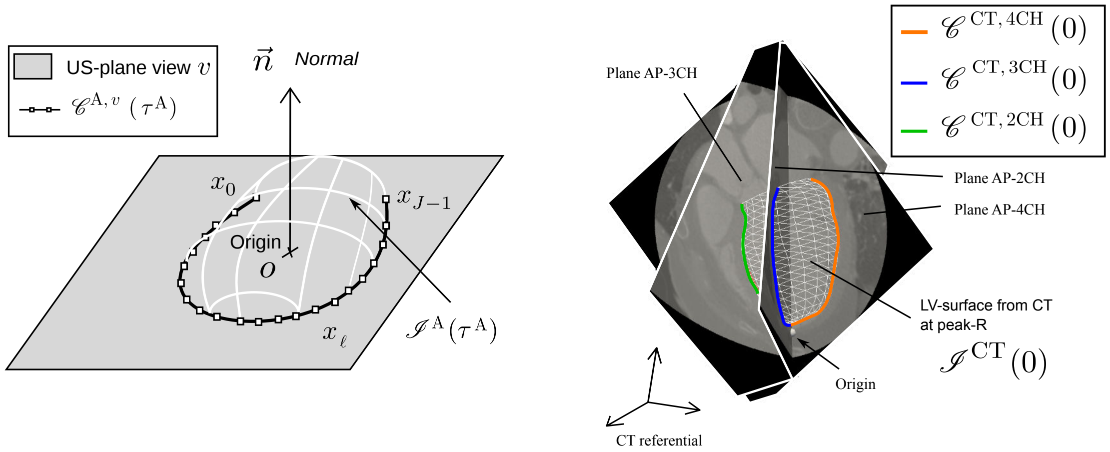

(a) Slicing: using a US-plane defined in the anatomical referential to cut the LV-surface.

(b) Slicing of the LV-surface from the CT image volume at phase 0 with multiview apical US-planes.

Figure 3.11: Slicing a LV-surface ($\mathscr{I}^A(\tau^A)$) to extract the multiview LV contours ($\mathscr{C}^{\mathrm{A},v}(\tau^{\mathrm{A}})$) to be compared with multiview STE-contours ($\mathscr{C}^{\mathrm{US},v}(\tau^{\mathrm{US},v})$, not showed). (a) Definition of a contour lying in a plane for the view v in the anatomical coordinate system (CT referential) at phase τ^A. (b) Extracted multiview contours (in orange, blue and green) from the LV-surface at peak-R ($\tau^{\mathrm{A}} = 0$) after slicing.

where Z^κ is the κ-th Fourier descriptor computed using the discrete Fourier transform (DTF). $\mathscr{C}(\tau)$ can be reconstructed from $\hat{\mathscr{C}}(\tau)$ using the inverse DTF (iDTF).

Invariant Fourier descriptors. LV-contour deformation during the cardiac cycle contains complementary information that needs to be exploited. Thus, we force the Fourier descriptors to be translation and rotation invariant because we are interested at finding the US plane parameters only. Fourier descriptors can be made:

— Translation invariant if Z_0 is set to null ($Z_0 \leftarrow 0$).

— Scale invariant if they are normalized by the norm of Z_1 ($Z_\kappa \leftarrow {}^{Z_\kappa}/_{||Z_1||}$).

— Rotation invariant if only the magnitude of each descriptor is used ($Z_\kappa \leftarrow ||Z_\kappa||$).

Spatio-temporal similarity measure. The ADTW procedure is used to compute the nonlinear temporal alignment between STE-contours and the LV-surface. A weighted distance between a couple of time-samples is used to perform the ADTW. This aims to favor the influence of rough and medium shape details in the computation. The ADTW cross-matrix distance is given by:

$$d\,(i,j) = \sum_{\kappa=0}^{L-1} \frac{1}{\kappa+1} \left| Z_\kappa^{\mathrm{US},v}(i) - Z_\kappa^{\mathrm{A},v}(j) \right|, \tag{3.23}$$

where L is the number of FDs, $Z_\kappa(i)$ is the κ-th FD of contour $\mathscr{C}$ at phase i, and $i \in \{0, \ldots, \top^{\mathrm{US},v}\}$ and $j \in \{0, \ldots, \top^{\mathrm{A}}\}$. The number of FDs ($L$) used to compute the distance is limited in order to account only for rough shape details that are described with the STE-contours. Also, the ADTW computation is constrained as described in 3.2.1.2. The similarity measure between a STE-contour from view v and the sliced LV-surface using the plane parameters μ^v is given by the ADTW distance between them (cf. Equation 3.18). Let $\boldsymbol{\mu}^{\mathrm{US}}$ be an array containing the parameters of all multiview US planes. Also, let $\boldsymbol{F}$ be of the time warping curve for all views. The similarity measure between all multiview dynamic STE-contours and the dynamic LV-surface is given by:

$$\{\tilde{\boldsymbol{\mu}}^{\mathrm{US}}, \tilde{\boldsymbol{F}}\} = \underset{\boldsymbol{\mu}^{\mathrm{US}},\boldsymbol{F}}{\arg\min} \sum_{\forall v} \sum_{k=0}^{K-1} d\left(F^{\mathrm{US},v}(k), F^{\mathrm{A},v}(k)\right), \tag{3.24}$$

where $\mathscr{C}^{\mathrm{US}}$ is the set of STE-contours and K is the length of the time warping curve for view v $(F^v(k) = \left(F^{\mathrm{US},v}(k), F^{\mathrm{A},v}(k)\right))$. The optimization of this metric enables to obtain, in a single optimization, the parameters for all US-planes and the deformation of the time axes of the multiview US acquisitions to the anatomic image (CT/MRI) that bring them as close as possible.

3.3.2 Alignment of LV contours

After obtaining the US planes in CT/MRI coordinate system, LV-contours from STE and sliced CT/MRI are aligned. This procedure is illustrated in Figure 3.12. First, the great of axis of a STE-contour ($\vec{ga}^{\mathrm{US},v}$) and the sliced LV-surface ($\vec{ga}^{\mathrm{A},v}$) is computed. This vector points from the centroid of the contours ($\bar{\mathscr{C}}^{\mathrm{US},v}$ and $\bar{\mathscr{C}}^{\mathrm{A},v}$, respectively) towards the mid-point lying in the line segment joining the initial and extrema points of the first acquired geometry (peak-R). Then, the STE-contour is rotated and translated such that both, its great axis and centroid, match those of the sliced LV-geometry. The rotation is performed around the normal vector of the resulting US plane.

The ADTW-based method described above enables to register multiview STE contours with LV surfaces from CT or MRI. This registration allows to describe the strain information issued from STE in a LV-surface with high spatial resolution. The evaluation of this registration procedure is presented in 4.5 and its use in HCM and cardiac asynchronism characterization is presented in Chapters 5 and 6, respectively.

3.4 Conclusion

The proposed image registration methods aiming at registering available cardiac MRI, CT and US acquisitions, were presented in this chapter. They share two methodological aspects: (i) the information contained by the entire dynamic image (surface) is exploited during the registration; (ii) the adaptive dynamic time warping procedure is used when two dynamic multimodal acquisitions need to be aligned in time.

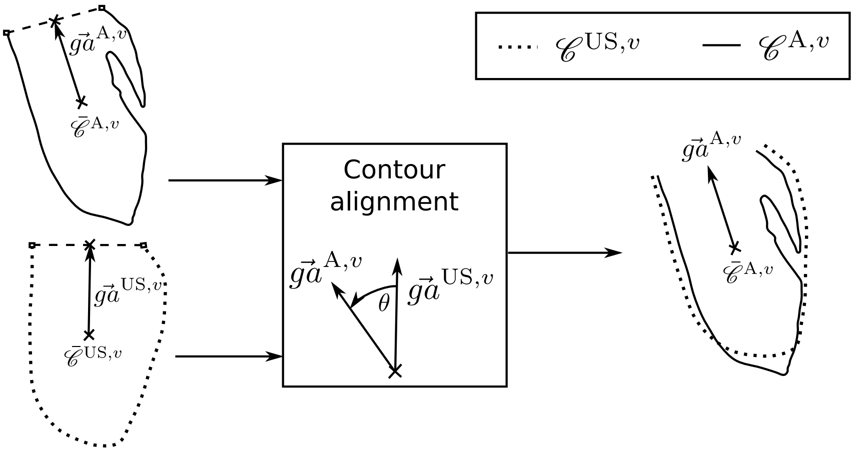

Figure 3.12: Alignment of STE and sliced CT/MRI contours of the left ventricle after US plane computation. The centroid and great axis of STE-contours are aligned with their counterparts from sliced CT/MRI LV-surface after localizing the US planes in the anatomical coordinate system.

Cardiac MRI slice misalignment correction and registration. Based on the literature, different methods have been proposed in order to correct the slice misalignment that may be present in cine-MRI and LGE-MRI, and to register LGE-MRI to corrected cine-MRI. These methods to correct slice misalignment are based on the registration of MRI slices using the intensity profiles from multiview slice intersections to compute the similarity measure. Different metrics will be evaluated in Chapter 4, both for LGE to LGE and for LGE to cine registrations.

Cine-MRI to CT registration. To our knowledge, any method has been proposed in literature to register cardiac MRI and CT. For this purpose, we proposed a spatio-temporal registration procedure exploiting the dynamic information in CT and cine-MRI. The procedure computes two curves from each dynamic acquisition that enable to align them over time using an adaptive DTW process. Then, the spatial registration is performed with a multi-image approach, i.e. using all the image volumes in both sequences, in order to make the registration more robust.

2D+t US to CT/cine-MRI registration. A spatio-temporal multiview US to CT/cine-MRI registration method, exploiting the dynamic information in LV-contours from STE and a LV-surface from CT/cine-MRI, was proposed to register them. In order to consider all the images and to compare contours with the same level of details, it uses a spatio-temporal metric based on the ADTW procedure applied to the dynamic contours described by their Fourier descriptors.

These methods are used to register available acquisitions used in the context of HCM and cardiac asynchronism characterization (cf. Chapters 5 and 6, respectively). Their evaluation is presented in the next chapter.

References

Bazett, H. (1920). “An analysis of the time-relations of electrocardiograms”. In: *Heart* 7, pp. 353–370.

Carminati, M., Maffessanti, F., and Caiani, E. (2012). “Automated motion artifacts removal between cardiac long- and short-axis magnetic resonance images”. In: *Computing in Cardiology (CinC), 2012*, pp. 689–692.

Cordero-Grande, L., Merino-Caviedes, S., Alba, X., Figueras i Ventura, R., Frangi, A. F., and Alberola-Lopez, C. (2012). “3D fusion of cine and late-enhanced cardiac magnetic resonance images”. In: *2012 9th IEEE International Symposium on Biomedical Imaging (ISBI)*, pp. 286–289.

Elen, A., Hermans, J., Ganame, J., Loeckx, D., Bogaert, J., Maes, F., and Suetens, P. (2010). “Automatic 3-D Breath-Hold Related Motion Correction of Dynamic Multislice MRI”. In: *IEEE Transactions on Medical Imaging* 29.3, pp. 868–878.

Fleureau, J., Garreau, M., Simon, A., Hachemani, R., and Boulmier, D. (2008). “Assessment of global cardiac function in MSCT imaging using fuzzy connectedness segmentation”. In: *Computers in Cardiology, 2008*. IEEE, pp. 725–728.

Giorgino, T. (2009). “Computing and Visualizing Dynamic Time Warping Alignments in R: The dtw Package”. In: *Journal of Statistical Software* 31.7, pp. 1–24.

Heldt, T., Shim, E., Kamm, R., and Mark, R. (2002). “Computational Modeling of Cardiovascular Response to Orthostatic Stress”. In: *Journal of Applied Physiology* 92.3, pp. 1239–1254.

Huang, X., Moore, J., Guiraudon, G., Jones, D., Bainbridge, D., Ren, J., and Peters, T. (2009). “Dynamic 2D Ultrasound and 3D CT Image Registration of the Beating Heart”. In: *Medical Imaging, IEEE Transactions on* 28.8, pp. 1179–1189.

Itakura, F. (1975). “Minimum prediction residual principle applied to speech recognition”. In: *Acoustics, Speech, and Signal Processing, IEEE Transactions on* ASSP-23.1, pp. 67–72.

Lötjönen, J., Pollari, M., Kivistö, S., and Lauerma, K. (2004). “Correction of Movement Artifacts from 4-D Cardiac Short- and Long-Axis MR Data”. In: *Medical Image Computing and Computer-Assisted Intervention – MICCAI 2004*. Vol. 3217. Lecture Notes in Computer Science. Springer Berlin / Heidelberg, pp. 405–412.

Lötjönen, J., Pollari, M., Kivistö, S., and Lauerma, K. (2005). “Correction of motion artifacts from cardiac cine magnetic resonance images”. eng. In: *Academic radiology* 12.10, pp. 1273–1284.

Perperidis, D., Mohiaddin, R., and Rueckert, D. (2005). “Spatio-temporal free-form registration of cardiac MR image sequences”. In: *Medical Image Analysis* 9.5, pp. 441–456.

Sakoe, H. and Chiba, S. (1978). "Dynamic programming algorithm optimization for spoken word recognition". In: *Acoustics, Speech and Signal Processing, IEEE Transactions on* 26.1, pp. 43–49.

Slomka, P. J., Fieno, D., Ramesh, A., Goyal, V., Nishina, H., Thompson, L. E. J., Saouaf, R., Berman, D. S., and Germano, G. (2007). "Patient motion correction for multiplanar, multi-breath-hold cardiac cine MR imaging". eng. In: *Journal of magnetic resonance imaging: JMRI* 25.5, pp. 965–973.

Tavard, F., Simon, A., Hernandez, A., Betancur, J., Donal, E., and Garreau, M. (2012). "Dynamic Registration of Cardiac US and CT Data Using Fourier Descriptors and Dynamic Time Warping". In: *Image Processing Theory, Tools and Applications, IEEE IPTA 2012 3dr International Conference*, pp. 198–203.

Trinh, N. H. and Kimia, B. B. (2011). "Skeleton Search: Category-Specific Object Recognition and Segmentation Using a Skeletal Shape Model". English. In: *International Journal of Computer Vision* 94.2, pp. 215–240.

Wachinger, C. and Navab, N. (2012). "Entropy and Laplacian images: Structural representations for multi-modal registration". In: *Medical Image Analysis* 16.1, pp. 1–17.

Yushkevich, P. A., Piven, J., Cody Hazlett, H., Gimpel Smith, R., Ho, S., Gee, J. C., and Gerig, G. (2006). "User-Guided 3D Active Contour Segmentation of Anatomical Structures: Significantly Improved Efficiency and Reliability". In: *Neuroimage* 31.3, pp. 1116–1128.

CHAPTER 4

Evaluation of the multimodal registration

In this chapter, we describe the evaluation of the image registration methods proposed in Chapter 3. The three main methods considered in this work are studied: (i) cardiac MRI registration; (ii) cine-SAX to dynamic CT registration; (iii) STE to cardiac MRI registration. For each of these methods, we studied the proposed metrics and we estimated the output accuracy on real data, either using quantitative indicators (if available), or qualitatively.

The method proposed by (Skerl et al., 2006) was used in order to provide quantitative elements to select the best similarity metric to use in iconic registration contexts (MRI, CT). This method is described below.

4.1 Quantitative descriptors of performance for similarity measures

The best similarity measure to use in an image registration procedure can be selected using a qualitative analysis of the metric evolution (e.g. visually assessing the metric smoothness and the position of the optimum), or using quantitative protocols. For the latter, (Skerl et al., 2006) proposed a protocol to evaluate similarity measures in a rigid registration procedure. It can be applied when the *gold standard* is known [1]. In the absence of the gold standard, the "bronze standard" protocol could be applicable (Glatard et al., 2006). This protocol is analogous to the well known STAPLE used to validate image segmentation (Warfield et al., 2004). The "bronze standard" protocol applies different registration methods to estimate a gold standard to compare with. Other evaluation

---

[1] Gold standard refers to the underlying optimal registration between input images, i.e. the transformation aligning them.

approaches are based on the comparison of methods by using the “Regression without Truth” approach (RWT) (Hoppin et al., 2002)(Lebenberg et al., 2012). These evaluation approaches are based on real images. Other methods, based on image simulation, have not been considered in this work.

We selected the protocol of (Skerl et al., 2006) to obtain the best similarity measure for a spatial registration procedure. Indeed, we seek to align acquisitions of the same patient, which we assumed as a rigid spatial registration problem. The gold standard is estimated manually. For example, in cardiac MRI registration context, acquisitions with no slice misalignment (e.g. cine-MRI without slice misalignment) may be selected. For the registration of dynamic CT and MRI, a manual alignment of the considered images may be performed.

The protocol of (Skerl et al., 2006) computes five properties describing the behavior of a given similarity measure. These properties are calculated from a set of measurements of similarity ($\mathcal{M}$), computed between the gold standard image (I^{GT}) and a moving image (I). These measurements are computed at sampled positions of the rigid parametric space. This 6D parametric space (translation: 3 dimensions, rotation: 3 dimensions) is normalized in order to scale the dynamic ranges of the translation and the rotation parameters to a common range. Then, a subspace of this parametric space, corresponding to an hypersphere centered in μ^{GT} (the gold standard transformation, i.e. the transformation aligning I with I^{GT}) with a given radius R, is considered. This hypersphere is randomly sampled with a given number of lines passing through its center. Each line is in turn evenly sampled with a given number of positions. These sampled positions define a metric profile and provide the set of measurements used to estimate the properties of $\mathcal{M}$. The sampling of the parametric space is illustrated in Figure 4.1 for a 2D parametric space.

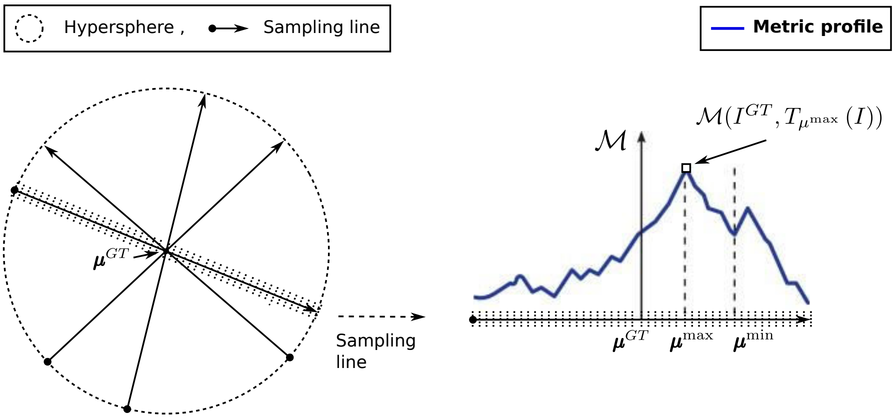

Figure 4.1: Illustration of the sampling performed during the protocol of (Skerl et al., 2006): sampling lines are randomly traced in a circle defining the domain of interest in a 2D parametric space. Then, they are evenly sampled and a metric profile is obtained from each line (Left). These profiles are used to compute the properties describing the behavior of the metric. Modified from (Sandoval et al., 2013).

The properties provided by the protocol of (Skerl et al., 2006) are statistical estimations computed from the set of similarity measurements and parameter samples (note that a measure of *similarity* is considered; hence, maximum values correspond to a good matching of input images):

ACC. The *accuracy* is defined as the root mean-square (along all the sampling lines) of distances between the origin (μ^{GT}) and each of the global maxima along sampled lines. It describes how far the maximum measure of similarity is from the known gold standard.

CR. The *capture range* is defined as the smallest (along all the sampling lines) of the distances between positions of the global maximum and the closest minimum along each line.

$DO(r)$. The *distinctiveness of the optimum* measures the visibility of the maximum value against the values around it. It is calculated as the average (along all the sampling lines) of the difference between twice the maximum value and the sum of the two values symmetrically located at their two sides at a given distance. It is defined as a function of the distance $r = k \cdot \delta$ from the maximum, where δ is the distance between two consecutive points along a line and $k = \{1, 2, \ldots\}$ is the number of steps.

$NOM(r)$. For each sampled line, the global maximum is considered and the number of minima of the similarity measure, within a distance r of the global maximum, is computed. The *number of minima* $NOM(r)$ corresponds to the sum of the number of minima over all lines.

$RON(r)$. The *risk of nonconvergence* is the property that describes the behavior of a similarity measure around all global maxima of sampling lines. It is defined as the average of positive gradients within distance r along each sampling line. A large value of RON indicates that a similarity measure has distinctive and/or broader local maxima.

The better a similarity measure, the smaller the values of accuracy, number of minima and risk of nonconvergence, and the larger the values of capture range and distinctiveness of the optimum. For DO(r) and RON(r), only the first ($r = \delta$) and the last (maximum r) were retained. They describe the values of these properties near to the ground truth (near GT) and far from it (far GT); thus, they provide information about the behavior of the metric when the registration procedure has a good initialization (near) or a rough initialization (far). Regarding NOM(r), we compute it for all the values of r and took the average value which provides the average indicator of the smoothness of the similarity measure. This is an important indicator to select, for instance, the optimization procedure best fitted to find the optimal value of the metric.

The protocol of (Skerl et al., 2006) is freely available at http://lit.fe.uni-lj.si/contents/tools/SimilarityEvalua
This tool provides the sampling of the parametric space to be evaluated.

The gold standard transform is not known in our data. Thus we consider, when possible, one acquisition with a low mismatch. This was the case for the cine-MRI and LGE-MRI slice misalignment corrections, for which an acquisition without slice misalignment have been selected. For the dynamic CT to cine-MRI registration, the gold standard was obtained manually. In all the cases, examples of profiles resulting from sampling lines were used to provide some qualitative elements of evaluation.

4.2 Implementation of the similarity measures

The elastix library (Klein et al., 2010) was used to compute the metrics. Elastix uses the ITK library (Ibanez et al., 2005) to implement most of the similarity measures it includes. The computation of the metric can be exhaustive (i.e. using the entire set of image voxel intensities), or non-exhaustive (i.e. an estimation of the similarity measure is computed instead). The benefit of the latter is that the time to compute the measure can be highly reduced yet obtaining a good estimation of the metric. In this case, a number of samples of the input images has to be defined. We used a non-exhaustive computation of the similarity measures to perform the metrics study. The samples required to compute the estimation were selected with a random sampler.

In this a context, the estimation of the *mean squares metric* (MS) and the *normalized correlation metric* (NC) only need the number of samples to be used. Regarding the mutual information metrics, ITK provides different implementations (Ibanez et al., 2005). We test here the following:

VWMI. This is the *Viola-Wells mutual information* metric. This metric computes the mutual information (MI) between two images from the intensity information that their voxels contain. In this implementation, the probability density distributions needed to compute the mutual information are estimated using *Parzen windows*. These are kernel density estimators that obtains the probability densities by taking intensity samples form the image and superpositioning kernel functions centered on these samples. The Viola-Wells implementation uses two separate intensity samples sets from the images: the first to compute the density and the second to approximate the entropy. Gaussian kernels are used as kernel functions; then, the standard deviation is a parameter to provide along with the number of samples to use.

MMI. This is the *Mattes mutual information* metric. In this implementation, the probability density distribution are estimated using Parzen histograms, requiring only one set of intensity samples to be drawn from the image. Using this set, the marginal and joint probability density functions are evaluated at discrete positions or bins, uniformly spread within the dynamic range of the images intensities. The entropy values are then computed by summing over the bins of the estimated histograms. Then, two main parameters are needed for the computation of MMI, the number of samples and the number of histogram bins.

NMI. This is the *normalized mutual information* metric. It is computed using the histograms of the intensities in the images as for MMI. The definition of this metric was provided in Equation (2.7).

For each test, we provide the parameters used to estimate the underlying similarity measure.

4.3 Evaluation of the cine-MRI and LGE-MRI registration

This section is focused on the evaluation of cine-MRI and LGE-MRI registration for the correction of slice misalignment and the inter-sequence registration.

In these contexts, three different processes have to be studied: (i) correction of slice misalignment in cine-MRI; (ii) correction of slice misalignment in LGE-MRI; (iii) LGE- to cine-MRI inter-sequence registration. For each of these processes, an evaluation may be performed in two steps: (i) selection of the most appropriate metric; (ii) evaluation of the final result. For the latter, we used a visual evaluation made by an expert using the data considered in HCM and cardiac asynchronism studies.

For the correction of slice misalignment in cine-MRI, (Elen et al., 2010) showed that the absolute difference of derivative profiles (ADD) and the normalized mutual information (NMI) are the most appropriated metrics. Thus, we used NMI for the correction of slice misalignment of cine-MRI. The results of this process, assessed by an expert, are presented in 4.3.3.

For the correction of slice misalignment in LGE-MRI, no reference work comparing the performance of different similarity measures has been, to our knowledge, reported. Thus we firstly used the protocol of (Skerl et al., 2006) to select the most appropriate metric. However, no further evaluation has been performed because the clinical data considered in HCM and cardiac asynchronism studies did not present such misalignment.

For the LGE- to cine-MRI inter-sequence registration, we also used the protocol of (Skerl et al., 2006) to select the most appropriate metric. Then, the best was used in the HCM study that involves the registration of STE with cine-MRI and then with LGE-MRI to integrate STE with LGE-MRI. Then, the final result was evaluated by the expert, i.e. the registration between STE and LGE-MRI. The results will therefore be presented in the Chapter 5.

In this section, we present the selection of the similarity measure between multiview LGE images and between cine and LGE images. Then, we present the visual evaluation of results provided by the correction of slice misalignment in cine-MRI.

4.3.1 Evaluation of similarity measures between multiview LGE-MRI

Two LGE images acquired with the inversion recovery (IR) technique from a HCM patient with late gadolinium-enhanced regions in the myocardial tissue (fibrosis), were used: one short axis view (IR-SAX) and one two-chamber view (2CH). In order to provide the gold standard transformation, these images were selected such that no mismatch between them were visually detected. Figure 4.2 shows five checkerboard images between these acquisitions, three at basal, medial and apical slices of the IR-SAX image and two for different slices of the IR-2CH image. Note the evident fibrosis in the antero-septal region (orange arrow). It can be observed that, visually, the matching between these images is satisfactory. Even if this alignment is not the gold standard, it provides elements of evaluation for the performance of the similarity measures. However, the accuracy, which relies on a the knowledge of μ^{GT}, must be interpreted carefully.

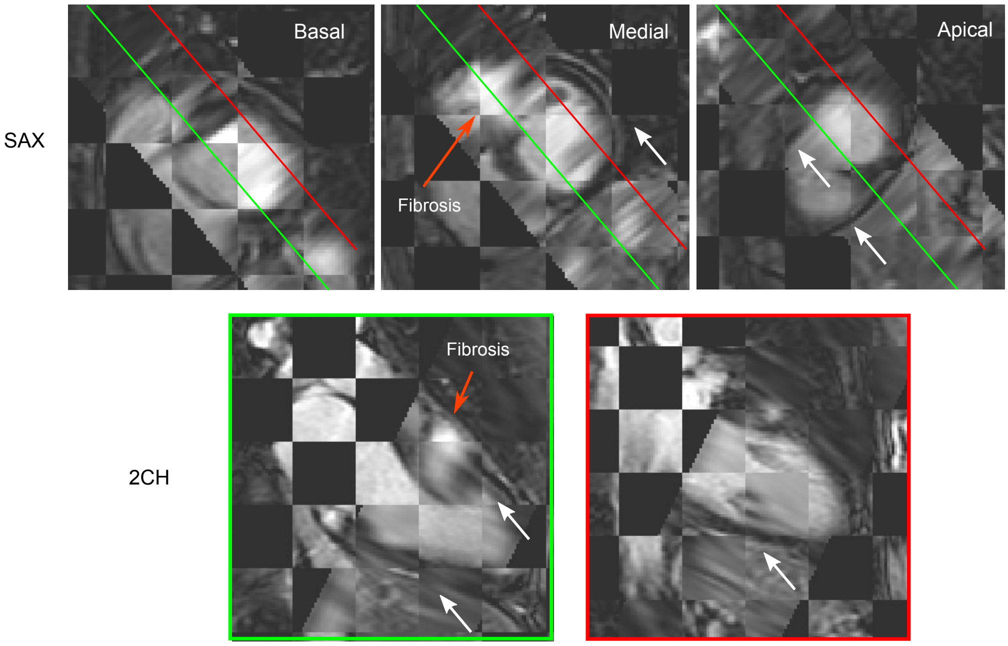

Figure 4.2: Checkerboard of IR-SAX and IR-2CH images used for the evaluation of the similarity metrics in multiview LGE-MRI rigid registration. (Top) Checkerboard in a basal, medial and apical slice from the IR-SAX image. (Bottom) Checkerboard from two slices in the IR-2CH image. The zone with fibrosis are pointed by orange arrows. White arrows point to some instances of good matching.

The protocol in (SKERL et al., 2006) was used to select the best similarity measure aligning these images. The parameters for this protocol were set as follows: N=50 (number of sample lines), M=200 (sampling points per line) and R=3 (radius of the hyper-sphere in normalized units, corresponding to a sampling of the searching region with a radius of 30% of the minimum size between the images). The resolution of the images were 256×256×16 voxels and 1.37×1.37×5 mm^3 for the IR-SAX, and 320×320×12 voxels and 1.25×1.25×5 mm^3 for the IR-2CH. In plane resolution of the IR-SAX image was resampled to 1.25×1.25×5 mm^3 to obtain both images with the same resolution.

MS, NC and MI-based metrics were included into the analysis. MS was analyzed between input IR images (MS) and between their structural representation using the local entropy filter (MS-S) defined in Chapter 3 (cf. 3.1.1.3). The size of the neighborhood used in local entropy image computation was 11×11×11 voxels. Figure 4.3 illustrates the resulting local entropy image for one SAX and one 2CH slice.

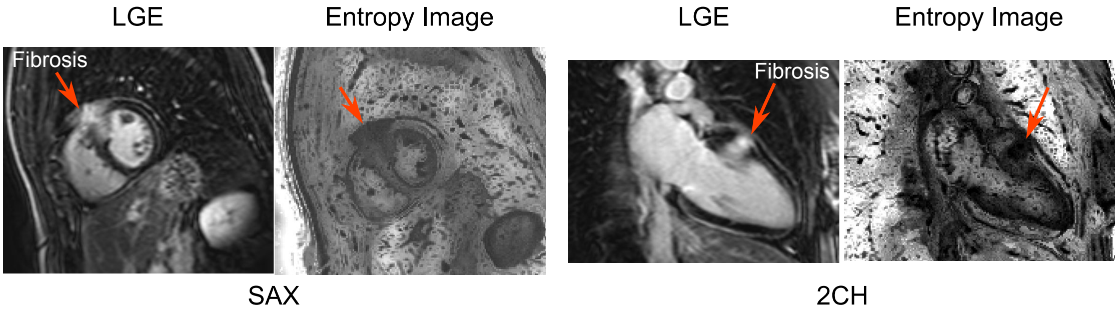

Figure 4.3: LGE image (IR sequence) and resulting local entropy image for one SAX slice (two images at left) and one 2CH slice (two images at right). Orange arrow points to a region with fibrosis.

The metrics were implemented using the elastix[2] library (Klein et al., 2010), to take advantage of its static image sampler which speeds up the computation. This sampler randomly computes the locations used to estimate the metric value. It is static because the same locations were used for all the positions of the parametric space to be evaluated. The parameters used for the computation of the similarity metrics were: 420000 samples, 32 histogram bins (MS, NC, VWMI, MMI, NMI), 0.4 for the Gaussian kernel size for VWMI computation (input images were also normalized to estimate VWMI).

Figure 4.4 illustrates one metric profile, computed along one sampling line, for each similarity measure. The ground truth transformation parameters is represented using a dotted line. In terms of smoothness, MI-based metrics perform the best. In terms of accuracy, MS based metrics resulted the best. Nevertheless, MS-S outperformed classical MS, highlighting the benefits of the entropy filter.

Table 4.1 presents the similarity measure properties. MS-S metric performs the best for most of the indicators. However, it has the worst performance in terms of average NOM. Having the best capture range, we can conclude that, even if this metric shows a lot of minima, they are not near to the ground truth, which is in agreement with Figure 4.4.

From this analysis, we conclude that, if the registration is properly initialized, the MS-S metric will be the most appropriate to register the multiview IR acquisition. Given that LGE image views are normally performed sequentially during the MRI examination,

---

[2] Available at http://elastix.isi.uu.nl/

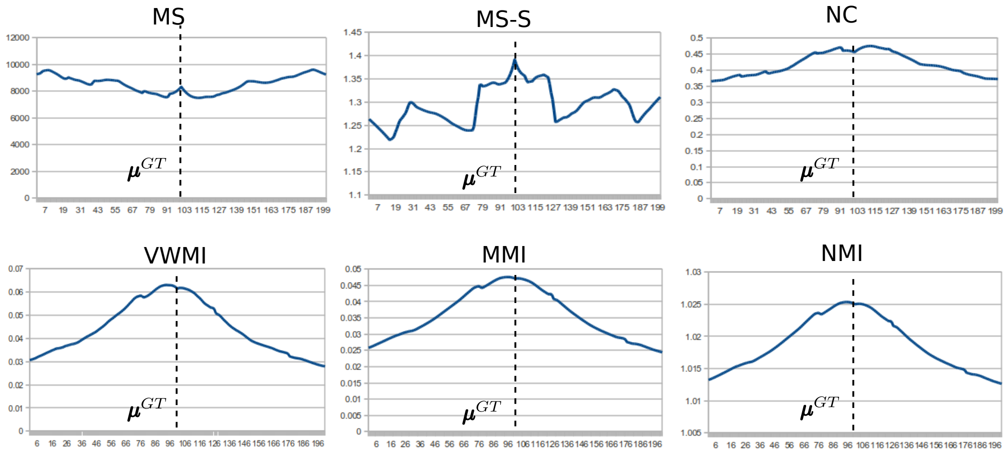

Figure 4.4: Instances of similarity measure profiles between multiview LGE images.

Table 4.1: Similarity measure properties for rigid intra-sequence LGE to LGE registration, for IR-SAX and IR-2CH images of a HCM patient with fibrosis. Best values per column are in bold type. The arrows indicate if the indicator has to be maximized (↗) or minimized (↘). ACRONYMS – *ACC*: accuracy, *CR*: capture range, *DO*: distinctiveness of optimum, MI: mutual information, MMI: Mattes MI, MS: mean squares metric, MS-S: MS of structural images, NMI: normalized MI, *NOM*: average number of minima, *RON*: risk of nonconvergence, VWMI: Viola-Wells MI.

	ACC(↘)	*DO*(↗)		*CR*(↗)	*NOM*(↘)	*RON*(↘)	
Metric		near GT	far GT			near GT	far GT
MS	**0**	1.65e^{-1}	-5.89e^{-3}	0.49	6.15	**0**	2.23e^{+4}
MS-S	**0**	**2.10e**$^{-1}$	**2.07e**$^{-2}$	**0.66**	7.68	**0**	1.21e^{+4}
NC	1.36	1.90e^{-2}	5.25e^{-3}	0.17	4.35	4.12e^{+3}	8.40e^{+3}
VWMI	0.68	9.57e^{-3}	1.33e^{-2}	0.17	1.34	1.81e^{+3}	1.38e^{+3}
MMI	0.53	3.17e^{-3}	1.12e^{-2}	0.17	0.89	1.30e^{+3}	**6.23e**$^{+2}$
NMI	0.59	4.08e^{-3}	1.75e^{-2}	0.17	**0.46**	3.26e^{+2}	7.42e^{+2}

this constraint seems to be satisfied. The findings of these evaluation provides a metric to be used during the intra-sequence slice misalignment correction of LGE-MRI.

4.3.2 Evaluation of similarity measures between cine- and LGE-MRI

A pair of corresponding IR-SAX and cine-SAX images from a HCM patient with late gadolinium-enhanced regions in the myocardial tissue (fibrosis) and no mismatch between them, were used as the reference. Figure 4.5 shows three checkerboard images between these acquisitions at basal, medial and apical slices. Note the evident fibrosis in the antero-septal and postero-septal regions (orange arrows). It can be observed that, visually, the matching between these images is satisfactory.

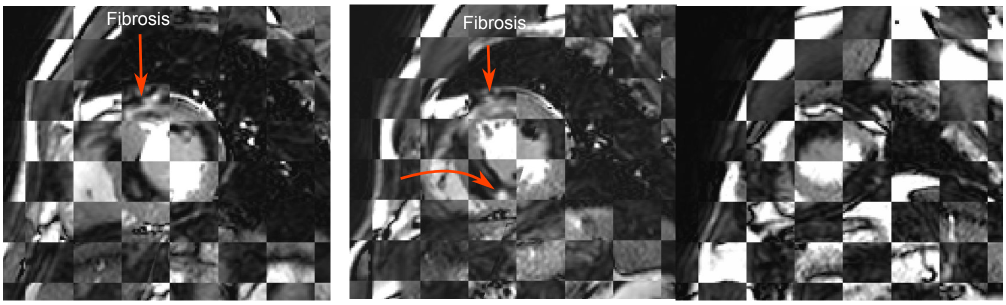

Figure 4.5: Checkerboard of IR-SAX and corresponding cine-SAX images used for the evaluation of similarity metrics between cine- and LGE-MRI in a rigid registration framework. From left to right the checkerboard images at a basal, medial and apical slice. Orange arrows points to regions with myocardial fibrosis.

As in the previous section, even if this alignment is not the gold standard, it provides elements of evaluation for the performance of the similarity measures. However, the accuracy, which relies on the knowledge of μ^{GT}, must be interpreted carefully.

The protocol in (Skerl et al., 2006) was then used to select the best similarity measure. The considered parameters were the same as in the previous section. The resolution of the images were 256×256×12 voxels and 1.25×1.25×7.5 mm^3 for the cine-SAX, and 256×256×16 voxels and 1.37×1.37×5 mm^3 for the IR-SAX. The resolution of both images was resampled to 1.25×1.25×1.25 mm^3 using a bi-cubic splines interpolator.

Given that this is an inter-sequence registration, MI metrics were included. However, we also included NC and MS-S (MS of structural images) metrics into the analysis. The use of MS-S is justified by the fact that LGE is an structural image modality. The size of the neighborhood used in the local entropy image computation was 11×11×11 voxels. Figure 4.6 illustrates the resulting local entropy image for LGE-SAX and cine-SAX at basal, medial and apical slices.

As in the LGE intra-sequence analysis, the similarity measures were implemented using elastix library (Klein et al., 2010) and the same parameters as before. Figure 4.7 shows a profile per metric along a sampling line. The profiles are quite smooth except for the one of NC. Note also that NMI and MMI have a wide flat maximum around the ground truth.

Table 4.2 summarizes the results of the protocol of Skerl. Note that CR is the same for all metrics which was explained by (Skerl et al., 2006) as a behavior of metrics in a multimodal registration problem. It can be observed that no similarity measure performed the best for all properties. In fact, best performances were distributed between NMI (2), VWMI (2), MMI (1) and NC (1). NC, not being commonly used in a multimodal registration procedure, performed more or less the same as MI metrics. However, it had the highest NOM, which is confirmed by the high number of minima in its profile; then, its optimization will be difficult. Finally, NMI and MMI have the highest DO far from

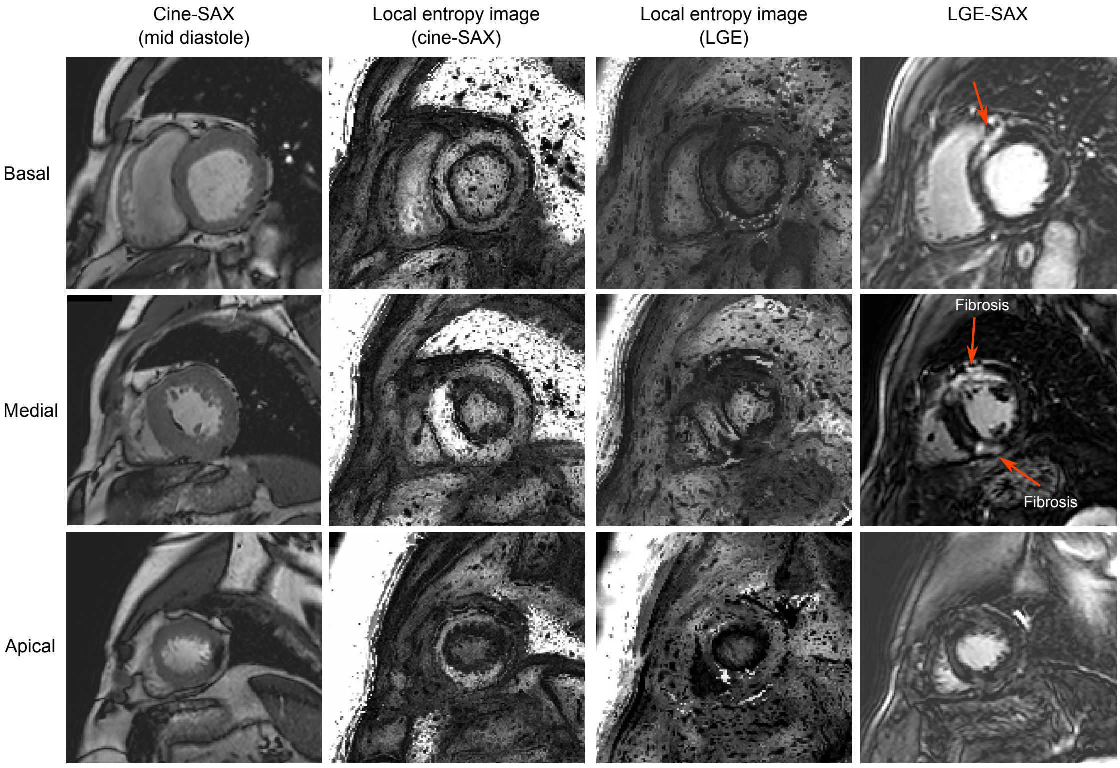

Figure 4.6: Cine-SAX and LGE-SAX (IR sequence) images and resulting local entropy images at basal, medial and apical slices. Orange arrow points to a region with fibrosis.

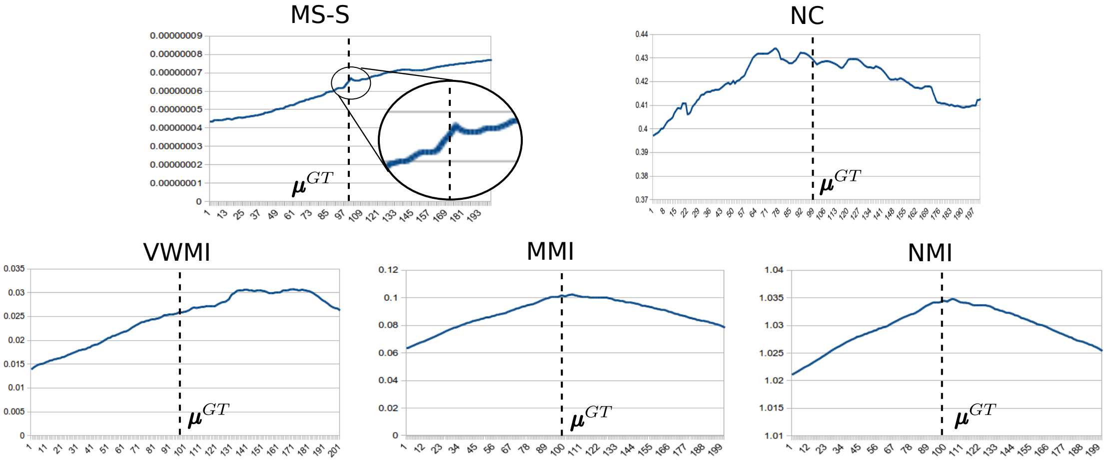

Figure 4.7: Similarity measure profiles between cine-SAX and LGE-SAX images along a sampling line.

Table 4.2: Similarity measure properties for rigid inter-sequence LGE- and cine-MRI registration, both in short axis view. Best values per column are in bold. The arrows indicate if the indicator has to be maximized (↗) or minimized (↘). ACRONYMS – *ACC*: accuracy, *CR*: capture range, *DO*: distinctiveness of optimum, MI: mutual information, MMI: Mattes MI, MS-S: mean squares of structural images, NMI: normalized MI, *NOM*(*r*): number of minima, *RON*: risk of nonconvergence, VWMI: Viola-Wells MI.

	ACC(↘)	*DO*(↗)		*CR*(↗)	*NOM*(↘)	*RON*(↘)	
Metric		near GT	far GT			near GT	far GT
MS-S	3.05	$1.70e^{-2}$	$-1.83e^{-2}$	0.24	6.42	$3.62e^{+3}$	$4.66e^{+3}$
NC	1.13	$\mathbf{2.08e}^{-2}$	$1.17e^{-3}$	0.24	12.77	$2.15e^{+3}$	$8.21e^{+3}$
VWMI	**0.78**	$6.49e^{-3}$	$3.65e^{-3}$	0.24	8.71	$\mathbf{8.86e}^{+2}$	$4.29e^{+3}$
MMI	5.07	$8.49e^{-3}$	$\mathbf{8.54e}^{-3}$	0.24	4.03	$1.87e^{+3}$	$2.29e^{+3}$
NMI	4.88	$8.78e^{-3}$	$8.52e^{-3}$	0.24	**2.92**	$1.71e^{+3}$	$\mathbf{2.20e}^{+3}$

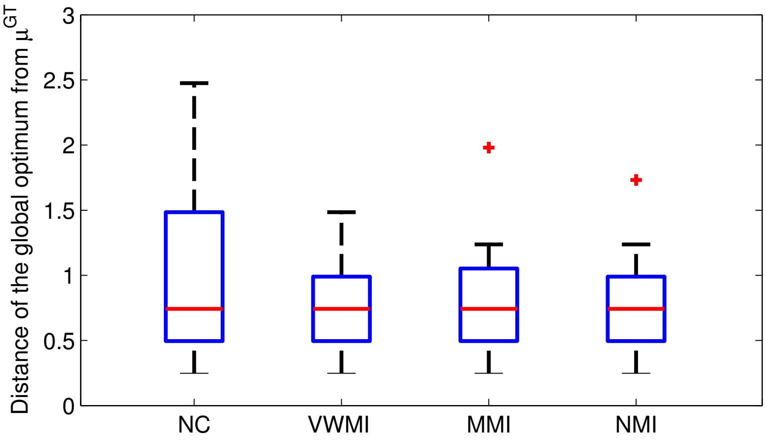

Figure 4.8: Boxplots of the distance from the normalized ground truth parameters to the position of the global optimum.

GT which is also in agreement with their profiles which present a unique wide and flat maximum.

The accuracy is a global property, very sensitive to outliers. Then, to enhance the study of NC, VWMI, MMI and NMI, we draw the boxplots of the distance of the global optimum to the ground truth in all sampling lines. They are shown in Figure 4.8. These boxplots confirmed that MI-based metrics perform the best. From them, NMI performed slightly better. Then, we selected it has the best metric to rigidly register cine- and LGE-MRI.

4.3.3 Evaluation of the cine-MRI slice misalignment correction

The sequential approach described in the previous chapter (cf. Figure 3.5) was implemented using NMI as the metric, to correct for slice misalignment in cine-MRI volume sequences used for HCM characterization (cf. Chapter 5).

Data. Retrospective ECG-gated cine-MRI acquisitions of four subjects with hypertrophic cardiomyopathy were used to assess the performance of the correction. Short-axis, two-chamber and four-chamber cine-MRI were acquired in a 3.0T MRI scanner (Phillips Achieva) as part of the clinical cardiac MRI examination. The number of slices was 12 for SAX, 3 for 2CH and 5 for 4CH views. The technique used to acquire these images was balanced fast-field-echo (b-FFE). Slice resolutions were: size from 256×256 to 320×320, pixel from 1.1875×1.1875 mm^2 to 1.25×1.25 mm^2, spacing between slices from 7 mm to 10.78 mm. Each cine acquisition had 30 phases.

Evaluation method. Based on (Elen et al., 2010), the NMI metric was used. For the sake of comparison, results were also computed using NC as the metric. Their implementations used the ITK library[3]. 32 histrogram bins were used in NMI computation. The implementation of the downhill simplex algorithm in the vision numerics library[4] was selected to compute the optimal transformation. The starting simplex was defined by adding 10 mm to the translation parameters and 0.1 to the scaling parameters.

Two observers assessed the misalignment of the LV anatomical structures. A plane perpendicular to the SAX slice was used to evaluate the alignment of SAX at peak-R. A mid-cavity plane was used to trace this perpendicular plane such that the LV was intersected between the anteroseptal and the inferoseptal regions, as shown in Figure 4.9a. The alignment between SAX and LAX was also evaluated at peak-R. For this purpose, a medial LAX plane was selected and then the alignment of the myocardium (and the interventricular septum) between 2CH/4CH and each SAX slice was assessed, as illustrated in Figure 4.9b.

The number of slices that were correctly aligned along the interventricular septum and the LV lateral wall from SAX plane cuts were assessed by the two observers. The alignment was considered as successful if maximum one slice had a slight misalignment.

Results and discussion. Figure 4.10 shows the resulting SAX evaluation by one observer.

The evaluation of SAX and 2CH/4CH alignment before (original) and after slice misalignment correction using NC and NMI is summarized in Table 4.3. A total of 24 evaluations were performed by each observer: 4 patients × 3 alignments (original, NC, NMI) × 2 intersections, each evaluation being made up of 12 instances (12 SAX slices).

---

[3] http://www.itk.org/

[4] http://vxl.sourceforge.net/

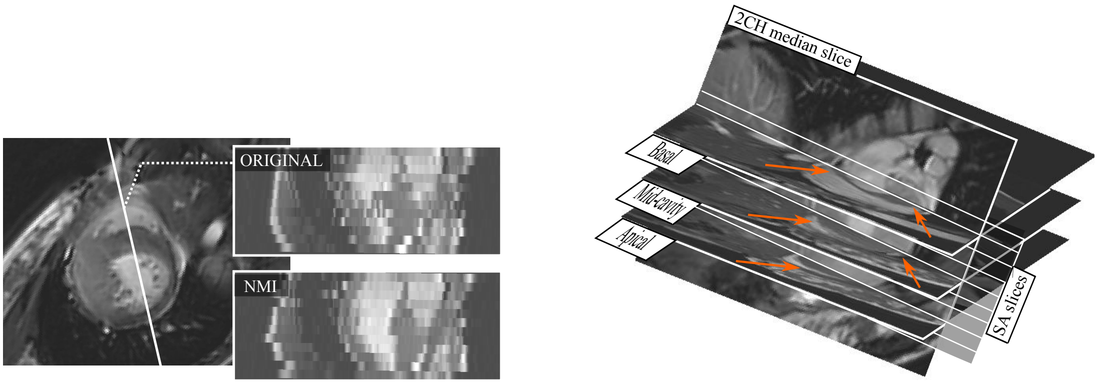

(a) Reformat slice in SAX to assess interventricular septum and LV lateral wall smoothness.

(b) Evaluation of SAX and 2CH alignment by assessing the myocardial match (arrows).

Figure 4.9: Evaluation protocol: 4.9a reformat slice used to evaluate SAX alignment, 4.9b evaluation approach for the alignment between SAX and 2CH.

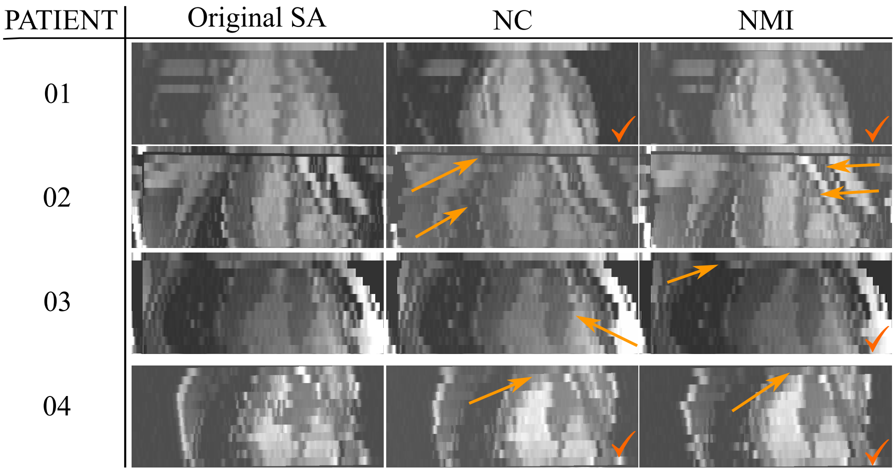

Figure 4.10: Evaluation of the slice misalignment correction using the short-axis reformat slices showing the interventricular septum. Arrows point to slices that were not successfully aligned. Checks indicates successful aligned images.

Both observers rated each alignment as successful, wrong or not-assessable. Then, only those evaluations with an agreement between observers above 66% were retained. At the end, 18 out of 24 evaluations were retained.

It can be observed from table 4.3 that NMI performed better than NC. Average NMI performance from both observers was 70.9%. Note also that observers had a high variation in their evaluation of NC results. Indeed, the agreement between observers is the lowest for NC (70%). Finally, we sought to establish how slice misalignment correction performed at each level of the SAX image; thus, the instances of wrong alignments in SAX planes were divided following their location, at basal, medial or apical zones. Table 4.4 presents the resulting division of SAX myocardial misalignment instances. It can be noted that most of the misalignments are located in the apical zone (8 out of 15). This

Table 4.3: Percentage of slices successfully aligned for input images (original) and the output of the method to correct slice misalignment using NC and NMI similarity measures.

	Original	NC	NMI
Observer 1	35.5%	53.7%	**68.2**%
Observer 2	33.8%	37%	**73.5**%
Retained evaluations	7 out of 8	5 out of 8	6 out of 8
Agreement	78.6 %	70%	**80.6**%

can be caused by the low quality of the apical zone depicted by cine-SAX images.

Table 4.4: Total instances of myocardial mismatch between each SA-view slice and the medial 2CH/4CH-view at apical, medial and basal levels of the left ventricle.

	2CH				4CH			
	Apical	Medial	Basal	Total	Apical	Medial	Basal	Total
Input	2	6	2	10	6	9	8	23
NMI	**3**	2	1	6	**5**	2	0	7

This sequential approach using NMI metric was used to correct for slice misalignment in cine-SAX images for the characterization of HCM (cf. Chapter 5). In that study, cine acquisitions from 30 patients were corrected and assessed visually by a cardiologist and those images with slices not successfully aligned were extracted from the study.

4.4 Evaluation of the ADTW-based registration of dynamic CT and cine-SAX

Two aspects of the registration of cine-SAX to dynamic CT images proposed in 3.2 were evaluated: (i) the ADTW temporal alignment, and (ii) the spatial alignment. They were evaluated using annotated time and spatial landmarks, respectively. Besides, in spatial alignment, we evaluated four multimodal similarity measures using the protocol proposed by (SKERL et al., 2006).

4.4.1 Data

ECG-gated CT and MRI pre-intervention acquisitions of 10 patients undergoing CRT (cardiac dyssynchrony), were used to evaluate the ADTW-based registration. On the one hand, a 3.0 Tesla MRI system (Philips Achieva, Eindhoven, The Netherlands) was used to acquire B-TFE cine images with SENSE coils. Cine-MRI SAX volume sequences had between 10 and 12 slices. Slice size was 256×256 pixels with a spacing varying from 1.56×1.56 mm^2 to 1.25×1.25 mm^2. The spacing between slices varied from 11.32 mm to 7.5 mm. Temporal resolutions were 30 phases for half the patients and 40 phases for the other half. Dynamic CT images were acquired with a GE LightSpeed VCT system. CT images had a resolution of 512×512 pixels for XY plane with the Z resolution varying from 212 to 157 slices. Voxel spacing has a typical value of $0.27\times0.27\times0.625$ mm^3 with little variations between patients. Temporal resolutions were 10 and 20 phases for 2 and 8 patients, respectively. Iodine contrast agent was used to enhance the left ventricle (100 a 150 cm^3 being at 300 mg/ml or 350 mg/ml).

4.4.2 Evaluation of the temporal alignment

The evaluation of the temporal alignment between cine-SAX and CT images after the ADTW alignment of normalized correlation curves (cf. 3.2.1) is difficult because ECGs were not available. Thus, a fiducial evaluation using annotated end-systolic phases in both dynamic acquisitions, was performed. We sought to measure the accuracy of the alignment of end-systolic phases by the time warping curve ($\tilde{F}$). This accuracy is used as an indicator of the quality of the alignment over time.

The end-systolic alignment was defined as the two distances (d^{CT} and d^{SAX}) from annotated end-systole and aligned end-systole along CT and cine-SAX time axes, respectively (cf. Figure 4.11). These distances are measured from the projection of the portion between misaligned end-systolic phases along the output time warping curve $\tilde{F}$ (red portion of the time warping curve in Figure 4.11). Given the differences in temporal resolution in input images, these distances were normalized with regards to the number of cardiac phases in order to made them comparable between both, multimodal images and patients:

$$\bar{d}^{\mathrm{CT}} = \frac{d^{\mathrm{CT}}}{\top^{\mathrm{CT}}}, \quad \bar{d}^{\mathrm{SAX}} = \frac{d^{\mathrm{SAX}}}{\top^{\mathrm{SAX}}}, \tag{4.1}$$

where $\bar{d}^{\mathrm{CT}}$, $\bar{d}^{\mathrm{SAX}}$ are the normalized distances along the time axes of dynamic CT and cine-SAX, respectively, and $\top$ the number of imaged cardiac phases.

The end-systolic phase was annotated in cine-SAX images by the MRI machine (τ_{ES}^{SAX}). The annotation of this phase in CT (τ_{ES}^{CT}) was performed manually by localizing the cardiac phase when the aortic valve closes (AVC).

Figure 4.12 shows the normalized distances (in %) after temporal alignment using a linear, classical DTW (slope constraint S=0, cf Figure 3.9a) and adaptive DTW, as presented in 3.2.1.2 (Equation 3.19). It can be noted that DTW outperformed linear alignment except in one case (CT and MRI alignment of patient 9). The average performance of ADTW improved by 7% compared to linear matching and by 2% compared to classical DTW. Standard deviation values of the performance indicator for CT and cine-SAX are reported in Table 4.5. It can be noted that ADTW had the lowest deviation which means that it is also more precise than the other approaches.

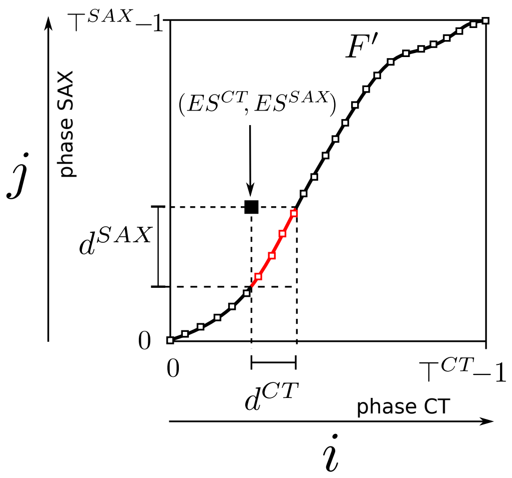

Figure 4.11: Distance to annotated end-systolic phases (ES^{CT},ES^{SAX}) along the time axis of dynamic CT (d^{CT}) and the time axis of cine-SAX (d^{SAX}. These distances are the length of the projection of the portion between misaligned end-systolic phases along the time warping curve $\tilde{F}$ (in red) to the time axes of CT and cine-SAX, respectively.

Table 4.5: Standard deviation of dynamic CT and cine-SAX distances to ES for ADTW, DTW (S=0) and linear matching.

	ADTW S adapted	DTW $S = 0/0$	Linear
CT	**3.33%**	3.91%	8.00%
Cine-SAX	**4.04%**	4.21%	7.86%

These results proved that ADTW has the ability to align CT and cine-SAX images in time using NCC curves.

4.4.3 Evaluation of the spatial alignment

Four mutual information measures were evaluated using the protocol of (SKERL et al., 2006). Then, the optimal MI-measure was included in a multi-image registration procedure.

4.4.3.1 Similarity measure selection

Viola-Wells MI (VWMI), Mattes MI (MMI) and normalized MI (NMI) were evaluated following the protocol of (SKERL et al., 2006).

Ground truth. These metrics were evaluated using peak-R cine-SAX and peak-R CT images. The acquisitions from one patient were selected such that CT and cine-SAX images were smooth: CT without discontinuity artifacts nor metal artifacts and with

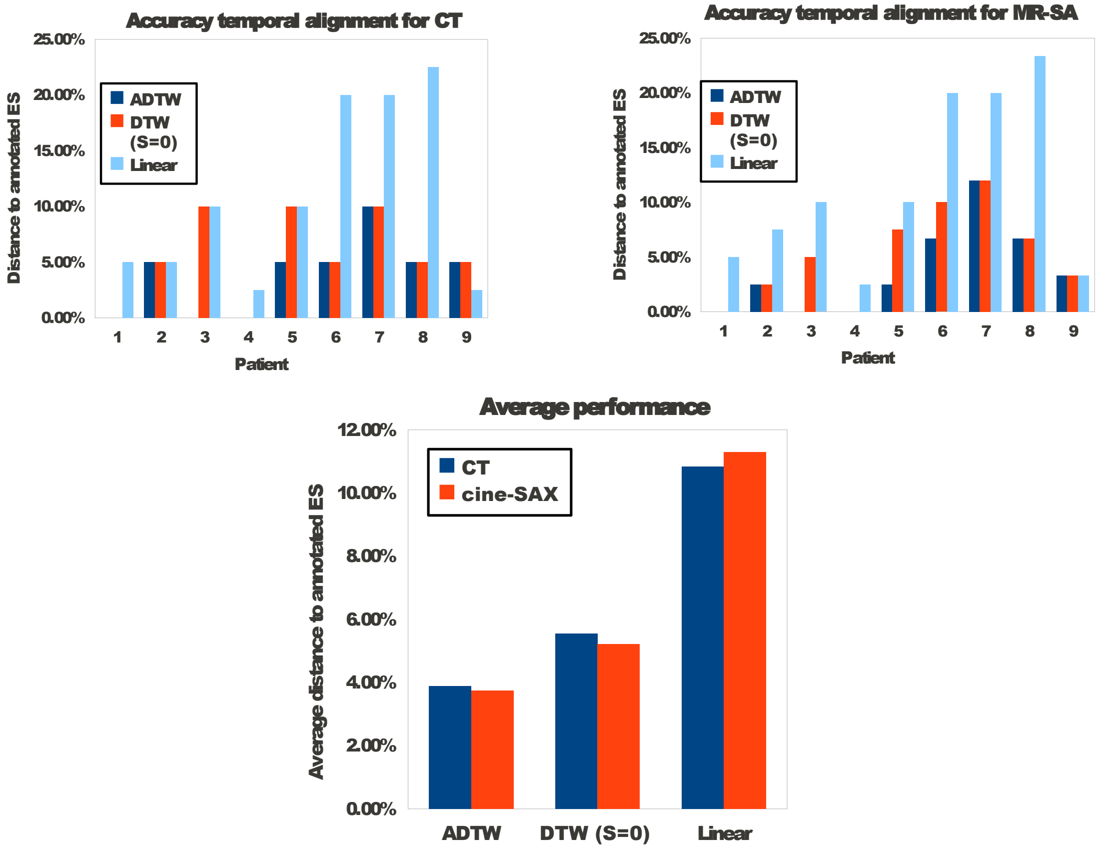

Figure 4.12: Evaluation of the temporal alignment for adaptive DTW (ADTW), DTW using a three-neighbors connectivity ($S = 0$) and linear matching. (Top-left, top-right) Evaluation of ADTW (blue), DTW with S=0 (red) and linear (light blue) alignment per-patient using the distance to ES as a percentage of RR-interval, for dynamic CT and cine-SAX, respectively. (Bottom) average accuracy per method for dynamic CT (blue) and cine-SAX (red).

smooth tissue gray levels; cine-SAX without slice misalignment nor metal artifacts and with low gray level artifacts due to magnetic field inhomogeneities. Patient's ground truth ($\mu^G T$) was obtained as follows: first, anatomical landmarks located into the papillary muscles were used in a fiducial registration; second, rigid registration was performed using VWMI, MMI and, NMI using fiducial registration output as initial transform; then, MI-registrations were qualitatively assessed and those showing an improvement against fiducial registration were manually adjusted. This manual alignment aimed to improve the registration output.

One patient fulfilled cine-SAX and CT requirements. For this patient, only NMI and MMI registrations improved fiducial alignment. We selected the one from MMI. Figure 4.13 shows the gold standard after the manual alignment of the result of fiducial and MMI registrations. Cine-SAX images were resampled to the CT space using the resulting transformation and bi-cubic splines interpolation. It can be observed that, visually, the matching between these images is satisfactory. For instance, the matching between boundaries of the blood pool in CT and cine-SAX images is improved (dotted white and yellow lines in Figure 4.13). Even if this alignment is an estimation of the gold standard, it provides elements to evaluate the performance of the similarity measures. However, the accuracy must be interpreted carefully.

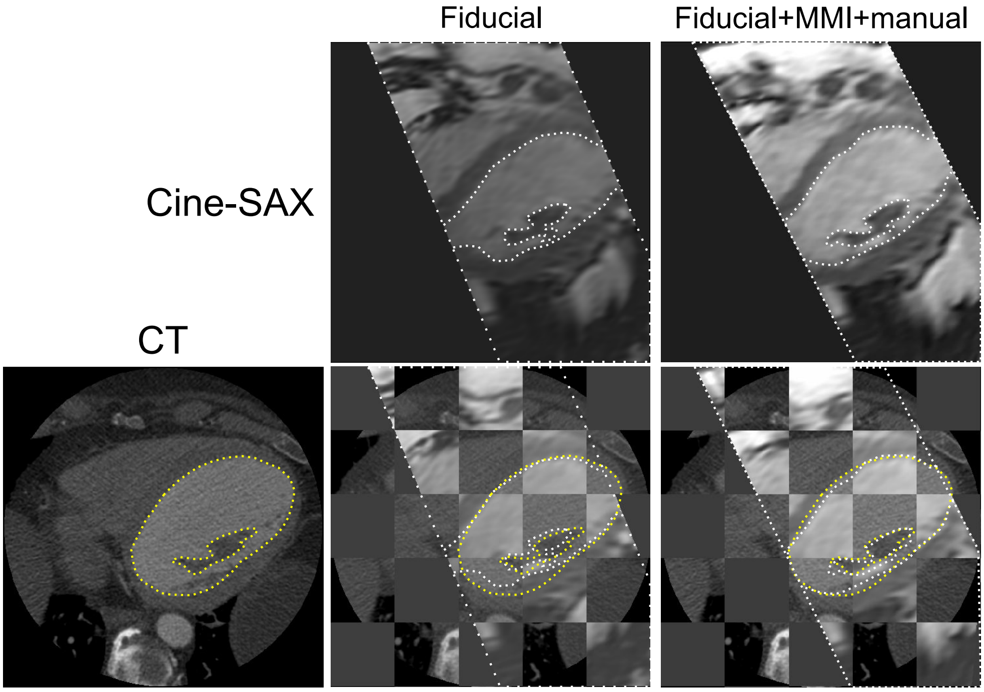

Figure 4.13: Computation of the ground truth transformation between CT and cine-MRI for similarity measures analysis. First, cine-SAX and CT images at peak-R are aligned using fiducials and MMI registrations. This alignment is then refined manually to obtain an estimation of the gold standard transform. (Bottom-middle and bottom-right) checkerboard between aligned cine and CT images after fiducial alignment (middle) and fiducial and manual alignment (right). Dotted lines were drawn manually to depict the LV endocardial contour and papillary muscles for CT (yellow) and cine-MRI (white). The cine-SAX field of view is also represented (white dotted lines).

Similarity measures evaluation. The protocol of (Skerl et al., 2006) was applied using the same parameters as in the previous studies. Normalization was performed using the CT resolution because cine-SAX images are in CT space. CT resolution was 512×512×161 voxels and 0.352×0.352×0.625 mm^3.

As previously, the similarity measures were implemented using elastix library (Klein et al., 2010). The parameters used for the computation of the similarity metrics were: 420000 samples, 32 histogram bins (VWMI, MMI, NMI), 0.4 for the Gausian kernel size in VWMI computation (input images were normalized in this case).

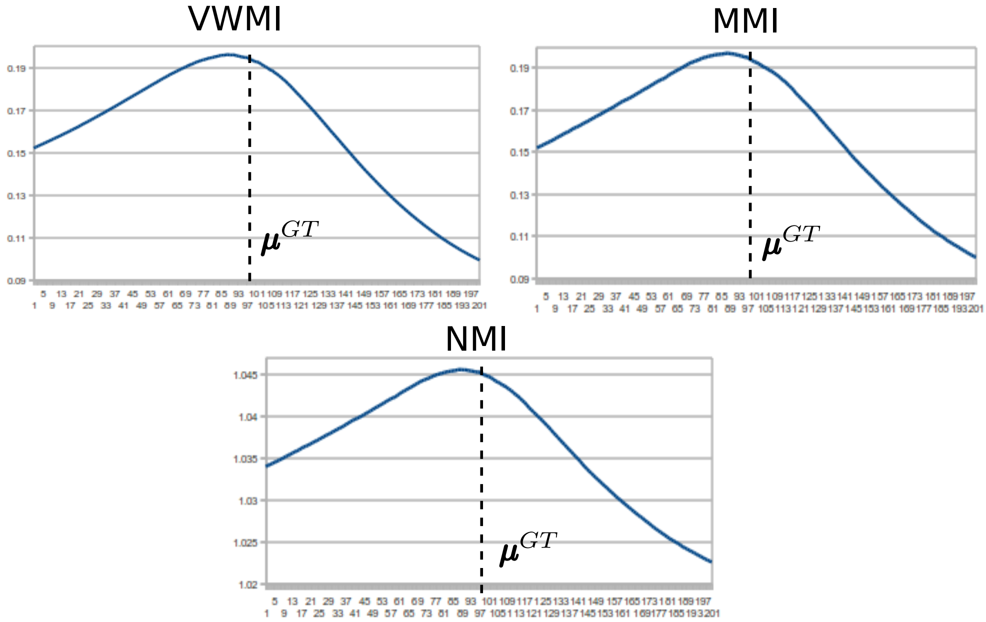

Figure 4.14: Similarity measure profiles between a cine-SAX and CT images along a sampling line .

Results. Figure 4.14 shows a profile per metric along a sampling line. The profiles are smooth and, visually, they present a quite similar profile: one flat maximum without local minima around it.

Resulting descriptors are in Table 4.6. It is observed that no measure ranked first for all indicators. One point to highlight is that, yet the ground truth computation used MMI, this metric obtained the worst ACC. NMI was the best in terms of NOM. CR is the same for all metrics which is explained by (Skerl et al., 2006) as a behavior in a multimodal registration setup. DO is almost the same for all metrics both, near GT and far GT, which is in agreement with the visual analysis of the profiles in Figure 4.14. From these results, the best tradeoff of ACC, DO, CR, NOM and RON was obtained by NMI. Thus, NMI was included in a multi-image registration procedure.

4.4.3.2 Evaluation of the multi-image registration of dynamic CT and cine-SAX

Based on the previous study, the multi-image registration of dynamic CT and cine-SAX images was parameterized as follows: multiresolution registration using one or two levels, NMI metric estimated from 75000 random spatial samples, regular gradient descent optimizer (maximum step: 0.5; minimum step: 1e-3), linear interpolator during the registration procedure, 3D Euler rigid transform, and bi-cubic splines interpolator to apply the final transform. This registration was implemented using the elastix library (Klein et al., 2010).

Table 4.6: Similarity measure properties between cine-SAX and CT images in a rigid registration framework. Best values per column are in bold type. The arrows indicate if the indicator has to be maximized ($\nearrow$) or minimized ($\searrow$). ACRONYMS – *ACC*: accuracy, *CR*: capture range, *DO*: distinctiveness of optimum, MI: mutual information, MMI: Mattes MI, NMI: normalized MI, *NOM*: number of minima, *RON*: risk of nonconvergence, VWMI: Viola-Wells MI.

	$ACC(\searrow)$	$DO(\nearrow)$		$CR(\nearrow)$	$NOM(\searrow)$	$RON(\searrow)$	
Metric		near GT	far GT			near GT	far GT
VWMI	**0.35**	0.01	**0.03**	0.2	1.34	3.97E+3	2.61E+2
MMI	0.89	0.01	0.02	0.2	1.27	**2.98E+3**	**2.07E+2**
NMI	0.39	0.01	**0.03**	0.2	**1.08**	3.60E+3	2.21E+2

Landmark error was used to evaluate the spatial alignment. It was calculated from anatomical landmarks located into papillary muscles. These landmarks were placed in two steps. First, at least one landmark ℓ_l^{SAX} was placed into each papillary muscle appearing in medial slices of cine-SAX at both peak-R and annotated end-systole phases. Then, the SAX plane was located in the CT image mimicking a cine-SAX acquisition: (i) localization of the LV great-axis of the two-chamber plane (2CH) from an axial cut containing left and right ventricles; (ii) estimation of the LV great-axis of the four-chamber plane (4CH); (iii) localization of the LV short-axis plane. After SAX plane localization in CT image, corresponding landmarks ℓ_l^{CT} were placed in CT following the same procedure as for cine-SAX. The landmark error was then measured for each patient as follows:

$$e = \frac{1}{\mathcal{L}} \sum_{l=0}^{L-1} \sqrt{\left\| \tilde{T}_{\mu}^{-1}(\ell_l^{CT}) - \ell_l^{SAX} \right\|^2}, \tag{4.2}$$

where ℓ_l^{CT} and ℓ_l^{SAX} are two corresponding landmarks placed in the CT and cine-SAX images, respectively, and $\mathcal{L}$ is the number of landmarks.

Here, it should be noted that this metric cannot, in most cases, reach a value of 0. Indeed, because selected landmarks are placed independently, there is not a rigid transformation that may perfectly align all of them. In order to estimate the minimal landmark error that may be reached by a rigid transformation, a fiducial registration (using placed landmarks) was applied for each patient. This registration computes the parameters of the rigid transformation that minimizes the sum of squares of the distances between corresponding fiducials. A least-squares solution for this fiducial registration was provided by (HORN, 1987) using unit quaternions. The output of the fiducial registration corresponds therefore to the optimal registration according to the landmark error. The average error after fiducial registration was 2.2 mm.

Figure 4.15 shows the landmark error e after three different registration approaches: (i) a static registration considering only one cardiac phase (peak-R), (ii) a multi-image

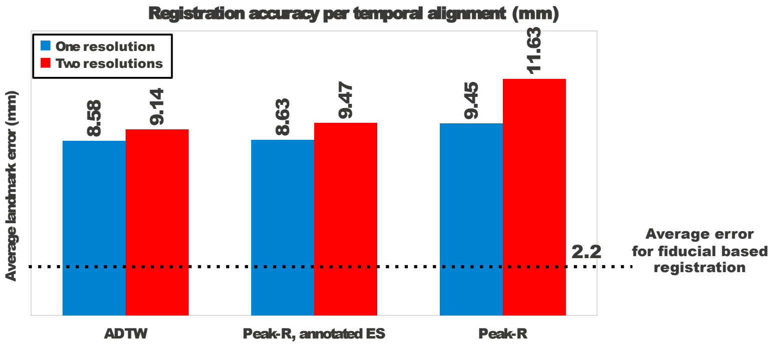

Figure 4.15: Spatial registration accuracy for cine-SAX to dynamic CT registration: average fiducial error after iconic registration using adaptive DTW (all phases: multi-image), peak-R/annotated-ES (two phases: multi-image) and peak-R (one phase: static) temporal alignment for one and two levels of resolutions. Please note that the average error after fiducial based registration is showed with a dotted line.

approach considering two cardiac phases (peak-R and annotated ES), and (iii) the multi-image ADTW registration using all cardiac phases. The three approaches were tested for one and two levels of resolutions. It can be noted that they had an average e greater than 2.2 mm (the average of e after fiducial registration). Fiducial error suggests that multi-image methods outperformed the static method. ADTW performance is slightly better than peak-R/annotated-ES but the ADTW multi-image approach is better because it is fully automatic.

These evaluation is limited because cine-SAX slices are thick ($\geq$ 8 mm). This explains why the fiducial error remains quite high for multi-image and static procedures compared with the fiducial registration.

4.5 Evaluation of multiview US to cine-SAX registration

The US registration method was previously proposed by (Tavard, 2012) in the context of US to CT registration. In addition to the application to cardiac MRI, this work proposes two important modifications: (i) the use of an adapted step pattern to both, handle the differences in time resolution and get a more physiologically realistic warping between cardiac phases; (ii) the optimization of multiview STE acquisition in a single optimization procedure (combined optimization) (cf. 3.3).

This study aims at evaluating the ADTW-based registration using a cine-SAX image dataset. It has three parts: (i) evaluation of the required number of Fourier descriptors; (ii) qualitative assessment of the metric convergence; (iii) visual evaluation of the resulting registration.

The proposed ADTW-based registration method was evaluated on US and cine-SAX acquisitions. This dataset is a subset of the one used for HCM characterization in Chapter 5. For each patient, it includes cine-SAX acquisitions and STE images (2CH

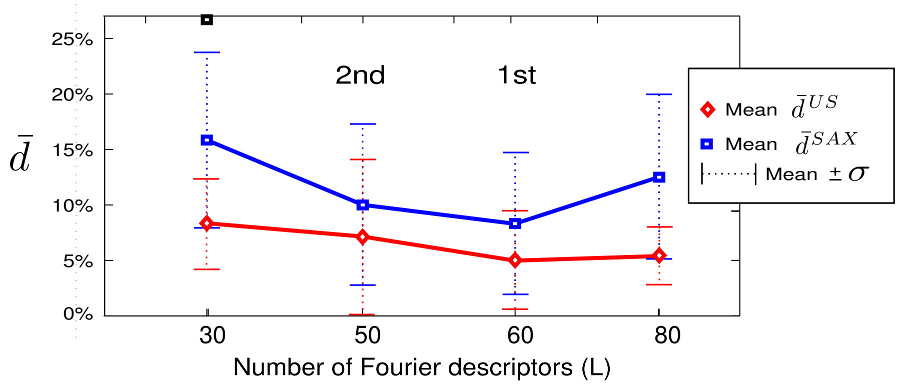

Figure 4.16: Evaluation of DTW alignment using $L \in \{30, 50, 60, 80\}$. $\bar{d}^{\mathrm{US}}$ and $\bar{d}^{\mathrm{MR}}$ are the distances of ES to $\tilde{F}$vfor US and MRI, respectively, expressed as a percentage of the RR-interval.

and 4CH). Details of the acquisition protocols are provided in Chapter 5.

In order to apply the registration process, relying on a contour-to-surface registration, the cine-SAX images have been segmented using ITKSNAP (cf. 5.3.2.2 for details and examples).

4.5.1 Selection of the number of Fourier descriptors

Because the ADTW-metric optimized during US to cine-SAX registration relies on the Fourier description (FD) of input geometries (cf. Equation (3.23)), the best number of descriptors needed to register multiview STE-contours, must be selected. The number of FDs fully describing a given contour equals its number of points. (TAVARD, 2012) used 50 FDs to register STE-4CH geometries to LV surfaces from CT images. Given that the spatial resolution of STE-geometries and cine-SAX geometries varies, we sought to find the optimal number of FDs to register them.

A random subsample of 4 patients were selected from the HCM dataset for this purpose. From this subsample, we performed the registration between STE-4CH and cine-SAX images using the ADTW-based approach in 3.3, using S=0. The number of Fourier descriptors tested for each sample was 30 (low resolution, below the typical number of points in STE geometries), 50, 60 and 80 (high resolution, above the typical number of points in STE geometries). The normalized distances to annotated end-systolic phases in STE-4CH ($\bar{d}^{US}$) and cine-SAX ($\bar{d}^{SAX}$) to the optimal time warping curve after registration ($\tilde{F}$), were used to select the optimal number of Fourier descriptors. These distances to ES were described in 4.4.2.

The mean and standard deviation of the normalized distance are represented in Figure 4.16. It is observed that the number of FDs has an influence in the performance. The best temporal alignment was obtained for L=60. Given that STE contours do not have geometrical components of high frequency as cine-SAX contours (STE contours are already smooth), this result shows that contour sequences should be compared using their low frequency FDs. Figure 4.16 also shows that US sequences were better aligned than cine-SAX sequences. This can be explained by the fact that US sequences have a higher temporal resolution than cine-SAX. Then, an error in one phase in US acquisition has a lower impact in the overall performance than the same error in cine-SAX.

4.5.2 Qualitative assessment of the metric convergence

The ADTW-based registration procedure was initialized with a fiducial placed in the apex (plane origin). The evolution of the ADTW-metric is presented in Figure 4.17 for a combined registration of STE-2CH and STE-4CH to cine-SAX, a STE-2CH to cine-SAX registration, and a STE-4CH to cine-SAX registration. It can be noted that all registrations converge. The number of iterations needed to converge is almost the same for the three procedures. However, the combined approach performs the registration of both STE views in a single optimization. Thus, given that the number of iterations required by the combined approach is far below the sum of those required by STE 2CH and 4CH registrations, the combined registration seems to be more appropriated.

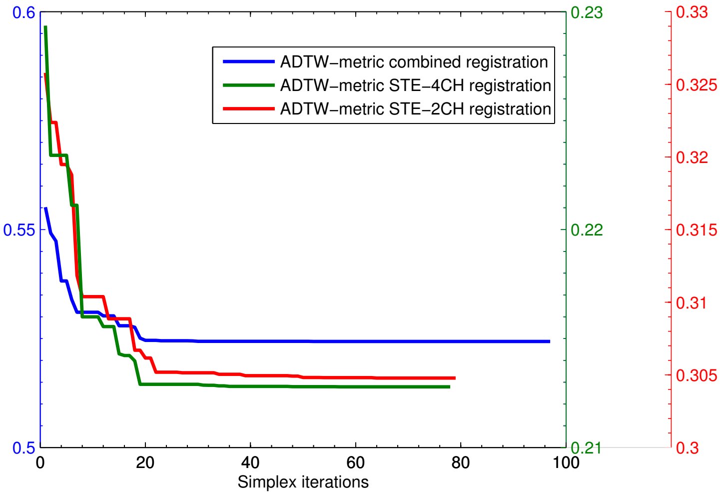

Figure 4.17: ADTW-metric evolution for a combined registration of STE-4CH and 2CH to cine-SAX (blue), STE-4CH to cine-SAX registration (green) and STE-2CH to cine-SAX registration (red).

4.5.3 Evaluation of the spatial alignment

STE-2CH and 4CH geometries were registered using the ADTW-based method proposed in 3.3, with an adapted slope constraint (S, Equation (3.19)). Given the lack of gold standard, the alignment of the STE-geometries and the cine-SAX image was visually assessed by a cardiologist at peak-R (end-diastole). For this purpose, STE contours (color

Table 4.7: Performance of the US to cine-SAX registration, per SAX region.

	Basal	Medial	Apical	Total
Number of segments	40	40	40	120
Exploitable	40	40	25	105

coded by segment) were superimposed to the cine-SAX plane resulting from slicing the cine volume with output 2CH and 4CH US planes.

Fig. 4.18 exemplifies this in one patient. Each segment was rated as exploitable or non-exploitable (1 or 0). Table 4.7 describe the distribution of misaligned STE geometries with regards to the LV region (basal, medial, apical). The sum of exploitable segments over the total number of segments was used as performance indicator (5 segments aligned out of 6 segments in total). From an evaluation dataset of 120 segments (10 patients, 2 US views, 6 segments per view), 105 segments (87.5%) were aligned. All not-aligned segments were located at apical level. This behavior can be explained by the lack of detailed information at apical level in both, US an cine-SAX images.

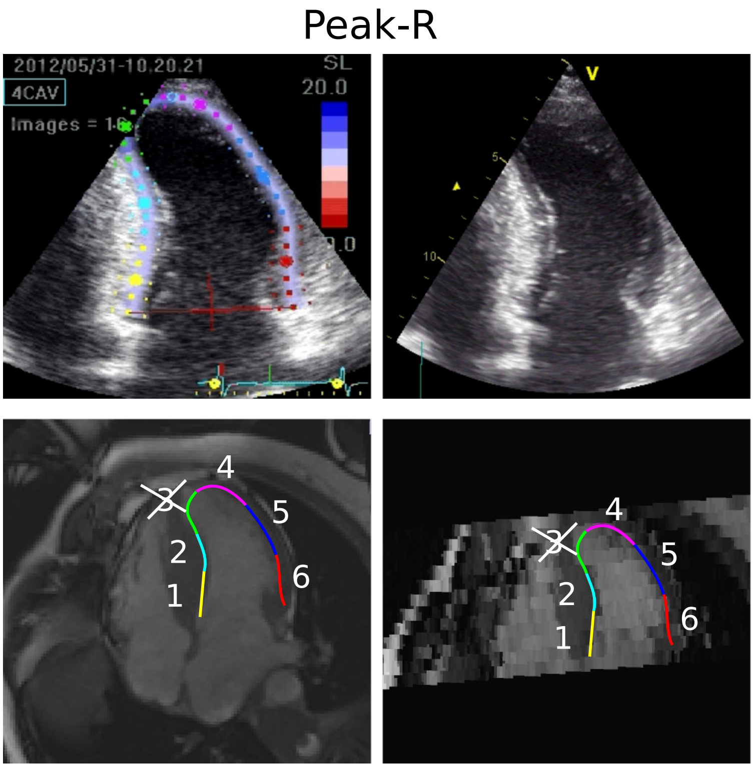

Figure 4.18: Instance of the visual assessment of the STE-4CH to cine-SAX registration. The matching of each STE-segment (1, 2, 3, 4, 5 and 6) with the myocardial wall from cine-SAX image, was assessed.

4.6 Conclusion

The evaluation of the multisensor registration methods proposed in chapter 3 was discussed in this chapter. Three main procedures were evaluated: cardiac MRI registration, cine-SAX to CT registration and US to CT/cardiac-MRI registration. Two main aspects of the registration process were considered: the selection of the metric and the quantification of the registration accuracy. An automatic protocol of evaluation of similarity measures properties was used to select the most appropriate.

The evaluation of similarity measures in the context of multiview intra-sequence LGE-MRI registration showed that the mean squares of structural images had the best performance. This finding revealed the benefits of the local entropy filter to measure the similarity between multiview images. To our knowledge, this is an evaluation that have not been reported yet in literature. However, given that our dataset of LGE-MRI did not present slice misalignment, the abilities of MS-S in correcting LGE-MRI slice misalignment were not further assessed. Thus, this study should be extended with LGE data presenting slice misalignment.

The evaluation of the similarity measure in the context of LGE- to cine-MRI registration showed that MI-based metrics are the most appropriate, with NMI having an slightly better performance. This metric was then used to align these inter-sequence cardiac MRI acquisitions in the HCM and cardiac asynchronism studies.

Two observers performed a qualitative evaluation of the slice misalignment correction procedure aiming at evaluating its performance in correcting cine-MRI of HCM patients. This analysis confirmed that NMI performs better than NC. However, it does not perform correctly at apical slices of cine-SAX images. In the next chapter describing the HCM study, the corrected cine-MRI will be fixed as the reference image to register US contours and LGE-MRI.

The method to register cine-MRI and CT images has also been evaluated. The metric analysis showed that MI-based metrics performs more or less the same, with NMI performing slightly better than the others. Using NMI as the metric, the evaluation of registration results was performed using annotated landmarks both, in time and space. The temporal alignment obtained from the ADTW of normalized correlation curves performed better than linear temporal matching and classical DTW alignment. This finding revealed the benefits of (i) performing the dynamic time warping procedure to account for the nonlinear change in ECG dynamics, and (ii) the adaptation of the slope constraint to take into consideration the differences in the temporal resolution of these multimodal acquisitions. Regarding the accuracy of the spatial registration using the multi-image registration procedure, annotated fiducials in papillary muscles revealed the benefits of including the dynamic information (multiple images) into the computation of the spatial alignment. However, given the thickness of cine-SAX slices, this evaluation remains quite coarse. It could be improved by considering more landmarks placed in complementary views, i.e. at the apex and the mitral annulus.

The registration of STE to cine-SAX was evaluated to (i) select the best number of Fourier descriptors needed to describe LV-geometries, (ii) evaluate the convergence of the ADTW-metric and (iii) assess the spatial alignment of STE geometries with the myocardial wall in cine-SAX acquisitions. First, the optimal number of FDs resulted in a value close to the resolution (number of points) of STE contours. Second, the combined procedure proved to converge as fast as using separate optimizations for each STE view, but with the benefit of using a unique procedure. Third, the evaluation of the spatial alignment was performed by a cardiologist who assessed the alignment for each contour in STE-geometries. This evaluation showed that apical segments account for all failed alignments. This can be explained by the lack of an appropriate description of the apical zone both, in US and in cine-SAX images.

The evaluated registration methods have been used in two studies related to HCM and cardiac asynchronism. These studies are detailed in the two following chapters.

References

Elen, A., Hermans, J., Ganame, J., Loeckx, D., Bogaert, J., Maes, F., and Suetens, P. (2010). “Automatic 3-D Breath-Hold Related Motion Correction of Dynamic Multislice MRI”. In: *IEEE Transactions on Medical Imaging* 29.3, pp. 868–878.

Glatard, T., Pennec, X., and Montagnat, J. (2006). “Performance evaluation of grid-enabled registration algorithms using bronze-standards”. eng. In: *Medical image computing and computer-assisted intervention: MICCAI ... International Conference on Medical Image Computing and Computer-Assisted Intervention* 9.Pt 2, pp. 152–160.

Hoppin, J., Kupinski, M., Kastis, G., Clarkson, E., and Barrett, H. (2002). “Objective comparison of quantitative imaging modalities without the use of a gold standard”. In: *Medical Imaging, IEEE Transactions on* 21.5, pp. 441–449.

Horn, B. K. (1987). “Closed-form solution of absolute orientation using unit quaternions”. In: *JOSA A* 4.4, pp. 629–642.

Ibanez, L., Schroeder, W., Ng, L., and Cates, J. (2005). *The ITK Software Guide*. Second. Kitware, Inc. ISBN 1-930934-15-7. http://www.itk.org/ItkSoftwareGuide.pdf.

Klein, S., Staring, M., Murphy, K., Viergever, M., and Pluim, J. (2010). “Elastix: a toolbox for intensity based medical image registration”. In: *IEEE TMI* 29.1, pp. 196–205.

Lebenberg, J., Buvat, I., Lalande, A., Clarysse, P., Casta, C., Cochet, A., Constantinides, C., Cousty, J., Cesare, A. de, Jehan-Besson, S., Lefort, M., Najman, L., Roullot, E., Sarry, L., Tilmant, C., Garreau, M., and Frouin, F. (2012). “Nonsupervised Ranking of Different Segmentation Approaches: Application to the Estimation of the Left Ventricular Ejection Fraction From Cardiac Cine MRI Sequences”. In: *Medical Imaging, IEEE Transactions on* 31.8, pp. 1651–1660.

SANDOVAL, Z. and DILLENSEGER, J.-L. (2013). “Intensity-based similarity measures evaluation for CT to ultrasound 2D registration”. In: *IRBM* 34.4–5. Numéro spécial - RITS 2013, pp. 278–282.

SKERL, D., LIKAR, B., and PERNUS, F. (2006). “A protocol for evaluation of similarity measures for rigid registration”. In: *IEEE Transactions on Medical Imaging* 25.6, pp. 779–791.

TAVARD, F. (2012). “Recalage et fusion d’informations multimodales pour l’optimisation de la thérapie de resyncrhonisation cardiaque”. PhD thesis. Université de Rennes 1.

WARFIELD, S. K., ZOU, K. H., and WELLS, W. M. (2004). “Simultaneous truth and performance level estimation (STAPLE): an algorithm for the validation of image segmentation”. eng. In: *IEEE transactions on medical imaging* 23.7, pp. 903–921.

CHAPTER 5

Hypertrophic cardiomyopathy characterization

The fusion of STE and LGE-MRI images would provide insights about the abilities of STE to characterize myocardial tissue, especially for premature HCM when structural changes in myocardial tissue could be reversed. As stated in 2.4, previous studies have reported that regional myocardial strain and wall thickening are affected by regional myocardial fibrosis in patients with HCM (Popović et al., 2008). However, the relationship between STE-strain and fibrosis has not been clarified. (Saito et al., 2012) reported a bulleye analysis of strain and substrate information; however, this approach does not consider the underlying mismatch between them (i.e. they lack of precise registration between acquisitions). This is magnified when regional functional information from dynamic 2D acquisitions like 2D-US needs to be compared with substrate information from 3D acquisitions like LGE-MRI. In this case, functional information will be extracted from a planar cut of the heart instead of a volumetric image. This planar cut does not depict the function of an entire region in a bulleye. In this context, multisensor image registration arises as an appropriate tool to overcome these problems.

The multisensor fusion procedure for HCM characterization is illustrated in Figure 5.1. It involves the registration of LGE-MRI and STE images using cine-MRI as the reference image. Fibrosis is then extracted from LGE-MRI to analyze its relationship with strain provided by STE. Below we describe the aims of this study and the methods used (i) to fuse STE and LGE data and (ii) to assess myocardial fibrosis. Then the results, including the analysis of the relationship between strain and fibrosis, are provided for the studied population. The end of this chapter contains the conclusions and perspectives of this study.

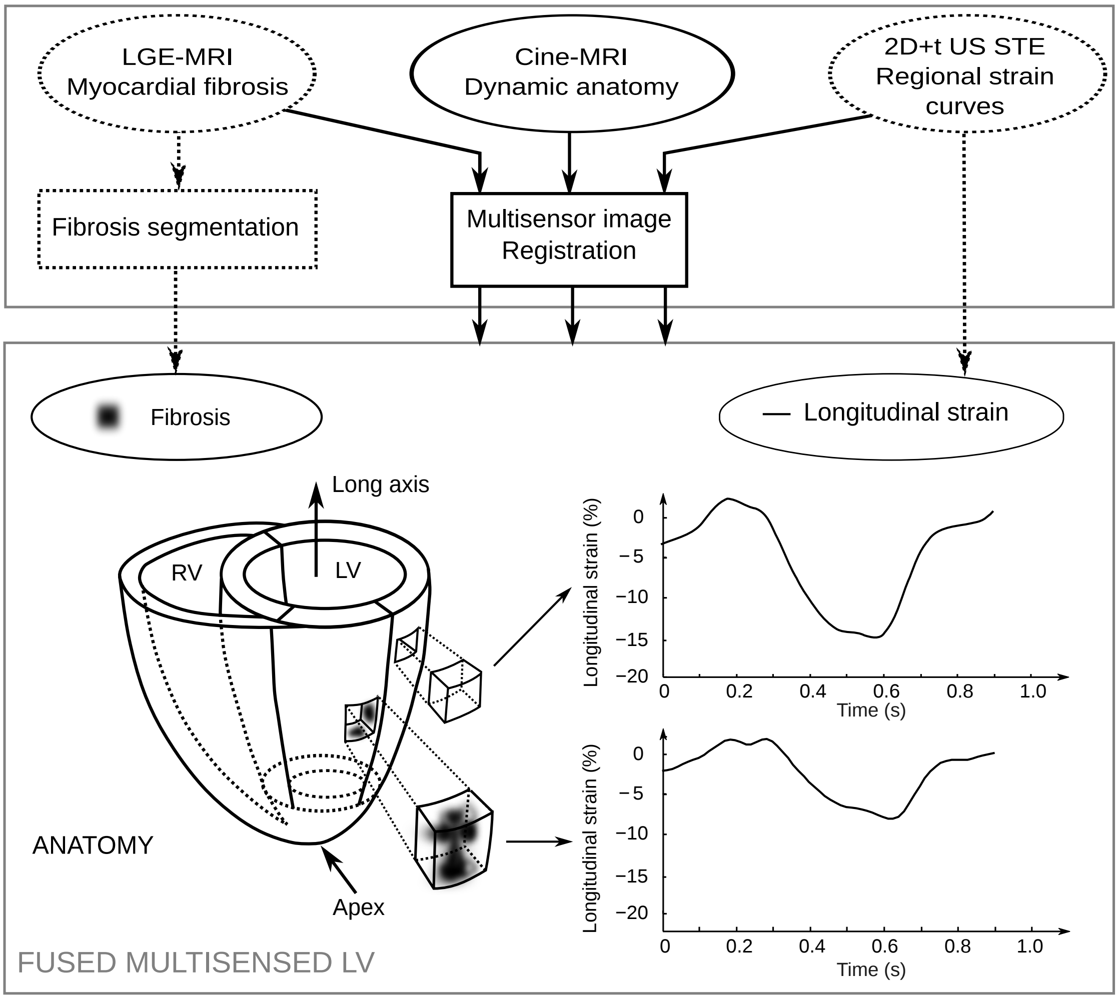

Figure 5.1: Multisensor image registration and fusion for the characterization of hypertrophic cardiomyopathy. (Top) Block diagram of the multisensor image sources and target information fused by multisensor image registration. (Bottom) Fused multisensed LV resulting from STE to LGE registration. Acronyms – MRI: Magnetic Resonance imaging, LGE: late gadolinium-enhanced, STE: speckle tracking echocardiography.

5.1 Objectives

This study aims to characterize hypertrophic cardiomyopathy. The objectives are:

1. To *associate* local myocardial fibrosis assessed from multiview LGE-MRI with regional myocardial strain resulting from speckle tracking echocardiography of multiview 2D+t US apical long axis view, acquired using a TTE probe.

2. To *describe* the statistical significance of indicators derived from regional strain curves with regards to the presence of macroscopic fibrosis.

5.2 Study population

This study was performed in collaboration with the CIC-IT [1] 804. It was approved by the ethics committee of CHU-Pontchaillou in Rennes, and was conducted in accordance with the Declaration of Helsinki. From January 2011 to April 2013, 30 HCM patients were prospectively and consecutively enrolled. All patients gave informed consent. HCM was defined as recommended by recent guidelines (Gersh et al., 2011). The inclusion and exclusion criteria were:

Inclusion criterion. Subjects carrying a primitive non obstructive HCM with left ventricular ejection fraction (LVEF) greater than 60%, in sinus rhythm.

Exclusion criteria. Prospective subjects with one of the following characteristics were disqualified from inclusion in this study: under legal age, unable to give a free and clear consent, refusal to sign their consent, contraindication to MRI (in particular, patients with an implanted cardiac stimulator/defibrillator at the moment of MRI acquisition), history of coronary artery disease, permanent atria fibrillation, left ventricular systolic dysfunction (LVEF $\leq$ 60%).

All patients had a clinical examination, a resting arterial blood pressure measurement (Dinamap Procare Auscultatory 100), a resting 12-lead electrocardiogram, a transthoracic echocardiography (Vivid 7, General Electric Healthcare, Horten, Norway) and a cardiac MRI (Philips Achieva 3T). Imaging protocols are described in the following section.

Table 5.1 presents the demographic statistics describing the retained population. These indicators are expressed as the average value ± standard deviation or as a percentage. Patients were mostly men (80%), Caucasians (73.3%) in adult age (46.8±15.5 years). In 14 patients (46.7%), HCM was diagnosed because of symptoms; in 16 patients (53.3%), the diagnosis was due to a routine screening (for systolic murmur, pathological ECG, familiar history of HCM). At inclusion, 53.5% of patients were in class NYHA 1, 42.8% class 2, and 3.6% class 3. This is corroborated by the NT pro BNP (a biochemical marker of heart failure), which shows that the population is symptomatic to HF (692.5 ± 1208.7). The demographic statistics described here were in agreement with the populations used in the literature (Popović et al., 2008) (Saito et al., 2012).

The medical treatment at inclusion are presented in Table 5.2: most of the patients are treated with beta-blockers (64.3%). This, and the other medical treatment at inclusion described in the table, are classical treatments for HCM patients. Medical treatment statistics were also in agreement with the literature (Popović et al., 2008) (Saito et al., 2012).

---

1. Acronym from the French “Centre d’Investigation Clinique Innovation Technologique”.
2. Screening: Systolic murmur, pathological ECG after sport participation, familiar history of HCM)
3. Symptoms: palpitation, syncope, dyspnea, stroke

Table 5.1: Demographic parameters in average value ± standard deviation or as a percentage of the retained population (28 patients). ACRONYMS – BP: blood pressure, NT pro BNP: biochemical marker of heart failure.

Age (years)	46.8 ± 16.05
Gender:	
Men	22 (78.6%)
Women	6 (21.4%)
Ethnic group:	
Caucasian	21 (75%)
Afro-Caribbean	7 (25%)
Circumstances of diagnosis:	
Screening of asymptomatic patients [2]	16 (57.1%)
Symptoms [3]	12 (42.9%)
NYHA at inclusion:	
1	15 (53.6%)
2	12 (42.8%)
3	1 (3.6%)
NT pro BNP(ng/ml)	692.5 ± 1208.7
Hypertension	6 (21.4%)
Systolic BP (mmHg)	131 ± 21
Diastolic BP (mmHg)	76 ± 9
Familial history of HCM	7 (25%)

Table 5.2: Medical treatment at inclusion. ACRONYMS – ACE inhibitors: angiotensin-converting-enzyme inhibitor, ARA2: Angiotensin II receptor antagonist, ICD: implantable cardiac defibrillator.

Current treatment at inclusion	
Beta-blocker	18 (64.3%)
Calcium inhibitor	2 (7.1%)
ACE inhibitors/ARA2/antialdosterone	8 (28.6%)
Antiagregant	5 (17.8%)
Anticoagulation	5 (17.8%)

5.3 Methods for image registration and fibrosis estimation

30 HCM patients were evaluated with MRI and apical 2, 3 and 4 chambers views echocardiography (US-2CH, US-3CH, US-4CH). We describe below the imaging protocol and methods used for the fusion of STE and LGE-MRI, and for the characterization of HCM.

5.3.1 Image acquisition

US and MRI were acquired for those patients fulfilling the selection guidelines at CHU-Pontchaillou in Rennes, in collaboration with the CIC-IT 804.

5.3.1.1 Echocardiography and STE

TTE acquisitions included parasternal apical LAX (4CH, 2CH, 3CH) and SAX acquisitions. A cardiologist, expert in echocardiography, performed TTE image acquisition at rest using a GE Vivid7 station (GE Healthcare, Horten, Norway). All data were stored on a workstation for off-line analysis (Echo PAC BT12, GE Healthcare, Horten, Norway). Echocardiography readers were blinded to the results of MRI, and they did not have any clinical data when reading these files. For each patient, conventional analysis of the echocardiogram preceded a 2D strain analysis. For each measurement, at least two cardiac cycles were averaged. Left ventricular diameters and wall thicknesses were assessed using the M-mode. The greatest thickness measured in the LV wall at any short-axis parasternal view was considered to represent maximal LV wall thickness. Left ventricular end-diastolic and end-systolic volumes (LVDD Vol, LVES Vol) and ejection fraction (EF) were measured by the biplane method of discs. The left ventricular end-diastolic diameter was also measured (LVEDD). These global parameters are analyzed in 5.4.1.

Strain measurement was based on the speckle tracking approach: to complete the analysis of the LV systolic function, the global longitudinal deformations were evaluated from standard two-dimensional images using a 2D strain software (Echo PAC BT 12, GE Healthcare, Horten, Norway). Image acquisition frame rate was 60-90 Hz (mean value 75 Hz). In brief, by tracing the endocardial borders on an end-systolic frame, the software automatically tracked the contour at subsequent frames. Adequate tracking was verified in real-time and was manually corrected, if necessary. The end-systolic phase was annotated in US acquisitions using the ECG and the closure of the aortic valve. An instance of a multiview STE acquisition is presented in Figure 5.2. STE traces and strain curves were limited to the RR-interval (using peak-R).

It can be noted from STE images (Figure 5.2) that the peak-strain, defined has the most negative value of the strain curve, varies. Echocardiographic guidelines state a peak strain lower or equal to -20% as an indicator of normal systolic function. Higher values are considered abnormal and are interpreted according to the particularities of the patient, including age and familiar history. A peak-strain above -15% is considered as an indicator of abnormal systolic function, and describe a bad contraction of the muscle. Note that most of the regional strain curves in Figure 5.2 present an abnormal peak-strain value.

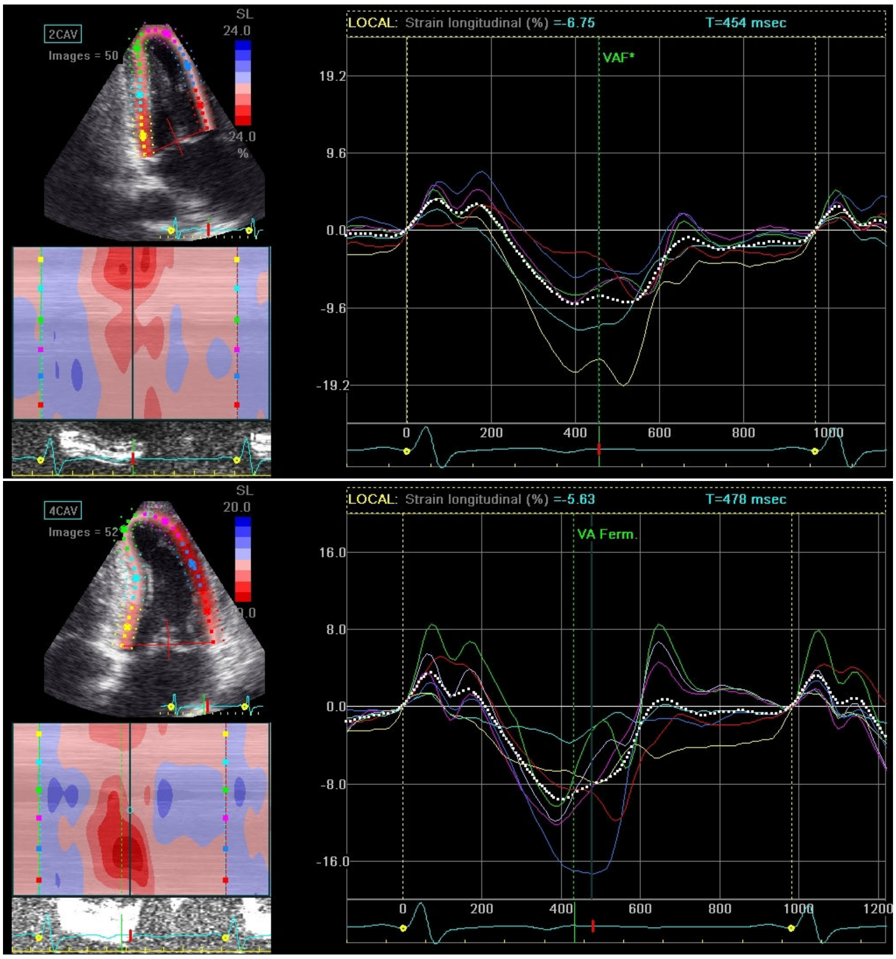

Figure 5.2: Multiview speckle tracking echocardiography from one patient with HCM diagnosis included in this study: (top) apical TTE image 2CH view, (bottom) apical TTE image 4CH view.

5.3.1.2 Cardiac magnetic resonance imaging

Cardiac MRI was performed with a 3T Achieva® clinical imager (Philips Medical Systems, Best, The Netherlands), using cardiac SENSE Coils (multicoil). Cardiac synchronization was performed using a four-electrode vectorcardiogram. Scout images were acquired initially to identify the cardiac axes. MRI acquisitions included cine-SAX, cine-LAX (4CH, 2CH), LGE-SAX and LGE-LAX (4CH, 2CH). An instance of cine and LGE images is presented in Figure 5.3. The following sequences were acquired:

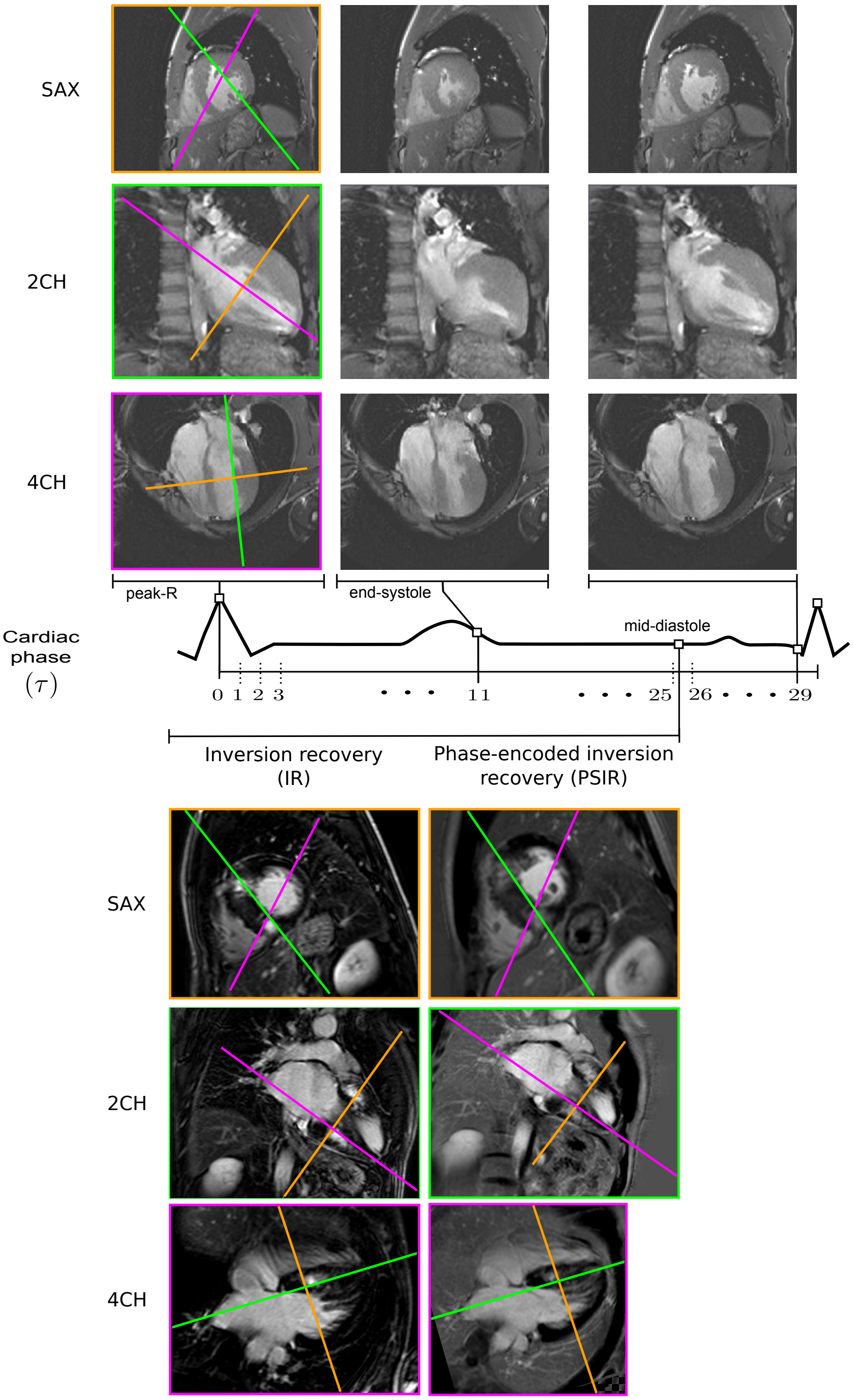

Figure 5.3: Illustration of cardiac magnetic resonance images from one patient with HCM diagnosis enrolled in this study. Lines correspond to the intersection of slices from complementary views. (Top) Cine-SAX, cine-2CH and cine-4CH at three different cardiac phases. (Middle) Cardiac phases on a ECG; for instance, cine-MRI is depicted at peak-R (corresponding to τ=0), end-systole (τ=11), and the last phase imaged (τ=29). (Bottom) LGE-SAX, LGE-2CH and LGE-4CH acquired using both, IR and PSIR techniques, at mid diastole (between τ=25 and τ=26).

Cine-MRI. Restrospective ECG-gated (RR-interval) breath-hold multiplanar SAX, 4CH and 2CH. Typical parameters for this acquisition were:

Acquisition. bTFE sequence, TR/TE/FA [4] = 3.79 ms/1.894 ms/45°,

Resolution. 30 cardiac phases, 256×256 pixels (in-plane) with 12 and 3-5 slices for SAX and LAX, respectively. In-plane pixel size=1.25×1.25 mm^2, slice thickness=8-10 mm,

LGE-MRI. IR and PSIR sequences. Restrospective ECG-gated acquisition at mid-diastole. Breath-hold volumetric SAX, 4CH and 2CH. Typical parameters for these acquisitions were:

IR Acquisition. Turbo field echo (IR-TFE). TR/TE/FA=4.01 ms/1.23 ms/15°, IR prepulse delay = 280 ms,

PSIR acquisition. TR/TE/FA = 4.50 ms/2.19 ms/15°, IR prepulse delay = 280 ms,

IR, PSIR resolution. 256×256 pixels (in-plane) with 16 and 12 slices for SAX and LAX, respectively. In-plane pixel size=1.25×1.25 mm^2, spacing between slices=5 mm, slice thickness=10 mm. Given that the spacing between slices is half the slice thickness, image slices overlaps in half their thickness. This resulted in an output image volume with slice thickness=5 mm. All IR and PSIR acquisitions were acquired following this procedure (slice overlapping). This aimed at improving the observability of small portions with fibrosis, i.e. to reduce the partial volume effect.

For each patient, the following global indicators were computed from cine-SAX images: maximal wall thickness, myocardial fibrosis volume (cf. 5.3.3.2), left ventricular end-diastolic diameter (LVEDD), left ventricular end-diastolic and end-systolic volumes (LVED Vol and LVES Vol, respectively), and left ventricular ejection fraction (LVEF).

From the 30 patients enrolled, two had non-exploitable LGE images (both, IR and PSIR sequences). Then, **28 patients were retained** in this study.

5.3.2 Image registration workflow

Figure 5.4 shows the procedure used to register STE traces to LGE images. Two registration processes are involved: LGE to cine registration and STE to cine-SAX registration. Cine images provide the dynamic geometry to be use in the registration of ultrasound images. The methods described in Chapter 3 were used to perform these registrations.

---

[4] TR: repetition time, TE: echo time, FA: flip angle (cf 1.3.4.1).

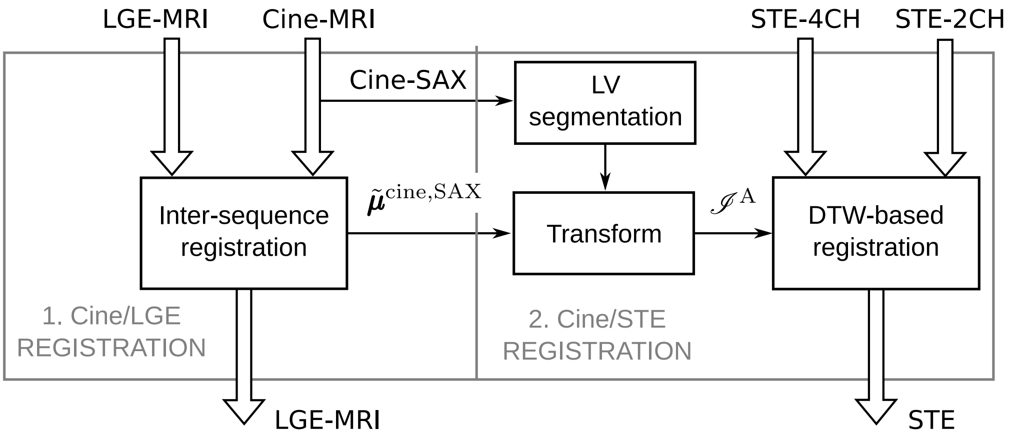

Figure 5.4: Block diagram of the multisensor registration procedure used to fuse cardiac MRI and STE acquisitions of HCM patients. Note that cine-MRI is the reference image. Acronyms – ⇒ connections representing multiview dynamic/static images.

5.3.2.1 LGE to cine registration

Cine- and LGE-MRI were registered with the procedure proposed in 3.1, using the sequential slice misalignment correction approach (cf. Figure 3.5) and NMI similarity measure. This procedure was used because (i) it was the only available at the moment where this HCM study started and (ii) slice misalignment in LGE acquisitions were low. The evaluation of this method was discussed in 4.3.3. Thus, slice misalignment in cine-MRI are corrected and the output image is registered to LGE-MRI using a rigid transformation. After registration, the set of transformations aligning cine-SAX slices ($\boldsymbol{T}_{\boldsymbol{\mu}^{\text{cine,SAX}}}$) are applied to the LV endocardium segmented in cine-SAX (cf. 5.3.2.2).

Figure 5.5 shows two instances of registration results for two patients with fibrosis (patient 01 in Figure 5.5a and patient 02 in Figure 5.5b). The upper rows display the images before registration, and the lower rows after registration. To illustrate the correction of slice misalignment, the result of the segmentation of the endocardium in cine-MRI before and after registration was overimposed on the images (the description of the considered segmentation method is in the next section). The images of patient 01 show an important initial misalignment between LGE- and cine-MRI, which is successfully corrected by the registration process (see, for example, the green arrow). For the patient 02, the initial alignment is already good and thus the rigid registration has a lower impact. However, as noticed in the previous chapter, the efficiency of the slice misalignment correction process is not optimal (see, for example, the red arrow).

5.3.2.2 STE to cine-SAX registration

STE LAX traces were registered to cine-SAX segmentations of the LV endocardium using the simultaneous DTW-based approach (cf. 3.3.1). STE to cine-SAX registration consists of three steps: LV-segmentation, propagation of the slice misalignment correction

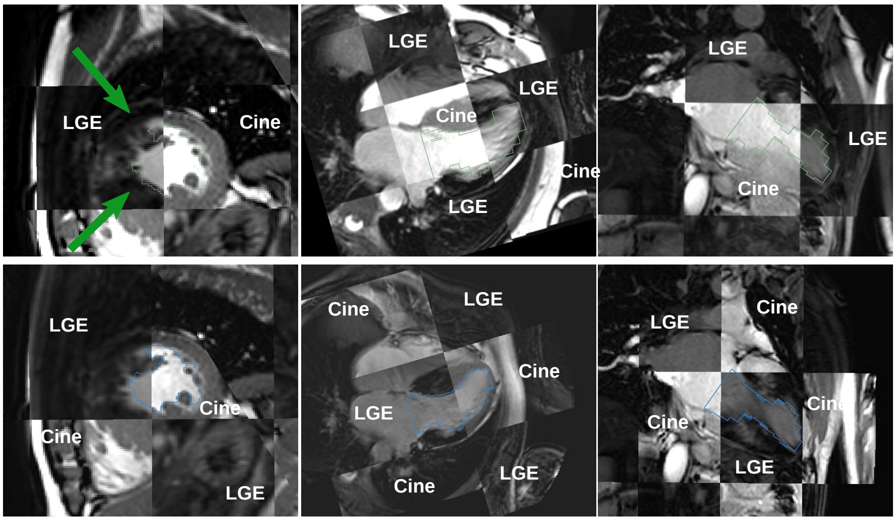

(a) Checkerboard after LGE to cine registration for patient 01: before registration (top) and after registration (bottom).

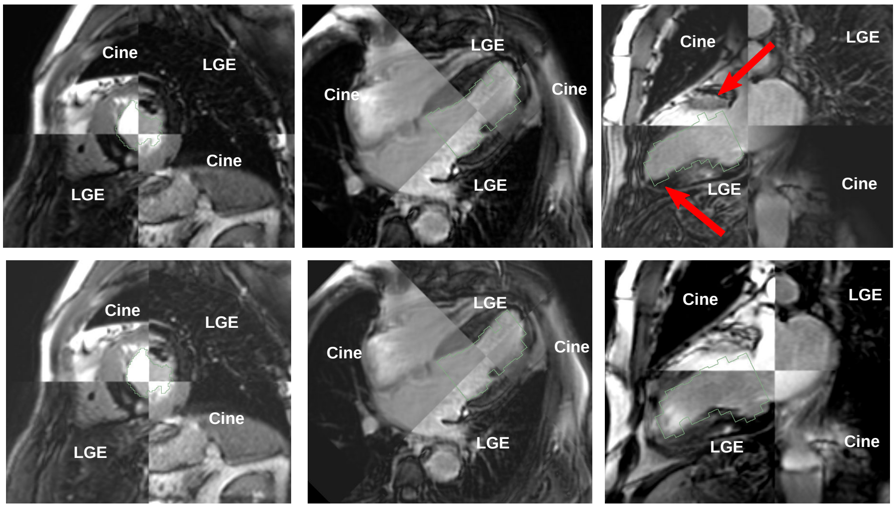

(b) Checkerboard after LGE to cine registration for patient 02: before registration (top) and after registration (bottom).

Figure 5.5: Checkerboard before and after cine-MRI slice misalignment correction and LGE to cine rigid registration. LV endocardial segmentation is also included (segmentation performed in cine-MRI before registration, using the method described in 5.3.2.2), for two HCM patients with fibrosis. From left to right: SAX, 4CH, 2CH.

and DTW-based registration.

LV segmentation. The dynamic LV endocardial surface was extracted from cine-SAX. ITKSNAP[5] implementation of the *active contour* segmentation (Yushkevich et al., 2006) was used to segment each dynamic slice in cine-SAX. Figure 5.6 illustrates a dynamic slice from a cine-SAX acquisition. This dynamic slice is then stored as an image volume with the z axis being the temporal axis and entered to the segmentation

---

[5] http://www.itksnap.org

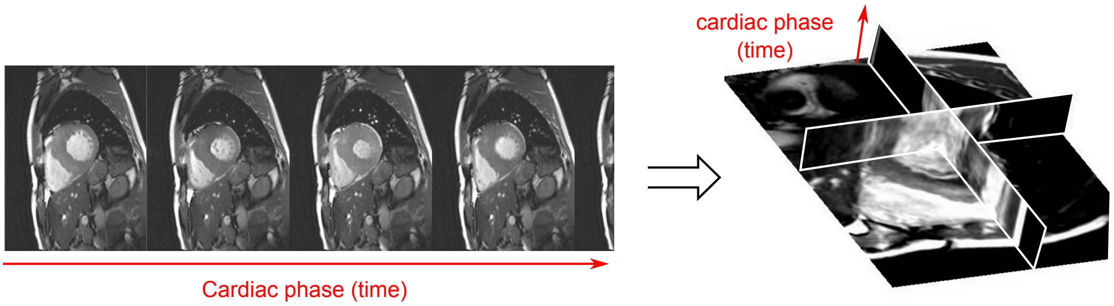

Figure 5.6: Dynamic slice from a cine-SAX image (left) depicted as a volumetric image (right).

procedure. The active contour method is based on *snake*[6] *evolution*. The evolution of the snake is governed by the front propagation equation. This equation describes the velocity of every point in the snake ($C_t \in \mathbf{C}_t$) at any particular time (t) and is given by:

$$\mathbf{C}_t = (\alpha \mathbf{g_I} - \beta \mathbf{k})\vec{\mathbf{n}} \tag{5.1}$$

where α and β are user-defined factors weighting the feature-based propagation force term and the curvature term, respectively. $\vec{n} \in \vec{\mathbf{n}}$ is the normal vector for a given point, $g_\mathbf{I} \in \mathbf{g_I}$ the region feature image (cf. step 2 below) component at that point and $k \in \mathbf{k}$ the k-level curvature at that point. The value of k, which is computed at each iteration, controls the shape of the evolving snake. Sharp corners in the snake boundary have high curvature, while points where the snake is straight have low curvature. The effect of the $-\beta k$ component is to slow down the evolution of the snake at places of high curvature, smoothing out the sharp corners that may otherwise be formed.

The segmentation of the LV blood pool in each dynamic slice followed the steps described below (cf. Figure 5.7a):

1. **ROI selection.** First, an LV region of interest (ROI) was manually defined by the user.
2. **Intensity region filtering.** We used a *region competition image* as the feature image in Equation (5.1) because the blood pool has a good contrast with the surrounding myocardium. In this approach, the feature image represents the regions with homogeneous intensity value. This feature image was computed by thresholding the dynamic slice intensities such that the LV blood pool appeared in the foreground and the myocardium in the background. The parameters used in the thresholding procedure were set by the user manually.
3. **Seed region initialization.** The active contour segmentation was initialized with spherical surfaces covering the blood pool along the z axis (i.e. along the time axis of the dynamic slice).

---

[6] *Snake* is the name given to a closed curve (or surface) that represents the object being segmented.

4. **Snake evolution.** This procedure was started to fit the boundaries of the initial snake (spheres) to the boundaries of the LV blood pool, using Equation (5.1). α and β were set by the user (typical values: 1.0 and 0.3, respectively).

If needed, a manual refining was performed to improve the resulting contour delineation after the active contour procedure described above. When all dynamic slices of cine-SAX were segmented, the dynamic LV surface was obtained by stacking these segmentations. Figure 5.7b and (c) present the resulting LV segmentation for patients 01 and 02, respectively, at end-diastole, end-systole and mid-diastole phases. It can be noted the gross thickness of the slices in cine-SAX.

Propagation of the slice misalignment correction. Output transforms correcting for slice misalignment in the slices of cine-SAX (cf. 5.3.2.1) were propagated to the labeled image resulting from the segmentation process. Because cine-MRI was set as the reference image during the registration of cine and LGE sequences, this propagation aligns LV segmentation to both, corrected cine-MRI and LGE-MRI.

DTW-based registration. STE-SAX traces were excluded because the geometry (contour) of the left ventricle depicted by this view does not allow to get a reliable registration. This was discussed by (Tavard, 2012). The initial parameters required for the registration of STE 4CH, 2CH and 3CH views (cf 3.3.1) were annotated in cine-SAX, as follows:

Origin. A common origin was annotated for all US planes at apical level such that initial 4CH, 2CH and 3CH planes intersect cine-SAX segmentation.

Aortic landmark. A landmark was placed into the ascending aorta to be used in 3CH plane initialization.

US planes normal. Normal vectors of 4CH and 2CH US planes were initialized with the normal vector of the slices in cine-4CH and cine-2CH, respectively. The 3CH plane was initialized by rotating the 2CH plane around a vector perpendicular to both, its normal and the vector pointing from the apex to the aortic landmark. The angle of rotation is given by the angle between the 2CH plane and the apex-aorta vector.

The evaluation of the STE to cine-SAX registration using acquisitions from HCM patients, was discussed in 4.5.

5.3.2.3 Propagation of STE traces to LGE-MRI

After STE to cine-SAX registration, STE traces were propagated to registered LGE-MRI following these steps:

1. The cardiac phase in the cine-SAX image that matches the one of LGE-MRI (i.e. the mid-diastole), was computed using the TriggerTime (0018,1060) and average

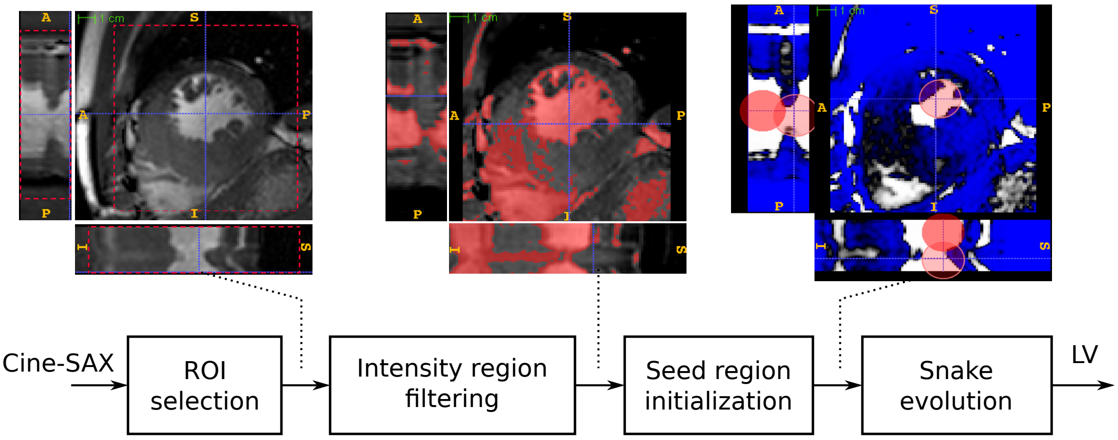

(a) Block diagram of the LV segmentation process using ITKSNAP.

(b) Resulting LV segmentation from the cine-SAX image of patient 01 at end-diastole ($\tau = 0$), end-systole ($\tau = 11$) and mid-diastole ($\tau = 25$).

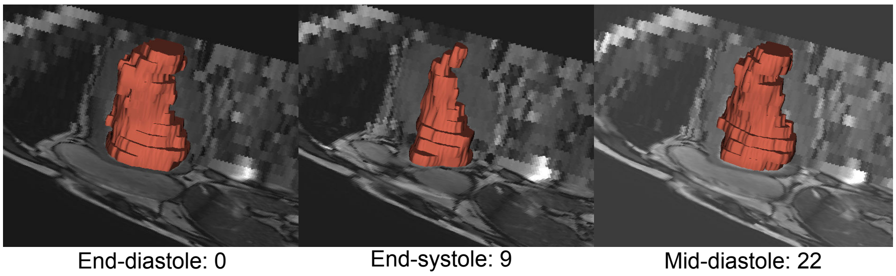

(c) Resulting LV segmentation from the cine-SAX image of patient 02 at end-diastole ($\tau = 0$), end-systole ($\tau = 9$) and mid-diastole ($\tau = 22$).

Figure 5.7: LV endocardial surface segmentation of two HCM patients. (Top) LV segmentation procedure. (Middle, bottom) Resulting dynamic LV endocardial segmentation. For the patient 01, the parameters defined by the user were: lower threshold = 389.70 and smoothness = 3.0 (region feature image), $\alpha = 1$, $\beta = 0.20$ and number of iterations = 100 (snake evolution). Acronyms – ROI: region of interest.

heart rate (0018,1088) DICOM tags extracted from these acquisitions, following Equation 3.12,

2. The matched cine-SAX phase was then propagated to both, 2CH and 4CH STE acquisitions, using the DTW warping time functions resulting from the registration of cine-SAX and multiview STE (cf. 5.3.2.2),
3. Two reformat planes were then obtained from LGE-MRI using output 4CH and 2CH US planes parameters.

Figure 5.8 illustrates the registration of STE and LGE-MRI for patients 01 and 02. Both patients presented myocardial regions with late gadolinium enhancement indicating the presence of fibrosis. Output STE registration for patient 01 (Figure 5.8a) successfully matched the inner myocardial wall in LGE-4CH (left) and LGE-2CH (right). For patient 02 (Figure 5.8b), the registration was also satisfactory for most of the contours. However, the red myocardial region in STE-2CH (antero-basal) did not match perfectly the inner LV boundary in LGE-2CH. The lack of resolution in STE-contours at apical levels can also be appreciated in these images.

The registration of US to cine/LGE-MRI were visually assessed by a cardiologist. The segments in STE not successfully matched with LGE-MRI were discarded from this study. In total, 24 STE segments were not successfully aligned to LGE-MRI, from a total of 306 segments.

5.3.3 Analysis of myocardial fibrosis and strain

STE to LGE-MRI registration enabled to *associate* strain-derived indicators from STE strain curves with LGE-MRI indicators describing myocardial fibrosis. Two indicators of fibrosis have been computed: (i) a local binary indicator of the presence of fibrosis (fibrosis yes/no) associated to each STE-segment; (ii) a global indicator corresponding to the percentage of myocardial tissue with fibrosis (i.e. the extent of myocardial fibrosis). The computation of these indicators is detailed below.

5.3.3.1 Local characterization of fibrosis

For each STE-segment, the presence of fibrosis in the corresponding region in LGE-MRI was assessed. This was performed visually by placing the registered US contours in LGE-MRI coordinate system, and visualizing multiview LGE-MRI volumes (SAX, 2CH and 4CH). All LGE volumes were used to assess not only if the US planes contain fibrosis, as in Figure 5.8, but also if there is a zone with fibrosis close to the STE-contour. This visual assessment of fibrosis was performed on IR and/or PSIR sequences as follows: first the IR was evaluated; if fibrosis was visible and the assessment possible, this was the only sequence assessed. In case of bad quality or doubt in fibrosis assessment, the PSIR image was used.

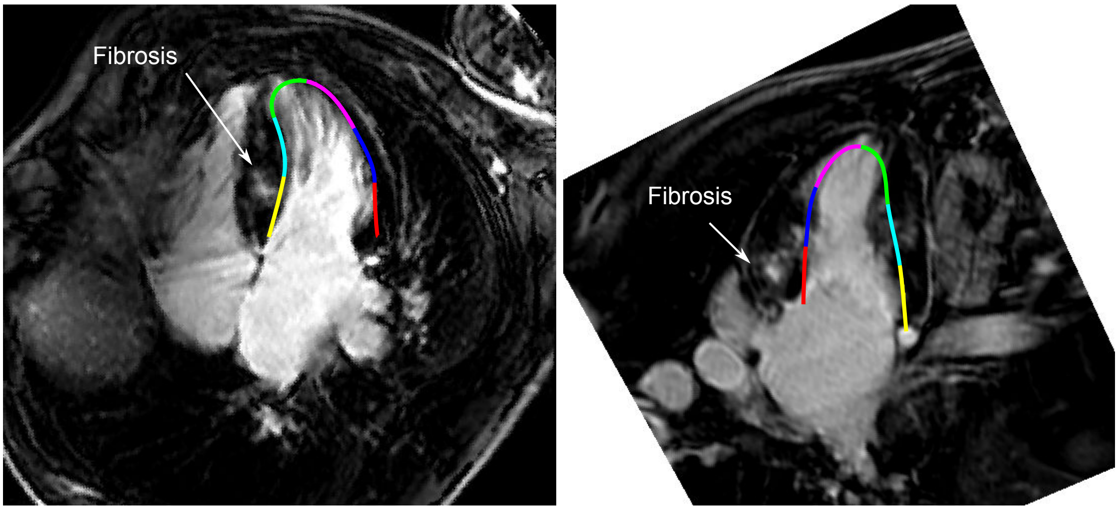

(a) STE to LGE-MRI registration for patient 01. (Left) Registered STE-2CH at mid-diastole and the sliced LGE-2CH using output US plane, (right) registered STE-4CH at mid-diastole and the sliced LGE-4CH using output US plane.

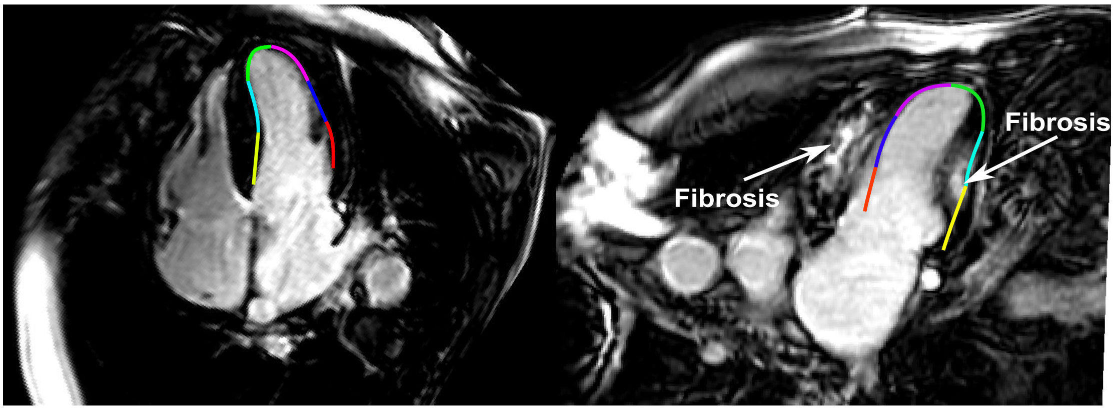

(b) STE to LGE-MRI registration for patient 02. (Left) Registered STE-2CH at mid-diastole and the sliced LGE-2CH using output US plane, (right) registered STE-4CH at mid-diastole and the sliced LGE-4CH using output US plane.

Figure 5.8: STE to LGE-MRI registration for patients 01 (top) and 02 (bottom), for the 4CH view (left) and the 2CH view (right). Note the presence of myocardial regions with late gadolinium enhancement indicating the presence of fibrosis.

All STE regional segments retained were assessed, resulting in 73 segments with fibrosis out of 306 segments in total.

5.3.3.2 Estimation of the global extent of fibrosis

The extent of fibrous tissue was estimated by the percentage of fibrosis in the total myocardial volume in LGE-SAX. Its computation required the inner an outer contours of the myocardium to be delineated. The inner contours can be propagated from the LV endocardial surfaces extracted in cine-SAX (cf. 5.3.2.2). However, to have a precise estimation of the extent of fibrosis, both, the inner and the outer contours, were manually delineated by a cardiologist on LGE-SAX using ITKSNAP (Yushkevich et al., 2006), for those patients with fibrosis.

Then, the fuzzy c-means method proposed by (Kachenoura et al., 2008) was used to delineate myocardial fibrosis. This is an unsupervised method classifying the voxels in the myocardium into one out of two possible classes: late gadolinium-enhanced voxel of non-LGE voxel. This method proved appropriate correlations with biochemical myocardial infarct (scar) quantifications as well as LV function parameters (Baron et al., 2013).

The fuzzy c-means method is an unsupervised clustering procedure providing to each voxel a level of membership to two fuzzy classes: LGE and non-LGE (one membership value per class). The membership value describes the belongingness of the voxel to the class. This value is a number between 0 and 1. The fuzzy c-means approach is advantageous in the case of fibrosis quantification because, except for highly enhanced pixels with a bright intensity value, the enhancement between fibrous and non-fibrous tissues is not always well defined (i.e. it is fuzzy). The fuzzy c-means method was applied independently on each slice to avoid misclassification related to eventual inter-slice differences in signal intensity. Moreover, it was applied for a region including the myocardium and the LV blood pool which avoid misclassification, especially in slices without scar (Baron et al., 2013). Figure 5.9 presents the membership value of the LGE-voxel class after fuzzy c-means, for the voxels into the myocardium.

After fuzzy c-means, a defuzzification procedure was performed to obtain a binary description of those voxels being part of fibrosis and those that not. Then, for the entire myocardium, a threshold of the LGE-class membership was varied between 0.25 and 0.5, and the curve representing the number of LGE-voxels was plotted over these varying threshold. Then the threshold value providing the most stable output (the longest portion in the plot were the number of LGE-voxels remains the same), was selected as the optimal one (indicated with and arrow in the colorbar in Figure 5.9) (Baron et al., 2013). This threshold is then used to deffuzyfy (get a binary image) the output of the fuzzy c-means method. Figure 5.10a and (b) presents the resulting delineation of fibrosis in patients 01 and 02, respectively. It can be noted that the region with fibrosis is accurately delineated in those portions with a high concentration of voxels with late gadolinium enhancement.

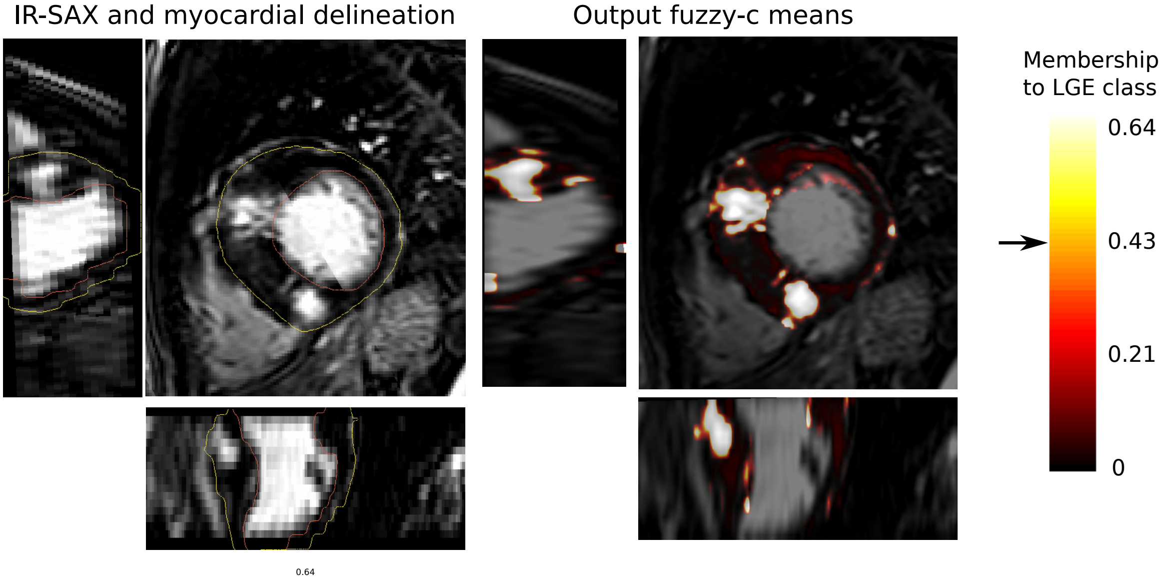

Figure 5.9: Input LGE-SAX volume (inversion recovery) and output fuzzy c-means clustering revealing the degree of late gadolinium enhancement for each voxel in the myocardium. Arrow points to the optimal threshold to defuzzyfy the output LGE-class image.

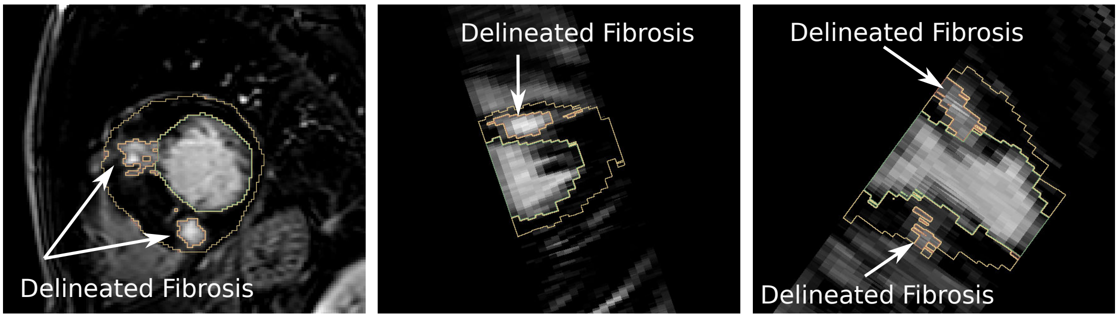

(a) Fibrosis delineated in the LGE-SAX volume for patient 01. From left to right the SAX, 4CH and 2CH views, respectively.

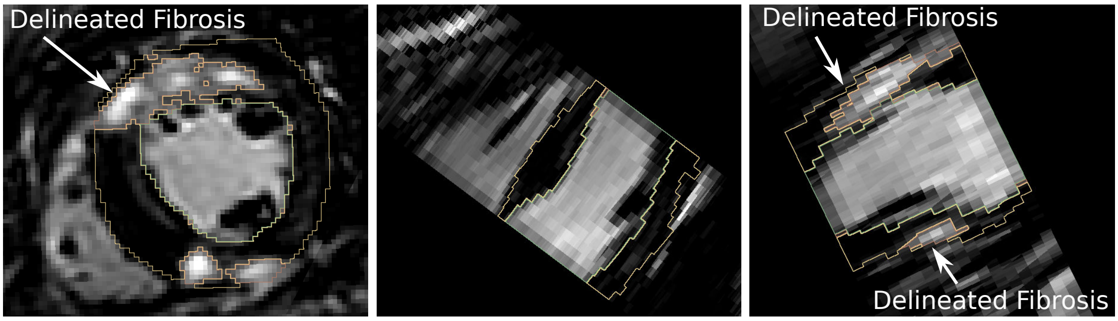

(b) Fibrosis delineated in the LGE-SAX volume for patient 02. From left to right the SAX, 4CH and 2CH views, respectively.

Figure 5.10: Fibrosis delineated in LGE-SAX volumes for patients 01 (top) and 02 (bottom). The inner contours and outer contours needed for fibrosis delineation are also showed.

5.4 Results and discussion

28 patients were retained to perform this study (patients with exploitable LGE images). STE to cine-SAX registration was visually assessed, by depicting the registered STE contours at peak-R in cine-SAX space. After this assessment, STE-3CH was excluded because the registration results were not satisfactory given that output 3CH planes approached 2CH planes. After this registration, a cardiologist visually assessed the STE to LGE-MRI registration before associating the presence of fibrosis with regional strain-derived indicators. This led to a population of 336 myocardial segments to be analyzed: 28 patients, 2 STE views, 6 segments per view. From them, 306 segments were retained by the cardiologist after visual assessment. The causes to reject the 30 segments were:

1. There was no 2D strain curve available: 6 segments,
2. The registration was not satisfactory after visual assessment: 24 segments.

Two studies were performed: a global and a local characterization of the HCM. The global characterization is based on global values (i.e. values measured for the whole heart, e.g. the extent of fibrosis, without using the result of the registration workflow). The local characterization relies on the registration results to locally evaluate the relationship between strain and fibrosis. During these studies, the readers of the echocardiographies were blinded to the results of MRI, and they did not have any clinical data when reading echocardiographic files.

5.4.1 Global characterization of HCM

Table 5.3 provides the global indicators that were measured to describe the hypertrophic pattern, the systolic function and the myocardial fibrosis extent. These indicators were analyzed to characterize HCM in the retained population. They are presented as the mean value ± standard deviation.

The maximal wall thickness was 19.1±5.1 mm and most of the hypertrophies were of type III[7] from Maron's classification (Maron et al., 1981). Also, hypertrophy was associated with a small LV cavity (LVEDd 42.6±5.0 mm). Even with a portion of the population with mild to moderate heart failure (NYHA class 1 and 2, cf. 5.1), they do not present a modification of the ejection fraction which is normal (64.7±9.0 from MRI); however, the global longitudinal peak-strain (mean value of the peak-strain amplitude computed over all segments of the three great-axis views: 2CH, 3CH and 4CH) is slightly altered (-15.4±3.4), with a normal peak-stain value being -20%. The longitudinal strain has been privileged because it is the component whose measurement is the most reproducible and robust.

---

[7] Morphologic classification of HCM. In type III, hypertrophy is present in three of four zones of the left ventricle, e.g. the septal, anterior and lateral zones.

Table 5.3: Descriptive global indicators of HCM from US and cardiac MRI. Acronyms – LVEDD: left ventricular end-diastolic diameter, LVED Vol: left ventricular end-diastolic volume; LEVF: left ventricular ejection fraction (biplane method), Global longitudinal strain = mean peak-strain in 4CH+3CH+2CH.

	US	**Cardiac MRI**
Cardiac hypertrophy pattern:		
Maximal wall thickness (mm)	20.1 ± 4.4	19.1±5.1
LVEDD (mm)	42.5±5.0	
LVED Vol (ml)	89.7±26.0	148.1±32.6
LVES Vol (ml)	31.3±13.2	53.1±21.0
Myocardial Fibrosis:		
Patients with LGE (fibrosis)		22 (78.6%)
Percentage of the myocardium (if fibrosis)		10.5%±11.7% [0.6-43.5%]
LV systolic function:		
LVEF (%)	65.6±8.4	64.7±9.0
Global longitudinal peak-strain (%)	-15.4±3.4	
Longitudinal peak-strain (4CH)	-15.0±3.6	
Longitudinal peak-strain (2CH)	-15.8±3.8	
Longitudinal peak-strain (3CH)	-15.0±3.5	
Circumferential LV peak-strain (%)	-17.8±5.0	
Radial LV peak-strain (%)	35.8±16.9	

The quantification of the extent of fibrosis for the HCM population gave 10.5%±11.7% of the total myocardial volume. This extent in agreement with literature (Popović et al., 2008) (Saito et al., 2012). This is, arguably, an indicator of the good performance of the semi-automatic quantification of myocardial fibrosis volume. We measured the Pearson correlation index between global peak-strain and the percentage of fibrosis in the myocardial tissue, per patient. The Pearson correlation was 0.5624 with a p=0.0042 (null hypothesis rejected). Then, the global peak-strain and the volume of myocardial fibrosis are correlated: a patient with fibrosis will have a probability to get altered the systolic function. This finding is also in agreement with literature: (Pearson=0.46, p=0.003) in (Popović et al., 2008); however, they quantified the extent of fibrosis using the 2SD method (a method based on the standard-deviation of voxels intensities), and required the delineation of a portion of viable myocardium per slice in LGE which is not required by the fuzzy c-means method.

These global descriptors enabled to characterize HCM from a global point of view. However, given that the regional peak-strains are altered (cf. Figure 5.12b) but the global longitudinal peak-strain does not reflect this alteration (it is just slightly altered), we sought to analyze the abilities of regional strain curves in localizing the regions with myocardial fibrosis.

5.4.2 Local characterization of HCM: Relationship between regional longitudinal strain and fibrosis

From the retained population made up of 306 segments, we sought to determine the statistical significance of the relationships between the following indicators:

1. Regional longitudinal peak-strain amplitude or time in one hand;
2. The presence or not of fibrosis in the other hand.

These indicators were selected because they are potentially modified in the presence of fibrosis. Fibrosis is a non-contractile tissue. Therefore, its presence should result in an alteration of myocardial deformation and thus in an altered 2D strain. The peak strain (most negative value of the longitudinal strain curve), being an indicator of the systolic function, describes the strength of myocardial contraction. It is expected that the maximum longitudinal deformation in a STE region will be modified by the presence of fibrosis. On the other hand, the time-to-peak, defined as the time delay from the beginning of the R-wave (annotated during US acquisition) to the peak-stain, describes the heterogeneity of the instants of maximal contraction for the myocardial regions, i.e. the dyssynchrony of myocardial regions. The time-to-peak may also be modified by the presence of fibrosis. In this case, it would take more time for a region with fibrosis to attain its maximum deformation than for a viable region. Figure 5.11 illustrates the computation of these indicators. We measured the Pearson correlation index between regional longitudinal peak-strain and regional time-to-peak measurements for all patients. The Pearson correlation was estimated to be 0.226 with a p=0.0001; then, these indicators had a very low correlation.

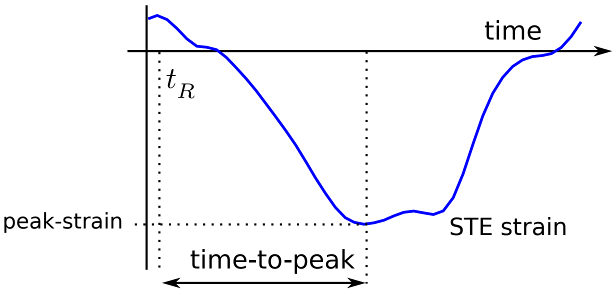

Figure 5.11: Peak-strain and time-to-peak indicators computed from regional longitudinal strain curves (blue).

Two instances of STE to LGE registration and associated regional strain curves and myocardial regions with fibrosis are presented in Figure 5.12a and Figure 5.13a, for patients 01 and 02, respectively. For the patient 01, it can be noted that myocardial fibrosis appeared at yellow and cyan regions of STE-4CH (basal- and mid-septal) and at red, blue and cyan regions of STE-2CH (basal,mid-ant and mid-inf). These segments corresponded to an altered strain, as shown by the strain curves. For the patient 02, the red, blue, yellow and cyan regions of the STE-2CH contours were affected by fibrosis and the corresponding strain curves were also altered (cf. Figure 5.13b(left)). In the case of STE-4CH, despite the fact that any region with fibrosis appeared at the US plane in LGE-MRI, the strain curves were altered (even more than for STE-2CH).

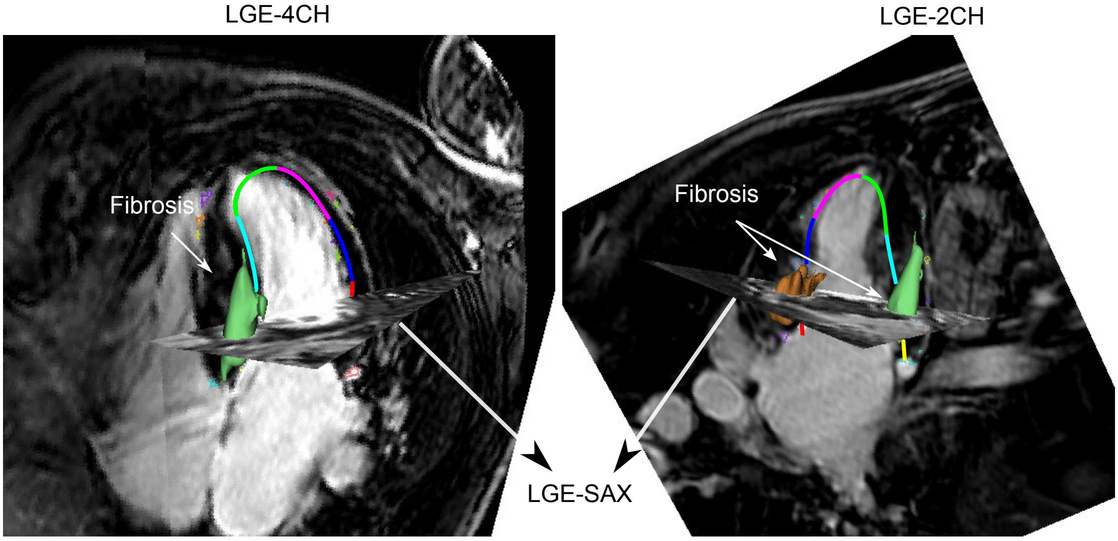

(a) STE to LGE-MRI registration and delineated fibrosis from LGE-SAX.

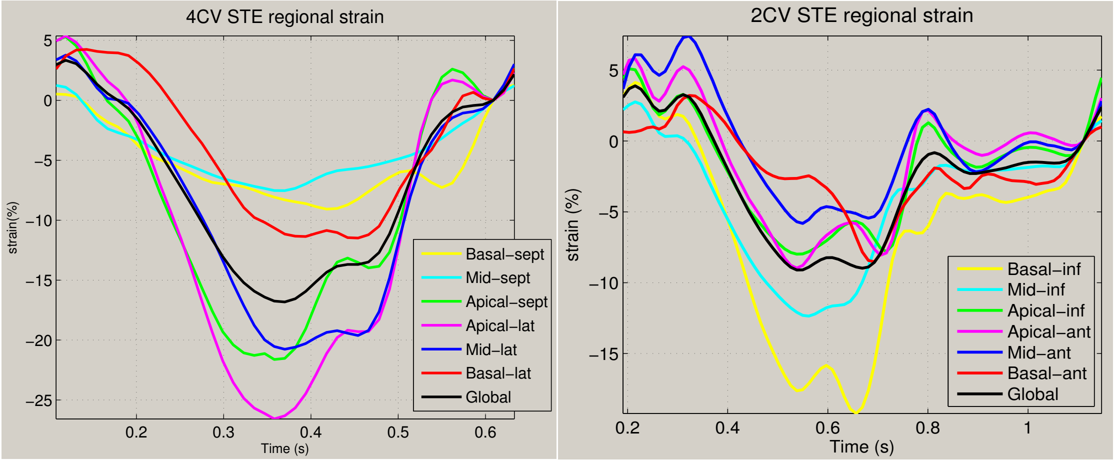

(b) Longitudinal 4CH and 2CH strain curves from STE.

Figure 5.12: STE-2CH and 4CH registration to LGE-MRI, and strain curves for patient 01. The regions with fibrosis, computed with the fuzzy c-means procedure in LGE-SAX, are also shown. (Top) STE contours superimposed to LGE-MRI and regions with fibrosis from LGE-SAX (colored surfaces). (Bottom) Regional strain curves from STE-4CH (left) and STE-2CH (right).

To consider all patients, two subpopulations of myocardial segments (as defined by STE) were constructed after STE to LGE-MRI registration: (i) myocardial regions without regional fibrosis (235 segments, 76.79%) and (ii) myocardial regions with regional fibrosis

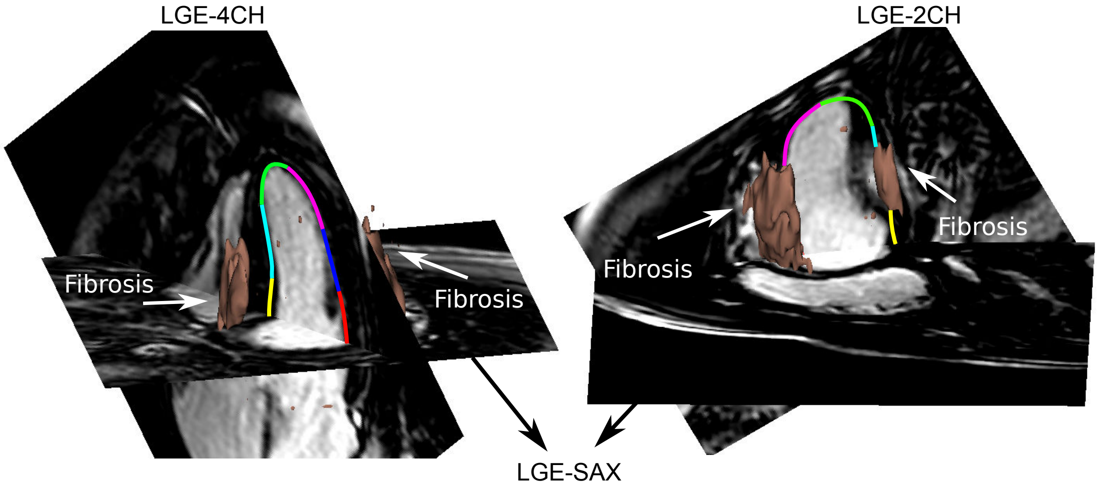

(a) STE to LGE-MRI registration and delineated fibrosis from LGE-SAX.

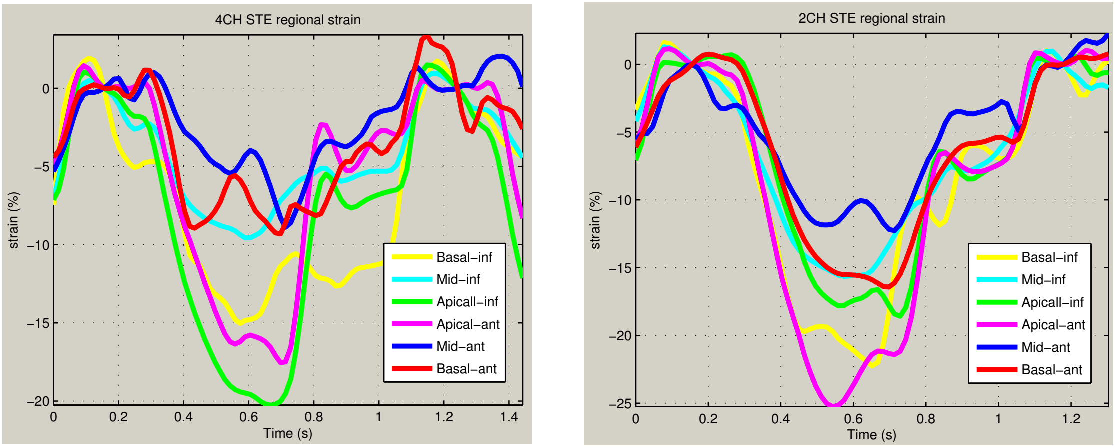

(b) Longitudinal 4CH and 2CH strain curves from STE.

Figure 5.13: STE-2CH and 4CH registration to LGE-MRI, and strain curves for patient 02. The regions with fibrosis, computed with the fuzzy c-means procedure in LGE-SAX, are also shown. (Top) STE contours superimposed to LGE-MRI and regions with fibrosis from LGE-SAX (colored surfaces). (Bottom) Regional strain curves from STE-4CH (left) and STE-2CH (right).

(71 segments, 23.20%). Two boxplots depicting (i) peak-strain of regional longitudinal 2D strain curves and (ii) the time-to-peak for these regions, are presented in Figure 5.14. Unpaired Student's t-tests results are reported in Table 5.4.

Table 5.4: Statistical significance of strain-derived indicators for the populations of STE myocardial segments without and with fibrosis.

Indicator	Statistical significance
Peak-strain	Null hypothesis rejected ($\alpha = 0.01$, p-value $= 4.78\text{e}^{-9}$)
Time-to-peak	Null hypothesis rejected ($\alpha = 0.01$, p-value $= 1.62\text{e}^{-6}$)

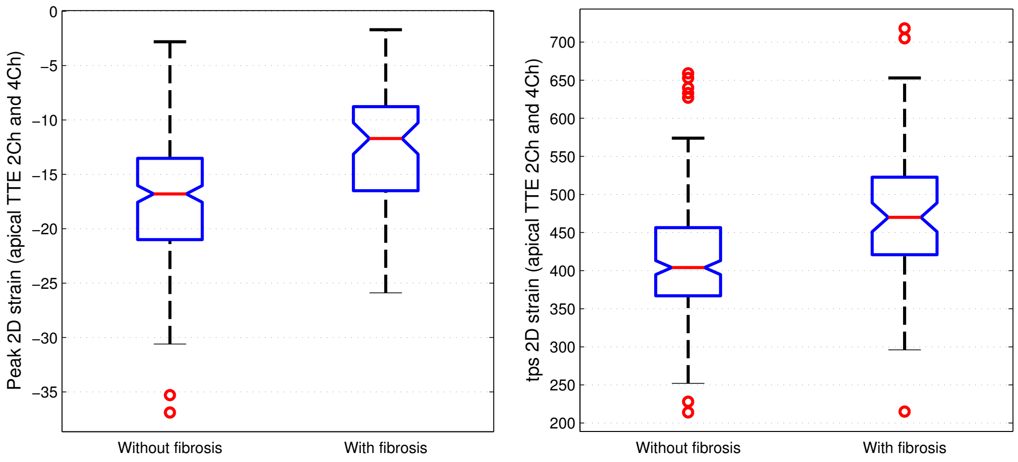

(a) Boxplot 2D peak-strain

(b) Boxplot time-to-peak

Figure 5.14: Boxplots of the STE strain indicators under evaluation for two populations: without fibrosis and with fibrosis. Boxplots are between the 25th and 75th percentiles. Whiskers correspond to approximately ± 2.7 sigma (99.3% coverage). Red circles correspond to outliers. (Left) Boxplot for the regional peak-strain, (right) bloxplot for the regional time-to-peak.

Results from Student's t-tests proved that the expected value of both indicators change if the underlying myocardial region from 2D STE 2CH and 4CH have a degree of fibrosis as assessed from LGE-MRI (peak-strain: $\alpha = 0.01$ and p-value$=4.78\text{e}^{-9}$, time-to-peak: $\alpha = 0.01$ and p-value$=1.62\text{e}^{-6}$). These can be observed from box plots in Figure 5.14 where it can be noted that the expected values of fibrosis and without-fibrosis populations are clearly differentiated for both indicators. The analysis of the modification of regional peak-strain showed that a low regional longitudinal contraction is an indicator of the presence of fibrosis. Then, the magnitude of the peak-strain decreases with the presence of fibrosis. On the other hand, the change of the time-to-peak indicator means that a high time to peak is related to the presence of fibrosis.

Although the variation of STE-indicators was significant according to Student's test, the distribution of the measurements of these indicators, for the subpopulations with and without fibrosis, overlapped. This overlap is highlighted in Figure 5.15a where the distribution of the observations for viable STE-regions (blue triangles) and STE-regions with fibrosis (red triangles) is shown. Each observation in this figure is a point in a 2D space, with the X axis being the peak-strain and the Y axis the time-to-peak. We used a linear classifier to draw a line such that the viable population and the population with fibrosis were separated by minimizing the mean squares distance of the observations to the line. Two zones were defined: blue zone (viable) and red zone (fibrosis). The blue triangles into the red area correspond to segments without fibrosis in the area of regions with fibrosis in Figure 5.15a. Different hypotheses may be considered to explain this overlapping: (i) processing uncertainties in the registration and/or the estimation of fibrosis estimation; (ii) presence of diffuse fibrosis that cannot be assessed with LGE-MRI.

To elucidate the strength of these indicators to predict if a STE-region has fibrosis, a receiver operating characteristic (ROC) curve was plotted for three binary classifiers: one for each indicator and another for a linear classifier using both indicators. The ROC curve is a plot of the *true positive rate* (TPR: percentage of regions with fibrosis effectively classified as regions with fibrosis), and the *false positive rate* (FPR: percentage of regions classified with fibrosis but being in reality regions without fibrosis), computed when the decision boundary of a binary classifier are moved (e.g. a threshold for the peak-strain and time-to-peak parameters, the position of the line for the linear classifier). TPR depicts the *sensitivity* of the indicator while the inverse of the FPR (1-FPR) depicts the *specificity* of the indicator (proportion of regions without fibrosis being classified as regions without fibrosis).

The three ROC curves are in Figure 5.15b. The *area under the curve* (AUC), computed using the trapezoidal integration rule, were 0.7237, 0.7001 and 0.7609 for peak-strain, time-to-peak and the linear classifier, respectively (the ideal AUC being 1.0). This suggests that linear classification outperforms the classification using one indicator only.

ROC curves provide one important insight about strain curves: *2D strain is not only altered by fibrosis.* Some other parameters may alter it including the age of the patient, loading condition (volemia, blood pressure), etc. This is derived from the fact that a high sensitivity is obtained at a cost of the specificity, i.e. *strain indicators are more sensible than specific.* For instance, for the peak-strain indicator a sensitivity of 80% is obtained with a specificity of 45% (an equivalent trend is obtained for time-to-peak). Therefore, the strain indicators, though changing under fibrosis, are modified by other factors not included into this study: *fibrosis is one among multiple factors altering the strain curve.*

5.4.3 Study limitations

The limitations of this study are:

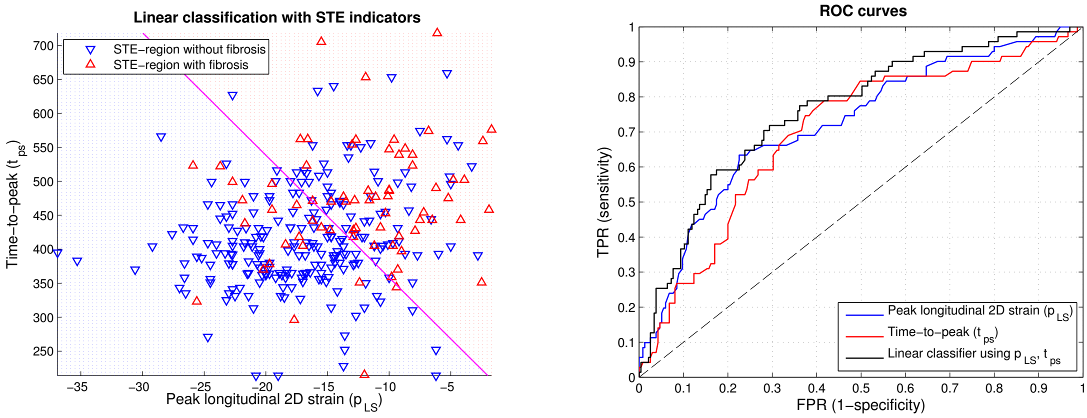

(a) Distribution of the observations for viable STE-region and fibrotic STE-region populations and classification using a linear classifier.

(b) ROC curves for peak-strain(p_{LS}), time-to-peak (t_{ps}) and a linear classifier using both indicators.

Figure 5.15: Analysis of the prediction of the presence of fibrosis by strain indicators in HCM patients. 5.15a distribution of observations of the peak longitudinal 2D strain (p_{LS}) and the time-to-peak of this peak (t_{ps}) for the populations of STE-regions without and with fibrosis. 5.15b ROC curves of peak-strain (p_{LS}, red), time-to-peak (t_{ps}, blue) and a linear classifier using both indicators (black). The area under the ROC curves, using a trapezoidal integration rule, were 0.7237, 0.7001 and 0.7609, respectively. Acronyms – ROC: receiver operating characteristic.

— LGE-MRI volumes were acquired using the IR and PSIR techniques (cf. 1.3.4.1). They require a sample of viable myocardium to null its MR signal; thus, *diffuse fibrosis* is out of the scope of this acquisition. Although the use of T1-mapping techniques (e.g. MOLLI sequence) may overcome this (Lima, 2013) (Puntmann et al., 2013), they were not available from our clinical acquisition protocol and, thus, were not used here.

— The *mechanisms* describing the impact of the extent of fibrosis of each STE region and the corresponding regional strain curve are out of the scope of this study. However, a step further is included here: the quantification of the volume of myocardial fibrosis.

— The global strain indicators were not available for all patients. This was due to the bad quality of some planes acquired during US.

— The segments with altered strain but without fibrosis quantified in LGE-MRI cannot been explained here.

5.5 Conclusions and perspectives

The fusion of STE traces extracted from ultrasound images with LGE-MRI for a significant number of patients with HCM enabled to study if regional strain-derived indicators from STE surrogated to the presence of fibrosis.

STE to cine-SAX and LGE-MRI registration based on the DTW enabled to align STE traces with LGE-MRI. This registration enabled to associate the regional strain curves from STE with the corresponding regional myocardial fibrosis from LGE-MRI. After this association, Student's test proved that the expected value of the longitudinal peak-strain and the longitudinal time-to-peak are statistically different with regards to the presence of fibrosis assessed from LGE. This finding is important because it means that analyzed STE strain indicators are surrogated to the presence of fibrosis.

The interactive active-contour segmentation of the left ventricular endocardial surface from cine-SAX images, based on snake evolution, enabled to extract dynamic LV surfaces of the LV. ITKSNAP tool used to perform this segmentation is easy to use. However, it required the interaction with the user and, in some cases, a posterior correction of endocardial delineations.

The registration of cine-MRI and LGE-MRI enabled to correct for slice misalignment in cine-SAX volumes and to integrate LGE-MRI to cine-MRI. This registration was suitable because multiview LGE-MRI volumes did not presented slice misalignment.

The registration of STE contours with the LV surface from cine-SAX volumes, enabled to overlap STE geometries with LGE images. However, after visual assessment by a cardiologist, 24 segments were not successfully aligned (for a total of 300 segments). This fail rate is explained by the rough resolution of LV segmentation (due to cine-SAX slice thickness), the performance of the cine-SAX slice misalignment correction that has an effect on US registration output, and the lack of detailed information at apical level in both acquisitions (cf. 4.5.3)

The fuzzy c-means procedure to quantify the extension of myocardial fibrosis enabled to quantify a global indicator describing the extent of fibrosis of each patient. This indicator, expressed as the percentage of the volume of regions with fibrosis in the total myocardial volume, was in agreement with the literature. This method, needing only the inner and outer contours, is automatic, thus, with high reproducibility.

Global characterization of HCM proved that the population under analysis have global indicators in agreement with the literature, notably, the correlation between global strain and the percentage of fibrosis.

The registration of STE data with cine-MRI and LGE-MRI, allowed to perform a local (regional) analysis of longitudinal strain parameters aiming at studying if they are related with the presence or not of fibrosis. This study enabled to describe the sensitivity and specificity of the strain in detecting the regional fibrosis. Student's t-test proved that the expected value of the peak-strain and time-to-peak parameters change with the presence of fibrosis ($p < 1e^{-5}$ for both indicators). Besides, boxplots of the observations of these indicators, for the populations of STE-regions without and with fibrosis, showed that they overlap. Then, despite the fact that the change is significant, it has a wide range, leading to overlapping in the observations of healthy and fibrotic STE-segments. This overlap could be explained by the presence of diffuse fibrosis that is not possible to assess from LGE-MRI.

The overlapping of strain indicators for myocardial regions without and with fibrosis resulted in a decreased strength to predicting the presence of fibrosis, which was evaluated using ROC curves. This evaluation showed a high correlation in the behavior of input indicators and their combination using a linear classifier. We conclude from ROC analysis that fibrosis is one out of different factors modifying peak-strain and time-to-peak in the analyzed population of HCM patients.

Perspectives. This study can be enhanced by improving STE to LGE registration performance such that more regions can be added to the analysis, including those from STE-SAX and 3CH. We hypothesize that a constrained iconic registration can solve this. Some works exist in the literature performing US iconic registration. The challenges in such a case are: the selection of the similarity metric, the synchronization of the LGE and STE acquisitions and the access to raw US images to perform this iconic procedure.

STE-segments with non altered strain but fibrosis in LGE could be explained by the size of the regional fibrosis. Then, this study may be improved by quantifying the size of regional fibrosis. In this case, the incidence of fibrous tissue not cut by the output US plane but near to it should be considered because it will have, potentially, an effect in measured STE-indicators .

Another perspective is to perform the same study using 3D echocardiography. In that case, all STE-strain measures can be explored at once: longitudinal, circumferential, radial and area strains. The challenges in such a case are the access to raw US images and STE-information (contours, surfaces) to perform TTE registration. Moreover, the metric and synchronization challenges mentioned above in the context of 2D TTE remain as well.

Other perspective is to include STE strain measures from US acquisitions in effort. This could aid to improve the strength of strain-derived indicators in predicting fibrosis, improving the specificity of such measures. We can suppose that the modification of loading condition and contractility, induced by exercise, could add relevant information.

References

Baron, N., Kachenoura, N., Cluzel, P., Frouin, F., Herment, A., Grenier, P., Montalescot, G., and Beygui, F. (2013). “Comparison of various methods for quantitative evaluation of myocardial infarct volume from magnetic resonance delayed enhancement data”. eng. In: *International journal of cardiology* 167.3, pp. 739–744.

Gersh, B. J., Maron, B. J., Bonow, R. O., Dearani, J. A., Fifer, M. A., Link, M. S., Naidu, S. S., Nishimura, R. A., Ommen, S. R., Rakowski, H., Seidman, C. E., Towbin, J. A., Udelson, J. E., and Yancy, C. W. (2011). “2011 ACCF/AHA Guideline for the Diagnosis and Treatment of Hypertrophic Cardiomyopathy A Report of the American College of Cardiology Foundation/American Heart Association Task Force on Practice Guidelines”. en. In: *Circulation* 124.24, e783–e831.

Kachenoura, N., Redheuil, A., Herment, A., Mousseaux, E., and Frouin, F. (2008). “Robust assessment of the transmural extent of myocardial infarction in late gadolinium-enhanced MRI studies using appropriate angular and circumferential subdivision of the myocardium”. eng. In: *European radiology* 18.10, pp. 2140–2147.

Lima, J. A. (2013). “The Promise of Myocardial Fibrosis Assessment by T1 Mapping∗∗”. In: *JACC: Cardiovascular Imaging* 6.4, pp. 485–487.

Maron, B. J., Gottdiener, J. S., and Epstein, S. E. (1981). “Patterns and significance of distribution of left ventricular hypertrophy in hypertrophic cardiomyopathy: A wide angle, two dimensional echocardiographic study of 125 patients”. In: *The American Journal of Cardiology* 48.3, pp. 418–428.

Popović, Z., Kwon, D., Mishra, M., Buakhamsri, A., Greenberg, N., Thamilarasan, M., Flamm, S., Thomas, J., Lever, H., and Desai, M. (2008). “Association Between Regional Ventricular Function and Myocardial Fibrosis in Hypertrophic Cardiomyopathy Assessed by Speckle Tracking Echocardiography and Delayed Hyperenhancement Magnetic Resonance Imaging”. In: *Journal of the American Society of Echocardiography* 21.12, pp. 1299–1305.

Puntmann, V. O., Voigt, T., Chen, Z., Mayr, M., Karim, R., Rhode, K., Pastor, A., Carr-White, G., Razavi, R., Schaeffter, T., and Nagel, E. (2013). “Native T1 mapping in differentiation of normal myocardium from diffuse disease in hypertrophic and dilated cardiomyopathy”. eng. In: *JACC. Cardiovascular imaging* 6.4, pp. 475–484.

Saito, M., Okayama, H., Yoshii, T., Higashi, H., Morioka, H., Hiasa, G., Sumimoto, T., Inaba, S., Nishimura, K., Inoue, K., Ogimoto, A., Shigematsu, Y., Hamada, M., and Higaki, J. (2012). “Clinical significance of global two-dimensional strain as a surrogate parameter of myocardial fibrosis and cardiac events in patients with hypertrophic cardiomyopathy”. en. In: *European Heart Journal – Cardiovascular Imaging*, jer318.

Tavard, F. (2012). “Recalage et fusion d’informations multimodales pour l’optimisation de la thérapie de resyncrhonisation cardiaque”. PhD thesis. Université de Rennes 1.

Yushkevich, P. A., Piven, J., Cody Hazlett, H., Gimpel Smith, R., Ho, S., Gee, J. C., and Gerig, G. (2006). “User-Guided 3D Active Contour Segmentation of Anatomical Structures: Significantly Improved Efficiency and Reliability”. In: *Neuroimage* 31.3, pp. 1116–1128.

CHAPTER 6

Cardiac asynchronism characterization for Cardiac Resynchronization Therapy optimization

The fusion of data from multimodal images is of increasing interest in cardiac resynchronization therapy (CRT) optimization. As stated in the clinical context (cf. 1.2.2.4), CRT optimization is three folded: (i) improvement of patient selection guidelines, (ii) optimization of device implantation and, (iii) optimization of the stimulation. The improvement of the patient selection guidelines needs randomized multicenter clinical trials and is out of the scope of this work. Concerning the optimization of the implantation and of the stimulation, they are more related to the specificities of the patient and, in such a case, image fusion would provide a valuable tool to describe the best sites for left ventricular stimulation in terms of their mechanical, electrical and tissue characteristics, and to plan and to guide CRT-device implantation. We use the multisensor registration approaches discussed in chapter 3 for characterizing the cardiac asynchronism of CRT patients.

Figure 6.1 illustrates the main steps of the proposed workflow: multisensor image fusion of CT, MRI, STE and EAM information after the registration of these image modalities, to obtain a fused multisensed description of the left ventricle, allowing to analyze the viability, mechanical, electrical and electromechanical information in a common referential.

Below we detail the scope of this study, the methods used to register and fuse CT, MRI, US and EAM data aiming to study the feasibility of deriving dyssynchrony descriptors of the LV ventricle. Results obtained for two CRT patients are then described. The end

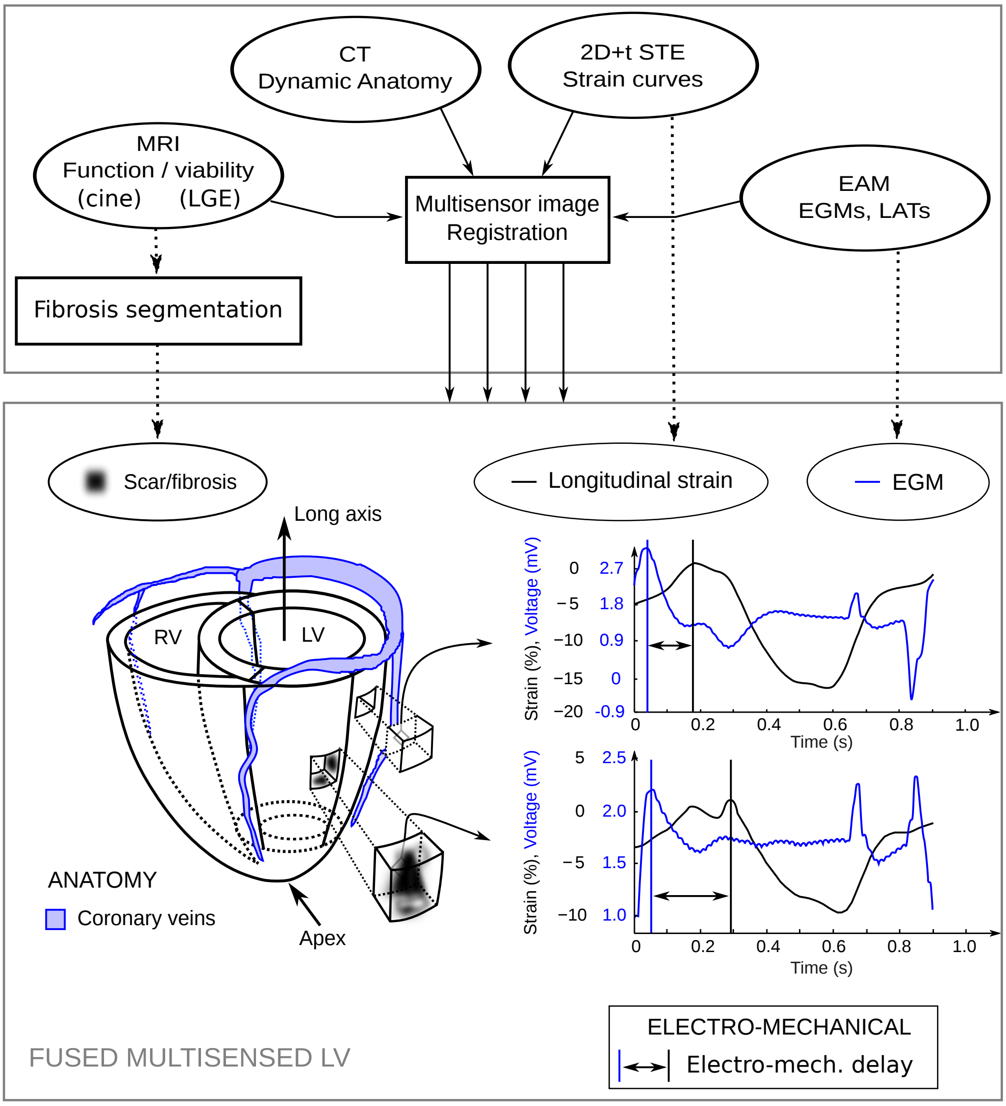

Figure 6.1: General scheme of CT, MRI, US and EAM image registration enabling to obtain a fused multisensed LV description of a CRT patient. This description is required to compute dyssynchrony markers, such as those describing the electromechanical coupling, enabling to characterize cardiac asynchronism and, potentially, to optimize CRT outcome.

of this chapter contains the conclusions and perspectives of this study.

6.1 Aims and scope

The objectives of this study, aiming at characterizing cardiac asynchronism, are:

1. To *associate* LV anatomy, regional myocardial viability from late gadolinium-enhanced MRI, regional myocardial strain curves from speckle tracking echocardiography and endocardial electrograms from EAM in the anatomical referential provided by CT images.
2. To *compute* electromechanical descriptors characterizing the electromechanical coupling of the LV ventricle.
3. To *assess* the insights that such characterization would provide in LV stimulation lead optimization.

This study is complex because it involves different methods aiming at registering multisensor acquisitions. Moreover, even if nine patients have been included in the euHeart database, given the high number of modalities, it is difficult to have patients with complete and satisfactory acquired data. Then, two patients (euHeart 04 and euHeart 06) were analyzed aiming at illustrating a comprehensive procedure required to characterize (i) left ventricular anatomy, (ii) myocardial tissue characteristics and, (iii) the electromechanical function before and after the implantation of a BIV pacemaker.

This study enhances the one of (Tavard, Simon, Leclercq, Donal, et al., 2014) (to appear), where the patients belonging to IMOP database (cf. 6.2.1), were described in terms of the global and local electromechanical behavior. Our main contribution to this work are (i) the addition and processing of cardiac MRI (cine and LGE sequences), (ii) the addition and processing of simultaneous acquisitions of the LV electrical function (balloon catheter), (iii) the consideration of multiview US data and (iv) the processing of euHeart patient database.

6.2 Multisensor data acquisition

We describe below the two projects that provides two multimodal LV datasets from CRT patients, the patient selection criteria and the imaging protocol.

6.2.1 IMOP and euHeart projects

The *Laboratory of Signal and Image Processing* (*LTSI*[1], INSERM-U1099[2]), participated in the development of two research projects in the context of CRT optimization:

---

[1] Acronym from the French “Laboratoire Traitement du Signal et de l’Image” from the University of Rennes 1.

[2] LTSI is the research unit number 1099 into the French Institute of Health and Medical Research (INSERM, acronym from the French “Institut national de la santé et de la recherche médicale”).

IMOP and euHeart.

IMOP[3] (2005-2008) was a project funded by the French Ministry of Research. The partners of IMOP were the department of cardiology and vascular diseases of the CHU-Pontchaillou in Rennes, LTSI, CIC-IT in Tours and ELA Medical Group SORIN.

The goal of IMOP project was to analyze different approaches to improve the exploitation of multisensor acquisitions from CRT candidate patients (anatomical, electrical, hemodynamical and mechanical from both, multiple imaging systems and multiple electrophysiological signals), in order to optimize BIV device implantation, by following up these candidates at pre-, per- and post-operative stages. At pre-operative stage, the goal was the identification of best stimulation sites (one or more) for LV and the optimal path(s) to access them via the coronary venous system. At per-operative stage, the goal was to analyze how to assist the clinician during CRT device implantation, stimulation leads positioning and device parameterization. Finally, at post-operative stage the goal was to derive a method allowing to validate the results of CRT-device pose on a cohort of implanted patients.

The European project *euHeart*[4] (June/2008-November/2012) (Weese, Smith, et al., 2013), lead by Philips Research and Philips Healthcare, combined sixteen industrial, clinical and academic partners, including *INSERM-U1099* (i.e. the LTSI) in cooperation with the CHU-Pontchaillou. The specific objective of euHeart was to improve diagnosis, treatment planning and delivery, and optimization of implantable devices by making patient-specific cardiac models using clinical measurements. euHeart partners were organized into different work-packages (WPs), that were in turn grouped into the technical and application (clinical) WPs. Technical WPs focused on the development of generic tools to model, treat, visualize and analyze multimodal images. These tools supported the work of application WPs. Each WP in the application group focused on a particular cardiovascular decease and in the optimization of cardiovascular therapies into the clinical environment.

LTSI-INSERM U1099 was part of technical work package WP3, and of the application work group WP5 which focused on CRT, and WP10 which was focused on clinical data acquisition and validation. The goals of WP5 were the same as those defined in the context of the IMOP project. LTSI-INSERM participated in euHeart mainly:

1. To develop methods to extract the coronary arterial and venous network from 3D imaging (WP3) (Weese, Groth, et al., 2013),
2. CHU-Pontchaillou with LTSI-INSERM was one of the three clinical centers retained in WP5 and WP10 to acquire CRT patient data. Its role was focused on the collection of extensive data (Data Base 1). These datasets included data

---

[3] ANR CIC-IT n° 04 187-188-189-190. Acronym from the French "Utilité de l'Imagerie Médicale dans l'Optimisation de la Pose de prothèses cardiaques implantables", utility of medical imaging in the optimization of the implantation of implantable cardiac prosthesis.

[4] euHeart: Personalised & Integrated Cardiac Care, FP7/2008-2012.

acquired in pre-, per- and post-intervention: CT, MRI, ultrasound (pre- and post-TTE), ECG and electroanatomical mapping data (invasive electro-physiological mapping), with intra left ventricular cavity pressure capture for some of them. This highly multivariate database is unique, made up of different observation modalities providing a comprehensive view of the patient's cardiac electromechanical function (Marchesseau et al., 2013).

These projects aided to build a database made up of pre-, per- and post-operative acquisitions of different signals and images from different modalities: electrocardiogram, EAM, CT, MRI, angiography and US.

6.2.2 Patient selection

The inclusion and exclusion criteria of IMOP and euHeart projects, were:

Inclusion criteria. Patients in sinus rhythm, with chronic heart failure (NYHA III or IV) despite optimal medical treatment, systolic left ventricular dysfunction, wide QRS complex (QRS $\geq$ 120 ms), low ejection fraction (LVEF $\leq$ 35%) and left ventricular diameter $\geq$ 27 mm/m^2 at end-diastole.

Exclusion criteria. Patients suffering from permanent or persistent atria arrhythmia, who had a cardiac defibrillation or a sudden cardiac death episode during the last three months. Obstructive or restrictive hypertrophic cardiomyopathy, suspicion of presence or presence of acute myocarditis. Systolic pressure $\geq$ 90 mmHg non controlled with medical treatment, diastolic pressure $\geq$ 95 mmHg non controlled with medical treatment. Corrigible cardiovascular disease, symptoms of coronary origin (chest angina or infarct) during the last three months, recent (last three months) or programmed cardiac revascularization. Patient allergic to iodine or with severe renal insufficiency contraindicating the use of iodine. Contraindication to surgical procedures. Dependence to a substance, resulting in a rupture of the social behavior. Patient unable to understand the goals of the study (or unwilling to cooperate). Patient non available for follow-up. Patient with a life expectancy lower than one year. Patient enrolled in another study. Patient under legal age or pregnant woman.

6.2.3 Acquisition protocol

The images used in this study were acquired in the context of euHeart project.

6.2.3.1 Cardiac magnetic resonance

Cardiac MRI acquisitions included cine-SAX, cine-LAX (4CH, 2CH), LGE-SAX and LGE-LAX (4CH, 2CH). Cardiac MRI was performed with a Philips Achieva 3T machine using cardiac SENSE Coil (multicoil). An instance of cine and LGE images is presented in Figure 6.2:

Cine-MRI. Retrospective ECG-gated (RR-interval) breath-hold multiplanar SAX, 4CH and 2CH. Typical parameters for this acquisition were:

Acquisition. Gradient echo (bTFE sequence), TR/TE/FA [5] = 3.69 ms/1.85 ms/45°,

Resolution. 30 cardiac phases in IMOP, 40 and 60 cardiac phases for SAX and LAX in euHeart, respectively, 256×256 pixels (in-plane) with 10 and 2 slices for SAX and LAX, respectively. In-plane pixel resolution=1.25×1.25 mm^2, slice thickness=7 mm, spacing between slices = 9 mm,

LGE-MRI. IR and PSIR sequences. Breath-hold volumetric SAX, 4CH and 2CH acquisitions using retrospective ECG-gating, at mid-diastole. Gadolinium bolus injection (0.1 to 0.2 mmol/kg). Acquisition at 10 min after injection. Multiplanar images of a given view were jointly acquired (i.e. they intersect), in order to improve resulting slice thickness in volumetric images (i.e. to reduce the partial volume effect). Typical parameters for these acquisitions were:

IR Acquisition. Turbo field echo (IR-TFE). TR/TE/FA=4.01 ms/1.23 ms/15°, IR prepulse delay = 280 ms,

PSIR Acquisition. TR/TE/FA = 4.07 ms/1.25 ms/15°, IR prepulse delay = 215 ms,

IR, PSIR resolution. 256×256 pixels (in-plane) with 12 and 12 slices for SAX and LAX, respectively. In-plane pixel resolution=1.37×1.37 mm^2, spacing between slices=5 mm, acquisition slice thickness=10 mm, image (volume) slice thickness=5 mm.

6.2.3.2 Computed tomography

ECG-gated dynamic CT volumes were acquired in a Discovery CT750 HD CT scanner (GE Healthcare, WI, USA), in apnea (20 to 25 s). The temporal resolution varied from 10 phases (3 patients) to 20 phases (12 patients). The CT image of the patient euHeart 04 and euHeart 06 had 10 and 20 phases, respectively. Typical image extension was 512×512×193 voxels, with a voxel resolution of 0.3×0.3×0.63 mm^3. Iodine contrast product injection (100 a 150 cm^3 being at 300 mg/ml or 350 mg/ml) was used to enhance the left heart inner cavities (bright blood). Figure 6.3 illustrates the dynamic CT image of euHeart 06.

---

[5] TR: repetition time, TE: echo time, FA: flip angle (cf 1.3.4.1).

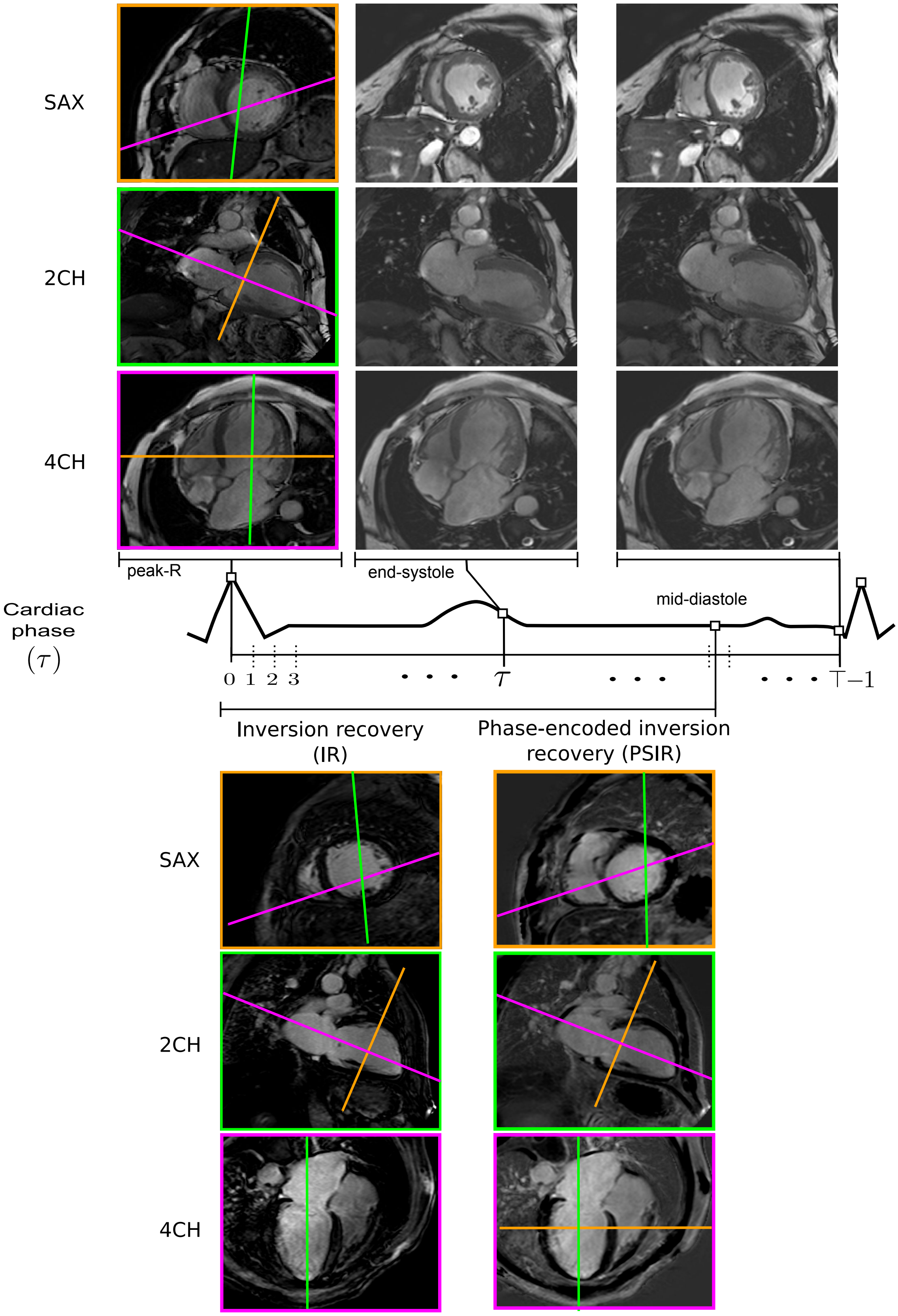

Figure 6.2: Pre-operative Cardiac MRI acquisitions of one patient undergoing CRT enrolled into the euHeart project (euHeart 02). Lines illustrate the intersection of planes from complementary views. (Top) Cine-SAX, cine-2CH and cine-4CH at peak-R, end-systole and the last cardiac phase imaged. (Bottom) LGE-SAX, LGE-2CH and LGE-4CH acquired at mid-diastole using both IR and PSIR techniques.

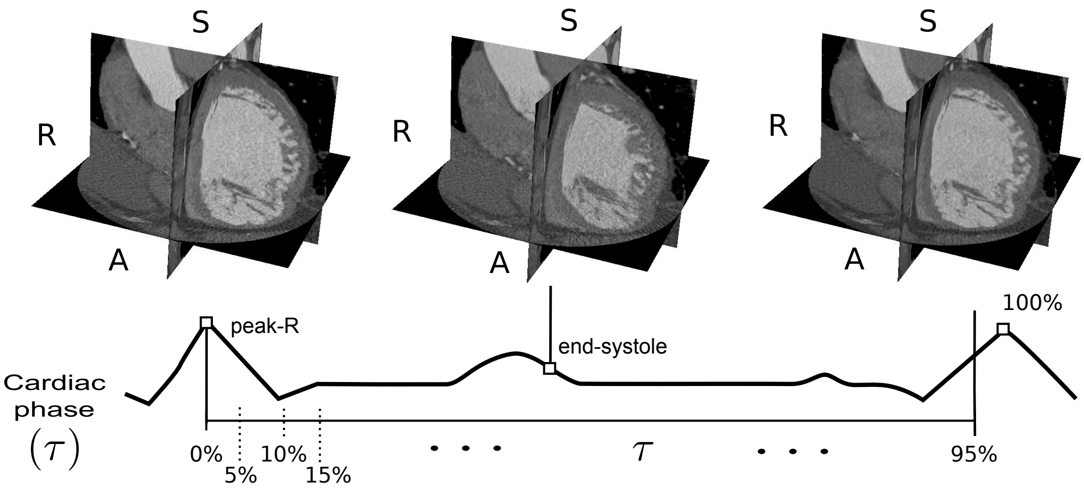

Figure 6.3: Pre-operative dynamic CT acquisition at peak-R, end-systole and the last cardiac phase imaged (euHeart 06).

6.2.3.3 Echocardiography and STE

TTE US acquisitions included parasternal apical LAX (4CH, 2CH, 3CH) and SAX images. A cardiologist, expert in echocardiography, performed TTE acquisitions at pre/post-implantation (3 and/or 6 months). The end-systolic phase was annotated in US acquisitions. STE traces and regional strain curves were computed and exported using an echoPAC clinical workstation software (GE). An instance of STE acquisition is presented in Figure 6.4.

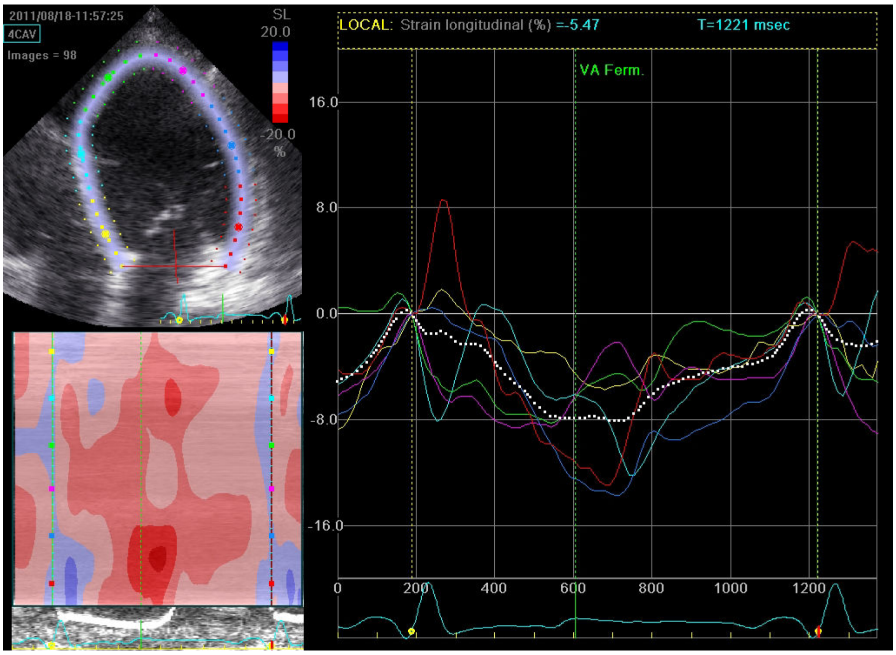

Figure 6.4: Pre-operative speckle tracking echocardiography from an apical TTE image 4CH view, for the patient euHeart 06. Acronyms – VA Ferm: aortic valve closure.

6.2.3.4 Electroanatomical mapping

Electroanatomical mappings of the inner left ventricular cavity were acquired using a balloon catheter (non-contact), also called a *multi-electrode array (MEA).* An ellipsoidal array of 64 electrodes was used to record the electrical activity of the LV inner chamber in real-time and with high-temporal resolution. The acquisition took place after BIV device implantation. Different electrical mappings were recorded, one in sinus rhythm and the others for different types of stimulation (atrial, ventricular, bi-ventricular) and for different parameters: atrio-ventricular delay (AV delay), inter-ventricular delay (VV delay). The set of recordings for a given stimulation parameters (including sinus rhythm), is called an *EAM study.* These recordings were exported in an EnSite system with Velocity®2.0 software (St. Jude Medical, Inc.). MEA and endocardial surfaces, being assumed to remain static during EAM acquisition, were exported along with the electrical recordings on MEA, the EGMs in selected points of the endocardium (called *virtuals*) [6], and the 12-lead ECG. Both, raw and filtered MEA recordings and ECG derivations, were exported. Anatomical landmarks, annotated by the physician, were also exported. They often included the apex, mitral valve and aorta. Figure 6.5 shows an screenshot captured by the EnSite station (Velocity®2.0), depicting a voltage map and electrical recordings for euHeart 06.

6.3 Multisensor image registration

Figure 6.6 shows the procedure used to register CT, MRI, US and EAM images. Four registration procedures are involved: LGE to cine registration, cine to CT registration, STE to CT registration and EAM to CT registration. STE and EAM to CT registrations are surface-based; thus, they need the segmentation of the left ventricle as input.

---

[6] EGMs are obtained by backprojecting the electrical information from MEA to the endocardial surface, solving the electrical inverse problem. In this problem, first the direct function transfer from the conductor geometry (endocardium) to the inner geometry (MEA) is computed (direct problem). Then, using for example the Boundary Element Method (BEM), the observations on MEA are backprojected to the endocardium by optimizing a regularized objective function.

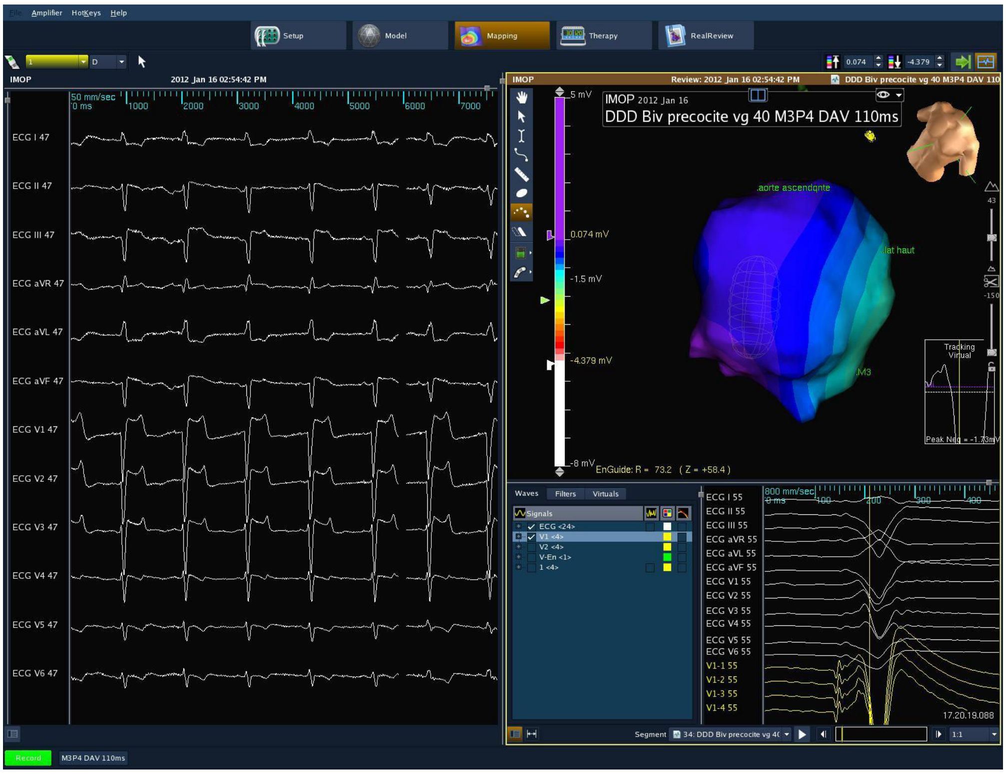

Figure 6.5: Screenshot of the EAM mapping captured by an EnSite station with Velocity®2.0 (euHeart 06). EAM was acquired using a non-contact balloon catheter. It shows the study name (DDD Biv precocite vg M3P4 DAV 110ms), the endocardial geometry, a color coded voltage map and some electrical activity: (left) 12-lead surface ECG, (bottom-right) 12-lead EGC in white and some EGMs in yellow d one heartbeat.

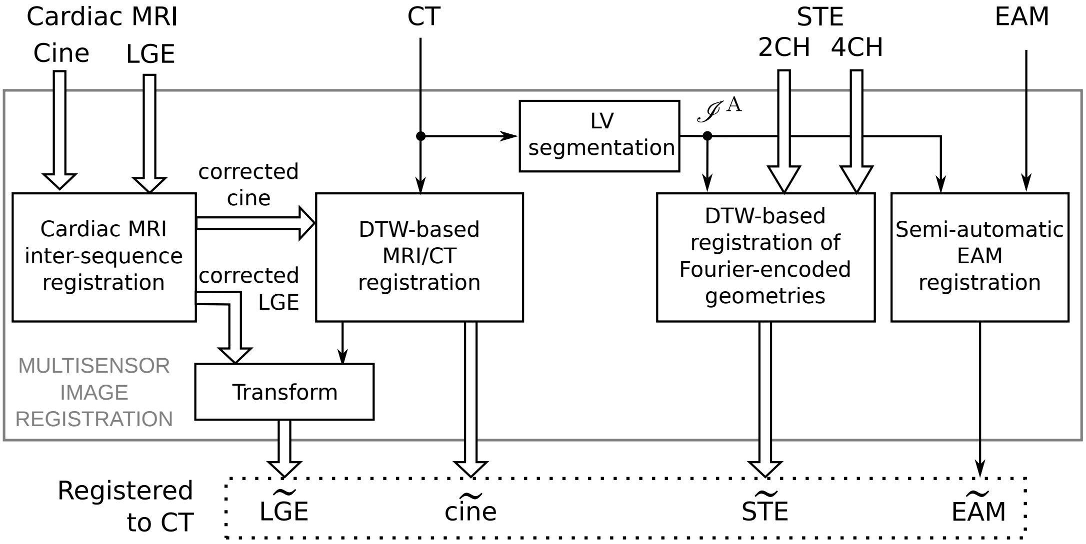

Figure 6.6: Block diagram of the multisensor registration procedure used to fuse CT, MRI, EAM and US acquisitions of patients undergoing CRT. Note that the CT image is the fixed image. ACRONYMS – ⇒: multiview dynamic/static image.

6.3.1 Segmentation of the left ventricle from dynamic CT

The endocardial surface of the left ventricle was extracted from dynamic CT segmentations of the left cardiac cavities. This segmentation procedure used the multi-agent method proposed by (Fleureau, Garreau, Boulmier, et al., 2009) (Fleureau, Garreau, Simon, et al., 2008). In this multi-object segmentation method, user-defined points seeds or *agents*, located into specific objects of interest (here the left ventricle), compete between them in an iterative process to aggregate new voxels in the objects. This segmentation method uses texture information to aggregate new voxels to competing agents and is based on the fuzzy connectedness approach (Udupa et al., 1996).

After segmentation, the LV endocardial surface is extracted from the inner left heart contours and a LV model is constructed for visualization purpose (Tavard, 2012). To extract the LV endocardial surface, first the apex and great axis were estimated by searching the largest distance between two points in input CT surfaces. From these points, the apex is discerned considering the orientation of the heart in CT acquisitions. Then, an optimization procedure slices the left heart surface from the apex towards left atria in the direction of the great axis to find the plane corresponding to the mitral valve. This mitral plane is used to extract the LV endocardial surface. Finally, the LV model corresponds to a truncated ellipsoidal representation of this endocardial surface.

Figure 6.7 illustrates an instance of the multi-agent segmentation (in blue) and the corresponding LV model (in red) computed from CT images at peak-R and end-systole. It can be observed, from the left cavity and LV meshes intersections with axial, sagittal and coronal slices from CT, depicted in blue and red lines, respectively, that the multi-agent segmentation procedure provides a detailed description of the inner geometry, including the delineation of the papillary muscles. On the other hand, the LV model provides a simplified delineation of the LV inner cavity placing these muscles into the LV cavity.

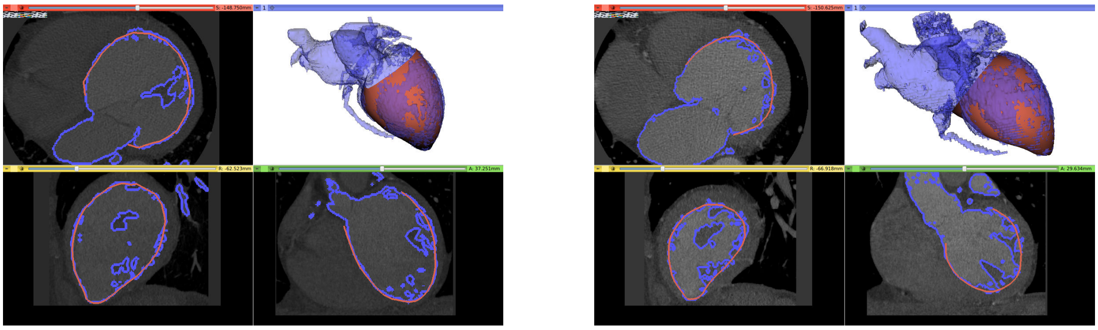
(a) Peak-R

(b) End-systole

Figure 6.7: Segmentation of the inner left heart (blue) and resulting LV model (red) at (a) peak-R and (b) end-systole. Axial (top-left), sagittal (bottom-left) and coronal (bottom-right) slices of the CT image and lines resulting from the intersection of each slice with the meshes representing both the multi-agent based segmentation (blue lines) and the LV model (red lines).

6.3.2 Registration of LGE- and cine-MRI

The goal of the LGE- to cine-MRI registration process is to describe the relationship of myocardial tissue state (from LGE-MRI) with electrical and mechanical information (from EAM and STE). In fact, the state of the tissue around the site of LV stimulation has been considered as an important variable impacting CRT outcome (Jansen et al., 2008). In this work, we focus in the analysis of LGE-MRI in CRT context.

The cine correction and LGE rigid registration process described in 3.1.3 can be used for this purpose. Nevertheless, patients euHeart 04 and euHeart 06 did not presented slice misalignment in cine and LGE images; then, in that case, we performed the rigid registration only. Figure 6.8 presents checkerboard images of the LGE-MRI to cine-MRI acquisitions before and after rigid registration for euHeart 04.

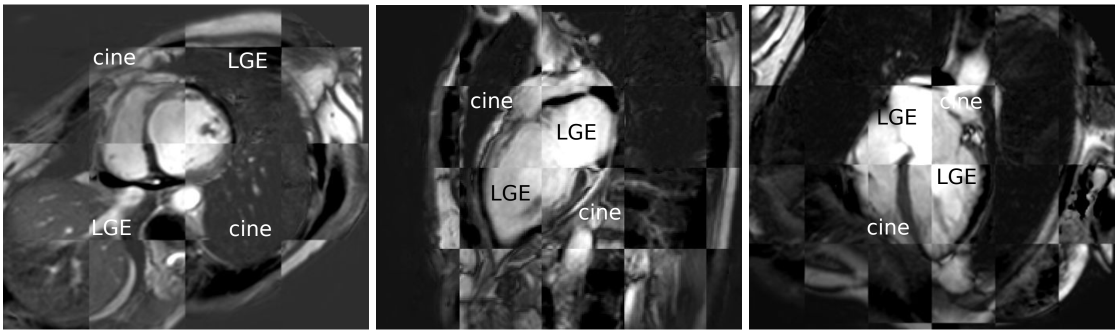

(a) Checkerboard of LGE and cine images before registration.

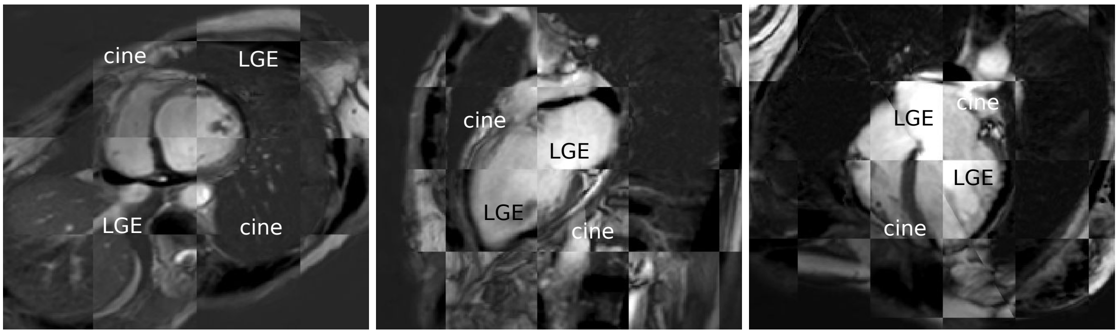

(b) Checkerboard of LGE and cine images after registration.

Figure 6.8: Checkerboard of LGE- and cine-MRI volumes before (top) and after (bottom) registration for euHeart 06. From left to right: SAX, 2CH, 4CH.

6.3.3 Dynamic registration of cine-MRI and dynamic CT volume sequences

The cine-SAX volume sequence was registered to the dynamic CT volume sequence using the multi-image registration method described in 3.2. Figure 6.9 presents an instance of this registration for the patient euHeart 06. Checkerboard images before registration is not presented because input images have almost no intersection between them. It can be noted that LV myocardial septum, lateral walls and LV papillary muscles match at both, end-diastolic and end-systolic phases. Cine-SAX to dynamic CT iconic registration was evaluated in 4.4, resulting in a good performance.

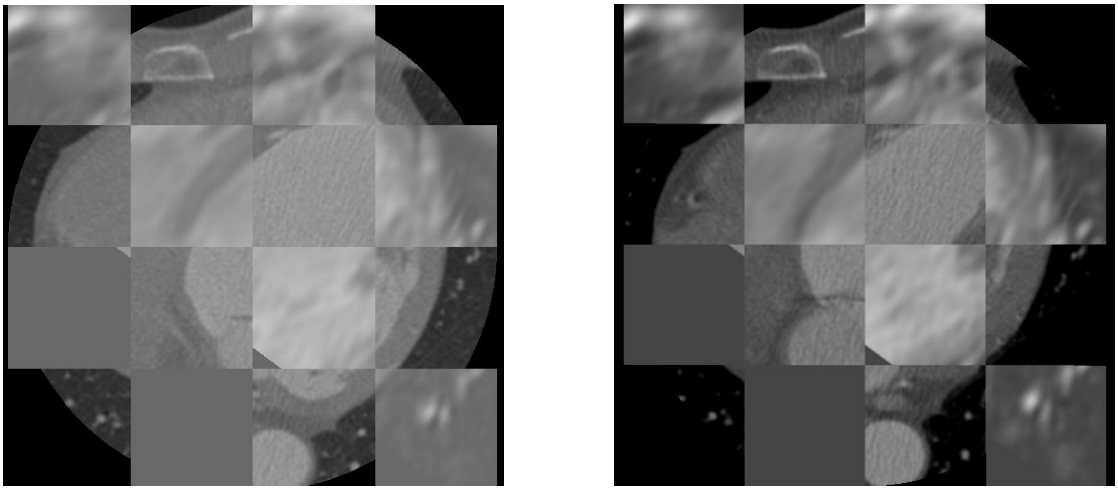

(a) End-diastole

(b) End-systole

Figure 6.9: Checkerboard illustrating cine-SAX and dynamic CT alignment after ADTW registration at (a) peak-R and (b) end-systole (axial view), for euHeart 06.

The output rigid spatial transformation and DTW temporal alignment were propagated to cine-LAX (2CH, 4CH) and LGE-MRI. Thus, cine-MRI and LGE-MRI match the dynamic CT acquisition in space and time. This alignment enables to add myocardial viability information from LGE-MRI to the high-resolution LV anatomy provided by CT scan.

6.3.4 Surface-based registration US and dynamic CT

The goal of this process is to integrate strain curves resulting from STE to the dynamic LV anatomy in CT images. For this purpose, the simultaneous DTW-based approach described in 3.3 was used. 2CH and 4CH STE traces were exported for the RR-interval (using peak-R) to be registered with dynamic CT segmentations of the LV endocardium. We considered STE acquisitions providing the longitudinal strain which is the most robust, reproducible and significant in CRT.

2CH and 4CH STE traces were registered to LV surface from CT by optimizing the DTW-based spatio-temporal similarity measure between them (cf. Equation (3.24)). Figure 6.10 shows the resulting US/CT registration for euHeart 06. Note that LV traces match myocardial wall boundaries in CT.

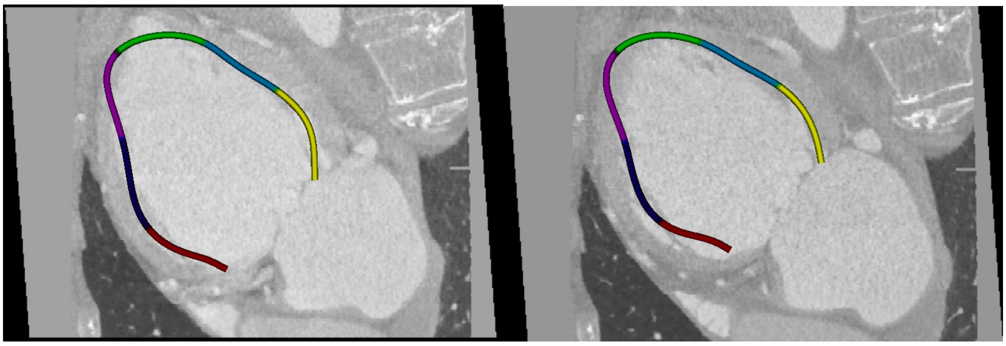

(a) Registration of STE 2CH and CT at peak-R (left) and end-systole (right)

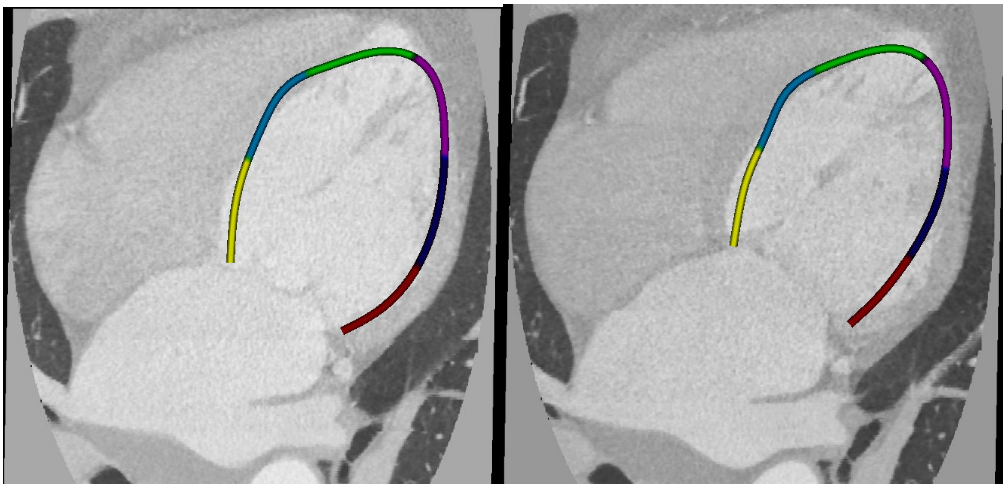

(b) Registration of STE 4CH and CT at peak-R (left) and end-systole (right)

Figure 6.10: STE contour superimposed to the dynamic CT image after the combined DTW-based registration of multiview STE acquisitions: (top) output registration for the STE-2CH, (bottom) output registration for the STE-4CH.

6.3.5 Surface-based registration of EAM and CT

A semi-automatic method proposed by (Tavard, Simon, Leclercq, Donal, et al., 2014) was firstly used to register the EAM data and LV surface segmented from the CT acquisition. We used the first LV surface over the cardiac cycle (normally end-diastole), because EAM geometry describes locally the inner chamber wall at its maximal relaxation. This EAM to CT registration method estimates the apex and long axis from input surfaces (CT and EAM) and then registers them using this information. The apex and long axis for CT have been already estimated during the computation of the LV model (cf 6.3.1). In the case the EAM geometry, the long axis an the apex were estimated from the inertia matrix and annotated fiducials, respectively. In both cases, the long axis is a vector pointing from the apex to the surface centroid. Then, the registration procedure used *a priori* knowledge of the heart geometry: first EAM surface is registered to CT surface using the location of the apex and the long axes; then, the user can apply a rotation to the EAM surface around the long axis in order to reduce rotational mismatch (Tavard,

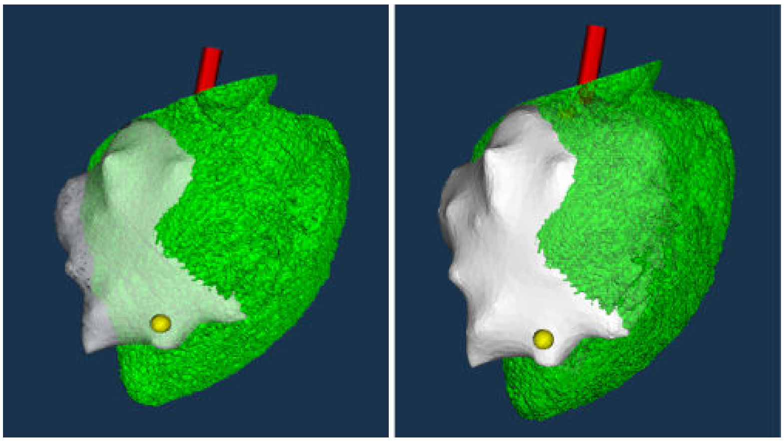

Figure 6.11: Resulting EAM to CT registration using the semi-automatic method. Registered surfaces do not match due to the morphology of the EAM surface with does not allow to get a reliable estimation of the apex and long axis. The yellow point correspond t the localization of the RV lead.

Simon, Leclercq, Pavin, et al., 2009). Figure 6.11 shows the resulting registration for euHeart 06. It can be observed that EAM and LV surfaces do not match. This is because EAM geometry is almost round, and did not provide discriminant information to obtain the apex and long axis. The results for the patient euHeart 04 were similar.

Therefore, the landmarks annotated during EAM acquisition localizing the aortic chamber, right ventricular lead and the upper part of the lateral wall were used in a landmark based registration. To perform this procedure, corresponding landmarks were annotated in the CT image. Then, the rigid registration transformation minimizing the sum of squares of the distances between corresponding fiducials, was computed. A least-squares solution for this fiducial registration was provided by (Horn, 1987). Figure 6.12 depicts the output of the EAM to CT fiducial-based registration.

After EAM to CT registration, the electrical information on EAM surface was (i) radially projected using a cylindrical coordinate system of the cardiac model and (ii) interpolated using radial basis functions. Since no interpolation occurs in the projection step, the accuracy of measurement points is preserved (Tavard, Simon, Leclercq, Donal, et al., 2014).

6.4 Characterization of cardiac asynchronism in patients undergoing CRT

Below we discuss the methods used to associate the information resulting from registered multimodal images in order to provide an enhanced description of the heart with asynchronism.

The descriptors of cardiac asynchronism are described first (in terms of electrical and mechanical functions, and then of electromechanical coupling). Acquired data was

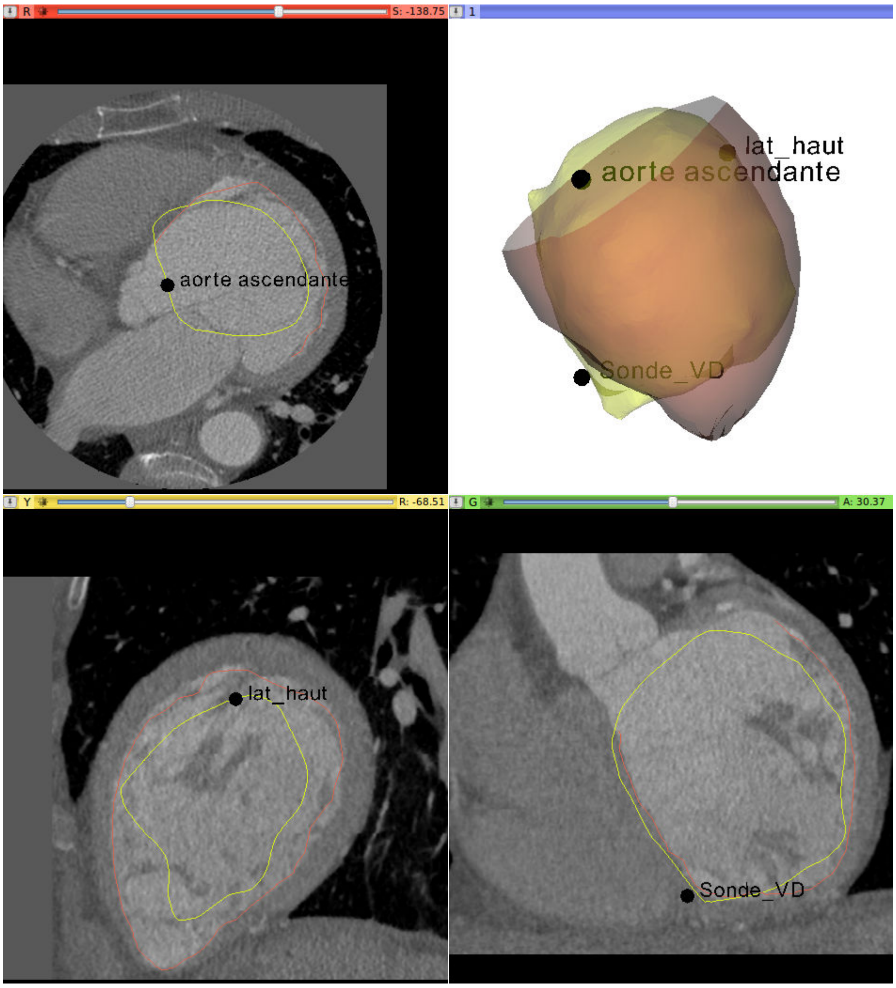

Figure 6.12: Illustration of EAM to CT registration using a fiducial-based approach. The fiducials annotated during EAM acquisition are also depicted after being registered to the CT image. Black points correspond to annotated EAM landmarks after fiducial registration: ascending aorta (aorte ascendante), top of the lateral wall (lat_haut) and RV lead position (Sonde_VD).

exploited to compute *monomodal* and *multimodal descriptors* of cardiac asynchronism at sinus rhythm and BIV stimulation. Monomodal descriptors describe the local electrical activation (from EAM), mechanical behavior and global electromechanical coupling (from STE). Then, the multimodal registration process enabled to fuse EAM and STE data to compute local electromechanical delays. Next, the incorporation of the information about myocardial tissue is considered.

6.4.1 Local activation time from EAM

From the EAM data, we extracted the local activation time (LAT) and the magnitude of the peak-voltage of local EGMs. The local activation time is the delay between a reference time and the local electrical activation measured from EGMs. It provides a description of the electrical propagation within the myocardium. The reference time is generally the activation in the coronary sinus; however, patients euHeart 06 and euHeart 04 lacked from this reference recording. Thus, the peak of the P-wave (peak-P) at the 12-lead ECG of the EAM was considered as the time reference from which the delay was computed. The resulting LAT was denoted as LAT_{ECG}:

$$LAT_{ECG} = t_{LAT} - t_P, \tag{6.1}$$

where t_P is the time instant of the peak of the P-wave and t_{LAT} is the time instant of the voltage peak of the local EGM (peak-EGM). t_p was selected because, in the absence of recordings of the electrical activity at the coronary sinus, the P-wave, providing the information about atria depolarization, is a more reliable referential than, for instance, the QRS complex, whose morphology and dynamics will be greatly altered by BIV pacing.

The magnitude of the peak-voltage of local EGMs (V_{LAT} or peak-EGM) was also computed to describe the magnitude of the local electrical stimulation:

$$V_{LAT} = EAM(t_{LAT}). \tag{6.2}$$

LAT_{ECG} and V_{LAT} were computed for sinus rhythm and under BIV stimulation conditions. Figure 6.13 illustrates the extraction of these indicators.

6.4.2 Peak-strain and global electromechanical delays from STE

The descriptors detailed in this section have been extracted from STE, for each segment considered during STE acquisition (6 segments for each view). We first extracted the peak-strain amplitude (peak-strain):

$$\text{peak-strain} = strain(t_{ps}), \tag{6.3}$$

where t_{ps} is the time instant for the peak of the regional longitudinal strain.

The *global electromechanical delays* (gEMD) were also computed from STE data. They are measured between: (i) the beginning of the QRS and (ii) the regional peak-strain instant (t_{ps}). These delays provide a characterization of the electromechanical coupling, i.e. the coupling between the electrical activation of the cardiac tissue and its mechanical contraction. They are defined as (cf. Figure 6.13):

$$g\text{EMD} = t_{ps} - t_{QRS}. \tag{6.4}$$

However, the surface ECG is a global view of the cardiac electrical activation. Therefore, these delays consider that all cardiac segments are electrically activated simultaneously. This is why they are referred to as “global”.

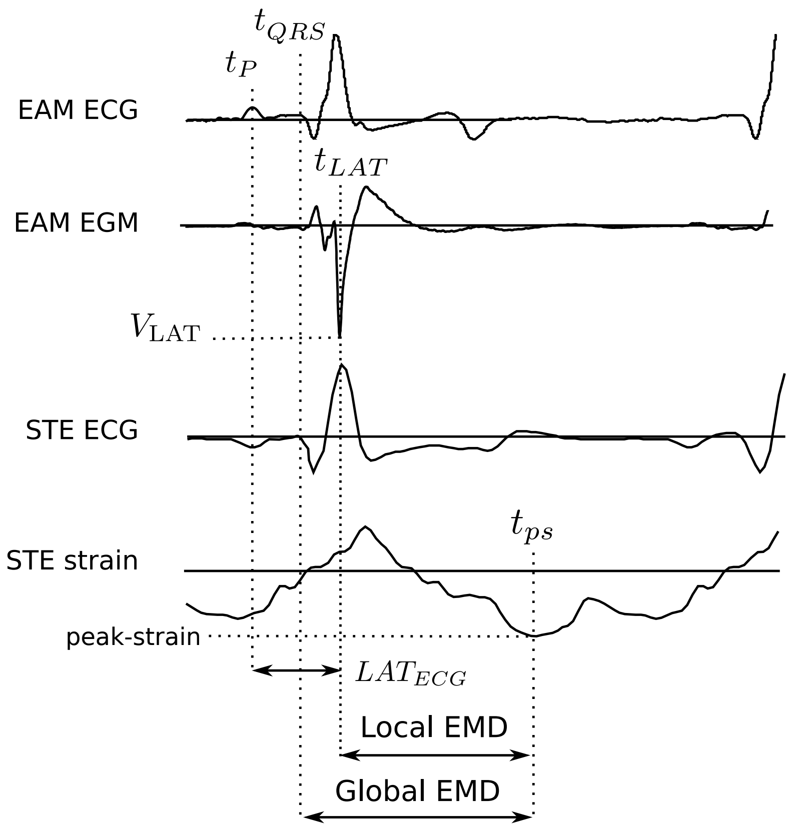

Figure 6.13: Illustration of the computation of global and local indicators of cardiac asynchronism.

Synchronization of multiview STE acquisitions. These global electromechanical delays were computed both, for the STE-2CH and for the STE-4CH acquisitions. However, even if they were acquired during the same examination, the STE-2CH ECG and the STE-4CH ECG may differ. Then, the adaptive DTW procedure described in 3.2.1.2 was used to align STE-4CH and STE-2CH acquisitions over time. We used the derivative of the ECG signals as input of the DTW procedure. Figure 6.14 presents and instance of the DTW alignment of STE-4CH and STE-2CH.

6.4.3 Local electromechanical delays

The results of the multimodal registration between EAM and STE enabled to compute, for each STE-segment, multimodal indicators describing the local coupling of the electrical and mechanical function, i.e. the intra-segment delay between its electrical stimulation and its mechanical response. Thus, we computed the *local electromechanical delay* (ℓEMD), defined as:

$$\ell\text{EMD} = t_{ps} - t_{LAT} \tag{6.5}$$

where t_{ps} is the time instant of the peak strain and t_{LAT} is the time instant of the peak-EGM. The computation of ℓEMD is illustrated in Figure 6.13. This indicator was

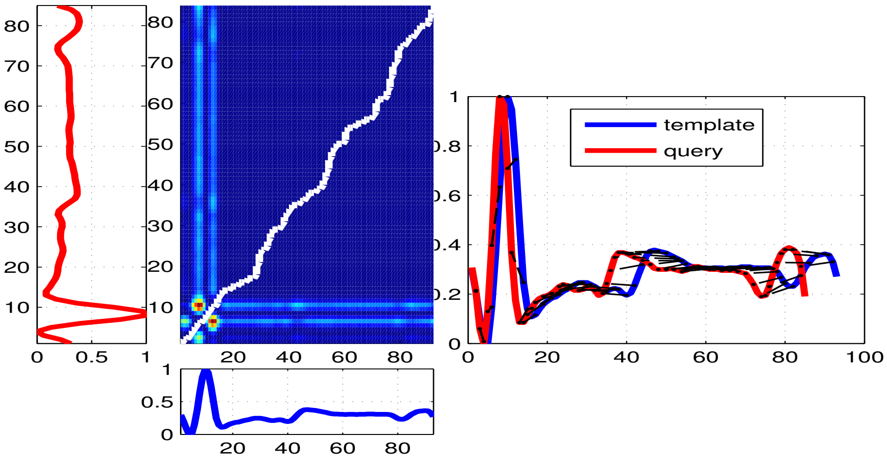

Figure 6.14: DTW output between the STE-2CH ECG (template) and STE-4CH ECG (query) signals.

computed for sinus rhythm and under BIV stimulation conditions.

Synchronization of STE and EAM data. Because ECG dynamics vary nonlinearly between STE and EAM acquisitions, the computation of these multimodal markers needs a previous synchronization of strain curves from STE with EAM maps. We used the a DTW procedure between the ECGs acquired during both acquisitions to perform this synchronization (Tavard, Simon, Leclercq, Donal, et al., 2014) (Tavard, 2012). The ADTW procedure described in 3.2.1.2, which did not need additional constraints except for the slope constraint, was used. It was applied to the ECGs of STE and EAM. This synchronization was performed in two steps. Given that the 12-lead ECG was stored for each EAM study while only one did during US, a classical approach based on the calculation of the cross correlation between the unique ECG from STE and the different derivations in EAM was applied in order to select the best-matching in EAM derivations. The maximum cross-correlation index was used with this purpose. In the second step, the dynamic time warping between matched ECGs was performed in order to align ECG dynamics. These acquisition ECGs were delimited to the beginnings of two consecutive QRS complexes. Then, the DTW procedure described in 3.2.1 was applied between ECG derivatives over time, previously normalized to have a range of one and a mean value of zero, and interpolated to have the highest temporal resolution between them (the one from EAM, with a sampling period of 0.5 ms). Given that input signals have the same resolution, the slope constraint is set to one ($S = 1$) in the DTW alignment. Figure 6.15 illustrates the output warping of the time domains for the sinus rhythm study in EAM and the pre-implantation STE-2CH acquisition.

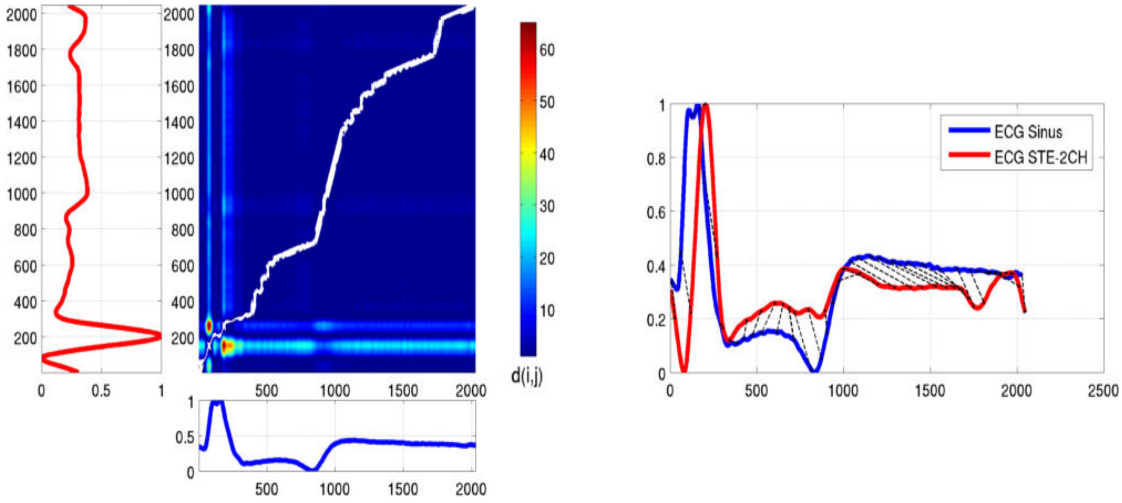

Figure 6.15: DTW output ($S = 1$) for the temporal derivatives of the matched EAM ECG (sinus rhythm) and STE ECG (pre CRT, 2CH) for patient euHeart 06. $d(i, j)$ is the distance between two time instants in input signals (derivative of ECGs). The red line represents the normalized ECG of the STE-2CH acquisition and the blue line the normalized ECG of the EAM acquisition.

6.4.4 Adding tissue state from LGE-MRI

As stated in 1.2.2.4, an overall conclusion is that postero-lateral (transmurality) scar and dyssynchrony markers are important indicators of CRT-outcome (Jansen et al., 2008). In fact, the extent of scar/fibrosis plays a central role in the success of LV stimulation. For instance, if the LV stimulation lead is placed in a zone with fibrosis/scar, the stimulation will be suboptimal or inefficient. Therefore, we are interested in characterizing the myocardial tissue state to enable the physician to detect potential optimal LV stimulation sites considering both, the asynchronism indicators described above and the extent of fibrosis.

As performed in the HCM study (cf. chapter 5), the degree of late gadolinium enhancement of a given voxel can be computed using the fuzzy c-means method proposed by (Kachenoura et al., 2008) (cf. 5.3.3.2). It requires the inner and outer contours of the myocardium to be delineated. Inner contours were obtained by propagating the LV extracted model computed from CT image segmentations (cf. 6.3.1). Outer contours were manually delineated in LGE-SAX using ITKSNAP (Yushkevich et al., 2006). However, none of the available patients in euHeart study was reported with scar/fibrosis. Thus, it was not possible to test the impact of this process for CRT application.

The descriptors presented above were used to characterize the cardiac asynchronism of the CRT patients under study.

6.5 Results and discussion

The fusion of such an heterogeneous multisensor dataset, requiring different steps to exploit the complementary information they contain, is a complex procedure. The lack of complete acquisitions (e.g. from the nine patients enrolled in the euHeart study at CHU-Pontchaillou in Rennes, only five had the EAM acquisition), the preprocessing of these data, the parametrization of each registration procedure and the required interaction with some of them, harden this task.

One issue to highlight concerns the preprocessing of EAM data: a typical acquisition includes more than 30 studies performed in sinus rhythm and under 29 different types of BIV stimulation. Although we focus on sinus rhythm and the retained BIV stimulation mode in this work, each acquisition contains different signal recordings including the raw/filtered ECGs and the raw/filtered voltage maps, recorded during multiple heartbeats. Moreover, not all acquisitions presented a consistent EGM morphology (i.e. the same EGM morphology during the acquisition), reducing the number of cases for which the EAM analysis can be performed. This is illustrated in Figure 6.16 where, for one EAM study, it can be noted that EGMs presented different morphologies (at least three). The difficulty in such a case is to determine which of the morphologies is the result of the underlying BIV-pacemaker configuration. Then, only consistent acquisitions of BIV stimulation were considered.

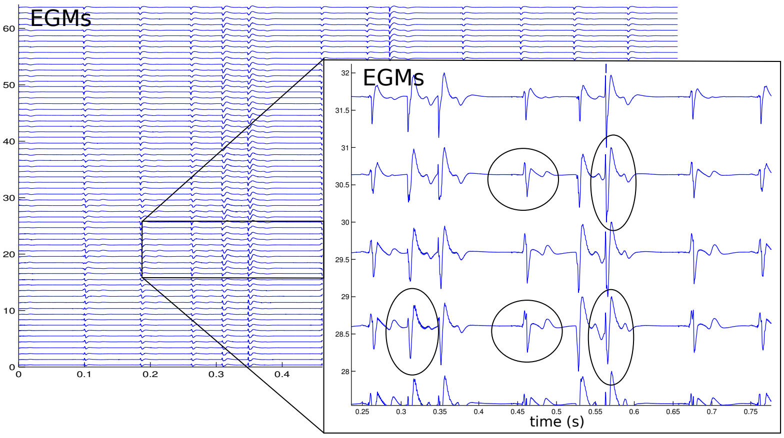

Figure 6.16: EAM recordings of endocardial EGMs (64 points) with variations in morphology for a given EGM (some of them highlighted with ellipses). Note that this acquisition was performed for a unique type of BIV stimulation.

Another issue concerned the computation of LATs which was harden by the fact that it was difficult to automate both, the isolation of one EGM and the detection of the parameters needed to compute the global and local indicators of cardiac asynchronism (t_{LAT} and t_P), because multiple heartbeats were recorded. Figure 6.17 illustrates this difficulty: for the highlighted EGM (arrows), the corresponding time instant of the peak-EGM (t_{LAT}) was difficult to define given that it presented two peaks. Then, t_{LAT}

and t_P instants were manually annotated on EGM recordings.

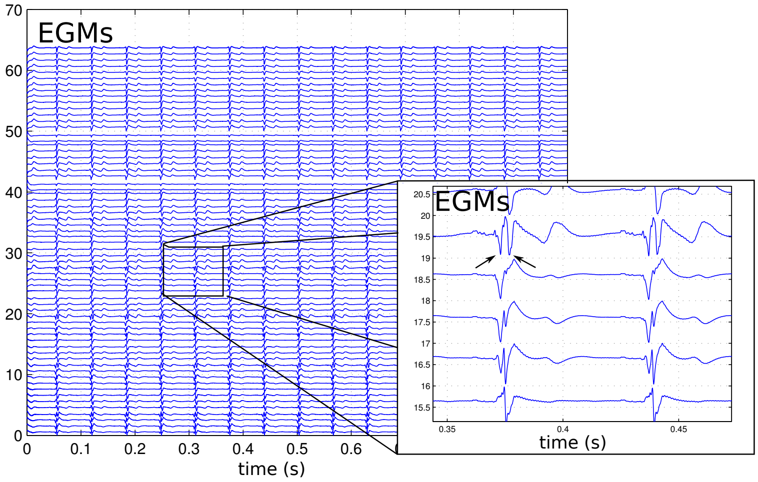

Figure 6.17: EAM recordings of EGMs (64 points) in sinus rhythm with consistent morphologies, highlighting an EGM for which it is difficult to determine the time instant corresponding to the peak-EGM (arrows).

We studied the feasibility of characterizing the cardiac asynchronism of patients euHeart 04 and euHeart 06 using the descriptors discussed before. These patients were selected because, from the patients with all multimodal images acquired, they represent the cases that best and worst responded to CRT, respectively. Moreover, their EAM examinations were acquired with a multi-electrode array, with the sinus and the retained stimulation presenting consistent EGM morphology. Table 6.1 presents the statistics for these patients. It can be noted that the response to CRT is better for euHeart 04 than for euHeart 06 with regards to the improvement of the LVEF and the QRS length, when comparing the parameters at inclusion and at six months.

Table 6.1: Parameters for euHeart 06 and euHeart 04. ACRONYMS – FU: follow-up, n.a.: non available.

Patient	euHeart 04	euHeart 06
Age (years)	74	64
Gender	Man	Woman
Ischemic etiology	No	Yes
BIV pacemaker parameters:		
Stimulation	Unipolar	Quadripolar, M2P4 (Figure 6.18)
DAV stimulated	140	150 ms
VV stimulated	n.a.	0 ms
LV stimulation site		LV postero-lateral wall
Parameters at inclusion:		
QRS	170	151 ms
NYHA	III	III
LVEF	25% (US)	20% (US)
FU three months:		
QRS	142	146 ms
NYHA	II	II
LVEF	26% (US)	29% (US)
FU six months:		
QRS	122	120 ms
NYHA	II	n.a.
LVEF	40% (US)	25% (US)

6.5.1 Characterization of the cardiac asynchronism for the patient euHeart 06

euHeart 06 was implanted with the most recent type of stimulation lead available: a quadripolar lead (a lead with four electrodes distributed from the tip of the lead (distal) towards its proximal part, cf. Figure 6.18a). The retained stimulation was: BIV stimulation (right atrium and both ventricles), with DAV=150 ms (delay between atrial and ventricular stimulation), VV=0 (right and left ventricles stimulated simultaneously) and M2P4 configuration of the quadripolar lead (highlighted with a red square in Figure 6.18a). The LV stimulation site was located in the postero-lateral LV wall. It can be noted from the follow-up parameters reported in Table 6.1 (three and six months) that LVEF and QRS remained above current CRT patient inclusion guidelines, then, euHeart 06 is a non-responder to CRT.

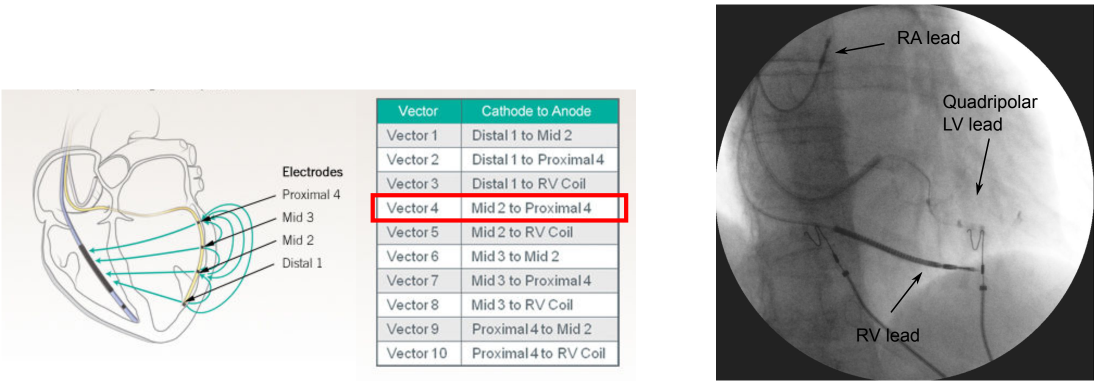

Vector	Cathode to Anode
Vector 1	Distal 1 to Mid 2
Vector 2	Distal 1 to Proximal 4
Vector 3	Distal 1 to RV Coil
Vector 4	Mid 2 to Proximal 4
Vector 5	Mid 2 to RV Coil
Vector 6	Mid 3 to Mid 2
Vector 7	Mid 3 to Proximal 4
Vector 8	Mid 3 to RV Coil
Vector 9	Proximal 4 to Mid 2
Vector 10	Proximal 4 to RV Coil

(a) Quadripolar lead and retained LV stimulation (red square). From StJude Medical.

(b) Angiographic image revealing the location of each stimulation lead.

Figure 6.18: Retained LV stimulation (left) and stimulation leads reveled by an angiographic image from euHeart 06.

6.5.1.1 Electrical function from EAM

We present in this section the results of the computation of the local activation time taking t_P (instant time of the peak-P) on surface ECG as reference (LAT_{ECG}), and of the peak-voltage (peak-EGMs). Figure 6.19 presents these information for sinus rhythm (left) and BIV pacing (right) visualized on the LV model extracted from CT segmentation. Two views are presented for the 3D surfaces: the right anterior oblique (RAO), and the left anterior oblique (LAO). To illustrate the result of the multisensor registration procedure, the electrical information was superimposed to the LGE-MRI volume (top of each subfigure) and the CT volume (bottom of each subfigure). It can be noted that the LAT_{ECG}, either for sinus rhythm or with stimulation, was lower at the septal wall and higher at the lateral wall. This is similar to the expected propagation of the depolarization front in a healthy myocardium: the first regions to be activated were in the septal wall (low LAT delays represented by dark colors), and the last regions to be activated were in the antero-lateral wall at basal level (high LAT delays represented by warm colors: yellow or white). The magnitude of the peak-EGM voltage, was stronger in the posterio-lateral wall than in the septum, both for sinus and BIV stimulation. Low differences could be visually appreciated from these images.

Bulleye maps of these information were also built. Four bulleyes maps are presented in Figure 6.20: LAT_{ECG} (top) and the peak-EGM (bottom) for sinus rhythm (left) and for the BIV stimulation (right). These bulleyes enabled to have an overall view of the electrical function regarding the delay of the electrical activity (LAT) and the intensity of this activation. From these maps, we can conclude that, overall, the distribution of the electrical activation is similar in sinus rhythm and under stimulation. Nevertheless, local activation times are slightly shorter under BIV stimulation. The decrease of the LAT were more important for the antero-lateral wall (about 20 ms). Regarding the magnitude

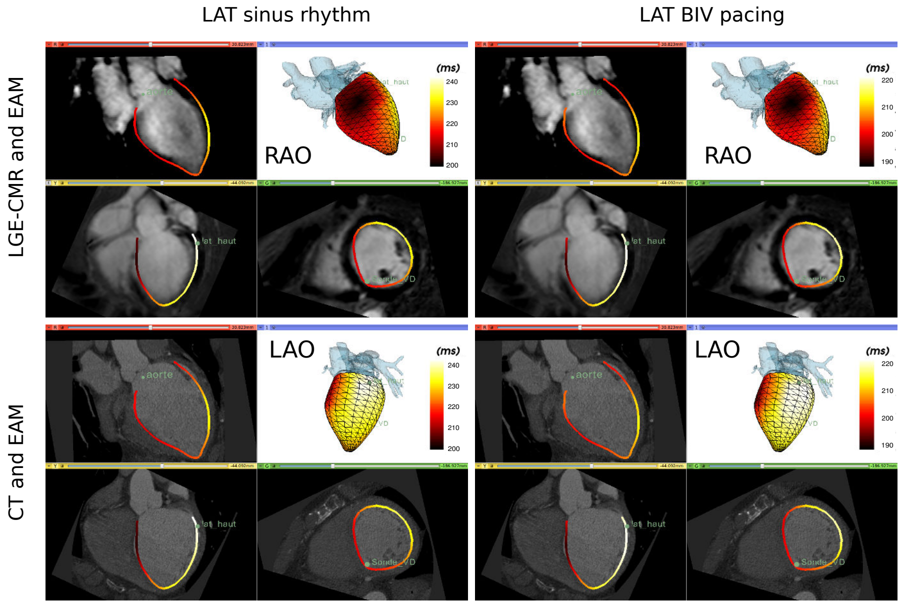

(a) LAT_{ECG}: (top) local electrical delays for sinus rhythm (left) and BIV pacing (right), superimposed to LGE-MRI (top) and CT (bottom) image volumes.

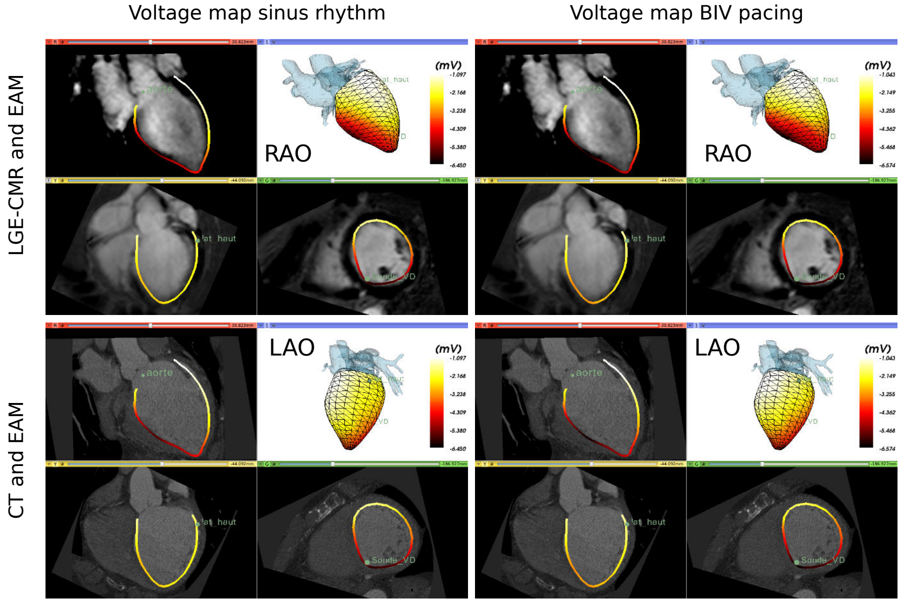

(b) Peak-EGM: (top) voltage map for sinus rhythm (left) and BIV pacing (right), superimposed to LGE-MRI (top) and CT (bottom) image volumes.

Figure 6.19: Local activation delays (top) and peak-EGMs (bottom) superimposed to the registered LGE-MRI and CT image volumes for patient euHeart 06 at sinus rhythm (left) and BIV stimulation (right). Reference time instant to compute local delays was the peak of the P wave in the ECG-derivation aVF. Acronyms – LAO: left anterior oblique view, RAO: right anterior oblique view.

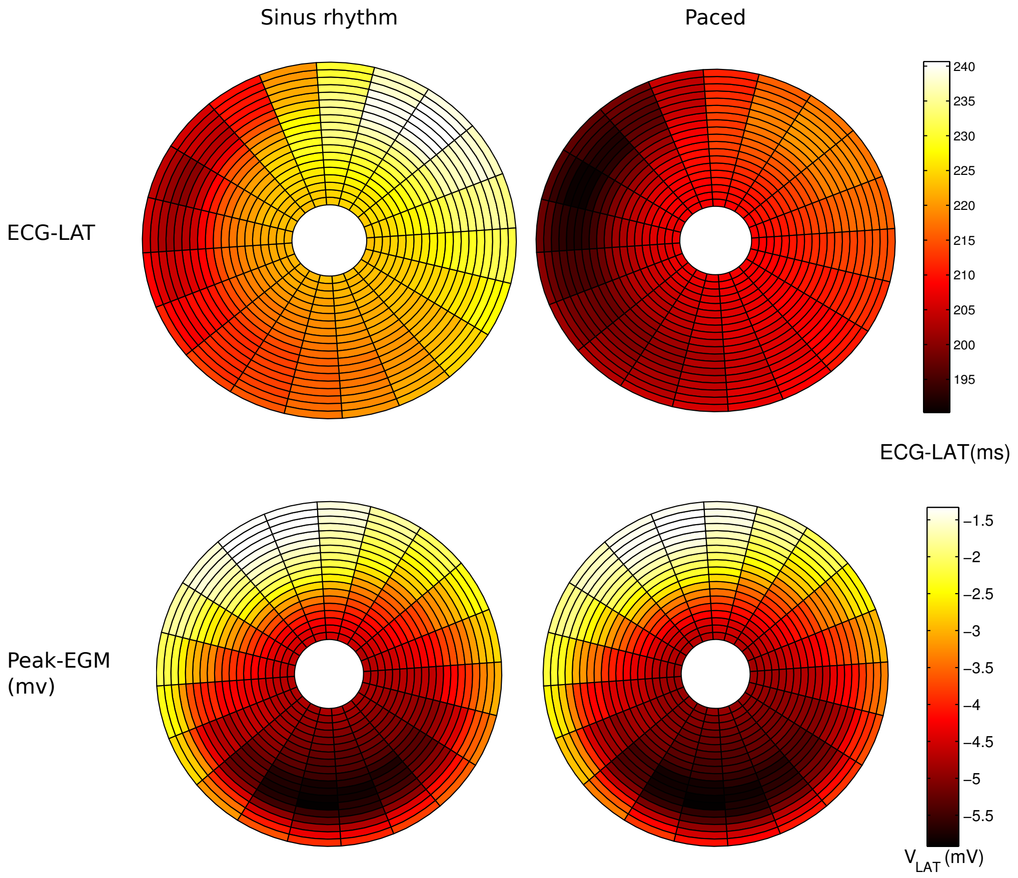

Figure 6.20: Bulleyes (380 segments) for the local electrical delays (top) and the magnitude of the peak-EGM voltage (bottom) for euHeart 06 at sinus rhythm (left) and retained stimulation mode (right). BULLEYE READING – east: lateral wall, north: anterior wall, west: septal wall, south: inferior wall, circle at center: apex, inner/medial/outer circles: apical/medial/basal zones.

of the peak-EGM, the differences were less important and the distribution did not vary when comparing sinus rhythm and BIV stimulation mode.

The analysis of these electrical indicators enabled to describe the propagation of the electrical wavefront throughout the myocardial wall in sinus rhythm and BIV stimulation. Now, we are interested to analyze the mechanical function triggered by this wavefront.

6.5.1.2 Global electromechanical delays and peak-strain from STE

Speckle tracking echocardiography was acquired before BIV-pacemaker implantation (PRE) and in follow-up at three months (POST). Figure 6.21 presents four graphics containing regional strain curves for the patient euHeart 06. The longitudinal strain curves computed from pre-implantation STE 2CH and 4CH are at top-left and top-right, respectively. The longitudinal strain curves computed from post-implantation STE 2CH and 4CH at three months are at bottom-left and bottom-right, respectively. The apical-

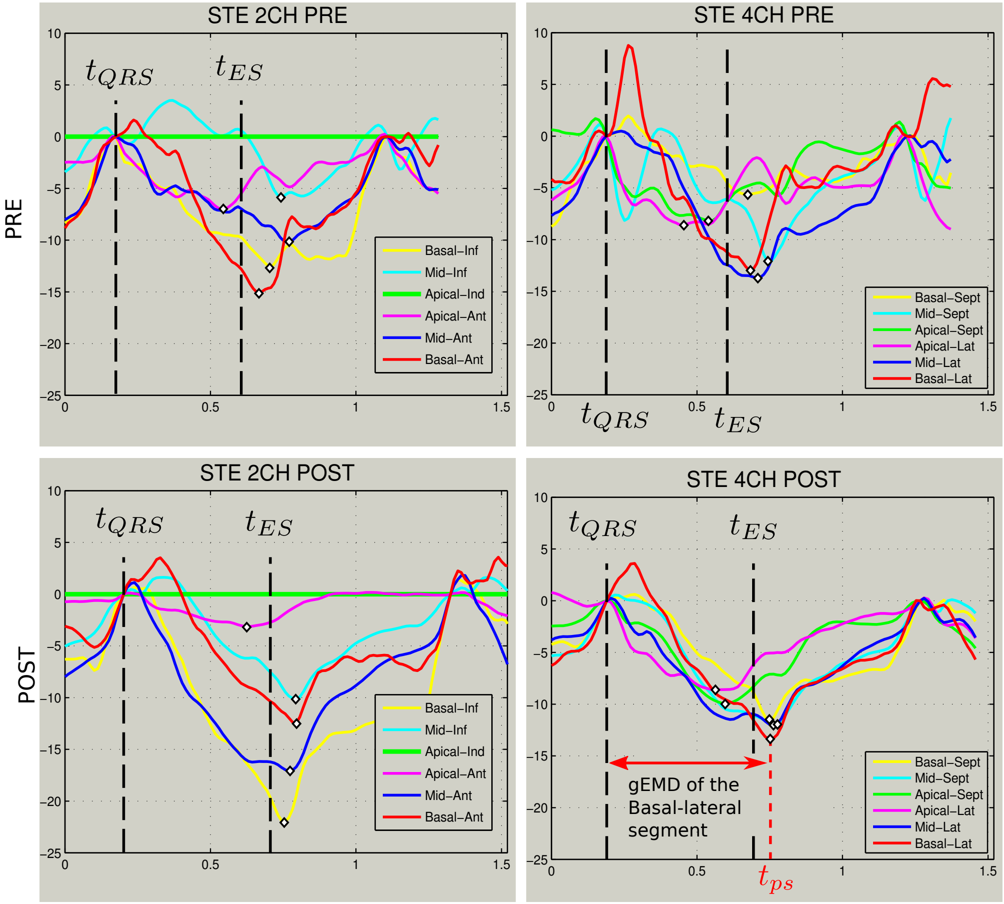

Figure 6.21: Longitudinal strain curves computed by Speckle Tracking Echocardiography for the patient euHeart 06 at pre-implantation (top, sinus rhythm) and post-implantation (bottom, retained stimulation) after three months (follow-up). (Left) curves from the STE-2CH acquisition and, (right) curves from the STE-4CH acquisition. Note that the apical-inferior strain curve is not available. The gEMD is illustrated for the basal-lateral segments in post-intervention STE. Acronyms – t_{ES}: annotated end-systolic time instant using the closure of the aortic valve, t_{ps}: instant of the maximal contraction (diamond points), t_{QRS}: annotated time corresponding to the starting of the QRS-complex.

inferior strain curve was not available in STE data. It can be noted that pre-implantation strain curves were irregular, with many peaks (notably for STE-4CH), which means different periods of longitudinal contraction and relaxation during the cardiac cycle and not a well defined contraction/relaxation per region, as in a healthy heart. Strain curves from post-implantation acquisitions were more regular.

Three time instants were annotated in the STE examination: t_{QRS} which is the time instant corresponding to the beginning of the QRS-complex, t_{ES} which is the time instant corresponding to the end-systole (commonly when the aortic valve closes), and the time of the peak-strain (t_{ps}).

The delay from t_{QRS} to the instants of the peak-strain (t_{ps}, illustrated in red for the STE-4CH basal-lateral segment in Figure 6.21 (bottom-right)), corresponds to the

gEMD (cf. Equation (6.4)), and describes the delay of the regional peak-strain from the moment of the starting of the electrical function. This is an indicator of how fast the global starting of the depolarization wavefront triggers a mechanical regional longitudinal deformation (strain). The computation of this indicator is illustrated in Figure 6.21 (bottom-right).

t_{ES} enables to know if, for a given region, the instant of the maximum longitudinal strain (longitudinal contraction) occurs before or after end-systole. This allows to tag those regions being effective in the deformation of the myocardial wall and, thus, contributing to the ejection of blood towards the systemic circulation. This was marked in the bulleye maps with a star. Table 6.2 contains the computed gEMD and resulting bulleye maps are in Figure 6.22 (top). Note that, because gEMDs were computed from 2D STE acquisitions, the bulleye maps only contains information in 12 regions: 6 regions from the STE-2CH acquisition (anterior and inferior walls, regions arranged vertically in the bulleye), and 6 regions from the STE-4CH acquisition (septal and lateral walls, regions arranged horizontally in the bulleye). Acquisition ECGs were used to synchronize 2CH and 4CH STE acquisitions. Given that the morphology of the ECG change greatly between PRE and POST acquisitions, the synchronization of PRE and POST acquisition is difficult. Then, STE-4CH acquisitions were synchronized to STE-2CH, independently for PRE and POST (cf. 6.4.2). Thus, the comparison between PRE and POST global electromechanical delays must be performed carefully because of the difference in cardiac frequency and ECG dynamics. Then, gEMDs were extracted from STE-2CH (anterior and inferior regions) and from synchronized STE-4CH (lateral and septal regions), acquired at pre-implantation (sinus rhythm) and post-implantation (BIV stimulation).

gEMD was lower in apical regions than in medial and basal regions both, in pre- and post-implantation. The effect on gEMD of the BIV stimulation varied between the regions represented in the bulleye: gEMD was shorter than in sinus rhythm for the lateral and septal walls and for the mid-anterior region, and it was delayed for the basal- and apical-anterior regions and the inferior wall. Thus, BIV stimulation modified the electromechanical activity non uniformly: it was decreased in most regions (7 out of 12) but delayed for the others. In addition, the number of segments reaching the peak-strain after the end-systole did not varied.

Global electromechanical delays computed from STE provided insights about the electromechanical coupling of the patient's LV. However, the ECG is a global view of the cardiac electrical activation; thus, considering it as the electrical reference leads to the assumption that electrical delays within cardiac segments (intra-segment delays) are negligible compared to delays between cardiac segments (inter-segment delays). In other words, these delays consider that all cardiac segments are electrically activated simultaneously. Moreover, the correlation between electrical and mechanical dyssynchrony has not proven to be strong (Varma et al., 2010). This may explain why the use of

Table 6.2: Global electromechanical delay computed from pre- and post-implantation STE. Values in bold type correspond to peak-strain occurring after the end systole (aortic valve closure), i.e. a region with non-effective contraction. ACCRONYMS – n.a. = not available.

		Basal-Inf	Mid-Inf	Apical-Inf	Apical-Ant	Mid-Ant	Basal-Ant
2CH	PRE	**595**	**626**	n.a.	431	**657**	**554**
	POST	**605**	**643**	n.a.	479	**618**	**643**
		Basal-Sept	Mid-Sept	Apical-Sept	Apical-Lat	Mid-Lat	Basal-Lat
4CH	PRE	**735**	**773**	495	470	**773**	**735**
	POST	**694**	**732**	454	429	**732**	**694**

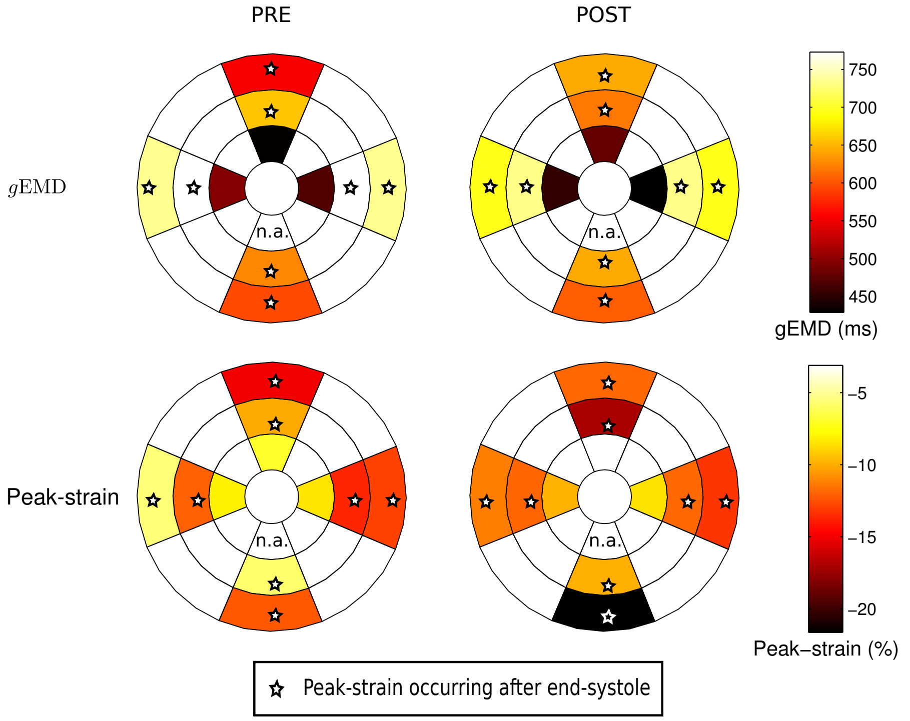

Figure 6.22: Bulleye maps of the global electromechanical delay (top) and peak-strain (bottom) at sinus rhythm (left) and BIV stimulation (right), for patient euHeart 06. BULLEYE READING – east: LV lateral wall, north: LV anterior wall, west: septal wall, south: inferior wall, circle at center: apex, inner, medial and outer circles: apical, medial and basal zones, respectively. ACRONYMS – n.a.: not available.

echocardiography only for the analysis of mechanical dyssynchrony has been shown as an insufficient mean for a better selection of patients undergoing CRT (RethinQ and POSPECT studies (Beshai et al., 2007) (Chung et al., 2008)).

From the analysis of these monomodal indicators, it was observed that, even if LAT_{ECG} are slightly improved as well as the peak-EGMs values, the contractions of most of the STE regions continues to be non-effective, except for the apical region (whose contraction was also effective in sinus rhythm). The gEMD indicator did not allow to discern about the origin of the asynchronism, i.e. if it is of electrical or mechanical causes. Note also that gEMD values will change if another STE to STE synchronization were used (e.g. synchronizing PRE and POST acquisitions). However, it is difficult to provide a synchronization between PRE and POST acquisitions given the big change in ECG morphologies. In this context, the fusion of STE information with EAM acquisitions enabled to compute a description of the local electromechanical coupling providing a more comprehensive characterization of the cardiac asynchronism.

6.5.1.3 Local electromechanical delays from the fusion of EAM and STE

Local electromechanical delays (ℓEMD) were calculated from registered EAM and STE images. This indicator is a local description of the mechanical response to an electrical stimulus, i.e. a local description of the electromechanical coupling. In a healthy heart, the value of ℓEMD should be more or less the same for all cardiac segments, i.e., the dispersion of this indicator should be low. Then, if the depolarization wavefront propagates in some milliseconds throughout the myocardial tissue, in a healthy heart, the mechanical response will be homogeneous, assuring a synchronous and efficient contraction of the myocardium. Moreover, given that the time reference in ℓEMD computation is local (EMGs and regional strain curves), this descriptor should be less sensitive than gEMD to changes of the cardiac frequency. Thus, the comparison of ℓEMD values acquired for different conditions (such as PRE and POST), is straightforward.

Table 6.3 provides ℓEMD (in milliseconds) for the patient euHeart 06 in sinus rhythm and under BIV stimulation. The synchronization of STE and EAM data was performed as follows: PRE and POST STE (both, 2CH and 4CH) were synchronized to EAM data acquired in sinus and under BIV estimulation, respectively (cf. 6.4.3). Figure 6.23 presents the corresponding bulleye mapping. Here, it is important to note that the ℓEMDs with BIV stimulation was computed by considering: (i) EAM data acquired after the implantation (few weeks); (ii) STE data acquired three months after the implantation. Thus, if the ℓEMDs with BIV stimulation are given here, their interpretation should be made carefully.

It can be observed that the ℓEMD was lower in magnitude in sinus rhythm. The mean and standard deviation values of ℓEMD in sinus rhythm were 539.9 ms and 101.1 ms, respectively, versus 647.9 ms and 78.5 ms for BIV stimulation, respectively. Then, BIV pacing decreased the dispersion of local delays, providing the heart with a more homogeneous but delayed electromechanical coupling. Note that, for this patient, the bulleyes for gEMD and ℓEMD presented dissimilar trends: gEMD changed non uniformly between sinus and BIV pacing while the ℓEMD changed uniformly. However, contrary to global delays, the computation of the local electromechanical delays use a local reference (the EGM), then the comparison between PRE and POST quantifications do not require the synchronization between them. Then, even it this trend seems contradictory, ℓEMDs provide a more reliable source for the analysis of the electromechanical coupling of the left ventricle than gEMDs.

Table 6.3: Local electromechanical delays computed for the patient euHeart 06. Values in bold type correspond to peak-strain occurring after end systole (aortic valve closure). ACCRONYMS – n.a. = not available.

Indicator	2CH	Basal-Inf	Mid-Inf	Apical-Inf	Apical-Ant	Mid-Ant	Basal-Ant
ℓEMD, sinus		**640.4**	**668.4**	n.a.	484.5	**661.8**	**560.5**
ℓEMD, paced		**658.7**	**686.4**	n.a.	534	**669.2**	**683.2**

Indicator	4CH	Basal-Sept	Mid-Sept	Apical-Sept	Apical-Lat	Mid-Lat	Basal-Lat
ℓEMD, sinus		**539.6**	**567.4**	466.9	316.6	**523.6**	**508.6**
ℓEMD, paced		**675.3**	**724.4**	536.5	523.2	**739.8**	**696.3**

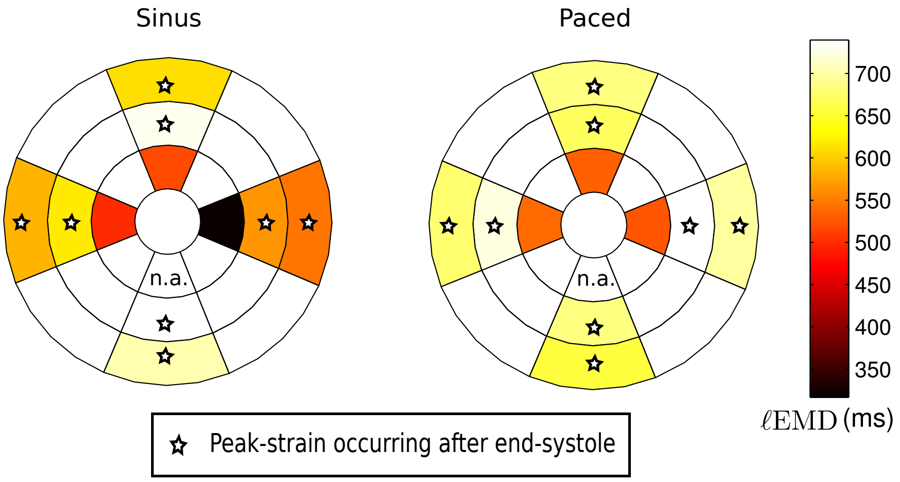

Figure 6.23: Bulleye mappings of the local electromechanical delay (ℓEMD) of euHeart 06 patient, in sinus rhythm (left) and in BIV stimulation (right). ℓEMDs were obtained by comparing the time instants of local peak-EGMs extracted from EAM and peak-strain from STE, after temporal synchronization using the DTW. Note that ℓEMD for the apical-inferior segment is absent.

The analysis of ℓEMD should be performed considering the behavior of neighboring regions. The goal of CRT is to stimulate segments that are delayed but that present a good intra-segment electromechanical coupling so that they could provide a good local mechanical response to the electrical stimulation. Therefore, as stated by (TAVARD, Simon, Leclercq, Donal, et al., 2014), these targeted segments should present homogeneous local EMDs with low values. In the case of euHeart 06, LV stimulation was performed in the lateral/posterio-lateral wall, in the medial and basal segments, with a quadripolar lead (cf. Figure 6.18a). From Figure 6.23, we observe that (i) ℓEMD of the lateral wall was not homogeneous before stimulation and (ii) the stimulation was performed in regions with medium to high ℓEMD in sinus rhythm (medial 523.6 ms, basal 508.6 ms).

6.5.2 Characterization of the cardiac asynchronism for the patient euHeart 04

The parameters of the retained BIV stimulation for euHeart 04 were not available at the moment of this study. Then, this patient was characterized with regards to their ECG-LAT, peak-EGM, and ℓEMD in sinus rhythm only. Global electromechanical delays and peak-strains, being quantified from STE, were computed in PRE and POST implantation. The LV stimulation site was located in the lateral LV wall. This patient was the one with the best response between the two analyzed. It can be noted from follow-up parameters at six months in Table 6.1 that his QRS length was slightly wide (in fact, it is into CRT patient inclusion guidelines), but his LVEF was improved beyond CRT inclusion guidelines.

6.5.2.1 Electrical function from EAM

ECG-LAT and V_{LAT} were computed as for euHeart 06 (cf. 6.5.1.1), in sinus rhythm. Bulleye maps of these indicators are in Figure 6.24: LAT_{ECG} (top) and peak-EGM (bottom). From these maps, we can observe that the electrical activation was more delayed in the inferior wall and faster in the anterior wall, which differs from the behavior of euHeart 06. Concerning the magnitudes, ECG-LATs had an analogous range than for euHeart 06 but peak-EGMs were higher. In fact, the voltage map revealed a higher voltage peak in the septal wall and a lower magnitude towards the lateral wall.

6.5.2.2 Global electromechanical delays and peak-strain from STE

Speckle tracking echocardiography was performed from US images acquired before BIV-pacemaker implantation (PRE) and in follow-up at six months (POST). Figure 6.25 presents four graphics containing regional strain curves for the patient euHeart 04. The longitudinal strain curves computed from pre-implantation STE 2CH and 4CH are at top-left and top-right, respectively. The longitudinal strain curves computed from post-implantation STE 2CH and 4CH at three months are at bottom-left and bottom-right, respectively. It can be noted that pre-implantation strain curves were irregular, with many peaks (notably for STE-4CH), which means different periods of longitudinal contraction and relaxation during the cardiac cycle. Note also that post-implantation strain curves

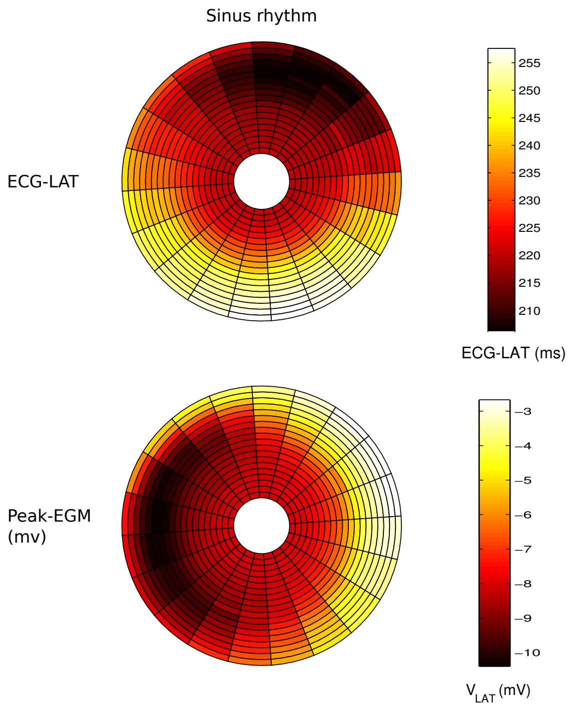

Figure 6.24: Bulleyes (380 segments) for the local electrical delays (top) and the magnitude of the peak-EGM voltage (bottom) for euHeart 04, in sinus rhythm.

presented a lower magnitude than pre-implantation curves, and they continued to have some irregularities. In fact, euHeart 04 had a poorest change in strain magnitude and smoothness after BIV pacing than euHeart 06, whose strain peaks increased and the irregularities decreased (cf. 6.21).

Table 6.4 contains the computed gEMD and resulting bulleye maps are in Figure 6.26 (top). Acquisition ECGs were used to synchronize 2CH and 4CH STE acquisitions as performed for euHeart 06. The change of the global delays under BIV stimulation was heterogeneous: it was decreased for most of the segments but some of them were delayed (mid-inferior, apical-inferior, Basal-anterior and apical-septal). The decrease after BIV pacing of the global delay in the basal and mid-septal regions and the mid- and apical-lateral regions were the highest. Nevertheless, as noted before, the regional peak strain was degraded (Figure 6.26 (bottom)). Note also that, contrary to patient euHeart 06, the regions having an effective contraction changed between sinus and BIV pacing, being less in number under BIV stimulation as well.

From the analysis of these monomodal indicators, it was observed that, even if gEMD were improved, the contraction of some STE regions continues to be non-effective. The gEMD indicator does not allowed to discern about the origin of the asynchronism. Then, we provide the computation of the local delays.

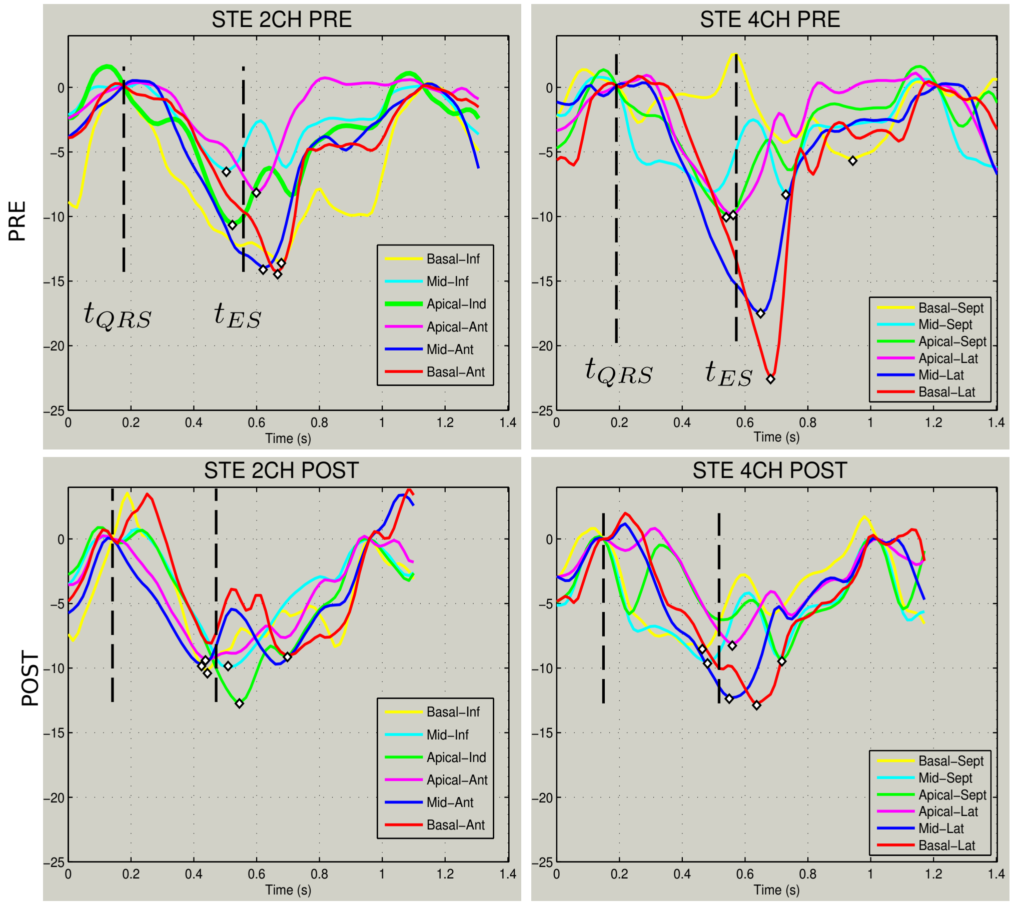

Figure 6.25: Longitudinal strain curves computed from Speckle Tracking Echocardiography for the patient euHeart 04 at pre-implantation (top) and post-implantation (bottom) after six months. (Left) Curves from the STE-2CH acquisition and, (right) curves from the STE-4CH acquisition. Acronyms – t_{ES}: annotated end-systolic time instant, t_{QRS}: annotated time instant for the beginning of the QRS-complex.

Table 6.4: Global electromechanical delay computed from pre- and post-implantation STE for euHeart 04. Values in bold type correspond to peak-strain occurring after the end systole (aortic valve closure), i.e. a region with non-effective contraction. Accronyms – n.a. = not available.

		Basal-Inf	Mid-Inf	Apical-Inf	Apical-Ant	Mid-Ant	Basal-Ant
2CH	PRE	**517**	340	368	**436**	**463**	**504**
	POST	315	378	**425**	**315**	299	**582**
		Basal-Sept	Mid-Sept	Apical-Sept	Apical-Lat	Mid-Lat	Basal-Lat
4CH	PRE	**667**	**572**	368	368	**477**	**531**
	POST	220	220	**425**	**252**	**252**	**393**

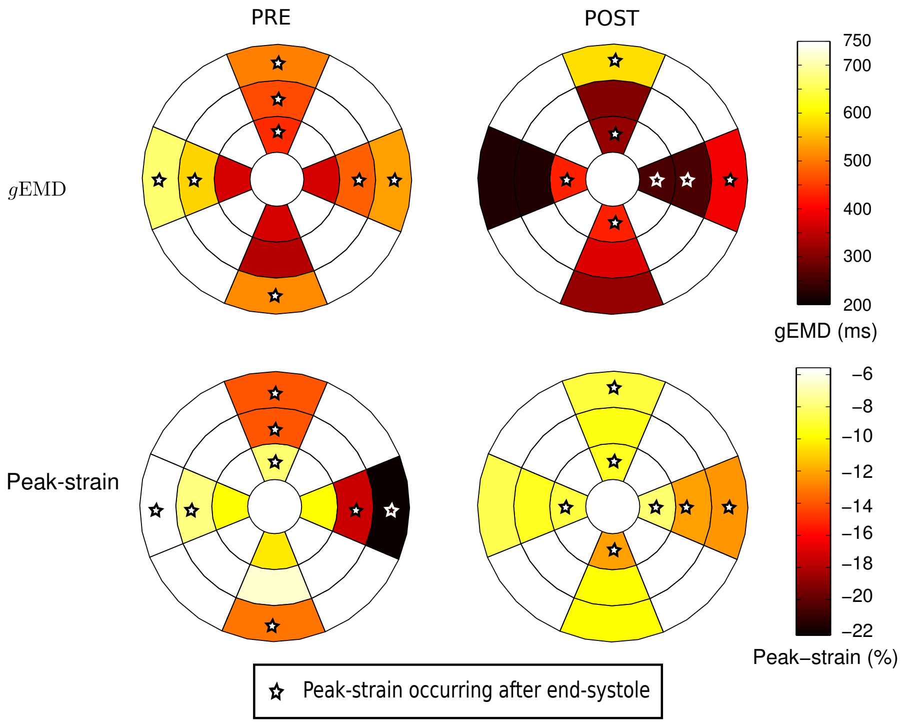

Figure 6.26: Bulleye maps of the global electromechanical delay (top) and peak-strain (bottom) at sinus rhythm (left) and BIV stimulation (right), for patient euHeart 04.

6.5.2.3 Local electromechanical delays from the fusion of EAM and STE

Local electromechanical delays (ℓEMD) were calculated from registered EAM and STE images. Given that the time reference in ℓEMD computation is local (EGMs and strain curves), the synchronization between PRE and POST data has no effect in ℓEMD behavior.

Table 6.5 provides the ℓEMD (in milliseconds) for the patient euHeart 04 in sinus rhythm. The synchronization of STE and EAM data was performed as for euHeart 06. Figure 6.27 presents the corresponding bulleye mapping. It can be observed that ℓEMD was lower in magnitude than for euHeart 06. The mean and standard deviation values of ℓEMD in sinus rhythm were 441.8 ms and 134.2 ms, respectively, versus 539.9 ms and 101.1 ms for euHeart 06. Moreover, if we focus on the stimulated zone (lateral wall), the magnitude and homogeneity of the local delays in this zone were better (lower and higher, respectively) than for euHeart 06 (compare the east side of the bulleyes in Figure 6.27 and Figure 6.23, respectively). Then, ℓEMD suggests that the response will be better for this patient (as stated by (Tavard, Simon, Leclercq, Donal, et al., 2014)), which was the case.

Figure 6.28 summarizes the bulleyes for the indicators computed for both patients, in sinus rhythm. Regarding ECG-LAT and V_{LAT} (peak-EGM), the patterns of electrical conduction showed to be quite dissimilar between these patients. The global electrome-

Table 6.5: Local electromechanical delays computed for the patient euHeart 04 in sinus rhythm. Numbers in bold type correspond to peak-strain occurring after end systole. ACCRONYMS – n.a. = not available.

Indicator		Basal-Inf	Mid-Inf	Apical-Inf	Apical-Ant	Mid-Ant	Basal-Ant
ℓEMD, sinus	2CH	**456**	215.2	310.4	**448.8**	**463.8**	**486.1**

Indicator		Basal-Sept	Mid-Sept	Apical-Sept	Apical-Lat	Mid-Lat	Basal-Lat
ℓEMD, sinus	4CH	**740**	**558.2**	318.9	356.7	**474.3**	**473.3**

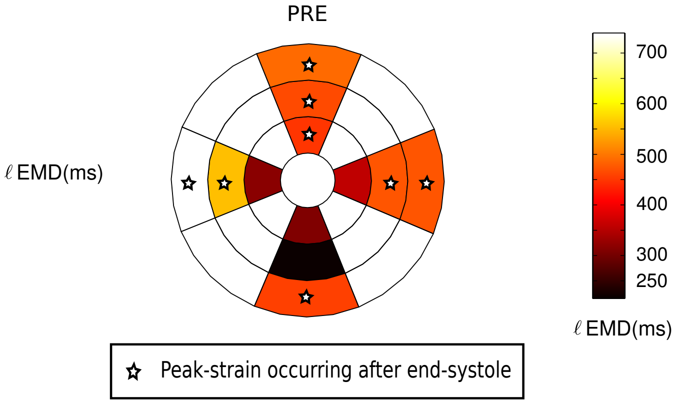

Figure 6.27: Bulleye mapping of the local electromechanical delay (ℓEMD) of euHeart 04 patient in sinus rhythm.

chanical delays also differed between them. However, the correlation between electrical and mechanical dyssynchrony from STE and ECG (global reference) has not proven to be strong (VARMA et al., 2010). In this context, local electromechanical delays provides a reliable way to assess the electromechanical coupling of the heart. The comparison of the bulleyes mappings for this indicator revealed that the zone paced for euHeart 04 presented a lower delay and a higher homogeneity than for euHeart 06. This, finding is in agreement with the hypothesis that a good stimulation site should correspond to a region with local electromechanical delays of low and homogeneous values (TAVARD, SIMON, LECLERCQ, DONAL, et al., 2014).

Study limitations. The limitations of this study are:

- This is a feasibility study; thus, the statistical significance of the descriptors used to characterize cardiac asynchronism is out of the scope of this study.
- Follow-up US information (STE) was propagated using the transform resulting from pre-operative US registration. This assumes that US acquisition planes did not change between pre and post STE acquisitions. However, given the resolution of gEMD and ℓEMD bulleyes, the effect of this assumption may be low or null.

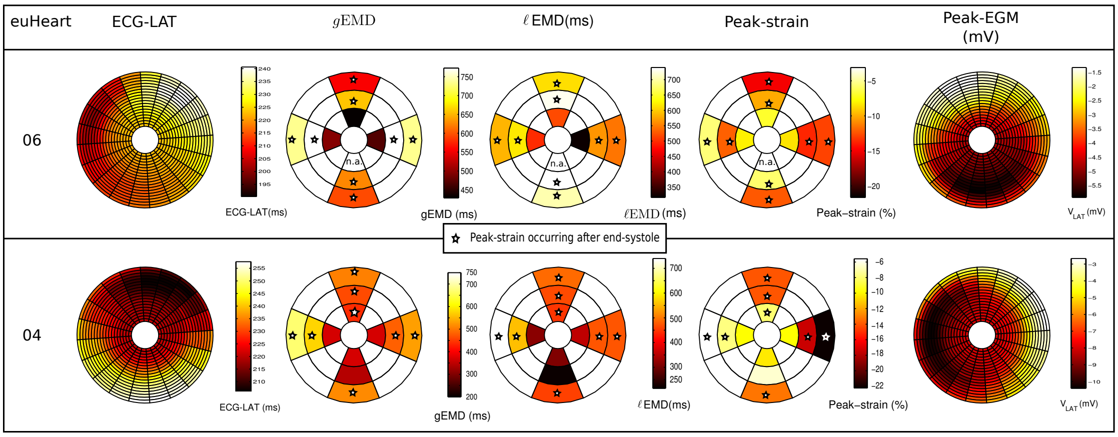

Figure 6.28: Bulleye visualization of ECG-LAT, gEMD, ℓEMD, peak-strain and peak-EGM for euHeart 06 (top) and euHeart 04 (bottom), in sinus rhythm.

- EAM data processed here lacked of a recording of a reference signal, commonly from a lead located at the coronary sinus, which would enable to compute the local activation times. Then, the peak of the P-wave at surface ECG, which depicts atrial depolarization, was used as reference given that it is more reliable between pre- and post-implantation acquisitions, than the other time instants (e.g. the starting of the QRS).
- The use of 2D US images limited the spatial resolution of the electromechanical coupling analysis (i.e. number of regions in gEMD and ℓEMD bulleyes and the size of each region). The acquisition of 3D US may improve this.

6.6 Conclusions and perspectives

The characterization of cardiac asynchronism on two heart failure patients undergoing Cardiac Resynchronization Therapy was discussed in this chapter.

Multisensor image registration enabled to associate electrical, mechanical and viability information. However, the patients under analysis for demonstration of feasibility did not presented myocardial scar nor fibrosis. The electrical information was analyzed from EAM acquisitions. Given that available EAM acquisitions lacked from both, a computation of the local electrical delays and recordings of a reference signal (commonly, the electrical activity at coronary sinus), these indicators were computed using the 12-lead ECG recordings and acquired EGMs, then being a ECG referenced LAT. Finally, longitudinal strain curves from STE 2CH and 4CH were fused with electrical recordings, in a first time, from the STE acquisition itself (acquisition ECG), providing the global electromechanical delays and, in a second time, with local EGMs recordings from EAM providing the local electromechanical delays.

This analysis of the global electromechanical delays computed from STE acquisitions enabled to study the electromechanical coupling of the heart, using a global electrical reference, i.e. considering that all cardiac segments are electrically activated simultaneously. This monomodal analysis also enabled to study the effectiveness of the contraction before and after CRT. For the patient with worst response, the retained configuration of the BIV pacemaker did not eliminate the non-effective contractions of some myocardial regions. For the patient with best response, BIV pacing changed the distribution of non-effective contraction even eliminating some of them.

The local (intra-segment) electromechanical delays showed heterogeneous values in sinus rhythm for the worst responder, especially in the lateral segments which corresponded to the localization of the quadripolar LV stimulation lead. An hypothesis of the relationship between ℓEMD and the response to stimulation is that, to response well to the stimulation, the targeted segments should present low and homogeneous ℓEMD. This hypothesis was corroborated by the patient with best response, for which the paced zone (lateral wall) presented these characteristics. Then, the analysis of the local electromechanical delays for the patients under study was in agreement.

Perspectives. Even if this study is complex, it proved the feasibility of performing an integrated multimodal description of the left ventricle in CRT patients. This study should be extended to more patients to compare the benefits for responder/nonresponder patient characterization. Thus, more data acquired in the euHeart project will be processed.

None of the patients included in euHeart database whose acquisitions were performed in CHU-Rennes had a degree of scar/fibrosis. Therefore, to better evaluate the interest to add the myocardial tissue state from MRI data, it is desirable to perform this study on a cohort of patients with fibrosis/scar to describe its impact. This would provide the opportunity to characterize the candidate zones of stimulation in LV beyond the electromechanical coupling analysis, to better localize the LV stimulation site.

References

Beshai, J. and Grimm, R. (2007). “The resynchronization therapy in narrow QRS study (RethinQ study): Methods and protocol design”. English. In: *Journal of Interventional Cardiac Electrophysiology* 19.3, pp. 149–155.

Betancur, J., Simon, A., Tavard, F., Langella, B., Leclercq, C., and Garreau, M. (2012). “Segmentation-free MRI to CT 3D registration for Cardiac Resynchronization Therapy optimization”. In: *Computing in Cardiology (CinC), 2012*, pp. 701–704.

Betancur, J., Schnell, F., Simon, A., Tavard, F., Donal, E., Hernández, A., and Garreau, M. (2013). “Spatio-temporal Registration of 2D US and 3D MR Images for the Characterization of Hypertrophic Cardiomyopathy”. In: ed. by S. Ourselin, D. Rueckert, and N. Smith. Vol. 7945. Lecture Notes in Computer Science. Springer Berlin Heidelberg, pp. 292–299.

Betancur, J., Simon, A., Schnell, F., Donal, E., Hernández, A., and Garreau, M. (2013). "Evaluation of a motion artifacts removal approach on breath-hold cine-magnetic resonance images of hypertrophic cardiomyopathy subjects". In: *IX International Seminar on Medical Information Processing and Analysis*. Vol. 8922. Proceedings of the SPIE, pages.

Chung, E. S., Leon, A. R., Tavazzi, L., Sun, J., Nihoyannopoulos, P., Merlino, J., Abraham, W. T., Ghio, S., Leclercq, C., Bax, J. J., Yu, C., Gorcsan, J., Sutton, M. S. J., Sutter, J. D., and Murillo, J. (2008). "Results of the Predictors of Response to CRT (PROSPECT) Trial". In: *Circulation* 117.20, pp. 2608–2616.

Fleureau, J., Garreau, M., Boulmier, D., Leclercq, C., and Hernandez, A. (2009). "Segmentation 3D multi-objets d'images scanner cardiaques : une approche multi-agents". In: *IRBM* 30.3, pp. 104–113.

Fleureau, J., Garreau, M., Simon, A., Hachemani, R., and Boulmier, D. (2008). "Assessment of global cardiac function in MSCT imaging using fuzzy connectedness segmentation". In: *Computers in Cardiology, 2008*. IEEE, pp. 725–728.

Horn, B. K. (1987). "Closed-form solution of absolute orientation using unit quaternions". In: *JOSA A* 4.4, pp. 629–642.

Jansen, A. H., Bracke, F., Dantzig, J. m. van, Peels, K. H., Post, J. C., Bosch, H. C. van den, Gelder, B. van, Meijer, A., Korsten, H. H., Vries, J. de, and Hemel, N. M. van (2008). "The influence of myocardial scar and dyssynchrony on reverse remodeling in cardiac resynchronization therapy". In: *European Journal of Echocardiography* 9.4, pp. 483–488.

Kachenoura, N., Redheuil, A., Herment, A., Mousseaux, E., and Frouin, F. (2008). "Robust assessment of the transmural extent of myocardial infarction in late gadolinium-enhanced MRI studies using appropriate angular and circumferential subdivision of the myocardium". eng. In: *European radiology* 18.10, pp. 2140–2147.

Marchesseau, S., Delingette, H., Sermesant, M., Cabrera-Lozoya, R., Tobon-Gomez, C., Moireau, P., Ventura, R. F. i, Lekadir, K., Hernandez, A., Garreau, M., Donal, E., Leclercq, C., Duckett, S., Rhode, K., Rinaldi, C., Frangi, A., Razavi, R., Chapelle, D., and Ayache, N. (2013). "Personalization of a cardiac electromechanical model using reduced order unscented Kalman filtering from regional volumes". In: *Medical Image Analysis* 17.7. Special Issue on the 2012 Conference on Medical Image Computing and Computer Assisted Intervention, pp. 816–829.

Schnell, F., Betancur, J., Daudin, M., Simon, A., Carre, F., Tavard, F., Hernandez, A., Garreau, M., and Donal (2013). "Alteration of longitudinal deformation is due to fibrosis in hypertrophic cardiomyopathy". In: *European Heart Journal – Cardiovascular Imaging.* 14.suppl 2, pp. ii67–ii95.

Skerl, D., Likar, B., and Pernus, F. (2006). “A protocol for evaluation of similarity measures for rigid registration”. In: *IEEE Transactions on Medical Imaging* 25.6, pp. 779–791.

Tavard, F., Simon, A., Leclercq, C., Donal, E., Hernández, A., and Garreau, M. (2014). “Multimodal Registration and Data Fusion for Cardiac Resynchronization Therapy Optimization”. In: *IEEE Transactions on Medical Imaging* 33.6, pp. 1363–1372.

Tavard, F., Simon, A., Leclercq, C., Pavin, D., Hernandez, A., and Garreau, M. (2009). “Data fusion of Left Ventricle Electro-Anatomical Mapping and Multislice Computerized Tomography”. In: *Image Processing (ICIP), 2009 16th IEEE International Conference on*, pp. 1745–1748.

Tavard, F. (2012). “Recalage et fusion d’informations multimodales pour l’optimisation de la thérapie de resyncrhonisation cardiaque”. PhD thesis. Université de Rennes 1.

Udupa, J. K. and Samarasekera, S. (1996). “Fuzzy connectedness and object definition: theory, algorithms, and applications in image segmentation”. In: *Graphical models and image processing* 58.3, pp. 246–261.

Varma, N., Jia, P., Ramanathan, C., and Rudy, Y. (2010). “{RV} Electrical Activation in Heart Failure During Right, Left, and Biventricular Pacing”. In: *JACC: Cardiovascular Imaging* 3.6, pp. 567–575.

Weese, J., Groth, A., Nickisch, H., Barschdorf, H., Weber, F., Velut, J., Castro, M., Toumoulin, C., Coatrieux, J., Craene, M., Piella, G., Tobón-Gomez, C., Frangi, A., Barber, D., Valverde, I., Shi, Y., Staicu, C., Brown, A., Beerbaum, P., and Hose, D. (2013). “Generating anatomical models of the heart and the aorta from medical images for personalized physiological simulations”. English. In: *Medical & Biological Engineering & Computing* 51.11, pp. 1209–1219.

Weese, J., Smith, N., Razavi, R., Chapelle D.and Delingette, H., Frangi, A., Hose, R., Hunter, P., and Spaan, J. (2013). *euHeart: Project Final Report.* project report. FP7-ICT-2007, IP Contract no: 224495.

Yushkevich, P. A., Piven, J., Cody Hazlett, H., Gimpel Smith, R., Ho, S., Gee, J. C., and Gerig, G. (2006). “User-Guided 3D Active Contour Segmentation of Anatomical Structures: Significantly Improved Efficiency and Reliability”. In: *Neuroimage* 31.3, pp. 1116–1128.

Conclusion and perspectives

This thesis was motivated by the needing for improving (i) the characterization of hypertrophic cardiomyopathy (HCM) and (ii) the characterization of cardiac asynchronism in the context of cardiac resynchronization therapy (CRT). The heart, being a complex multiphysics organ involving and coupling different physical phenomena, leads to consider multisensor cardiac imaging to perform these characterizations. Thus, we aimed at developing new methods for multimodal image registration and data fusion enabling to perform HCM and cardiac asynchronism characterizations and to provide new elements to help in disease diagnosis and intervention planning. The proposed methods for cardiac image registration enabled to obtain an integrated multisensed left ventricle with associated morphological and functional information. The considered imaging modalities were:

- Cardiac magnetic resonance imaging (MRI) whose late gadolinium-enhanced (LGE) sequence enables to assess myocardial viability. In the context of HCM, we were interested in analyzing myocardial fibrosis while for CRT patients, non-viable myocardial regions were of interest to characterize the stimulation sites.
- Cardiac computed tomography (CT) to represent the dynamic anatomy of the heart with a high spatial resolution enabling the assessment of the coronary veins. This ability is important in pre-operative planning of CRT. CT images were also used in this work to extract a 3D dynamic anatomical model of reference for data integration.
- 2D echocardiography imaging (US) and, specifically, speckle tracking echocardiography (STE) which offers the regional strain curves along the myocardial wall as observed in different plane cuts (2CH, 4CH, SAX views). These strain curves offer a description of the mechanical information, being the reference for the measurement of cardiac function and the asynchronism characterization in CRT. Concerning HCM, the goal was to study the relationship between cardiac mechanical function from STE and myocardial fibrosis assessed from LGE-MRI.
- Electroanatomical mappings (EAM) acquired with a balloon (non-contact) catheter, which provides the simultaneous acquisitions of the local electrical activity on the endocardial surface of patients undergoing CRT, for different stimulation modes of the biventricular (BIV) pacemaker. They allow to describe the electrical activity in

pre-implantation conditions and to evaluate the effects of CRT on the electrical activity.

These images were registered in order to provide an enhanced description of the left ventricle in a common spatio-temporal coordinate system.

The multimodal registration methods proposed in this work correspond either to improvements of those proposed in the literature or developed in previous works at LTSI-INSERM U1099 laboratory (Tavard, Simon, Leclercq, Donal, et al., 2014), or to novel methods. They were described in Chapter 3. They are characterized by some common aspects: the procedure registers multiview acquisitions when multiview images belonging to different spatial domains need to be registered; the information contained by the entire dynamic image is exploited during the registration; the adaptive dynamic time warping (ADTW) procedure is used when two dynamic multimodal acquisitions need to be aligned over time. These methods are:

MRI slice misalignment correction and registration. (Betancur, Simon, Schnell, et al., 2013) One novel method has been proposed to correct for slice misalignments that may be present in cine-MRI, and to register LGE-MRI to the corrected cine-MRI. The slice misalignment correction, using a profile based registration procedure, is guided by the information from the intersections between the slices of the different views. Different metrics have been evaluated in Chapter 4, both for LGE to LGE and cine to LGE registrations. For this purpose, a protocol for the quantitative evaluation of similarity measures, applied on real images (Skerl et al., 2006) was used.

We showed that, in the case of LGE to LGE registration, the most appropriate metric was the mean squares of structural images (MS-S), highlighting the interest of using the local entropy filter to generate a structural representation of these images. In the case of cine to LGE registration, the normalized mutual information (NMI) got the best results. To our knowledge, these evaluations have not been performed yet in literature. Finally, the slice misalignment correction of intra-sequence cine-MRI has been evaluated using expert visual assessment, showing satisfying results except for the apical region where the majority of misaligned segments were localized.

Cine-MRI to CT registration. (Betancur, Simon, Tavard, et al., 2012) To our knowledge, any method has been proposed in literature to register cine-MRI with CT image volume sequences. A spatio-temporal registration procedure exploiting the dynamic information both in CT and cine-MRI was proposed in this work. First, it uses an Adaptive Dynamic Time Warping (ADTW) method applied to normalized cross-correlation curves to align them in time. The ADTW enables to handle non-linearities related to the modification in cardiac dynamics between the acquisitions of both sequences. Then, a multi-image approach is used to register them in space. This process enables to consider all the available information (i.e. all the volumes in the two image sequences) to make the registration more robust. The evaluation of this method has been presented in Chapter 4 and includes three steps: (i) evaluation of the temporal alignment by checking the alignment of the end-systolic phase which proved that the ADTW outperforms a linear matching or a classical DTW process; (ii) similarity metric selection by using the protocol of (Skerl et al., 2006), showing that the normalized mutual information was the most appropriate metric; (iii) evaluation of the registration results using a landmark-based error measurement which showed that the use of the whole sequence in a multi-image approach increases the performance of the registration process.

2D US to CT or cine-MRI registration. (Betancur, Schnell, et al., 2013) A spatio-temporal method was proposed to register multiview US with CT or cine-MRI, exploiting the dynamic information provided by Speckle Tracking Echocardiography (STE) and by CT or cine-MRI. This method uses a spatio-temporal metric relying on the ADTW procedure applied to the Fourier descriptors of dynamic LV contours. The method improved previous works in LTSI (Tavard, Simon, Leclercq, Donal, et al., 2014) that were limited to a single-view STE registration with CT images. We proposed two improvements: (i) the use of an adapted step pattern both, to handle differences in time resolution and to get a more physiologically realistic warping between cardiac phases; (ii) the optimization of multiview STE acquisition in a single optimization procedure. US registration procedure has been evaluated with real data (cf. Chapter 4), first evaluating the temporal alignment (which also enabled to select the most appropriate number of Fourier descriptors), second assessing the metric convergence, and finally by visually assessing the registration results. It showed that 87.5% of the cardiac segments were well registered, with all the misaligned segments being localized in the apical area.

The application of these multimodal registration methods enabled to obtain an integrated multisensed left ventricle used to characterize HCM and cardiac asynchronism in the context of CRT.

In the *HCM study*, the goal was to assess the abilities of STE to describe the presence of myocardial fibrosis. For this purpose, MRI and US acquisition of 30 HCM patiens were considered. First, the traces obtained from STE were registered to cine-MRI using the ADTW-based method. Second, the registration of cine-MRI and LGE-MRI volumes enabled to correct for slice misalignments in cine-SAX and to integrate LGE-MRI to corrected cine-MRI. This registration was suitable because LGE-MRI volumes did not presented slice misalignment. Thus, US and LGE images were aligned using cine-MRI as the common reference image. An expert visual evaluation of the registration result showed that 306 segments, out of 336, were successfully registered.

Then, the fusion of strain curves extracted from echocardiography with LGE-MRI volumes enabled to study the relationship between strain and fibrosis and to assess if regional strain-derived indicators surrogates to the presence of fibrosis.

A fuzzy c-mean procedure enabled to quantify the burden of myocardial fibrosis. This indicator, expressed as the percentage of the volume of regions with fibrosis in the total myocardial volume, was in agreement with the literature. This method, needing only the inner and outer contours, is automatic, thus, with high reproducibility. A global characterization of HCM proved that the population under analysis had global indicators in agreement with the literature, notably, the correlation between global strain and the percentage of fibrosis.

A regional analysis of the longitudinal strain parameters was performed to study if they are related with the presence or not of fibrosis. This study enabled to describe the sensitivity and specificity of the strain to detect the regional fibrosis. Student's t-test proved that the expected value of the peak-strain and the time-to-peak parameters change with the presence of fibrosis ($p < 1e^{-5}$ for both indicators) (SCHNELL et al., 2013). Besides, boxplots of the observations of these indicators, for the populations of STE-regions without and with fibrosis, showed that they overlap. Then, despite the fact that the change is significant, it has a wide range, leading to an overlapping in the observations of healthy and fibrotic STE-segments. This overlapping may be explained by the presence of diffuse fibrosis that is not possible to assess from LGE-MRI.

The overlapping of strain indicators for myocardial regions without and with fibrosis resulted in a decreased strength to predicting the presence of fibrosis, which was evaluated using ROC curves. This evaluation showed a high similarity in the behavior of input indicators and their combination using a linear classifier. We conclude from ROC analysis that fibrosis is one out of different factors modifying the peak-strain and time-to-peak in the analyzed population of HCM patients.

These conclusions are interesting from a clinical point-of-view: if the US acquisition of an HCM patient shows a decreased strain, the presence of fibrosis may be suspected and a MRI acquisition may be prescribed to confirm this hypothesis. Considering that the US acquisition is far more widespread and inexpensive compared to MRI, this clinical workflow could be advantageous.

In the *cardiac asynchronism study*, the goal was to provide an enhanced description of the left ventricle in order to, in a CRT workflow, improve the selection of the LV stimulation site and to plan the intervention.

The proposed registration methods enabled to register EAM, CT, MRI and US data, in order to provide an integrated description including anatomical, electrical, mechanical and myocardial tissue information. The proposed workflow included four registration steps: LGE- to cine-MRI, cine-MRI to CT, US to CT and EAM to CT. The proposed methods enabled to perform the first three ones, the EAM registration being mainly manual.

This workflow relies on the acquisition of a large amount of data by using an invasive protocol (especially for EAM) which is nowadays possible only in experimental studies, such as euHeart, and included a limited number of patients. In order to demonstrate the feasibility of the proposed workflow, two patients were selected in the euHeart study, considering mainly the consistency of EGM recordings from EAM data and their level of response to the therapy.

From the registered data, the characterization of the asynchronism was assessed using local activation time (from EAM), peak-strain and global electromechanical delays (from STE) and local electromechanical delays (from the fusion of STE and EAM). If the characterization of the tissue state information was made possible thanks to the LGE-to cine-MRI registration, any data corresponding to a CRT patient with fibrosis and/or scar was available.

This registration and fusion workflow has been assessed on two patients undergoing CRT. The analysis of the global electromechanical delays computed from STE acquisition enabled to study the electromechanical coupling of the heart using a global electrical reference, i.e. without considering the inter-segment electrical delays. This monomodal analysis also enabled to study the effectiveness of the contraction before and after CRT, i.e. the fact that the peak-strain may occur after the aortic valve closure. For the patient with worst response, the retained configuration of the BIV pacemaker did not eliminated the non-effective contractions of some myocardial regions. For the patient with best response, the retained configuration changed the distribution of non-effective regions, eliminating one of them.

For the worst responder, the local (intra-segment) electromechanical delays showed heterogeneous values in sinus rhythm, especially in the lateral segments which corresponded to the localization of the quadripolar LV stimulation lead. In contrast, the patient with best response presented lower magnitude and more homogeneous values of local delays in the zone stimulated. An hypothesis on the relationship between local electromechanical delays and the response to stimulation is that, to response well to the stimulation, the targeted segments should present low and homogeneous delays. Thus, the analysis of the local electromechanical delays for the patients under study is in agreement with this hypothesis, even if this should be studied in depth with more patients.

The perspectives of this study include the following aspects.

From a methodological point of view, MRI slice misalignment correction and intersequence registration could be improved by adding to the metric some information related to the spatial continuity of the ventricle (e.g. by using segmentation), in order to consider not only the intersection profiles but also the whole continuity that should be observed in the final 3D volume.

The US to CT/MRI registrations could potentially be improved by considering not only the contour but also the intensity, e.g. developing a metric combining iconic and geometric information.

Both, US to CT/MRI and MRI to CT registration use the ADTW to temporally align the image sequences. However, even if some constraints have been added in the ADTW process, it may lead to matchings that are not physiologically realistic. New constraints, e.g. using a simple but realistic model of ECG dynamics, should be investigated.

The evaluation of the proposed methods has been performed with a specific protocol using real images. It could be extended to simulated images by using some simulation methods proposed in the literature and adapted to different modalities.

The two clinical studies could also be improved by incorporating more patients and new acquisitions. In particular, in the context of CRT, the study will be completed by the analysis of the other patients in the euHeart database. Also, data of patients presenting scar should be studied. Concerning new acquisitions, for instance the use of 3D-US acquisitions will be assessed in both studies. It would provide a full 3D description of the myocardium and probably facilitate the registration processes. However, the lower temporal resolution of 3D-US should be handled with care, especially for the assessment of the electromechanical delays in the asynchronism study.

In the HCM study, the inclusion of other MRI sequences should also be investigated, especially the MOLLI sequence to evaluate the fibrosis more precisely and to better differentiate patients with diffuse fibrosis from patients without fibrosis. In the cardiac asynchronism study, replacing the EAM acquisition, which is very invasive and can not be used in clinical routine, e.g. by a body surface potential mapping, would be very advantageous. The use of this modality will however imply to solve the inverse problem of electrical map estimation. Finally, the incorporation in the operating room of the proposed process should be made, using for instance per-treatment angiographic to pre-treatment CT images registration, in order to perform a new step towards an image-guided CRT workflow.

References

Beshai, J. and Grimm, R. (2007). “The resynchronization therapy in narrow QRS study (RethinQ study): Methods and protocol design”. English. In: *Journal of Interventional Cardiac Electrophysiology* 19.3, pp. 149–155.

Betancur, J., Simon, A., Tavard, F., Langella, B., Leclercq, C., and Garreau, M. (2012). “Segmentation-free MRI to CT 3D registration for Cardiac Resynchronization Therapy optimization”. In: *Computing in Cardiology (CinC), 2012*, pp. 701–704.

BETANCUR, J., SCHNELL, F., SIMON, A., TAVARD, F., DONAL, E., HERNÁNDEZ, A., and GARREAU, M. (2013). "Spatio-temporal Registration of 2D US and 3D MR Images for the Characterization of Hypertrophic Cardiomyopathy". In: ed. by S. OURSELIN, D. RUECKERT, and N. SMITH. Vol. 7945. Lecture Notes in Computer Science. Springer Berlin Heidelberg, pp. 292–299.

BETANCUR, J., SIMON, A., SCHNELL, F., DONAL, E., HERNÁNDEZ, A., and GARREAU, M. (2013). "Evaluation of a motion artifacts removal approach on breath-hold cine-magnetic resonance images of hypertrophic cardiomyopathy subjects". In: *IX International Seminar on Medical Information Processing and Analysis*. Vol. 8922. Proceedings of the SPIE, pages.

CHUNG, E. S., LEON, A. R., TAVAZZI, L., SUN, J., NIHOYANNOPOULOS, P., MERLINO, J., ABRAHAM, W. T., GHIO, S., LECLERCQ, C., BAX, J. J., YU, C., GORCSAN, J., SUTTON, M. S. J., SUTTER, J. D., and MURILLO, J. (2008). "Results of the Predictors of Response to CRT (PROSPECT) Trial". In: *Circulation* 117.20, pp. 2608–2616.

FLEUREAU, J., GARREAU, M., BOULMIER, D., LECLERCQ, C., and HERNANDEZ, A. (2009). "Segmentation 3D multi-objets d'images scanner cardiaques : une approche multi-agents". In: *IRBM* 30.3, pp. 104–113.

FLEUREAU, J., GARREAU, M., SIMON, A., HACHEMANI, R., and BOULMIER, D. (2008). "Assessment of global cardiac function in MSCT imaging using fuzzy connectedness segmentation". In: *Computers in Cardiology, 2008*. IEEE, pp. 725–728.

HORN, B. K. (1987). "Closed-form solution of absolute orientation using unit quaternions". In: *JOSA A* 4.4, pp. 629–642.

JANSEN, A. H., BRACKE, F., DANTZIG, J. M. VAN, PEELS, K. H., POST, J. C., BOSCH, H. C. VAN DEN, GELDER, B. VAN, MEIJER, A., KORSTEN, H. H., VRIES, J. DE, and HEMEL, N. M. VAN (2008). "The influence of myocardial scar and dyssynchrony on reverse remodeling in cardiac resynchronization therapy". In: *European Journal of Echocardiography* 9.4, pp. 483–488.

KACHENOURA, N., REDHEUIL, A., HERMENT, A., MOUSSEAUX, E., and FROUIN, F. (2008). "Robust assessment of the transmural extent of myocardial infarction in late gadolinium-enhanced MRI studies using appropriate angular and circumferential subdivision of the myocardium". eng. In: *European radiology* 18.10, pp. 2140–2147.

MARCHESSEAU, S., DELINGETTE, H., SERMESANT, M., CABRERA-LOZOYA, R., TOBON-GOMEZ, C., MOIREAU, P., VENTURA, R. F. I, LEKADIR, K., HERNANDEZ, A., GARREAU, M., DONAL, E., LECLERCQ, C., DUCKETT, S., RHODE, K., RINALDI, C., FRANGI, A., RAZAVI, R., CHAPELLE, D., and AYACHE, N. (2013). "Personalization of a cardiac electromechanical model using reduced order unscented Kalman filtering from regional volumes". In: *Medical Image Analysis* 17.7. Special Issue on the 2012 Conference on Medical Image Computing and Computer Assisted Intervention, pp. 816–829.

SCHNELL, F., BETANCUR, J., DAUDIN, M., SIMON, A., CARRE, F., TAVARD, F., HERNANDEZ, A., GARREAU, M., and DONAL (2013). “Alteration of longitudinal deformation is due to fibrosis in hypertrophic cardiomyopathy”. In: *European Heart Journal – Cardiovascular Imaging.* 14.suppl 2, pp. ii67–ii95.

SKERL, D., LIKAR, B., and PERNUS, F. (2006). “A protocol for evaluation of similarity measures for rigid registration”. In: *IEEE Transactions on Medical Imaging* 25.6, pp. 779–791.

TAVARD, F., SIMON, A., LECLERCQ, C., DONAL, E., HERNÁNDEZ, A., and GARREAU, M. (2014). “Multimodal Registration and Data Fusion for Cardiac Resynchronization Therapy Optimization”. In: *IEEE Transactions on Medical Imaging* 33.6, pp. 1363–1372.

TAVARD, F., SIMON, A., LECLERCQ, C., PAVIN, D., HERNANDEZ, A., and GARREAU, M. (2009). “Data fusion of Left Ventricle Electro-Anatomical Mapping and Multislice Computerized Tomography”. In: *Image Processing (ICIP), 2009 16th IEEE International Conference on*, pp. 1745–1748.

TAVARD, F. (2012). “Recalage et fusion d’informations multimodales pour l’optimisation de la thérapie de resyncrhonisation cardiaque”. PhD thesis. Université de Rennes 1.

UDUPA, J. K. and SAMARASEKERA, S. (1996). “Fuzzy connectedness and object definition: theory, algorithms, and applications in image segmentation”. In: *Graphical models and image processing* 58.3, pp. 246–261.

VARMA, N., JIA, P., RAMANATHAN, C., and RUDY, Y. (2010). “{RV} Electrical Activation in Heart Failure During Right, Left, and Biventricular Pacing”. In: *JACC: Cardiovascular Imaging* 3.6, pp. 567–575.

WEESE, J., GROTH, A., NICKISCH, H., BARSCHDORF, H., WEBER, F., VELUT, J., CASTRO, M., TOUMOULIN, C., COATRIEUX, J., CRAENE, M., PIELLA, G., TOBÓN-GOMEZ, C., FRANGI, A., BARBER, D., VALVERDE, I., SHI, Y., STAICU, C., BROWN, A., BEERBAUM, P., and HOSE, D. (2013). “Generating anatomical models of the heart and the aorta from medical images for personalized physiological simulations”. English. In: *Medical & Biological Engineering & Computing* 51.11, pp. 1209–1219.

WEESE, J., SMITH, N., RAZAVI, R., CHAPELLE D.AND DELINGETTE, H., FRANGI, A., HOSE, R., HUNTER, P., and SPAAN, J. (2013). *euHeart: Project Final Report.* project report. FP7-ICT-2007, IP Contract no: 224495.

YUSHKEVICH, P. A., PIVEN, J., CODY HAZLETT, H., GIMPEL SMITH, R., HO, S., GEE, J. C., and GERIG, G. (2006). “User-Guided 3D Active Contour Segmentation of Anatomical Structures: Significantly Improved Efficiency and Reliability”. In: *Neuroimage* 31.3, pp. 1116–1128.

APPENDIX A

List of associated publications

Conference proceedings

Betancur, J., Simon, A., Schnell, F., Tavard, F., Donal, E., Hernandez, A., and Garreau, M. (2013). "Dynamic registration of multiple-view-US and MRI for the characterization of hypertrophic cardiomyopathy". In: *Computing in Cardiology Conference (CinC), 2013*, pp. 237–240.

Betancur, J., Simon, A., Tavard, F., Langella, B., Leclercq, C., and Garreau, M. (2012). "Segmentation-free MRI to CT 3D registration for Cardiac Resynchronization Therapy optimization". In: *Computing in Cardiology (CinC), 2012*, pp. 701–704.

Betancur, J., Simon, A., Tavard, F., Langella, B., Leclercq, C., and M., G. (2012). "MRI to CT 3D+t Registration for Cardiac Resynchronization Therapy Optimization". In: *Proceedings of the 8th International Seminar on Medical Information Processing and Analysis, 2012*, pp. 67–74.

Betancur, J., Schnell, F., Simon, A., Tavard, F., Donal, E., Hernández, A., and Garreau, M. (2013a). "Spatio-temporal Registration of 2D US and 3D MR Images for the Characterization of Hypertrophic Cardiomyopathy". In: *Recherche en Imagerie et Technologies de la Santé (RITS)*.

Betancur, J., Schnell, F., Simon, A., Tavard, F., Donal, E., Hernández, A., and Garreau, M. (2013b). "Spatio-temporal Registration of 2D US and 3D MR Images for the Characterization of Hypertrophic Cardiomyopathy". In: ed. by S. Ourselin, D. Rueckert, and N. Smith. Vol. 7945. Lecture Notes in Computer Science. Springer Berlin Heidelberg, pp. 292–299.

Betancur, J., Simon, A., Schnell, F., Donal, E., Hernández, A., and Garreau, M. (2013). "Evaluation of a motion artifacts removal approach on breath-hold cine-magnetic resonance images of hypertrophic cardiomyopathy subjects". In: *IX*

International Seminar on Medical Information Processing and Analysis. Vol. 8922. Proceedings of the SPIE, pages.

Schnell, F., Betancur, J., Daudin, M., Simon, A., Carre, F., Tavard, F., Hernandez, A., Garreau, M., and Donal (2013). “Alteration of longitudinal deformation is due to fibrosis in hypertrophic cardiomyopathy”. In: *European Heart Journal – Cardiovascular Imaging*. 14.suppl 2, pp. ii67–ii95.

Tavard, F., Simon, A., Hernandez, A., Betancur, J., Donal, E., and Garreau, M. (2012). “Dynamic Registration of Cardiac US and CT Data Using Fourier Descriptors and Dynamic Time Warping”. In: *Image Processing Theory, Tools and Applications, IEEE IPTA 2012 3dr International Conference*, pp. 198–203.

Tavard, F., Simon, A., Hernandez, A., Betancur, J., Donal, E., Leclercq, C., and Garreau, M. (2012). “Spatio-temporal registration of electro-anatomical mappings with functional data for CRT optimization”. In: *Computing in Cardiology (CinC), 2012*, pp. 161–164.

Terms and abbreviations

Cardiac asynchronism. Medical condition wherein the activation of different parts of the heart is improperly synchronized (cf. 1.2.2.2).

Cardiac dyssynchony. Cardiac asynchronism.

Cardiac MRI. Cardiac magnetic resonance imaging.

Cine-MRI. A MRI sequence enabling to acquire dynamic images (called cine) with white blood and gray myocardium, allowing to assess heart dynamics (cf. 1.3.4.1).

CRT: Cardiac resynchronization therapy. Medical treatment that consists in the implantation of an electronic device with multiple stimulation leads (CRT-device) aiming to correct cardiac asynchronism. This device triggers and controls myocardial contraction in order to reestablish inter- and intra-ventricular synchronism (cf. 1.2.2.3).

CT: Computed tomography. Medical imaging technique that uses computer-processed X-rays to produce tomographic images (virtual 'slices') of specific areas of the human body (cf. 1.3.3).

DTW: Dynamic time warping. An algorithm for measuring similarity between two temporal sequences which may vary in time or speed. The sequences are "warped" non-linearly in the time dimension to determine a measure of their similarity independent of certain non-linear variations in the time dimension.

EAM: Electroanatomical mapping. Invasive medical imaging technique of the heart that use cardiac catheters to acquire precise local electrical recordings of inner cardiac cavities and to estimate their geometry. The information derived from these recordings are mapped to the geometry (cf. 1.3.2).

ECG: Electrocardiogram / Electrocardiography. Non-invasive examination of cardiac function that records the electrical activity of the heart during a period of time. ECG denotes both, the examination and the signal recorded (i.e. the electrocardiogram) (cf. 1.3.1).

Fibrosis. Fibrosis is the formation of excess fibrous connective tissue in an organ or tissue in a reparative or reactive process. This can be a reactive, benign, or pathological state. In response to injury this is called scarring. Physiologically this acts to deposit connective tissue, which can obliterate the architecture and function of the underlying organ or tissue. e.g. the myocardium.

HCM: Hypertrophic cardiomyopathy. Right and/or left ventricular hypertrophy with altered diastolic and systolic function, often asymmetric, often involving the interventricular septum but sometimes with preserved left ventricular ejection fraction (LVEF) (cf. 1.2.1).

HF: Heart failure. Abnormality of cardiac structure or function leading to failure of the heart to deliver oxygen at a rate commensurate with the requirements of the metabolizing tissues, despite normal filling pressures (or only at the expense of increased filling pressures)(cf. 1.2.2).

Image fusion. Multisensor image fusion is the process of integrating multiple images and/or image-derived data and knowledge representing the same object (heart) into a consistent, accurate, enhanced and useful representation. This allows a combined analysis of input data (cf. 2.1).

Image registration. Image registration is the problem of finding a transformation that allows to describe a pair of images using a common referential. This enables to *associate* their information (cf. 2.2).

LGE: Late gadolinium-enhanced MRI. A MRI sequence using gadolinium as contrast enhanced agent to acquire images describing the viability of the myocardial tissue (cf. 1.3.4.1).

Metric. Similarity measure.

MI: Mutual information. Information theoretic similarity measure that quantifies how much information about one random variable can be obtained from the information of another random variable (cf. 2.2.3.3).

MRI: Magnetic resonance imaging. Medical imaging technique using strong magnetic fields and radiowaves to form images of the body (cf. 1.3.4).

NMI. Normalized MI.

Similarity measure. In the context of image registration, is the component (also called metric) that quantitatively measures the similarity between the transformed moving image and the reference image. This similarity indicates how well these images match (cf. 2.2.3).

Slice. In the context of cardiac MRI, a slice is an image containing a slab of anatomy effectively acquired, located at a given plane in 3D space. In a more wide sense, it is an image containing a plane cut of the anatomy acquired using a volumetric imaging technology (such as CT).

US: Echocardiography. Medical imaging technique being a sonogram of the heart. Echocardiography uses standard two-dimensional, three-dimensional, and Doppler ultrasound to create images of the heart (cf. 1.3.5).

VU:

VU:

Le Directeur de Thèse
PRENOM NOM

Le Responsable de l'école doctorale

VU pour autorisation de soutenance
Rennes, le

Le Président de l'Université de Rennes 1

Guy CATHELINEAU

VU après soutenance pour autorisation de publication:

Le Président de Jury